Molecular Engineering of Metal-Organic Assemblies: Advances Toward Next Generation Porous and Magnetic Materials

by

Gabriel Brunet

Thesis submitted in partial fulfillment of the requirements
for the Doctorate in Philosophy degree in Chemistry

Department of Chemistry and Biomolecular Sciences
Faculty of Science
University of Ottawa

Molecular Engineering of Metal-Organic Assemblies: Advances Toward Next Generation Porous and Magnetic Materials

Gabriel Brunet

Ph.D. in Chemistry

Department of Chemistry and Biomolecular Sciences
University of Ottawa

2020

Abstract

The controlled assembly of molecular building blocks is an emerging strategy that allows for the preparation of materials with tailor-made properties. This involves the precise combination of molecular subunits that interact with one another *via* specifically designed reactive sites. Such a strategy has produced materials exhibiting remarkable properties, including those based on metal-organic frameworks and single-molecule magnets. The present *Thesis* aims to highlight how such metal-organic assemblies can be engineering at the molecular level to promote certain desired functionalities. Specifically, Chapter 2 will focus on the confinement effects of a crystalline sponge on a ferrocene-based guest molecule that is nanostructured within the porous cavities of a host material. In doing so, we evaluate how one can exert some level of control over the binding sites of the guest molecule, through the addition of electron-withdrawing group, as well as tune the physical properties of the guest itself through molecular encapsulation. Notably, we demonstrate a distinct change in the dynamic motion of the ferrocene molecules once confined within the crystalline sponge. In Chapter 3, we investigate the generation of slow relaxation of the magnetization from a Co^{II}-based metal-organic framework. We compare this to a closely related 2D Co^{II} sheet network, and how slight changes in the crystal field, probed through computational methods, can impact the magnetic behaviour. This type of study may be particularly beneficial in the optimization of single-ion magnets, by sequestering metal centres in select chemical environments, and minimizing molecular vibrations that may offer alternative magnetic relaxation pathways.

We extend these principles in Chapter 4, through the use of a nitrogen-rich ligand that acts as a scaffold for Ln^{III} ions, thereby yielding 0D and 1D architectures. The coordination chemistry of Ln^{III} ions with N-donor ligands remains scarce, especially when evaluated from a magnetic perspective, and therefore, we sought to determine the magnetic behaviour of such compounds. The monomeric unit displays clear single-molecule magnet behaviour with an energetic barrier for the reversal of the magnetization, while the 1D chain displays weaker magnetic characteristics. Nevertheless, such compounds incorporating nitrogen-rich ligands offer much promise in the design of environmentally-friendly energetic materials. In Chapter 5, we take a look at different two different systems that involve the formation of radical species. On one hand, we can promote enhanced magnetic communication between Ln^{III} ions, which is typically quite challenging to achieve given the buried nature of the 4f orbitals, and on the other hand, we rely on a redox-active ligand to design stimuli-responsive metal-organic assemblies. The latter case provides access to "smart" molecular materials that can respond to changes in their environment. Here, a multi-stimuli responsive nanobarrel was studied, which displayed sensitivity to ultraviolet radiation, heat and chemical reduction.

Lastly, Chapter 6 provides a new method for the systematic generation of cationic frameworks, termed asymmetric ligand exchange. This strategy focuses on the replacement of linear dicarboxylates with asymmetric linkers that features one less negative charge in order to tune the ionicity of porous frameworks. This allows for the retention of the structural topology and chemical reactivity of the original framework, representing distinct advantages over other similar strategies. Methods to retain permanent porosity in such cationic frameworks are also proposed. Altogether, these studies highlight how the directed assembly of ordered networks can generate varied properties of high scientific interest.

Acknowledgments

When I first joined Muralee's research group as an undergraduate student, I didn't quite know what I was getting myself into. At these early stages, my passion for science was fuelled in part by Muralee's enthusiasm and willingness to teach even the most fundamental aspects of chemistry. Under your tutelage, I have embraced being put in a position to lead and perform at the highest level, be it through international collaborations or the simple completion of academic requirements. I have also come to appreciate the flexibility you have offered me in selecting my research projects, thereby allowing me to delve into various fields of chemical research. I am particularly grateful for your encouragement in developing my oral and written communication skills; proficiencies that I will carry with me for the rest of my career. My decision to complete both my Master's and Doctorate degrees as part of your research group is a testament to how much I have enjoyed working alongside you. It has truly been a pleasure, and I am proud to belong to the Murugesu research group family.

The work described in this *Thesis* would not have been possible without the support of some fantastic collaborators. In particular, I would like to thank Christophe Bucher for hosting me in Lyon, and providing me with the utmost support throughout our research collaborations. I very much look forward to our next wine and cheese! To George Shimizu, you went out of your way to provide us with invaluable support and insight regarding our current and potential research projects, it has been much appreciated. I would also acknowledge the work of all the crystallographers that I have worked with over the years, including Ilia Korobkov, Bulat Gabidullin, Koen Robeyns and Jeffrey Ovens. We often state that our chemistry only begins once we have successfully obtained a single-crystal X-ray structure, clearly highlighting the importance of each of you on my research projects.

At the University of Ottawa, I have had the pleasure of collaborating with some amazing researchers, and want to take this opportunity to thank Eva Hemmer, Tom Woo, Glenn Facey and Jaclyn Brusso for being great teachers and supporters of my research. I would also extend a special thank you to Darrin Richeson for being a committee member for both my Master's and doctoral theses – I have always highly valued your advice and feedback.

Having been part of the Murugesu group for so long, I have had the opportunity to meet and befriend so many amazing people. To Becky, you have been thoroughly missed these last couple years - I still cherish the times we were sharing an office space and exchanging stories about Solls. Thank you for being a wonderful friend, and so understanding of the challenges related to being a grad student. Riccardo, its unfortunate your stay with us was so short, however you left a lasting impression on me in how you carried yourself on a day-to-day basis. You are everything we could possibly ask for in a postdoc, and I want to thank you for being such a great mentor and friend. Other group alumni that hold a special place for me include, in no particular order, Fatemah, Cyril, Maykon, Po-Heng, Tomasz, Jen, and Tom. I am grateful to have had the chance to work alongside each of you in some capacity or another; you all contributed to making my studies that much more enjoyable.

In terms of current group members, Katie, you've been with me the longest, and while our chemistries didn't often cross paths, you've been a fantastic labmate, and I want to thank you for organizing a bunch of fun activities with the group over the years. Paul - thank you for helping with all the little things that keep the lab running smoothly. You've been a true team player and I'll always remember the conference we attended together in Brazil. Diogo, it has been an absolute pleasure having you in Ottawa, and I hope that you will continue to share the caipirinha tradition with new members of the group. To Jeremy, Alex Goudreault, Alex Therien, Sven, and André, I couldn't ask for a better group of chemist friends to joke around and enjoy the moment with.

Lastly, thank you to my brother Alex, my aunt Suzanne, and my grandparents Lise and Raymond, for your unconditional support and love throughout these long academic years. Most importantly, thank you to my mom Diane, for your immeasurable support and contribution to my life. You have taught me the value of hard work, perseverance, and integrity in everything that I do. I couldn't ask for a better role model.

Table of Contents

List of Tables

List of Figures

List of Abbreviations

AC	Alternating current
ALE	Asymmetric ligand exchange
BET	Brunauer-Emmett-Teller
COF	Covalent organic framework
CPMAS	Cross polarized magic angle spinning
DC	Direct current
DFT	Density functional theory
DRS	Diffuse reflectance spectroscopy
EPR	Electron paramagnetic resonance
FID	Free induction decay
FR	Fast relaxation phase
FTIR	Fourier transform infrared spectroscopy
IUPAC	International union of pure and applied chemistry
KD	Kramer's doublet
MOF	Metal-organic framework
NMR	Nuclear magnetic resonance
pacs	Partitioned *acs* net
PXRD	Powder X-ray diffraction
QTM	Quantum tunelling of the magnetization
SCXRD	Single-crystal X-ray diffraction
SIM	Single-ion magnet
SMM	Single-molecule magnet
SQUID	Super-conducting quantum interference device
SR	Slow relaxation phase
SSNMR	Solid-state nuclear magnetic resonance
UV	Ultraviolet
Å	Angstrom
C	Curie constant
D	Axial magnetic anisotropy
E	Planar magnetic anisotropy
g	Landé factor
H	Magnetic field
H_c	Coercive field
Hz	Hertz
J	Coupling constant
K	Kelvin
K	Boltzmann constant
M	Magnetization
M_J	Azimuthal projection of J
M_r	Remnant magnetization
M_s	Magnetic spin states
M_{sat}	Saturation magnetization
N	Avogadro's number

n	Raman exponent
Oe	Oersted
S	Spin
T	Temperature
T_B	Blocking temperature
T_C	Curie temperature
T_N	Néel temperature
U	Energy barrier
U_{eff}	Effective energy barrier
α	Distribution parameter
χ	Magnetic susceptibility
χ'	In-phase magnetic susceptibility
χ''	Out-of-phase magnetic susceptibility
χ_S	Adiabatic susceptibility
χ_T	Isothermal susceptibility
ν	Frequency
μ_B	Bohr magneton
τ	Relaxation time
τ_0	Attempt time
θ	Weiss constant

Published Contributions

The contributions that have arisen during the course of this Ph.D. are listed below. Authorship contributions are in bold for clarity.

Peer-reviewed contributions:

1. **G. Brunet**, E. A. Suturina, G. P. C. George, J. S. Ovens, C. Bucher, M. Murugesu, A barrel-shaped metal-organic blue-box analog with photo-/redox-switchable behaviour, *Chem. Sci.*, 2019, submitted, SC-EDG-10-2019-004972.
2. R. Marin[+], **G. Brunet**[+], M. Murugesu, Shining new light on multifunctional lanthanide single-molecule magnets, *Angew. Chem. Int. Ed.*, 2019, *just accepted*, DOI: 10.1002/anie.201910299.
3. D. A. Gálico, R. Marin, **G. Brunet**, D. Errulat, E. Hemmer, S. A. Sigoli, J. Moilanen, M. Murugesu, Triplet-state position and crystal-field tuning in opto-magnetic lanthanide complexes: two sides of the same coin, *Chem. – Eur. J.*, 2019, **25**, 14625-14637.
4. **G. Brunet**, R. Marin, M.-J. Monks, U. Resch-Genger, D. A. Gálico, F. A. Sigoli, E. A. Suturina, E. Hemmer, M. Murugesu, Exploring the dual functionality of an ytterbium complex for molecular optical thermometry and slow magnetic relaxation, *Chem. Sci.*, 2019, **10**, 6799-6808.
5. **G. Brunet**, K. Robeyns, R. P. S. Huynh, J.-B. Lin, S. P. Collins, G. A. Facey, G. K. H. Shimizu, T. K. Woo, M. Murugesu, Design strategy for the controlled generation of cationic frameworks and ensuing anion-exchange capabilities, *ACS Appl. Mater. Int.*, 2018, **11**, 3181-3188.
6. **G. Brunet**, M. Hamwi, M. A. Lemes, B. Gabidullin, M. Murugesu, A tunable lanthanide cubane platform incorporating air-stable radical ligands for enhanced magnetic communication, *Commun. Chem.*, 2018, **1**, 88.
7. Y. Zhang, K. L. M. Harriman, **G. Brunet**, A. Pialat, B. Gabidullin, M. Murugesu, Reversible redox, spin crossover, and superexchange coupling in 3d transition-metal complexes of bis-azinyl analogues of 2,2':6',2"-terpyridine, *Eur. J. Inorg. Chem.*, 2018, **2018**, 1212-1223.
8. J. M. Savard, **G. Brunet**, A. Srinivasan, M. Murugesu, J. L. Brusso, Ferromagnetically coupled dinuclear M(II) complexes based on a boratriazine ligand framework, *Dalton Trans.*, 2018, **47**, 14875-14879.
9. **G. Brunet**, E. Sebastiao, T. G. Witkowski, I. Korobkov, B. Gabidullin, M. Murugesu, A nitrogen-rich ligand as a scaffold for slow magnetic relaxation in dysprosium-based 0D and 1D architectures, *Dalton Trans.*, 2018, **47**, 11782-11787.
10. T. Lacelle[+], **G. Brunet**[+], R. J. Holmberg, B. Gabidullin, M. Murugesu, Unprecedented octanuclear Dy^{III} cluster exhibiting single-molecule magnet behavior, *Cryst. Growth Des.*, 2017, **17**, 5044-5048.

11. M. A. Lemes, **G. Brunet**, A. Pialat, L. Ungur, I. Korobkov, M. Murugesu, Strong ferromagnetic exchange coupling in a $\{Ni^{II}_4\}$ cluster mediated through an air-stable tetrazine-based radical anion, *Chem. Commun.*, 2017, **53**, 8660-8663.
12. **G. Brunet**, D. A. Safin, K. Robeyns, G. A. Facey, I. Korobkov, Y. Filinchuk, M. Murugesu, Confinement effects of a crystalline sponge on ferrocene and ferrocene carboxyaldehyde, *Chem. Commun.*, 2017, **53**, 5645-5648.
13. T. Lacelle, **G. Brunet**, A. Pialiat, R. J. Holmberg, Y. Lan, B. Gabidullin, I. Korobkov, W. Wernsdorfer, M. Murugesu, Single-molecule magnet behavior in a tetranuclear Dy^{III} complex formed from a novel tetrazine-centered hydrazone Schiff base ligand, *Dalton Trans.*, 2017, **46**, 2471-2478.
14. **G. Brunet**, D. A. Safin, J. Jover, E. Ruiz, M. Murugesu, Single-molecule magnetism arising from cobalt(II) nodes of a crystalline sponge, *J. Mater. Chem. C*, 2017, **5**, 835-841.

Forthcoming contributions:

15. **G. Brunet**, A. Mansikkamäki, B. Gabidullin, R. Clérac, M. Murugesu, Tuning the magnetic behavior of Co(II) nanowires in high-dimensionality networks: from antiferromagnetic interactions to single-chain magnets, *manuscript in preparation*.
16. W. D. do Pim, F. G.Mendonça, **G. Brunet**, C. Bucher, R. T. Baker, M. Murugesu, Anion-dependent C-C cleavage of a lignin model within a cationic metal-organic framework, *manuscript in preparation*.

The future belongs to those who believe in the beauty of their dreams.
– Eleanor Roosevelt

Chapter 1
Introduction

1.1 Materials science

Today, technological progress is advancing at an extraordinary pace. Only a few decades ago did we observe the emergence of the internet and the now nearly ubiquitous so-called "smartphones". The driving force behind the development of such technologies stems from humanity's desire to continually improve upon older constructs in terms of both efficiency and functionality. In the field of computer science, this acceleration in technological innovation is expertly described by Moore's Law, which states that the number of transistors on a computer chip would double on a yearly basis.[1] While we may finally be nearing a physical limit to this trend – unless significant progress can be achieved in the fields of molecular magnetism and spintronics – a multitude of other technologies have demonstrated similar exponential growths. For example, we can think of DNA sequencing and the number of base pairs identified, or even in the energy density of batteries, each of which display similar accelerating profiles throughout the years. In this regard, materials science appears to be of critical importance in continuing our technological evolution. Modern day advances in this field prove to be a nearly inexhaustible source of new ideas and concepts, with applications ranging from green energy, to medicine and quantum computing. Ultimately, the future of this science will rely upon our understanding of molecules and the way they assemble themselves into ordered or disordered components, in addition to whether we are able to manipulate them as we so desire. The sub-microscopic

organization of atoms and molecules will inherently dictate the type of physical behaviour that we observe, and therefore, it is this great challenge, in controlling one aspect to influence another, that science continually seeks to carry out.

1.2 **Crystal Engineering**

The relationship between structure and property in solid-state materials is at the heart of crystal engineering. This field of research has its origins in the field of organic chemistry, where studies on solid-state photochemistry[2] and molecular packing[3] were carried out. Today, however, crystal engineering includes all those interested in designing specific organized phases and assemblies, thus encompassing a broad scope of disciplines. While we have yet to attain the exact level of control that the physicist Richard P. Feynman expressed in 1959 at the annual American Physical Society Meeting:

> *What would the properties of materials be if we could really arrange the atoms the way we want them? [...] I can't see exactly what would happen, but I can hardly doubt that when we have some control of the arrangement of things on a small scale we will get an enormously greater range of possible properties that substances can have, and of different things that we can do.*[1]

we have observed, in recent years, some exceptional developments in supramolecular chemistry and in controlled chemical synthesis. In fact, one could argue that the fields of metal- and covalent-organic frameworks (MOFs/COFs) are entirely founded within the principles of crystal engineering. The use of carefully designed molecular building blocks, that have an ability to be assembled using known or conceivable synthetic operations, provides access to structural and

[1] *There's Plenty of Room at the Bottom*, American Physical Society Meeting, California Institute of Technology: Pasadena, December 29th, 1959.

chemical predictability. In turn, this predictability can lead to the anticipation of specific physicochemical behaviours and complex molecular arrangements. The latter including one-, two-, or three-dimensional patterns, held together by intermolecular interactions.

As the name "crystal engineering" states, this field of research relies on the process of crystallization. One of the key advantages in working with crystalline materials, beyond the ability to perform the most accurate structure determination methods, is that we can reasonably expect the molecules to be packed in a regularly ordered fashion. While seemingly trivial, it is this characteristic which allows for establishing in-depth structure-property relationships.[4] Small deformations and the lack of continuous structures render any such correlations rather difficult. This is especially true in the field of molecular magnetism, where intermolecular and dipolar interactions are so critical. Moreover, the principles of crystal engineering can be employed to rationally improve or enhance a desired property, by changing one single feature of a molecular structure and keeping the other components identical.[5] Consequently, the effect of the structural/chemical change can be directly correlated back to the observed behaviour.

Within the context of this *Thesis,* we will take a look at how we can apply these strategies to rationally and systematically promote certain properties and behaviours in metal-organic assemblies. This will include the use of metal-organic frameworks for the targeted encapsulation of neutral and charged species, as well as the design of supramolecular assemblies for generating slow relaxation of the magnetization. Some overlap between magnetism and porosity will also be broached, through investigations on magnetic metal-organic frameworks. The common denominator among all such studies, however, lies in the fact that a certain level of chemical control can be exerted on these systems in order to promote a specific behaviour. As such, a

discussion on both crystalline porous frameworks and molecular magnetism, relevant to the subsequent projects, will be provided below.

1.3 Crystalline porous frameworks

1.3.1 Metal-organic frameworks

The development of metal-organic frameworks began with the seminal work of R. Robson and co-workers in the early 1990's, where they reported, for the first time, the possibility of generating a new class of scaffolding-like materials by linking together rod-shaped organic linkers and rigid inorganic units.[6] The fascination with this work, as highlighted by the authors, was in part due to the fact that "*approximately two-thirds by volume, of what is undoubtedly a crystal, is effectively a liquid*". The authors recognized, from a very early stage, the immense applicative potential of such assemblies, not only in generating permanently porous tunable structures, but also in imbuing them with catalytic functions. Shortly thereafter, the contributions of S. Kitagawa[7] and O. M. Yaghi[8] cemented the field of metal-organic frameworks, by demonstrating the feasibility of the approach put forward by R. Robson and synthesizing extensive families of crystalline porous frameworks. These compounds displayed porosity, crystallinity and chemical tunability. The key characteristic, however, that sets metal-organic frameworks apart from other porous materials is, without a doubt, the ability to design and control the three-dimensional arrangement of the metal clusters and organic linkers.[9] The basis of this assembly relies upon relatively robust coordination bonds that dictate the positioning of the different components of the polymeric framework. Although coordination bonds are able to direct the assembly, they are weak enough to break and re-form multiple times over during the synthetic process, allowing for the creation of highly crystalline structures.

Since the initial reports in the 1990's,[6,10] metal-organic frameworks have blossomed into an established field of research within the materials sciences. While we continue to unveil the intricacies of such materials to this day, their appeal arises mainly from the impressive pore spaces that we can potentially obtain from them. This was first proven by O. M. Yaghi using a material they entitled MOF-2 or $[Zn(bdc)\cdot(DMF)(H_2O)]_n$ where bdc = 1,4-benzenedicarboxylate, which yielded Langmuir surface areas of 270 m^2/g and 310 m^2/g from the CO_2 and N_2 gas adsorption isotherms.[11] Today, the record for surface area, which is a measure of the accessible pore space of a nanoporous framework, is held by S. Kaskel and co-workers, who have designed a framework (DUT-60) exhibiting an incredulous Brunauer-Emmett-Teller (BET) surface area of 7839 m^2/g.[12] To put this value in proper context, the area of a professional soccer pitch is roughly 7140 m^2. In order to synthesize this metal-organic framework, the authors combined the tritopic 1,3,5-tris(4'-carboxy[1,1'-biphenyl]-4-yl)benzene (bbc^{3-}) and ditopic 1,4-bis-p-carboxyphenylbuta-1,3-diene ($bcpbd^{2-}$) ligands with pre-formed $Zn_4O(CH_3COO)_6$ clusters (Fig. 1). Pre-synthesized $Zn_4O(CH_3COO)_6$ clusters were utilized as starting reagents to suppress the formation of interpenetrated structures and undesired zinc-based clusters.

The interest surrounding high surface areas is closely related to the fundamental application of metal-organic frameworks, which is their use as solid adsorbents for gas separation and purification.[13] A plethora of potential applications have been investigated in recent years for nanoporous frameworks, ranging from the removal of volatile organic compounds[14] to the capture of CO_2 from flue gas,[15] among many others. A distinct advantage of metal-organic frameworks over liquid absorbents, such as amine-based scrubbers, is that they typically exhibit weaker interactions with the guest molecules, allowing for lower energetic costs for regeneration of the material. This represents a major hurdle to overcome in the

implementation of greener and more efficient gas capture technologies. The general process of gas separation or purification involves passing a gaseous mixture through a column packed with the adsorbent, effectively yielding the porous material enriched with the select gas component. The subsequent desorption of the gas from the solid adsorbent would then permit reutilization of the material for multiple cycles.

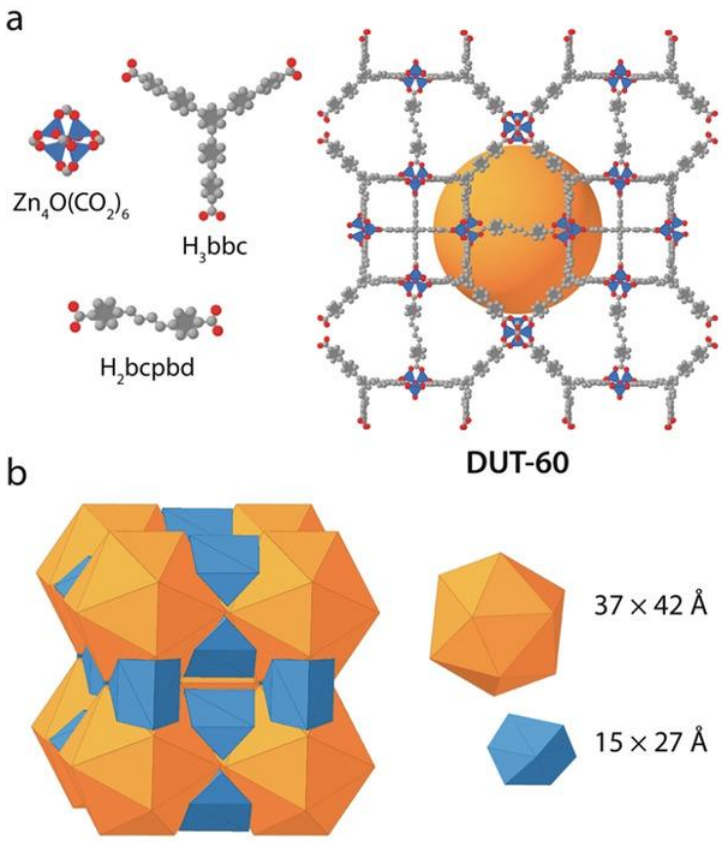

Figure 1. Assembly of the DUT-60 framework from the ditopic (H_2bcbpdc) and tritopic (H_3bbc) ligands with $Zn_4O(CO_2)_6$ clusters (a). The mesopore system is illustrated by orange and blue polygons. This figure is reproduced, with permission, from reference 12. Copyright 2018 WILEY-VCH Verlag GmbH & Co. KGaA, Weinheim.

A number of these cyclic processes are available to choose from, the most popular being thermal- or pressure-swing adsorption cycles. For such industrial processes, the thermal and

chemical stability of metal-organic frameworks is of utmost importance. While there were some initial concerns in whether hybrid inorganic-organic porous materials could exhibit sufficient stability for industrial uses, different strategies have been established over the years in order to address this specific issue. One of the most notable examples belongs to the UiO-66 family of MOFs, where they use highly oxophilic metals with high oxidation states (*i.e.* Zr^{IV}) to form strong metal-carboxylate bonding.[16] The resulting structures are stable in polar protic solvents, and even after treatment in highly acidic and basic conditions (Fig. 2).[17] With the advent of chemical stability in H_2O, the possibility of harvesting water from air has been recently envisioned using metal-organic frameworks. One particular material, developed by O. M. Yaghi, E. N. Wang and co-workers and abbreviated as MOF-801, has been shown to be able to harvest and deliver 2.8 L of water per kilogram of MOF per day at 20% relative humidity.[18] These characteristics become even more impressive considering they only required a nonconcentrated solar flux of less than 1 sun (1 kW/m^2) to produce the water. Such remarkable advances highlight not only the versatility of metal-organic frameworks for addressing pressing modern day issues,

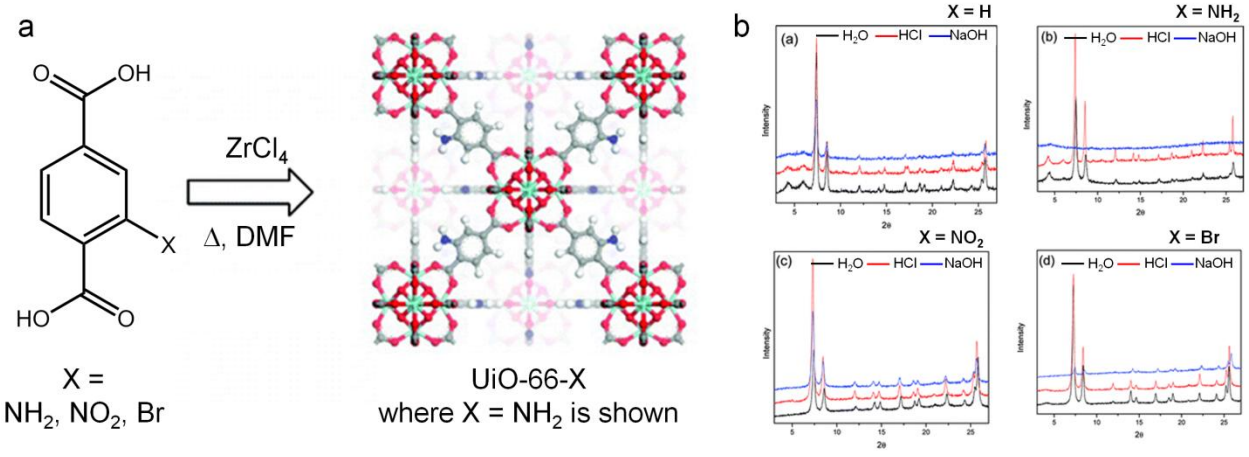

Figure 2. Synthesis of the UiO-66 family of MOFs (a), and powder X-ray diffractograms displaying their chemical stability after treatment with H_2O, HCl and NaOH (b). This figure is adapted with permission from reference 17. Copyright 2010 American Chemical Society.

but also how they may slowly begin to replace older technologies that have lower efficiencies and higher costs. Other niche applications for metal-organic frameworks, aside from gas capture, include their potential use as proton and electrical conductors,[19] molecular sensors[20] and drug delivery carriers.[21]

1.3.2 **Crystalline sponge method**

Beyond the aforementioned applications for metal-organic frameworks, a novel technique that utilizes their guest recognition capabilities for performing crystallographic studies was pioneered in 2013 by M. Fujita and co-workers.[22] This method, termed the crystalline sponge method, takes advantage of the fact that guest molecules can be efficiently trapped and regularly ordered throughout the host framework structure. This would allow for the structural determination of target molecules, using single-crystal X-ray diffraction, without the need to crystallize them independently. This section will provide a brief discussion of the technique in order to develop a background for the study presented in Chapter 2.

The crystalline sponge method consists of first selecting a porous host framework. While a few metal-organic frameworks have been identified as suitable crystalline sponges,[23] it should be mentioned that any MOF could potentially act as a suitable host, depending on the target molecule. Some key criteria for the proper selection of a host include the size of the cavities and the potential suitability of the host-guest interactions. Evaluation of the successes of this technique points towards MOFs with smaller cavities that are comparable to the size of the target molecule itself. This would simultaneously allow for the diffusion of the guest compound throughout the structure while also creating favorable intermolecular host-guest interactions that would orient and fix the guest molecule in a specific position. Thus, we restrict the movement of the guest and reduce the potential for disorder, which may hinder the crystallographic

visualization of such species. The next step – that of guest soaking – is critical. In principle, any guest that can interact more strongly with the pores of the sponge than the initial solvent can be absorbed. Solvent-exchange using the initial crystalline sponge is often suggested,[24] so as to minimize solvent-host interactions, and promote guest inclusion behaviours. However each subsequent solvent or guest exchange risks compromising the integrity of the single-crystal, through cracking and/or twinning. Thus, each soaking process should be optimized depending on the target compound and its size, polarity, flexibility and solubility. The soaking itself can be performed in a number of different ways, the most popular being either the simple dipping of the MOF crystals in a solution of the target compound (Fig. 3), or through slow evaporation. The latter is reminiscent of classical slow evaporation crystallization techniques, where a diluted solution of the guest molecule is slowly concentrated through evaporation, and forced to diffuse into the porous crystal upon reaching the saturation point.

Initially, the crystalline sponge method was met with much enthusiasm; however, several concerns were raised in terms of the quality of the crystallographic data that could be obtained from such a procedure. This was further accentuated by a correction that was brought to the original report where, due to "unnoticed ambiguities in the crystallographic data", the stereochemistry of the guest molecule (miyakosyne A) was incorrectly assigned.[22] Despite this, promising work by M. Fujita and others clearly established the viability and beauty of the method. The technique paved the way for the X-ray analysis of compounds that were previously impossible to crystallize. This could be due to the fact that the molecule in question is in short supply, difficult to produce, or even that it remains an oil or liquid at low temperatures. Consequently, we could gain access to a wealth of structural information from molecules that

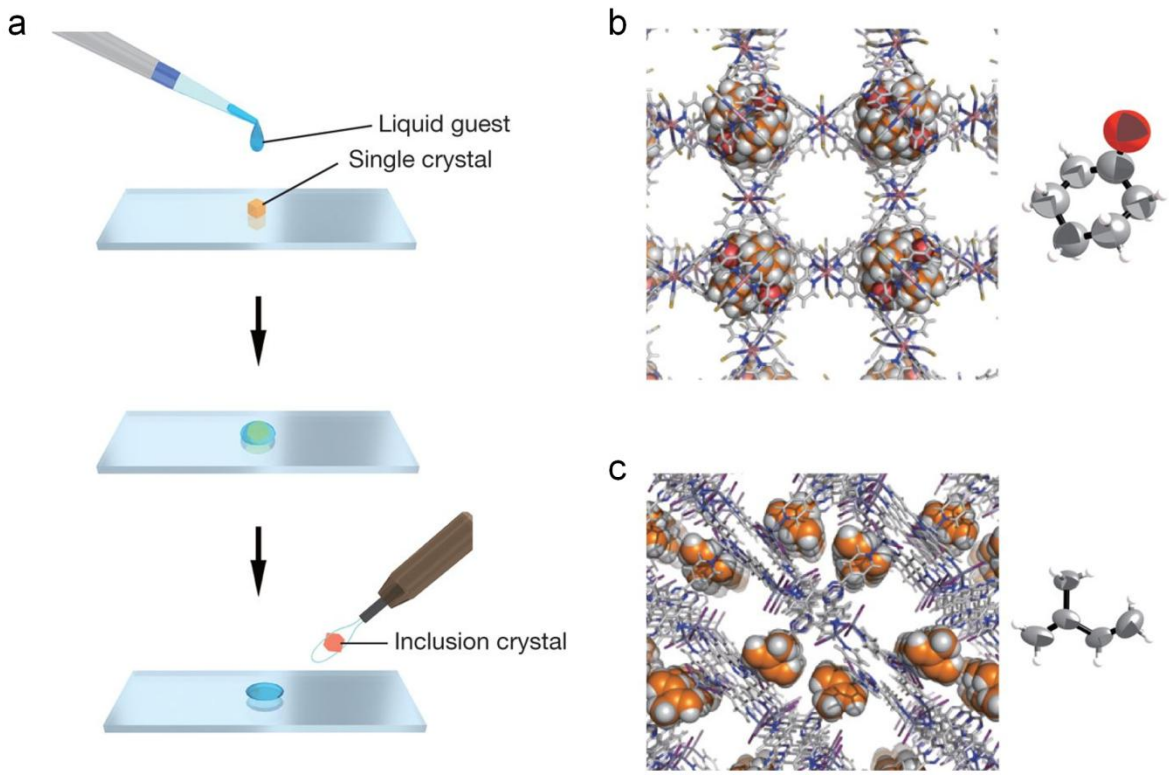

Figure 3. General outline for the soaking of a guest molecule within a porous crystal (a). X-ray crystal structure of the included cyclohexanone (b) and isoprene molecules (c), found within two different crystalline sponges. This figure is reproduced with permission from reference 22. Copyright 2013 Springer Nature.

were previously deemed impossible or challenging to crystallize. The most successful crystalline sponge to date remains the doubly-interpenetrated Zn-based MOF, $\{[ZnI_2)_3(TPT)_2]\cdot 5.5(C_6H_5NO_2)\}_n$ where TPT = 2,4,6-tris(4-pyridyl)-1,3,5-triazine, which features pore apertures of 8×5 Å^2.[25] Using this molecular sponge, I. Abe and co-workers elucidated the crystal structure of astellifadiene, a complex hydrocarbon-based natural product.[26] The characterization of natural products, available only in small quantities, typically relies on Nuclear Magnetic Resonance (NMR) and mass spectroscopy, thus providing, with relatively high reliability, the planar structure and the relative configuration of the compound. Determination of

the absolute stereochemistry, however, remains quite demanding. Through the use of the crystalline sponge method, the authors confirmed the absolute configuration, but also the conformations of the six- and eight-membered rings.

Beyond the use of these porous crystals for obtaining crystal structures, we can envision their applicability towards studying guest adsorption dynamics and for the formation of nanoconfined aggregrates. Along these lines, previous research in the M. Murugesu group sought to investigate the stepwise encapsulation of iodine within the Zn-based sponge.[27] Here, we focused on the fact that the porous channels were lined with terminal iodide groups that could act as anchor sites for incoming iodine gas molecules, and form strong halogen-halogen interactions. Through the use of single-crystal X-ray diffraction, we provided structural snapshots at different stages of iodine loading, thereby elucidating the mechanism by which I_2 became incorporated within the framework. We observed the initial formation of M–I···I–I···I–M, or $[I_4]^{2-}$, linkages, which displayed the strongest calculated binding energies among the different types of I_2 binding. Interestingly, these were quickly replaced by triiodide groups (I_3^-) upon further loading. Through computational studies, we concluded that the driving force towards observing this dynamic covalent binding was the overall energetic stability that is gained by incorporating increasing amounts of I_2 within the framework, even if they adopt less energetically favorable configurations. This example highlights how the crystalline sponge method could be expanded beyond a simple crystallographic tool to include the study of dynamic adsorption behaviours.

In the last few years, multiple strategies have been brought forward in order to improve the crystalline sponge method.[28] Despite this, only a handful of examples exist of successfully carrying out the crystalline sponge method. This testifies to the difficulty in retaining adequate

crystallinity following guest encapsulation and in controlling the inclusion behaviour of porous frameworks. As an extension of the work within the field of crystalline sponges, Chapter 2 will take a look at how confinement effects of a porous host can impact the guest molecule's properties.

1.3.3 **Charged frameworks**

Additional subclasses of metal-organic frameworks are those that contain a residual charge in the form of extra-framework ions. This effectively yields "charged" or ionic frameworks, wherein the scaffolding holds a net positive or negative charge. The vast majority of MOFs reported to date are electrically neutral, as in all of the examples discussed thus far, and so, specific synthetic strategies are usually exploited to generate charged frameworks. The reason behind this is that the positive charges of the metal ions are, more often than not, balanced by the negatively charged organic ligands (often carboxylate-based). Charged frameworks therefore offer some unique possibilities over their neutral counterparts. For example, the creation of charged surfaces within the pore environment could lead to polarization effects on guest molecules.[29] In terms of CO_2 adsorption, this can be especially beneficial, through the partial polarizability of the CO_2 molecule, leading to additional electrostatic interactions between the host and the guest. In the greater scheme of things, it expands the scope of metal-organic frameworks beyond the adsorption of neutral molecules, to include charged species. The capture and detection of ionic drugs or toxic pollutants using charged frameworks has become a significant area of research in recent years.[30] Despite this, strategies for the controlled generation of charged frameworks remain an important challenge. For this reason, we have explored new methods for systematically converting neutral frameworks, with desired topologies, into cationic frameworks (Chapter 6).

The existing strategies for framework cationization can be divided into two groups: pre- and post-synthetic (Fig. 4).[31] Pre-synthetic approaches rely on a "one-pot" combination of neutral ligands and metal ions. Here, the hope is that the neutral or positively-charged ligands would coordinate to the metal ions, forcing an anion to reside within the pore space. The most commonly used neutral ligands are based on polypyridines, as exemplified by the $[Ni(bpy)_{2.5}(H_2O)_2\cdot(ClO_4)_2\cdot 1.5(bpy)\cdot 2H_2O]_n$ MOF, where bpy = 4,4'-bipyridine, and is charged balanced by ClO_4^- anions within the pore space of the framework.[32] Ligands that feature positive charges within the ligand have also been known to generate a cationic framework. Examples include ligands that feature imidazolium or pyridinium moieties, such as the $\{[Cu_2(IMTA)(DMSO)_2]\cdot a Cl\cdot b NO_3\cdot 2H_2O\}_n$ MOF, where IMTA = N,N'-bis(2,6-dimethyl-3,5,-carboxylphenyl)imidazolium chloride, developed by J. T. Hupp, and is balanced by nitrate and chloride counterions in varying proportions.[33] Overall, however, the pre-synthetic approach is rather serendipitous, and offers less control and tunability than post-synthetic approaches. The first post-synthetic approach makes use of non-coordinated and accessible moieties within the framework to subsequently bind additional groups that would change the overall charge of the framework. This was beautifully demonstrated by K. Kim and co-workers, who, through *N*-alkylation of free pyridyl groups to form N-methylpyridinium ions, changed the overall charge of the framework from negative to positive.[34] More recently, X. Bu, P. Feng and co-workers employed $AlCl_3$ to essentially "strip" a terminally coordinated F^- ion simultaneously generating a cationic framework balanced by Cl^- ions and an open-metal site.[35] In both such examples, a significant change in the chemical composition of the MOF itself is occurring. This highlights the need for new design strategies to control the ionicity of nanoporous frameworks.

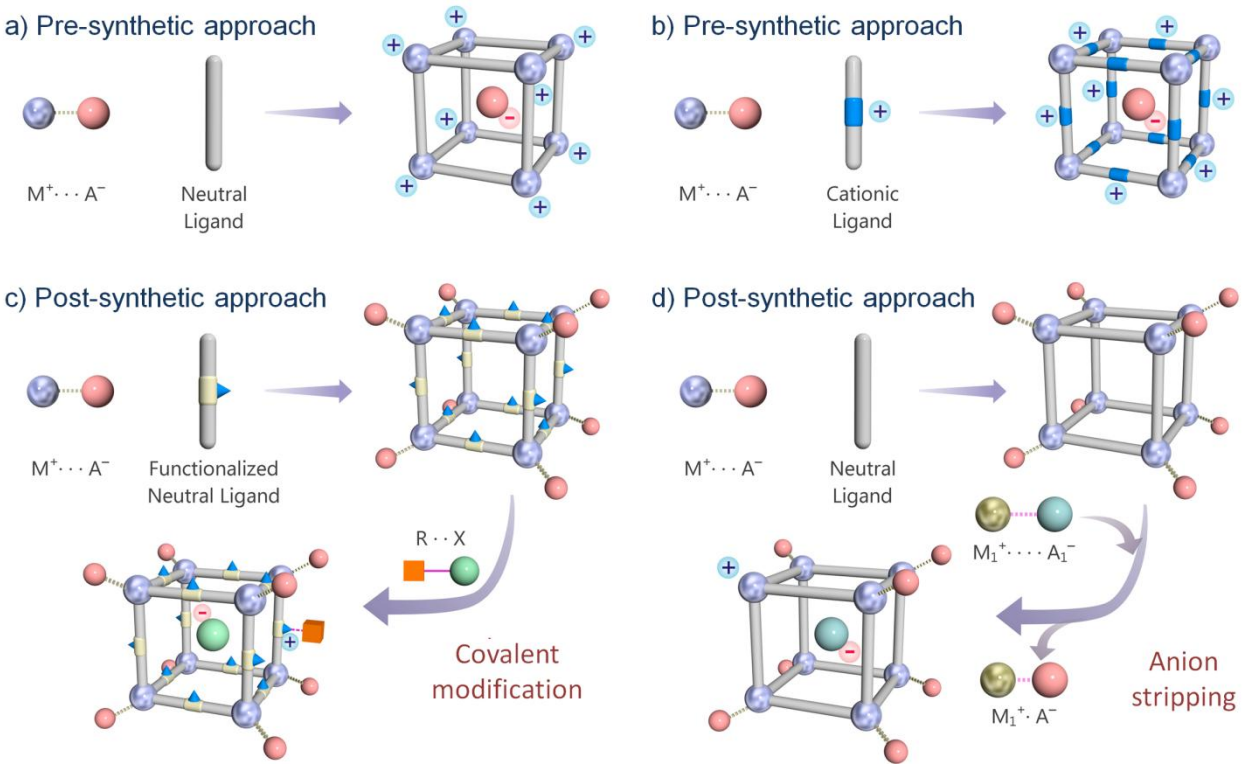

Figure 4. Schematic representation of some of the existing strategies to synthesize cationic MOFs. This figure is adapted with permission from reference 31. Copyright 2015 Elsevier B. V.

Nevertheless, the ability to exchange ions within MOFs has led to some fascinating results. The incorporation of a $Ru(bpy)_3^{2+}$ photocatalyst within a mesoporous anionic framework is a great example,[36] owing to the difficulties related to the recyclability this compound. The exceptional solubility of the catalyst in common solvents renders its reuse rather challenging, and therefore, immobilization of $Ru(bpy)_3^{2+}$ within the pores of the MOF could allow for multiple catalytic cycles to be carried out using a number of different substrates. Indeed, H.-C. Zhou and co-workers found that the hybrid material provided high yields of conversion (>97%) for aza-Henry reactions, without any obvious decrease in conversion yields over multiple cycles. Environmental applications for charged frameworks, such as toxic waste remediation, are also extremely appealing from a materials perspective. The work by S. Wang and co-workers on the

selective removal of $^{99}TcO_4^-$ from aqueous solution using a cationic framework is particularly notable.[37] The interest surrounding the removal of $^{99}TcO_4^-$ stems from the fact that it is produced during nuclear fission and is a long-lived radioisotope ($t_{1/2} = 2.13 \times 10^5$ years). This, in addition to its noncomplexing nature, high water solubility and significant stability, make it an important chemical species to address for nuclear fuel reprocessing and water purification. Current commercial products that efficiently remove $^{99}TcO_4^-$ (*i.e.* anion-exchange resins) suffer from poor radiation resistance and poor chemical stability. The cationic MOF in question, $[Ni_2(tipm)_2(C_2O_4)](NO_3)_2{\cdot}2H_2O$ (SCU-101, tipm = tetrakis[4-(1-imidazolyl)phenyl]methane), exhibits fast removal kinetics, high sorption capacity, and selectivity towards TcO_4^-. Impressively, SCU-101 maintains crystallinity and ion exchange capabilities even after signification exposure to β and γ radiation. Sorption equilibrium only requires a very short 10 minutes to achieve, in comparison to more than 24 h required for SLUG-21 and UiO-66-NH_3^+. The uptake of TcO_4^- occurs even while in the presence of competing anions such as NO_3^-, CO_3^{2-}, PO_4^{3-}, ClO_4^- and SO_4^{2-}, while maintaining removal percentages as high as ~90 %. The two abovementioned examples provide a flavor of the exciting research currently being done on charged frameworks, and how they may become integrated in modern society in the very near future.

1.4 **Molecular magnetism**

1.4.1 **Principles of magnetism**

In the quest of controlling and enhancing the properties of a given material, this *Thesis* investigates how one can tune and promote exciting magnetic behaviours within complex assemblies. This will include both discrete molecules as well as coordination polymers;

effectively combining the two subdisciplines of porous frameworks and magnetism into one, through the study a magnetic metal-organic frameworks in Chapter 3.

The appeal in magnetism originates from the ability to act upon an object at a distance. While our knowledge in this field of research has decidedly moved away from the description of the attractive forces between iron and lodestone by Gilbert in 1600, who stated that "*magnetic attraction arises because the Loadstone hath a soul*",[38] there is still much that remains to be fully understood. This is further complicated by the fact that the development of molecular magnetism requires both a chemical and physical background. In other words, it necessitates an understanding of the chemical nature of molecules and the physical origins of magnetism. At the core, the electronic structure of a given molecule is what dictates its magnetic behaviour. Therein lies the key difference between diamagnets and paramagnets; diamagnets have electrons that are fully paired, and thus repel a magnetic field, while a paramagnet contains at least one unpaired electron and attracts a magnetic field. Given the fact that paramagnetism is significantly greater in strength to diamagnetism, the field of molecular magnetism is focused the study of compounds that have unpaired electrons. Applications that stem from the magnetic behaviour of individual molecules include high-density information storage, quantum computing, and molecular spintronics. The discovery that a molecular magnet, or single-molecule magnet (SMM), could retain its magnetization even after the removal of an externally applied magnetic field, akin to classical bulk magnets, brought high hopes that one day, we could miniaturize data storage down to the molecular level. Molecular magnets also offer the incredible advantage that they can be crystallographically studied and chemically tailored to promote certain magnetic characteristics.

A brief discussion on the method by which a material can retain its magnetization, even after the removal of an applied magnetic field, and thus exhibit a "memory" effect, is warranted. As aforementioned, paramagnetic materials will attract an applied magnetic field – this causes its spins to align in the same direction as the field. Upon removal of the field, the spins would revert back to their randomized state. Below a certain temperature, however, the spins of a paramagnetic material may align themselves along a certain direction relative to their neighbor. This so-called magnetic ordering occurs in three different ways, depending on the type of magnetic interaction between the spins (Fig. 5). In a ferromagnet, all of the spins are aligned parallel to the direction of the magnetic field. In this case, even with the removal of the applied field, the spins will maintain their parallel alignment. A common example of a ferromagnet is a fridge magnet, which is magnetized by an applied field, and is able to retain its ferromagnetic state for a long period of time. An antiferromagnet refers to a material where the spins are aligned anti-parallel to one another, essentially resulting in a diamagnetic material at 0 K. It should be noted that there exists two types of magnetically ordered systems within the category of antiferromagnetism: antiferromagnets and metamagnets. The two differ slightly in terms of their magnetic phase diagram, where antiferromagnets display three different phases (paramagnetic, spin-flop and antiferromagnetic), while metamagnets only exhibit 2 phases (paramagnetic and antiferromagnetic).

Lastly, a ferrimagnet is similar to an antiferromagnet in the sense that the spins are aligned in an anti-parallel fashion, however the strength of the magnetic moment differs from one spin centre to another. For example, a material could contain two different metal ions (with varying spin states) that are arranged in an alternating fashion and aligned antiferromagnetically.

The critical temperature at which such a transition occurs is known as known as the Curie temperature (T_C) for ferro- and ferrimagnets, and the Néel temperature (T_N) for antiferromagnets.

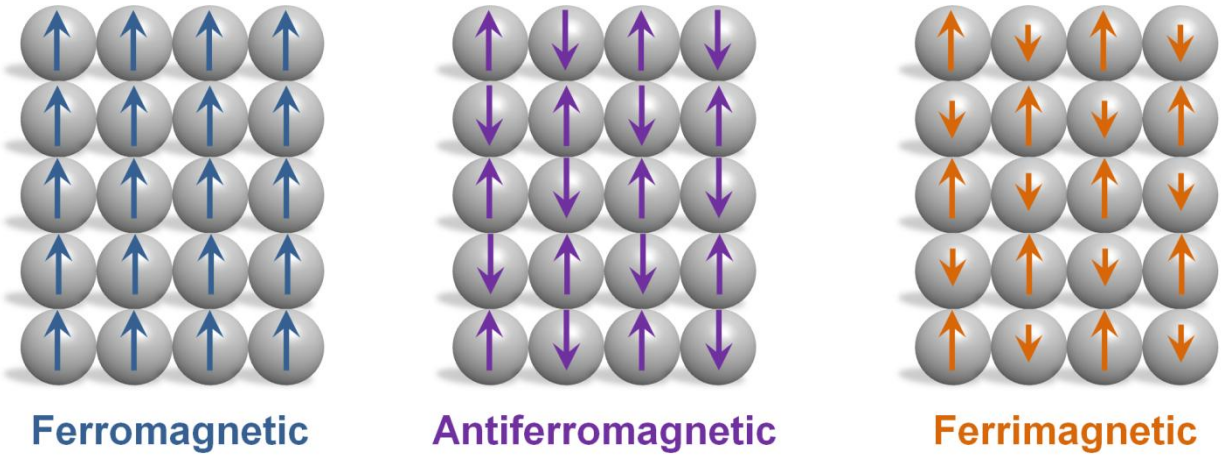

Figure 5. Schematic representation of the three main types of magnetic ordering found in two-dimensional material. The arrows represent the spins.

In an applied magnetic field, the measured response of a material is known as its magnetization:

$$M = \chi \times H \quad or \quad \chi = M / H \tag{1}$$

where M is the magnetization, χ is the magnetic susceptibility, and H is the applied magnetic field. A common method of determining whether a material can effectively act as a magnet, through the retention of a magnetized state, is by performing magnetic hysteresis measurements (Fig. 6). When a traditional ferromagnet is subjected to an increase in magnetic field strength, the spins will slowly begin to align themselves with applied field. This continues until we reach a saturation of the magnetization (M_{sat}), where all of the spins are aligned in the same direction. As we begin to remove the field, a certain remnant magnetization (M_r) remains with the material even at $H = 0$. This is a clear indication that the system retains some magnetic memory. If we

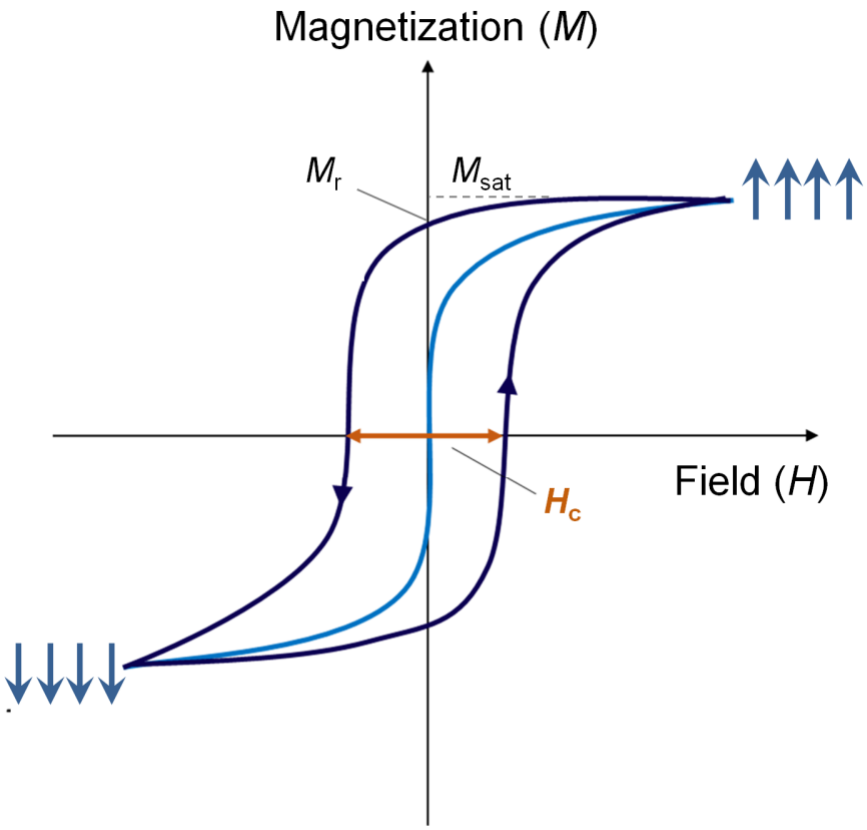

Figure 6. Comparison of the hysteresis curves for a ferromagnetic (dark blue) and paramagnetic (light blue) material. The cycling of the field is shown in blue arrows, while the saturation of the spins and the width of the hysteresis is also displayed. Adapted from reference 40.

reverse the direction of the applied field and increase its strength, we will eventually end up with another M_{sat}, but with the spins aligned along the new direction. Upon removal of the field, we should again observe another M_r. Upon cycling of the magnetic field in this manner, and whether magnetization is indeed retained, we should observe an opening of the hysteresis loop. The width of this opening, alternatively named the coercive field (H_c), is an indicator of the strength of the magnetic field that is required to demagnetize the material. For a long time, this behaviour was only observed in bulk materials, and originated from the formation of magnetic domains that contained a few or many thousands of atoms. In 1993 however, R. Sessoli and co-workers discovered a dodecametallic manganese-acetate cluster, often referred to as $\{Mn_{12}\}$, capable of

exhibiting magnet-like properties.[39] The truly fascinating aspect was that the ferromagnet-like behaviour was of molecular origin, and did not result from the motion of magnetic domain walls.

Molecular magnets, or SMMs, have since flourished. They rely on a blocking temperature (T_B), under which ferromagnet-like behaviour is observed. In order to compare the performances of SMMs, the calculation of an energy barrier (U) is commonplace. This parameter relies on non-negligible spin ground states (S) and significant uniaxial anisotropy (D), and essentially describes the energy that is required for the spin to flip from one orientation to the other (U, defined as $S^2|D|$ or $(S^2\text{-}1/4)|D|$ for integer and half integer spins, respectively).[41] The field initially focused on maximizing as much as possible the total spin of complexes, due to the exponential dependence to U. The result of this strategy was, in essence, a race to obtain the highest-spin ground state molecules. Unfortunately, the improvement in SMM behaviour was lacklustre or non-existent from this approach. In hindsight, we now understand that tuning the magnetic anisotropy of the system is of paramount importance in designing high performance SMMs, much more so than playing on the total spin of the molecule. It is also for this reason that the magnetic studies presented in this *Thesis* primarily make use of Co^{II} (Chapter 3) and Dy^{III} (Chapter 4 and 5), both of which are highly anisotropic metal ions.

Magnetic anisotropy, in simple terms, is the preferential orientation of the magnetic moment along a certain direction. This can either be along what is known as the easy-axis (z-direction) or the easy plane (xy plane). Crucial to SMMs, is the fact that magnetic anisotropy lifts the degeneracy of the spin microstates in the absence of an applied magnetic field. This allows for magnetic bistability and the differential population of the M_s states, both of which are required in order to observe slow relaxation of the magnetization, conducive to SMM behaviour. To illustrate this principle, let's consider a double-well energy diagram that displays the energies

of the different $\pm M_s$ states as a function of the orientation of the magnetic moment (Fig. 7). If the stable orientation of the magnetic moment is parallel to an easy axis (*z*), we have a negative *D* value, and stabilization of the highest $\pm M_s$ states. In order to observe magnetic relaxation from a $-M_s$ to a $+ M_s$ state, the spin must then traverse the electron density-rich *xy* plane. This process is energetically unfavorable, due to electron-electron repulsion, and therefore, we have the formation of two isolated magnetic states (magnetic bistability). To cross this energetic barrier to magnetic relaxation, the spin can follow a thermally-activated regime with an Arrhenius-like behaviour, allowing for the extraction of an effective energy barrier (U_{eff}). To promote highly anisotropic systems, we can take advantage of the first order orbital angular momentum of high-spin Co^{II} ions, or of the significant spin-orbital coupling found in Ln^{III} ions.

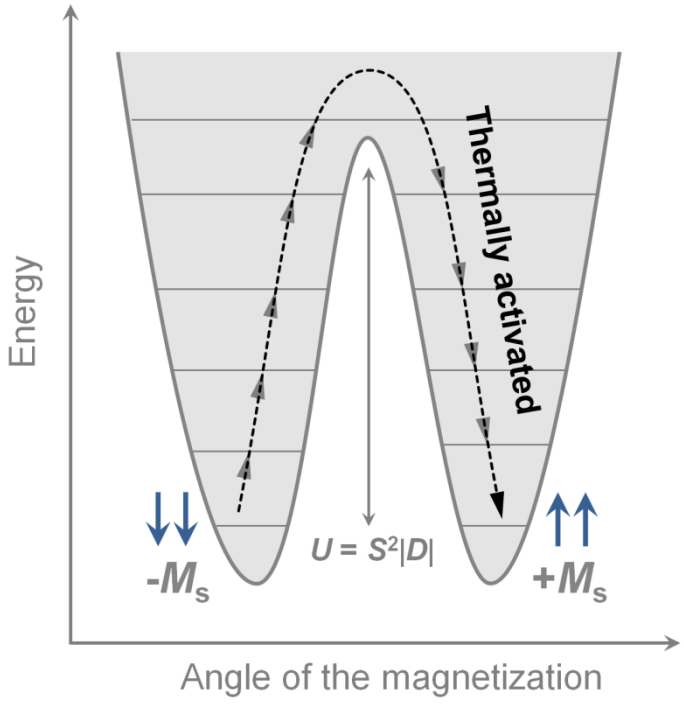

Figure 7. Schematic representation of a double-well energy diagram for an SMM as a function of the angle of the magnetization from an easy-axis (*z*).

1.4.2 **Direct current magnetometry**

Direct current (dc) magnetic measurements are performed through the application of a constant static dc field and by recording the magnetic response of the sample. Here, the most useful plots to consider are χT *vs*. T and M *vs*. H. The shapes of the curves, as well as any values obtained from the fit of these data, can yield a wealth of information regarding the type of magnetic interactions within the sample. In evaluating the temperature dependence of χ, we can plot the data according to $1/\chi$ or χT (Fig. 8). The latter allows for an easy visualization of any potential magnetic interactions. A paramagnetic sample with no clear magnetic interactions should follow

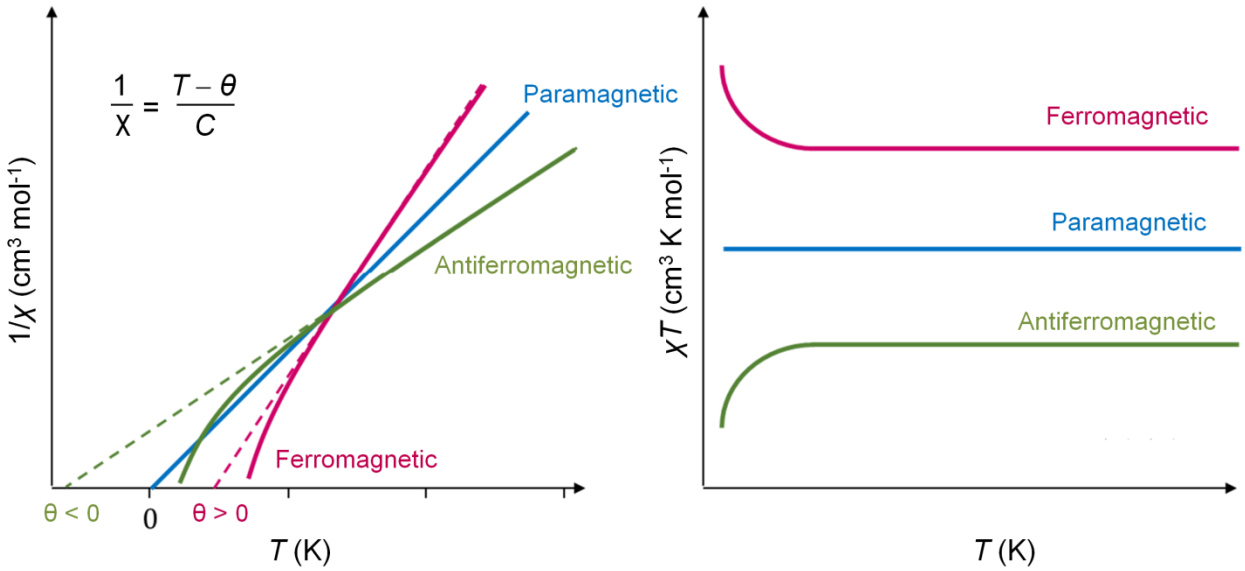

Figure 8. Temperature dependence of the magnetic susceptibility expressed as either $1/\chi$ or χT. Differences in the shape of the curves depending on the type of magnetic interactions are highlighted. Adapted from reference 40.

the Curie law, and appear as a horizontal line. Conversely, in the presence of magnetic interactions, the behaviour can deviate from the Curie behaviour, either through an increase (ferromagnetic interactions) or decrease (antiferromagnetic interactions) in the χT product. The strength of these interactions can be roughly estimated using the $1/\chi$ *vs*. T plots, through

calculation of the Weiss constant (θ). It is important to note that this should only be done on samples, or sections of data, that follow the Curie law:

$$\chi = \frac{Ng^2\mu_B S(S+1)}{3kT} \tag{2}$$

where N = Avogadro's number, g is the Landé factor, μ_B is the Bohr magneton, and k is the Boltzmann constant. To account for magnetic interactions between two spin centres, we add the Weiss constant (θ) and gather all the constant values under the Curie constant (C):

$$\chi = \frac{Ng^2\mu_B S(S+1)}{3kT} \times \frac{1}{T-\theta} = \frac{C}{T-\theta} \tag{3}$$

The Weiss constant can be calculated from the linear fit of the $1/\chi$ *vs*. T plot, and is represented by the x-intercept. A positive θ value indicates ferromagnetic interactions, while a negative θ suggests antiferromagnetic interactions. The Curie constant can also be compared to the room temperature χT value if there are no strong magnetic interactions within the system. Another key piece of information that can be extracted from χT *vs*. T plots, is the room-temperature χT value. Unless there are extremely strong magnetic interactions between the spin centres of the system, we can evaluate the magnetic moment of a sample simply based on the number of unpaired electrons (spin-only formula). We take the Curie law, and approximate all the constants to be approximately equal to 3/8. If we assume a g = 2, we can further simply the equation to:

$$\chi T = \frac{Ng^2\mu_B S(S+1)}{3k} = \frac{g^2}{8} S(S+1) = \frac{S(S+1)}{2} \tag{4}$$

From this equation, we can provide theoretical χT values that are typically compared to the experimentally obtained ones. In doing so, we can acquire some information regarding the

oxidation and spin states of the metal ions. It should be noted that compounds exhibiting significant spin-orbit coupling can deviate from this theoretical value.

Next, the field dependence of the magnetization remains a useful measurement to perform. This is the same type of measurement that would permit an analysis of the magnetic hysteresis. In particular, magnetochemists often evaluate the shape and saturation value of the magnetization curve at low temperatures (< 7 K) and high fields (> 7 T). In an isotropic system, the saturation value should be equal to $M = gS$, allowing for the determination of the Landé factor, g. In an M *vs.* H/T plot, the isothermal curves for an isotropic system will overlap on one another, while in anisotropic system, the magnetization curves will typically not saturate nor superimpose. In this latter case, it becomes difficult to extract meaningful information. Nevertheless, M *vs*. H plots can reveal the presence of strong magnetic interactions or even magnetic ordering, through the observation of S-shaped curves.

1.4.3 **Alternating current magnetometry**

In order to investigate possible slow relaxation of the magnetization, a defining criterion of SMMs, alternating current (ac) susceptibility measurements are routinely employed. In dc magnetic susceptibility measurements, we measure the magnetic moment of a sample when it is subjected to a static, or constant, applied field. In ac magnetometry, however, we are able to study the dynamics of the magnetization by applying a weak ac magnetic field that oscillates at a certain frequency (v). At very low frequencies, the ac measurement would give an essentially identical signal as in dc magnetometry, by following the expected M (H) curve. At higher oscillating frequencies, the ac moment of the sample does not follow the M (H) curve due to dynamic effects. In this particularly case, the magnetization of the sample may lag behind the ac field, an effect that is detected by the magnetometer. Therefore, the ac magnetic susceptibility is

typically divided into two components: the in-phase, or real component (χ'), and an out-of-phase, or imaginary component (χ'') (Fig. 9).

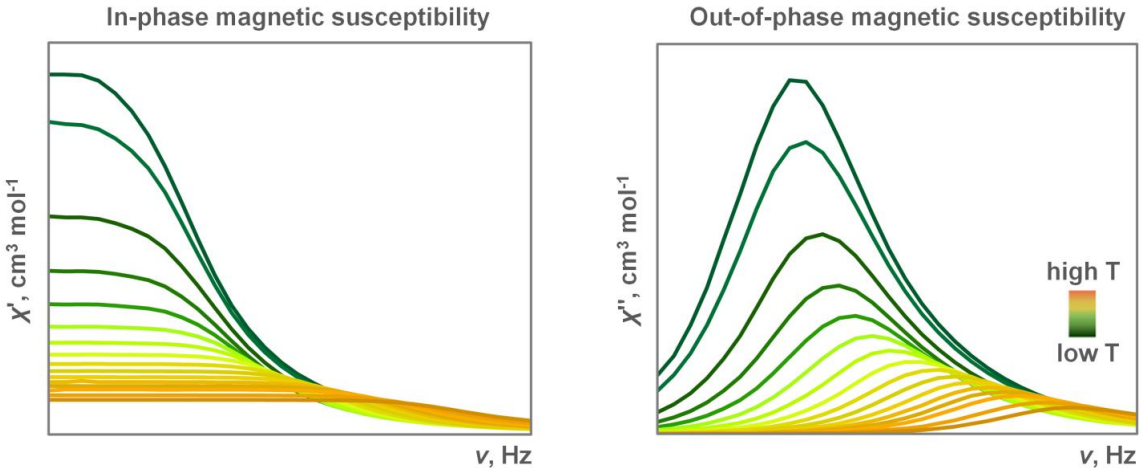

Figure 9. Frequency dependence of the in-phase (χ') and out-of-phase (χ'') magnetic susceptibilities.

In the limit of low frequencies, χ' is the first derivative of χ_{dc}, and therefore represents the slope of the M (H) curve. On the other hand, χ'' is a measure of the magnitude of the phase shift relative to the ac field. Since all paramagnetic samples show a χ' signal, a greater emphasis has been placed on the evaluation of the out-of-phase magnetic susceptibility for SMMs. If the sample completely follows the ac field, the χ'' component will be zero. Conversely, the observation of χ'' signals that are frequency and temperature dependent are a clear indication of the onset of slow relaxation of the magnetization. This can be seen in the form of peaks shifting to lower frequencies as the temperature is decreased. Alternatively, the overlapping of peaks in the χ'' data, throughout a temperature range, suggests the presence of significant quantum tunnelling of the magnetization (QTM). In either cases, the χ' and/or χ'' data can be fit to a generalized Debye model, from which a distribution (α) or relaxation times (τ) can be extracted:

$$\chi' = \chi'_{\infty} + \frac{(\chi'_0 - \chi'_\infty)[1+(2\pi\nu\tau)^{1-\alpha}\sin(\frac{\alpha\pi}{2})]}{1+2(2\pi\nu\tau)^{1-\alpha}\sin\left(\frac{\alpha\pi}{2}\right)+(2\pi\nu\tau)^{2(1-\alpha)}} \quad (5)$$

$$\chi'' = \frac{(\chi'_0 - \chi'_\infty)(2\pi\nu\tau)^{1-\alpha}\cos(\frac{\alpha\pi}{2})}{1+2(2\pi\nu\tau)^{1-\alpha}\sin\left(\frac{\alpha\pi}{2}\right)+(2\pi\nu\tau)^{2(1-\alpha)}} \quad (6)$$

From there, the influence of the temperature and the applied magnetic field on the relaxation time of the compound can be probed, thus providing some insight into the dominant pathways for magnetic relaxation.

1.4.4 **From polynuclear to single-ion magnets**[2]

The journey of SMMs is undoubtedly one that is continually in flux. Given the complexity of the interplay between the classical and quantum mechanical principles that dictate SMM behaviour, researchers in this field of science have repeatedly altered their approaches towards generating optimal systems (Fig. 10). Initially, much of the research was devoted to large polynuclear transition-metal based clusters,[43-45] mainly due to the fact that the first example of a molecule displaying traditional magnet-like properties was obtained in the form of the aforementioned cluster abbreviated $\{Mn_{12}\}$.[39] The particular approach utilized thereafter consisted of either generating high local symmetry or axial crystal fields. While some impressive spin ground states have been reported, such as those found in the $\{Mn_{19}\}$,[46] $\{Mn_{25}\}$[47] and $\{Fe_{42}\}$[48] cages, yielding S = 83/2, S = 61/2 and S = 45, respectively, there was no evident correlation in terms of improvement of the SMM behaviour. Nowadays, research efforts are focused on tuning the magnetic anisotropy of the system rather than on the total spin of the molecule.[49]

[2] A portion of the following two sections appeared previously in R. Marin[+], G. Brunet[+], and M. Murugesu, *Angew. Chem. Int. Ed.* **2019**, *just accepted*, DOI: 10.1002/anie.20191029, and is reproduced here with permission from WILEY-VCH Verlag GmbH & Co. KGaA, Weinheim.

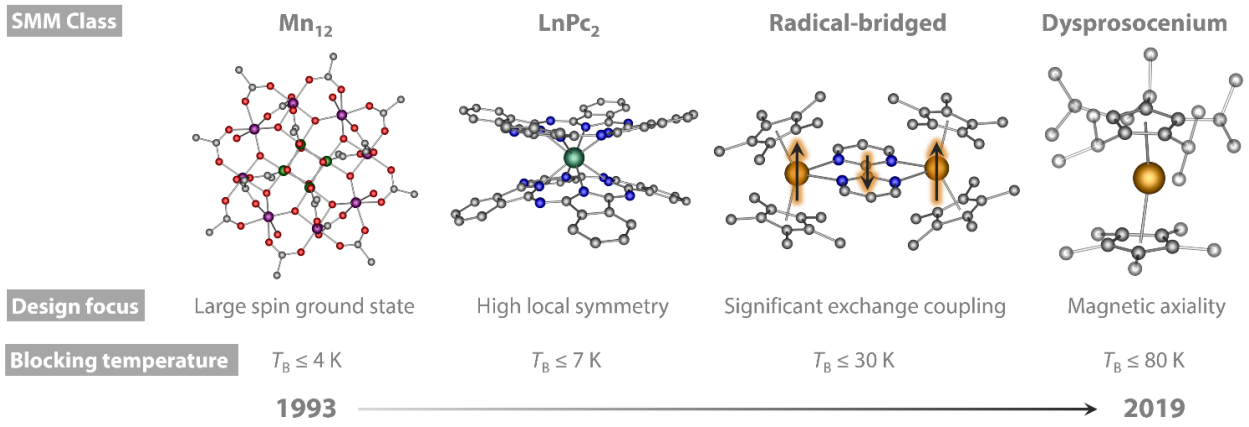

Figure 10. Schematic representation of the evolution in the design and development of high performance SMMs. The defining class of compounds that led to an overall shift in strategy over the years are highlighted, as are the highest blocking temperatures achieved within each family. This figure is reproduced, with permission, from reference 42. Copyright 2019 WILEY-VCH Verlag GmbH & Co. KGaA, Weinheim.

Therein begun the first revolution of the SMM field, spearheaded by Ishikawa and co-workers,[50] where a single lanthanide centre was shown to function as a magnet at the single-molecular level in the form of a $LnPc_2$ complex (Pc = phthalocyanine). This represented a decisive turning point in the advancement of SMMs, where it was shown that a single lanthanide centre, with a much smaller spin state, could match or outperform the aforementioned polynuclear clusters, in respect to the energy barrier (U_{eff}). In fact, lanthanide ions are ideal candidates in creating bistable magnetic ground states, necessary for the observation of SMM-type behaviour. In stark contrast to transition-metals, many of the lanthanides display a strong orbital contribution to the ground state, effectively yielding non-negligible inherent magnetic anisotropy. In turn, this approach has led to some of the highest blocking temperatures and energy barriers,[51-53] clearly re-affirming SMMs as viable candidates in molecular spintronics and quantum computing devices.

1.4.5 **Design strategies for generating SMM-type behaviours**

In the quest for increasingly higher blocking temperatures - which is defined by the highest temperature at which the material retains its magnetization under zero applied magnetic fields - a number of design strategies have been devised over the years for different types of SMMs.[54-57] While the underlying principles remain the same, distinct approaches are being utilized depending on whether a mononuclear or polynuclear system is being targeted. For example, lanthanides were originally unattractive targets in the SMM field, due to the "buried" nature of the 4*f* orbitals and the difficulty in promoting strong magnetic exchange interactions. Early work in the improvement of lanthanide SMMs focused on increasing U_{eff} as much as possible, however, it was quickly found that this parameter does not necessarily correlate with higher blocking temperatures. Indeed, the thermally-activated mechanism is one of many possible magnetic relaxation pathways that can govern the SMM behaviour of lanthanides. Thus, SMMs based on a single metal centre, or single-ion magnets (SIM), concern themselves not on promoting strong magnetic exchange interactions, but rather on tuning the local symmetry of the metal centre and on optimizing the "bath" (spin-phonon interactions) in which the molecule sits, so as to minimize through-barrier relaxation mechanisms.

Such processes, known as the Raman, Direct and quantum tunnelling of the magnetization (QTM) mechanisms, are often highly detrimental to the relaxation dynamics of SMMs. Here, we will briefly highlight the tremendous importance such mechanisms in the overall spin relaxation dynamics of SMMs. The performance of an SMM relies on both the electronic structure of the metal ion as well as the interaction of the magnetic moment to its surrounding environment. This encompasses lattice vibrations (acoustic phonons) and molecular vibrations (optical phonons). Both types of phonons are a result of the thermal energy that displaces atoms from their equilibrium positions; however they differ in terms of the origin of

this vibrational motion. In acoustic vibrations, we have the cooperative movement of atoms within the crystalline solid, while in optical vibrations, they are a result of intramolecular vibrations.

A precise understanding of the effects of such vibrations on the magnetic behaviour of complex molecular systems remains under intense investigation; however it is clear that these vibrations are critically important in the magnetic relaxation of SMMs. In fact, there are three types of spin-phonon interactions, all of which are temperature dependent. The first is the so-called Direct process, which occurs following the emission or absorption of a single phonon with an energy that corresponds to the difference between two crystal field microstates. This process can be straightforwardly identified in field-dependent measurements since the relaxation time (τ) varies according to H^{-4} or H^{-2}, for a Kramers and a non-Kramers ion, respectively. Consequently, if τ follows a H^{-4} decrease, then this would clearly indicate a Direct process (Fig. 11a). Using the same logic, and assuming a Kramers ion, a decrease of τ that follows a H^{-2} trend would indicate Raman type relaxation. In the case of a non-Kramers ion, the decrease of τ would be proportional to H^{-2}, and therefore, can originate from either Direct or Raman relaxation.

Evaluation of the temperature dependence of τ would then be required to distinguish between the two modes of relaxation. The second and third spin-lattice relaxation mechanisms, Orbach and Raman, are both two-phonon processes that involve the subsequent absorption and emission of phonons. They differ in terms of the energetic state by which they proceed; the Orbach mechanism takes place *via* crystal field excited states, while for Raman, the relaxation occurs through short-lived virtual excited states (Fig. 11b). The identification of Raman relaxation should be performed by evaluating both the temperature- and field-dependence of the

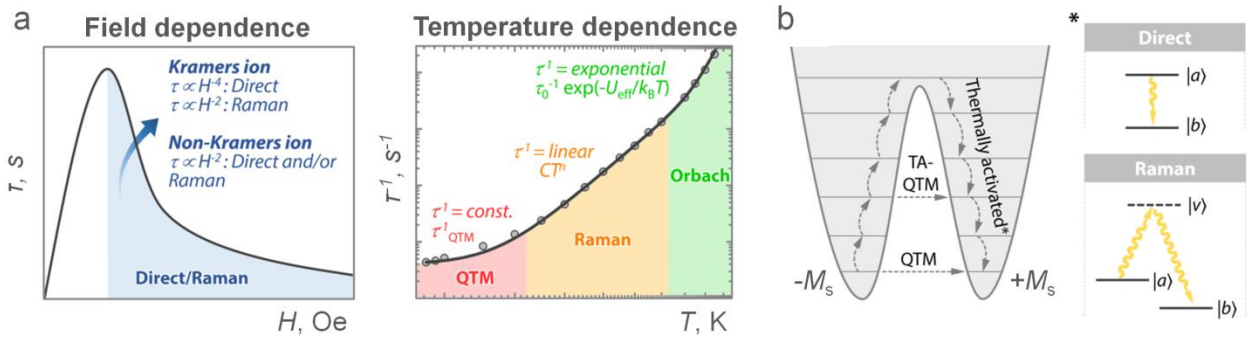

Figure 11. Schematic representation of the main magnetic relaxation mechanisms that are commonly observed in SMMs, with their respective field and temperature dependencies highlighted (a). Here, the temperature-dependence of the magnetic relaxation is plotted in a log-log scale. The double well energy potential illustrates the ideal pathway for magnetization reversal (multistep magnetic relaxation), while alternative detrimental temperature-dependent spin-lattice relaxation processes are also shown (b). This figure is adapted, with permission, from reference 42. Copyright 2019 WILEY-VCH Verlag GmbH & Co. KGaA, Weinheim.

relaxation time. One indication of an active Raman process can be found in the τ^{-1} *vs.* T plot, where the power law relationship of CT^n would appear as a linearly increasing function using log-log scales. In the case of Orbach relaxation, which is field independent, the relaxation time should be constant under variable applied magnetic fields, all the while being thermally activated. Equally important to consider in the design of high performance SMMs is QTM. This process occurs between two levels of nearly equal energies coming into resonance with one another, but with opposite orientations in their magnetic moment, and results in effectively shortcutting the energetic barrier to spin reversal. This phenomenon can materialize in both the ground- (QTM) and excited-states (through thermally assisted QTM; TA-QTM). To minimize QTM, one should focus on Kramers ions, or alternatively, on non-Kramers ions with highly axial crystal fields. This should reduce transverse interactions that would favour resonant energy levels, conducive to QTM. Hyperfine interactions with nuclear spins are also believed to play a major role in transverse interactions. However, at the moment, the exact nature of this coupling and its impact on the magnetic relaxation of SMMs remains under investigation.

The most prevalent method to design high performance SMMs relies on promoting multistep magnetic relaxation (Fig. 11b). This signifies that in the global picture, each excited-state doublet should maintain significant magnetic anisotropy.[58] Here, it is important to consider the relationship between spin-orbit interaction and crystal field. While the spin-orbit coupling energy is generally more significant than that of the crystal field in lanthanides, the latter can effectively remove the degeneracy of the ground state. As a consequence of this, the symmetry and strength of the ligand field is of paramount importance in achieving highly performing SMMs, particularly those focused on a single metal centre. The methods commonly employed in the molecular engineering of SMMs rely on promoting specific ligand architectures or local symmetries that would lead to an optimal slow relaxation of the magnetization, through the generation of highly anisotropic ground and excited states. For example, in lanthanides we focus on the differences in the electron distribution of the 4*f* elements (Fig. 12).[55] As we can see from the following figure, Er^{III} and Yb^{III} exhibit a prolate electron density, meaning that the ligand should be concentrated along the equatorial plane of the molecule to limit the charge contacts between the ligand and the 4*f* electron density. On the other hand, the remaining 4*f* ions are oblate, and the ligands should be preferentially aligned along the axial component. Just as importantly, high symmetry coordination environments, such as D_{4d} and D_{5h}, offer the potential of limiting transverse crystal field terms.[59] It is important to note that even slight distortions from a purely axial symmetry can open the door to tunnelling processes, which are highly detrimental to observing thermally-activated relaxation.

When targeting polynuclear SMMs, additional considerations come into play. The magnetic exchange interaction between metal ions is one of the most important factors to consider. In transition metals, this relies in part on superexchange pathways and the overlap

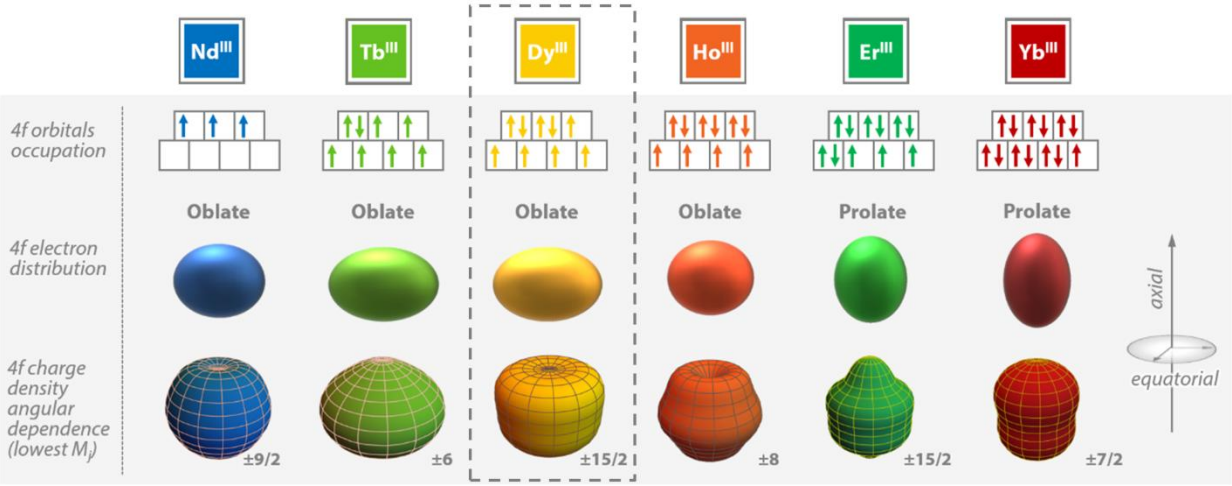

Figure 12. Key differences in the electronic structure of select lanthanide ions. This figure is adapted, with permission, from reference 42. Copyright 2019 WILEY-VCH Verlag GmbH & Co. KGaA, Weinheim.

between the magnetic and bridging ligand orbitals. For lanthanides, the exchange coupling is expected to be very weak, especially when using diamagnetic linkers. Hence, the overall magnetic behaviour is akin to a collection of SIMs, rather than a magnetically coupled system. From a synthetic approach, this makes it rather challenging to apply the aforementioned design strategies that will optimize the SMM properties, especially in complexes with nuclearities greater than two, where control over the symmetry and magnetic axiality can be challenging. Many recent developments are now focused on introducing radical ligands into metal complexes, which can give rise to stronger magnetic interactions, even with lanthanides.[60-65] As described in Chapter 5, this is due to the fact that radicals can better attain the deeply-buried 4*f* orbitals, allowing for direct exchange coupling between the lanthanide ion and the radical ligand. Large exchange coupling constants (*J*) can lead to significant separations between the ground and first-excited states, as well as circumventing QTM processes. In fact, in polynuclear complexes, the magnitude of *J* is crucial in attaining high blocking temperatures, by creating sufficient separations between these two states. The incorporation of radical ligands thus represents a

clever approach that attempts to combine all the key requirements of SMMs in a single system: high-spin ground state (*S*), uniaxial magnetic anisotropy (*D*), and significant exchange coupling (*J*). Of course, such targets are non-trivial and remain an important synthetic challenge.

Lastly, it is worth discussing the impact of applying an external magnetic field in regards to generating SMM-type behaviours. The application of a magnetic field results in the further separation of the M_J levels, according to the Zeeman effect. The magnitude of this splitting is typically quite small, only accounting for a few wavenumbers. From a magnetic standpoint, this results in a reduced chance of QTM phenomena (Fig. 13) and, in fact, a good number of paramagnets only display slow magnetic relaxation under applied magnetic fields (the so-called field-induced SMMs).

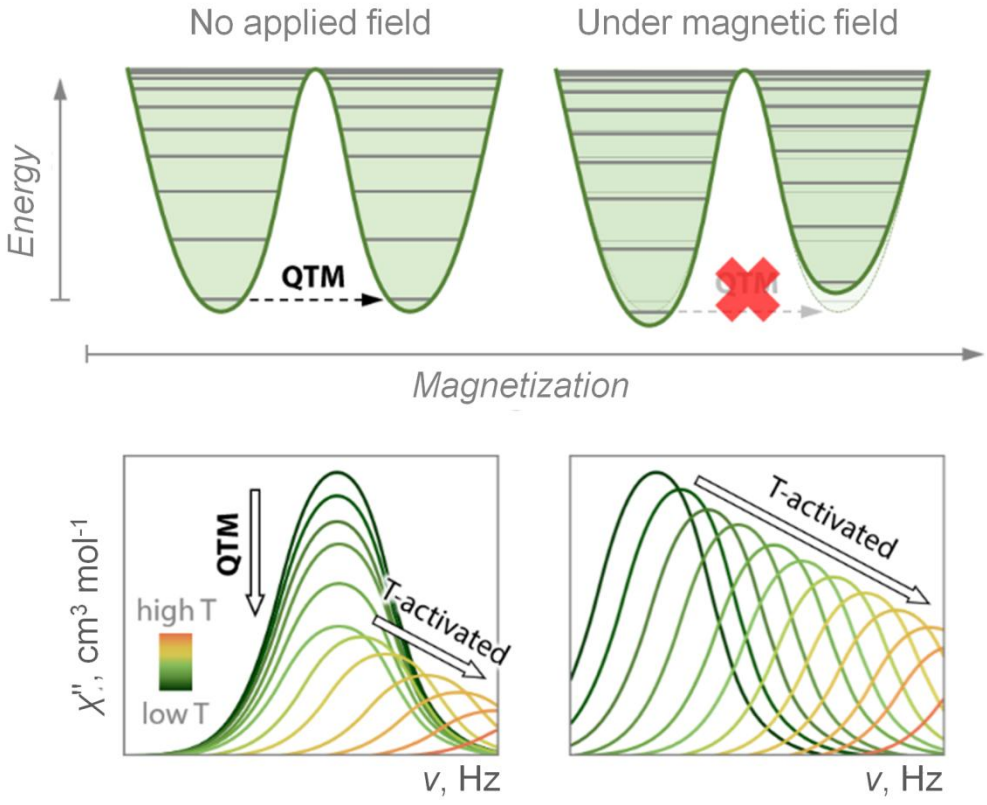

Figure 13. Impact of an external magnetic field on the energy levels of an SMM, resulting in the suppression of QTM, as shown through out-of-phase magnetic susceptibility measurements. This figure is adapted, with permission, from reference 42. Copyright 2019 WILEY-VCH Verlag GmbH & Co. KGaA, Weinheim.

The reason for this is that the application of an external magnetic field lifts the degeneracy between the "up" and "down" spin states. Even if the difference in energy induced by an external magnetic field is small, it can be sufficient to limit ground-state QTM processes. Thus, by minimizing ground-state QTM, magnetic relaxation has the potential to occur *via* low-lying excited states, generating improved SMM-like behaviour. Thus, if a compound displays weak (*i.e.* only tails of peaks) or overlapping ac signals, it is common practice to apply an external magnetic field in the hopes of revealing SMM-like behaviour, by suppressing QTM.

1.5 References

(1) G. E. Moore, *Electronics*, 1965, **38**, 114-117.

(2) G. M. J. Schmidt, *Pure Appl. Chem.*, 1971, **27**, 647-678.

(3) R. Pepinsky, *Phys. Rev.*, 1955, **100**, 971.

(4) G. R. Desiraju, *J. Am. Chem. Soc.*, 2013, **135**, 9952-9967.

(5) L. Brammer, *Chem. Soc. Rev.*, 2004, **33**, 476-489.

(6) B. F. Hoskins, R. Robson, *J. Am. Chem. Soc.*, 1990, **112**, 1546-1554.

(7) M. Kondo, T. Yoshitomi, H. Matsuzaka, S. Kitagawa, K. Seki, *Angew. Chem. Int. Ed. Engl.*, 1997, **36**, 1725-1727.

(8) N. W. Ockwig, O. Delgado-Friedrichs, M. O'Keeffe, O. M. Yaghi, *Acc. Chem. Res.*, 2005, **38**, 176-192.

(9) S. T. Meek, J. A. Greathouse, M. A. Allendorf, *Adv. Mater.*, 2011, **23**, 249-267.

(10) R. Robson, B. F. Abrahams, S. R. Batten, R. W. Gable, B. F. Hoskins, J. Liu, *ACS Symp. Ser.*, 1992, **499**, 256-273.

(11) H. Li, M. Eddaoudi, T. L. Groy, O. M. Yaghi, *J. Am. Chem. Soc.*, 1998, **120**, 8571-8572.

(12) I. M. Hönicke, I. Senkovska, V. Bon, I. A. Baburin, N. Bönisch, S. Raschke, J. D. Evans, S. Kaskel, *Angew. Chem. Int. Ed.*, 2018, **57**, 13780-13783.

(13) J.-R. Li, Y. Ma, M. C. McCarthy, J. Sculley, J. Yi, H.-W. Jeong, P. B. Balbuena, H.-C. Zhou, *Coord. Chem. Rev.*, 2011, **255**, 1791-1823.

(14) N. A. Khan, Z. Hasan, S. H. Jhung, *J. Hazard. Mater.*, 2013, **244-245**, 444-456.

(15) R. Sabouni, H. Kazemian, S. Rohani, *Environ. Sci. Pollut. Res.*, 2014, **21**, 5427-5449.

(16) J. H. Cavka, S. Jakobsen, U. Olsbye, N. Guillou, C. Lamberti, S. Bordiga, K. P. Lillerud, *J. Am. Chem. Soc.*, 2008, **130**, 13850-13851.

(17) M. Kandiah, M. H. Nilsen, S. Usseglio, S. Jakobsen, U. Olsbye, M. Tilset, C. Larabi, E. A. Quadrelli, F. Bonino, K. P. Lillerud, *Chem. Mater.*, 2010, **22**, 6632-6640.

(18) H. Kim, S. Yang, S. R. Rao, S. Narayanan, E. A. Kasputin, H. Furukawa, A. S. Umans, O. M. Yaghi, E. N. Wang, *Science*, 2017, **356**, 430-434.

(19) L. Sun, M. G. Campbell, M. Dincă, *Angew. Chem. Int. Ed.*, 2016, **55**, 3566-3579.

(20) S. Achman, G. Hagen, J. Kita, I. M. Malkowsky, C. Kiener, R. Moos, *Sensors*, 2009, **9**, 1574-1589.

(21) P. Horcajada, C. Serre, M. Vallet-Regí, M. Sebban, F. Taulelle, G. Férey, *Angew. Chem. Int. Ed.*, 2006, **45**, 5974-5978.

(22) Y. Inokuma, S. Yoshioka, J. Ariyoshi, T. Arai, Y. Hitora, K. Takada, S. Matsunaga, K. Rissanen, M. Fujita, *Nature*, 2013, **495**, 461-466.

(23) Y. Inokuma, K. Matsumura, S. Yoshioka, M. Fujita, *Chem. – Asian J.*, 2017, **12**, 208-211.

(24) Y. Inokuma, S. Yoshioka, J. Ariyoshi, T. Arai, M. Fujita, *Nat. Protoc.*, 2014, **9**, 246-252.

(25) K. Biradha, M. Fujita, 2002, *Angew. Chem. Int. Ed.*, 2002, **41**, 3392-3395.

(26) Y. Matsuda, T. Mitsuhashi, S. Lee, M. Hoshino, T. Mori, M. Okada, H. Zhang, F. Hayashi, M. Fujita, I. Abe, *Angew. Chem. Int. Ed.*, 2016, **55**, 5785-5788.

(27) G. Brunet, D. A. Safin, M. Z. Aghaji, K. Robeyns, I. Korobkov, T. K. Woo, M. Murugesu, *Chem. Sci.*, 2017, **8**, 3171-3177.

(28) M. Hoshino, A. Khutia, H. Xing, Y. Inokuma, M. Fujita, *IUCrJ*, 2016, **3**, 139-151.

(29) D. Aulakh, J. R. Varghese, M. Wriedt, *Inorg. Chem.*, 2015, **54**, 1756-1764.

(30) J. Li, X. Wang, G. Zhao, C. Chen, Z. Chai, A. Alsaedi, T. Hayat, X. Wang, *Chem. Soc. Rev.*, 2018, **47**, 2322-2356.

(31) A. Karmakar, A. V. Desai, S. K. Ghosh, *Coord. Chem. Rev.*, 2016, **307**, 313-341.

(32) O. M. Yaghi, H. Li, T. L. Groy, *Inorg. Chem.*, 1997, **36**, 4292-4293.

(33) J. Y. Lee, J. M. Roberts, O. K. Farha, A. A. Sarjeant, K. A. Scheidt, J. T. Hupp, *Inorg. Chem.*, 2009, **48**, 9971-9973.

(34) J. S. Seo, D. Whang, H. Lee, S. I. Jun, J. Oh, Y. J. Jeon, K. Kim, *Nature*, 2000, **404**, 982-986.

(35) C. Mao, R. A. Kudla, F. Zuo, X. Zhao, L. J. Mueller, X. Bu, P. Feng, *J. Am. Chem. Soc.*, 2014, **136**, 7579-7582.

(36) J. Pang, S. Yuan, J.-S. Qin, C. T. Lollar, N. Huang, J. Li, Q. Wang, M. Wu, D. Yuan, M. Hong, H.-C. Zhou, *J. Am. Chem. Soc.*, 2019, **141**, 3129-3136.

(37) L. Zhu, D. Sheng, C. Xu, X. Dai, M. A. Silver, J. Li, P. Li, Y. Wang, Y. Wang, L. Chen, C. Xiao, J. Chen, R. Zhou, C. Zhang, O. K. Farha, Z. Chai, T. E. Albrecht-Schmitt, S. Wang, *J. Am. Chem. Soc.*, 2017, **139**, 14873-14876.

(38) C. Benelli, D. Gatteschi, *Introduction to Molecular Magnetism: From Transition Metals to Lanthanides*; Wiley: Hoboken, NJ, 2015.

(39) R. Sessoli, D. Gatteschi, A. Caneschi, M. A. Novak, *Nature*, 1993, **365**, 141-143.

(40) R. J. Holmberg, *Probing Nanomagnetism Through a Materials Approach: Paramagnetic Ions Within Nanomaterials*, Thesis, University of Ottawa, 2016.

(41) Kahn, O. *Molecular Magnetism*; Wiley-VCH: New York, NY, 1993.

(42) R. Marin, G. Brunet, M. Murugesu, *Angew. Chem. Int. Ed.*, 2019, *just accepted*, DOI: 10.1002/anie.201910299.

(43) T. Mallah, C. Auberger, M. Verdaguer, P. Veillet, *J. Chem. Soc., Chem. Commun.*, 1995, 61-62.

(44) J. Yoo, A. Yamaguchi, M. Nakano, J. Krzystek, W. E. Streib, L.-C. Brunel, H. Ishimoto, G. Christou, D. N. Hendrickson, *Inorg. Chem.*, 2001, **40**, 4604-4616.

(45) S. M. J. Aubin, M. W. Wemple, D. M. Adams, H.-L. Tsai, G. Christou, D. N. Hendrickson, *J. Am. Chem. Soc.*, 1996, **118**, 7746-7754.

(46) A. M. Ako, I. J. Hewitt, V. Mereacre, R. Clérac, W. Wernsdorfer, C. E. Anson, A. K. Powell, *Angew. Chem. Int. Ed. Engl.*, 2006, **45**, 4926-4929.

(47) T. C. Stamatatos, K. A. Abboud, W. Wernsdorfer, G. Christou, *Angew. Chem. Int. Ed. Engl.*, 2007, **46**, 884-888.

(48) S. Kang, H. Zheng, T. Liu, K. Hamachi, S. Kanegawa, K. Sugimoto, Y. Shiota, S. Hayami, M. Mito, T. Nakamura, M. Nakano, M. L. Baker, H. Nojiri, K. Yoshizawa, C. Duan, O. Sato, *Nat. Commun.*, 2015, **6**, 5955.

(49) F. Neese, D. A. Pantazis, *Faraday Discuss.*, 2011, **148**, 229-238.

(50) N. Ishikawa, M. Sugita, T. Ishikawa, S. Y. Koshihara, Y. Kaizu, *J. Am. Chem. Soc.*, 2003, **125**, 8694-8695.

(51) C. A. P. Goodwin, F. Ortu, D. Reta, N. F. Chilton, D. P. Mills, *Nature*, 2017, **548**, 439-442.

(52) F. S. Guo, B. M. Day, Y. C. Chen, M. L. Tong, A. Mansikkamaki, R. A. Layfield, *Angew. Chem. Int. Ed. Engl.*, 2017, **56**, 11445-11449.

(53) F. S. Guo, B. M. Day, Y. C. Chen, M. L. Tong, A. Mansikkamaki, R. A. Layfield, *Science*, 2018, **362**, 1400-1403.

(54) F. Habib, G. Brunet, V. Vieru, I. Korobkov, L. F. Chibotaru, M. Murugesu, *J. Am. Chem. Soc.*, 2013, **135**, 13242-13245.

(55) J. D. Rinehart, J. R. Long, *Chem. Sci.*, 2011, **2**, 2078-2085.

(56) L. Ungur, L. F. Chibotaru, *Inorg. Chem.*, 2016, **55**, 10043-10056.

(57) N. F. Chilton, *Inorg. Chem.*, 2015, **54**, 2097-2099.

(58) L. Ungur, L. F. Chibotaru, *Phys. Chem. Chem. Phys.*, 2011, **13**, 20086-20090.

(59) J.-L. Liu, Y.-C. Chen, M.-L. Tong, *Chem. Soc. Rev.*, 2018, **47**, 2431-2453.

(60) J. D. Rinehart, M. Fang, W. J. Evans, J. R. Long, *Nat. Chem.* **2011**, *3*, 538-542.

(61) F.-S. Guo, R. A. Layfield, *Chem. Commun.* **2017**, *53*, 3130-3133.

(62) C. Das, A. Upadhyay, M. Shanmugam, *Inorg. Chem.* **2018**, *57*, 9002-9011.

(63) S. Demir, J. M. Zadrozny, M. Nippe, J. R. Long, *J. Am. Chem. Soc.* **2012**, *134*, 18546-18549.

(64) B. S. Dolinar, D. I. Alexandropoulos, K. R. Vignesh, T. A. James, K. R. Dunbar, *J. Am. Chem. Soc.* **2018**, *140*, 908-911.

(65) M. A. Lemes, G. Brunet, A Pialat, L. Ungur, I. Korobkov, M. Murugesu, *Chem. Commun.*, 2017, *53*, 8660-8663.

The important thing is not to stop questioning. Curiosity has its own reason for existence. One cannot help but be in awe when he contemplates the mysteries of eternity, of life, of the marvelous structure of reality. It is enough if one tries merely to comprehend a little of this mystery each day.
– Albert Einstein[3]

Chapter 2

Confinement effects of nanoporous materials

2.1 Published contributions

Confinement effects of a crystalline sponge on ferrocene and ferrocene carboxaldehyde

G. Brunet, D. A. Safin, K. Robeyns, G. A. Facey, I. Korobkov, Y. Filinchuk and M. Murugesu, *Chem. Commun.*, 2017, **53**, 5645-5648.

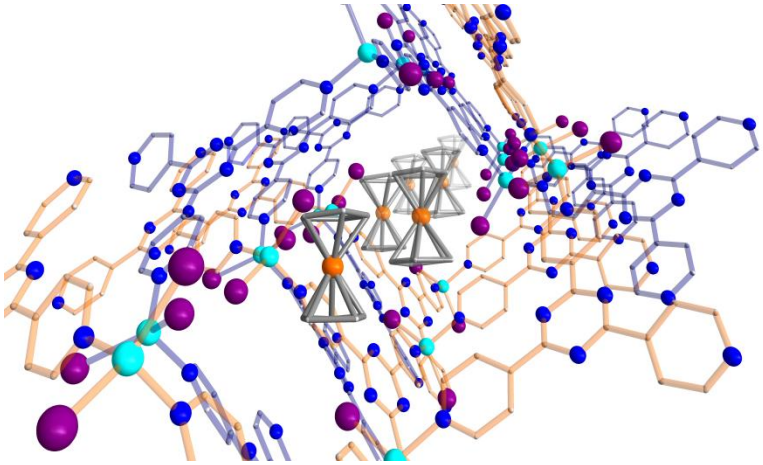

G. Brunet and M. Murugesu wrote the manuscript. G. Brunet performed the majority of the experiments. D. A. Safin assisted in the synthesis of the starting ligand.

G. A. Facey assisted with the solid-state NMR experiments.

I. Korobkov and Y. Filinchuk were responsible for the refinement of the single-crystal X-ray diffraction data.

[3] "Old Man's Advice to Youth: 'Never lose a Holy Curiosity.'" Life Magazine, May 2nd 1955, p. 64

2.2 **Abstract**

The pivotal role of $\pi\cdots\pi$ interactions in the inclusion behaviour of a series of organometallic sandwich compounds is studied through single-crystal X-ray diffraction. The confinement effects of a crystalline sponge host are investigated where, notably, we observe an enhanced rotation of the ligand ring once encapsulated by the nanoporous framework, as evidenced by SSNMR experiments.

2.3 **Introduction**

Over the past two decades, the scientific community has witnessed the unprecedented development of a new class of crystalline materials capable of offering easily tuneable porous structures. These multi-functional materials, termed metal-organic frameworks (MOFs), have excelled in providing promising alternatives for select applications in gas separation,[1] catalysis,[2] drug delivery,[3] and chemical separation.[4] A common denominator among all such space-specific functions involves molecular adsorption of the desired guest. While multiple experimental methods can be used to confirm successful guest inclusion,[5] the direct visualization of host-guest interactions, which drive the uptake process, remains a challenge. This is especially true when considering host-guest interactions that are non-covalent in nature, and thus exhibit a weaker and less directional binding. A recent advance in this regard involves the use of porous MOFs with high molecular recognition properties which allows guest molecules to become regularly ordered throughout the porous material in such a way to permit the subsequent use of single-crystal X-ray diffraction techniques.[6] This innovative protocol, termed the "crystalline sponge method", has the undeniable advantage of expanding the crystallographic database, by rendering the analysis of liquids and other non-crystallizing

compounds possible, however the impact of the host on the structure and electronic properties of the encapsulated guest has not been previously touched upon. Indeed, the confinement effects of the pores may significantly alter the physicochemical properties of the host and/or guest, as demonstrated in a number of zeolites, where the strength of the acidic sites were found to vary.[7] Thus, we investigate for the first time the confinement effects of a crystalline sponge on two organometallic guest compounds.

The host-guest chemistry of MOFs loaded with organometallic species is scarcely reported,[8] however, ferrocene (Fc) appears to be a suitable molecular probe for potential organometallic guest inclusion. While the loading of such guests can be confirmed by spectroscopic methods or by powder X-ray diffraction, an in-depth understanding of the host-guest interactions can only be truly achieved through single-crystal X-ray diffraction. Furthermore, visualization of the host-guest interactions at the atomic level is highly desirable in order to establish conclusive and precise structure-property relationships. Hence, our research efforts were directed towards the inclusion of organometallic sandwich compounds using the crystalline sponge method, which has seen some success in identifying non-trivial guests by single-crystal X-ray diffraction.[9] Furthermore, we also investigate the impact of changing the terminal halide ligand of the host framework from iodide to bromide on the inclusion of the selected guest molecules.

2.4 **Synthesis**

The crystalline sponges were synthesized by the slow diffusion of a solution of zinc iodide or zinc bromide layered onto a solution of tris(4-pyridyl)-1,3,5-triazine (TPT), yielding the doubly interpenetrated porous network $\{[(ZnX_2)_3(TPT)_2]\cdot 5.5(C_6H_5NO_2)\}_n$ (X = I, **1a**; Br, **1b**).[10] These MOFs are ideal hosts for guest inclusion due to their facile

synthesis, high stability and presence of large cavities (up to 5 × 8 $Å^2$). These large voids, or channels, display an inherent affinity for organic molecules, caused by the availability of $\pi\cdots\pi$ and charge-transfer interactions of the triazine-based ligand. With this in mind, we decided to first investigate the inclusion of Fc and ferrocene carboxaldehyde (FcCHO), which are highly stable, yet relatively small organometallic compounds. Moreover, the encapsulation of a similar family of compounds provides an effective method of directly evaluating the impact of functional groups on the host-guest interactions.

2.5 **Guest encapsulation**

Successful guest encapsulation was evidenced by a remarkable change in colour of the crystals, from nearly colourless to dark-brown. To obtain high quality single-crystals, the mother liquor was carefully decanted, and subsequently replaced by a solution of Fc in an optimal solvent (see the experimental details below). The single-crystal inclusion of metallocenes in MOFs is non-trivial, as there exists only a handful of examples to date.[11] In the study presented herein, structural refinement reveals the incorporation of Fc in both **1a** and **1b**. In addition to Fc, the pore space of the lattice is completed by partially occupied nitrobenzene and cyclohexane molecules, giving the chemical formulas $\{[ZnI_2)_3(TPT)_2]\cdot Fc\cdot(PhNO_2)_{0.5}\cdot(C_6H_{12})_2\}_n$ (**2a**) and $\{[ZnBr_2)_3(TPT)_2]\cdot Fc\cdot(PhNO_2)_{0.46}\cdot(C_6H_{12})_{2.92}\}_n$ (**2b**). The frameworks of **2a** and **2b** retain the structure of the parent MOFs **1a** and **1b**, respectively, which also leads to a unit cell symmetry that remains in the *C*2/*c* space group (Table 1). Following the incorporation of Fc however, we observe a contraction of the *a*-axis, leading to a decrease of the unit cell volume by 3.7 and 8.6% for **2a** and **2b**, respectively (Table 1). These contractions provide

Table 1. Summary of the crystal structure data and refinement for compounds **1a**, **1b**, **2a**, **2b** and **3**.

Complex	**1a**[10]	**1b**[23]	**2a**	**2b**	**3**
Formula	$C_{54}H_{39}I_6N_{15}O_{6.25}Zn_3$	$C_{54}Br_6N_{14}O_6Zn_3$	$C_{122}H_{121}Fe_2I_{12}N_{25}O_2Zn_6$	$C_{66.31}H_{71.37}Br_6FeN_{12.46}O_{0.93}Zn_3$	$C_{151}H_{121}Fe_5I_{12}N_{24}O_5Zn_6$
FW, g mol^{-1}	1955.51	1630.29	3996.15	1789.18	4545.98
Crystal system	triclinic	monoclinic	monoclinic	monoclinic	monoclinic
Space group	*P*–1	*C*2/*c*	*C*2/*c*	*C*2/*c*	*C*2/*c*
T, K	193(2)	300	200(2)	150(2)	150(2)
a, Å	14.297(3)	35.218(2)	35.0063(17)	34.1904(4)	38.059(5)
b, Å	17.164(3)	14.6836(7)	15.0958(7)	14.67836(15)	14.2182(11)
c, Å	27.333(5)	30.951(2)	30.2162(15)	30.1683(4)	34.848(6)
α, ^{o}	89.970(5)	90	90	90	90
β, ^{o}	77.104(4)	103.036(3)	102.0881(19)	101.7441(13)	110.753(16)
γ, ^{o}	74.591(4)	90	90	90	90
V, Å^3	6291(2)	15593(9)	15 613.6(13)	14 823.3(3)	17 634(4)
Z	4	8	4	8	4
ρ_{calcd}, g cm^{-3}	2.065		1.700	1.603	1.717
μ (Mo, Kα), mm^{-1}	4.139		3.508	4.434	3.353
reflns collected	21 852		14 326	13 771	15 898
R_1, wR_2 (I > 2 σ (*I*))[a]	0.1194, 0.2720		0.0633, 0.1591	0.0503, 0.1336	0.0492, 0.1184
R_1, wR_2 (all data)	0.3110, 0.3103		0.0739, 0.1655	0.0652, 0.1442	0.0784, 0.1317

[a] $R = R_1 = \| |F_o| - |F_c| / |F_o|$; $wR2 = \{[w(F_o - F_c^2)^2] / [w(F_o^2)^2]\}^{1/2}$; $w = 1/[\sigma_2(F_o^2) + (ap)^2 + bp]$, where $p = [\max(F_o^2, 0) + 2F_c^2]/3$; and $Rw = [w(|F_o| - |F_c|)^2 / w|F_o|^2]^{1/2}$, where $w = 1 / \sigma^2(|F_o|)$.

an initial indication of host-guest interactions, where the flexibility of the interpenetrated structure to accommodate various guest molecules is highlighted. Close inspection of the crystal structures of **2a** and **2b** reveals two Fc molecules in close proximity to one another, with the closest Fe···Fe separations being 6.02 and 5.96 Å, respectively (Fig. 14). It is important to note that an inversion centre resides near the middle of the channels of the MOF, yielding one crystallographically independent Fc molecule for each structure. The cyclopentadienyl (Cp) rings are nearly eclipsed by one another and the average Fe–C distances in Fc were calculated to be 2.03 Å (Tables 2 and 3). These structural details and the lack of significant distortions highlight the limited interactions that occur between the Fc guest and the host framework, and are somewhat surprising considering the

availability of aromatic rings from the TPT ligand to form face-to-face $\pi\cdots\pi$ interactions. Despite such seemingly weak interactions, the Fc guests in **2a** and **2b** are seen to take up the exact same orientation and position within the porous framework. Two conclusions can be drawn here: *i*) the terminal halide ligand doesn't appear to have an effect on the positioning of the Fc molecules, and *ii*) there is a certain driving force which locks the metallocene guest into this preferred position. In order to shed some light on this notable behaviour, we have carefully investigated the host-guest interactions (Fig. 15).

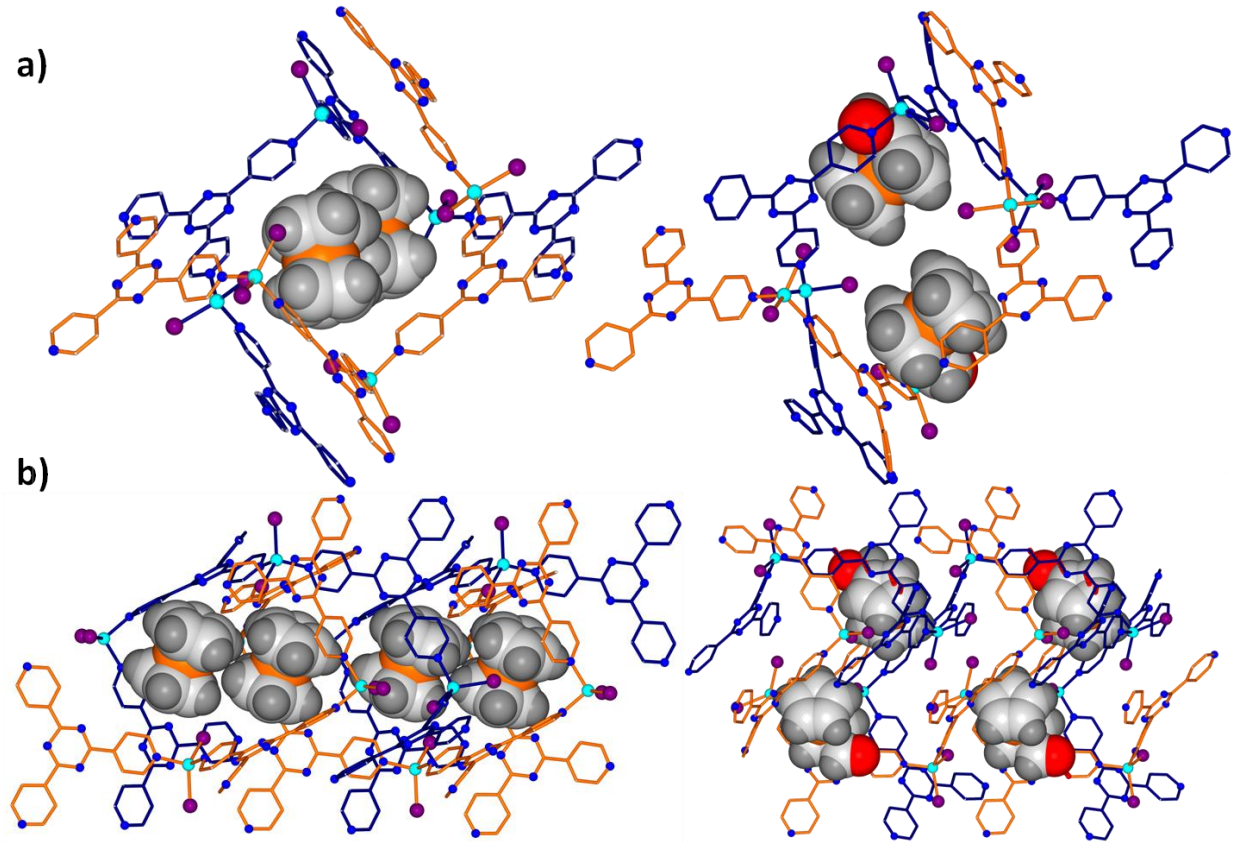

Figure 14. Molecular structure of the inclusion compounds. (a) Single pore view of **2a** (left) and **3** (right) displaying the orientation and positioning of the Fc-based guests. (b) Side view of the continuous channels highlighting the preferential arrangement of the Fc-based guests in **2a** (left) and **3** (right). Guest molecules are shown using a space-filling model. Solvent molecules, hydrogen atoms of the framework, and positional disorder have been omitted for clarity. Color code: orange (Fe), blue (N), cyan (Zn), light grey (H), dark grey (C). Interpenetration is displayed by the orange and blue bonds.

Table 2. Select bond distances of ferrocene in **2a** and CH···π interactions in a pure ferrocene crystal.

Fe–C bonds (Å)					
Fe61–C62	2.05	Fe61–C66	2.05	Fe61–C70	2.06
Fe61–C63	2.04	Fe61–C67	2.00	Fe61–C71	2.02
Fe61–C64	2.02	Fe61–C68	2.04		
Fe61–C65	2.02	Fe61–C69	2.07		
π···π interactions in 2a (as defined in Fig. 15a)					
1 (Å)		2 (Å)	3 (Å)	α (°)	β (°)
5.45		3.99	3.41	118.32	144.98
π···π interactions in a pure ferrocene crystal (as defined in Fig. 15b)					
1 (Å)		2 (Å)	3 (Å)	α (°)	β (°)
4.81		3.59	3.03	112.60	141.16

Table 3. Select bond distances of ferrocene in **2b**.

Fe–C bonds (Å)					
Fe61–C62	2.03	Fe61–C66	2.03	Fe61–C70	2.02
Fe61–C63	2.00	Fe61–C67	2.04	Fe61–C71	2.04
Fe61–C64	2.01	Fe61–C68	2.06		
Fe61–C65	2.02	Fe61–C69	2.03		
π···π interactions in 2b (as defined in Fig. 15a)					
1 (Å)		2 (Å)	3 (Å)	α (°)	β (°)
5.38		4.01	3.28	115.49	148.83

In the case of **2a**, the Fc guest adopts a perpendicular y-shaped arrangement, where the hydrogen and carbon atoms of a Cp ring are seen to interact with two pyridine moieties belonging to the TPT ligand. The electrostatic interactions directing this orientation are the centroid···$HC_{pyridine}$ interactions, which occur at distances of 3.41 and 4.00 Å (Fig. 15c). Consequently, these interactions can be described as an intermediate between the T-shaped and edge-to-face π-stacking modes, however, due to the closer interaction of the Cp centroid with one of the H atoms of the pyridine ring, the T-shaped mode is likely more favoured. Contact measurements further revealed C_{Cp}···$HC_{pyridine}$ and $C_{pyridine}H$···HC_{Cp} interactions at distances of 2.74 and 2.39 Å, respectively, the latter of

which is slightly smaller than the sum of the van der Waals radii of the individual atoms. On the other side of the Fc molecule, the Cp ring also interacts with a pyridine centroid, yielding a slight tilt angle of 2.48° between the planes of the Cp rings. In **2b** however, the Cp rings are very nearly eclipsed and exhibit a slight tilt angle of 0.33° between the two planes. One Cp ring participates in the formation of an H···Br interaction, through a distance of 2.90 Å. The other Cp ring also exhibits a number of $\pi\cdots\pi$ interactions between the guest and two framework pyridine rings, as in **2a** (Fig. 15d). Interestingly, the same Cp ring also engages in multiple guest-solvent interactions

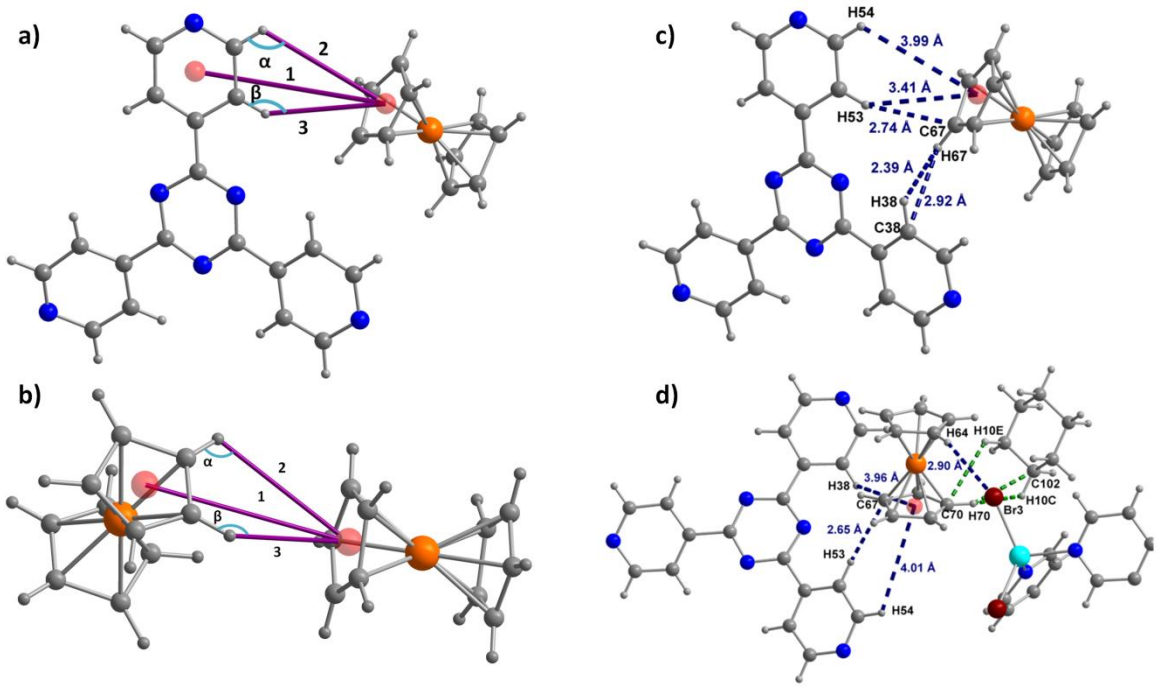

Figure 15. Representative $\pi\cdots\pi$ interactions between the ferrocene molecules and the host framework found in **2a** and **2b** (a), and analogous interactions found in the structure of pure ferrocene (b). Offset y-shaped interactions of ferrocene in **2a** (c) and **2b** (d). Host-guest interactions are shown in blue, while guest-solvent interactions are displayed in green. Cp ring centroids are displayed as red spheres. Color code: orange (Fe), blue (N), maroon (Br), cyan (Zn), gray (C), white (H).

with a cyclohexane molecule, yielding contacts that fall in the range of 2.15–2.88 Å (Fig. 15d). Overall, the observed host-guest interactions in **2a** and **2b** are similar, as the relative position of the Fc molecules are identical. Thus, T-shaped $\pi\cdots\pi$ interactions play a crucial role in directing the assembly of Fc in **1**, and are prevalent over face-to-face $\pi\cdots\pi$ interactions.

In order to obtain an enhanced understanding of host-guest interactions specific to metallocenes, we have loaded **1a** with FcCHO. The presence of FcCHO in the channels of the MOF was first confirmed by ^{1}H NMR spectroscopy after suitable washings with cyclohexane to remove any surface adsorption. The signals belonging to the framework are not shifted; the two peaks corresponding to the TPT ligand are located at 8.63 and 8.92 ppm, while the four signals corresponding to FcCHO are clearly defined. The single-crystal structure is best refined in the *C*2/*c* space group, and hence, the symmetry of the as-synthesized MOF remains unchanged. The void space of the MOF is further filled by cyclohexane and benzene solvent molecules, yielding the compound $\{[ZnI_2)_3(TPT)_2]\cdot(FcCHO)_{2.5}\cdot(C_6H_{12})\cdot(C_6H_6)\}_n$ (**3**), with an asymmetric unit containing two and a half FcCHO molecules. Looking closely at the packing arrangement of **3**, it is evident that the FcCHO guest molecules take up drastically different positions within the pores of the MOF compared to the Fc guests in **2a** and **2b** (Fig. 14). The FcCHO guests are stabilized by a number of interactions with the host framework (Fig. 16a). Notably, the guest molecules in **3** participate in face-to-face $\pi\cdots\pi$ interactions with the triazine rings of the TPT ligand, as determined by a centroid-centroid distance of 3.40 Å, and a dihedral angle between the mean planes of the guest and host rings of 5.9° (Fig. 16b). The addition of an –CHO functional group on the guest molecule results in a drastic

modification of the host-guest interactions, as was previously observed for a number of small organic benzene-based molecules.[9b] We corroborate that imparting an electron-withdrawing functionality on the guest molecule of interest favors a face-to-face $\pi\cdots\pi$ arrangement with either the electron-deficient triazine or pyridyl rings. Hence, we envision being able to control not only the host-guest interactions, but also predict the specific locations of the binding sites through a fundamental understanding of the dominant interactions that drive guest encapsulation.

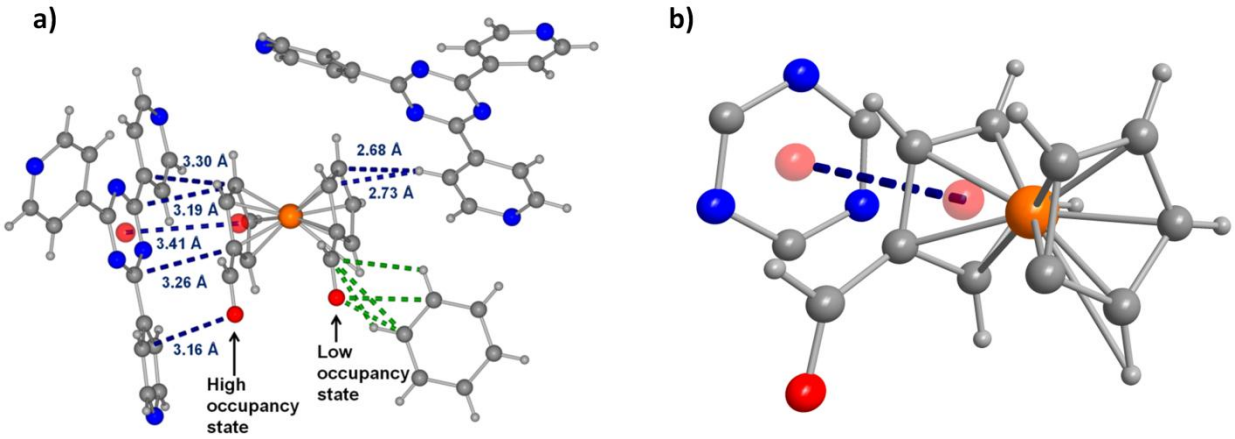

Figure 16. Stabilization of the FcCHO guests in **3**, through numerous close contacts (a). Host-guest interactions are shown in dashed blue bonds, while guest-solvent interactions are in green. Ring centroids are displayed as transparent red spheres. Positional disorder of the FcCHO molecule, with high and low occupancy states, is shown to highlight the full range of host-guest interactions. Face-to-face $\pi\cdots\pi$ stacking interactions between the ferrocene carboxaldehyde guest and the triazine ring of TPT in **3** (b).

It is also important to note that the –CHO moieties of all FcCHO guests are positionally disordered over two sites. The preferential arrangement of the guests however, is clearly evidenced by the considerable difference between the occupancies of the –CHO functional group. The orientation which allows the –CHO moiety to interact more closely with the framework is highly favored. The FcCHO guests are further

stabilized by multiple $\pi\cdots\pi$ interactions with the TPT ligand as well as guest-solvent interactions with benzene.

2.6 **Spectroscopic characterizations**

In order to further investigate the inclusion of the metallocene guests within the pores of the Zn-based MOFs, the pure solid materials were analyzed by diffuse reflectance spectroscopy at room temperature. This allows us to directly probe any confinement effects of the crystalline sponge on the electronic properties of the organometallic guests. Overall, the diffuse reflectance spectra of all guest inclusion compounds exhibit a superposition of the bands observed in the starting MOF and of the selected guests (Fig. 17a). This is not entirely surprising since all guest molecules only exhibit non-covalent interactions with the host framework. The non-covalent interactions are, however, of different nature and strength, as evidenced by the single-crystal X-ray structures. Notably, we observe a significantly higher intensity of the shoulder at 600–800 nm in the spectra of **2a** and **2b**, when compared to the intensity of the same shoulder in the spectrum of Fc, which is negligible. Conversely, the shoulders in the visible range of **3**, which account for

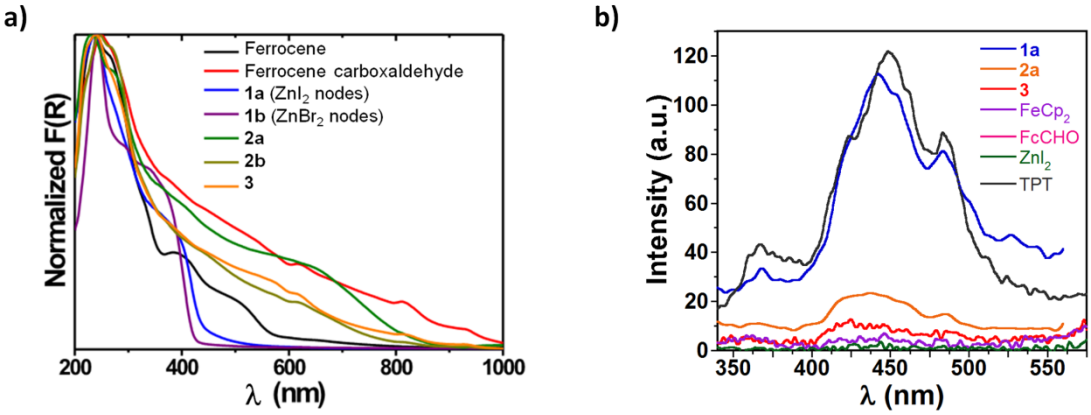

Figure 17. Normalized Kubelka-Munk spectra of the guest molecules, starting MOFs, and inclusion compounds (a). Solid-state photoluminescence spectra of **1a**, **2a** and **3**, and of the starting materials (b).

the presence of FcCHO, are lower in intensity when compared to the spectrum of pure FcCHO. Consequently, the interactions of the metallocene guests with the crystalline sponge **1**, most likely influence the *d-d* transitions, and hence, the HOMO-LUMO energy gap of the encapsulated guests. To gain insight into the exact nature of these spectroscopic changes, future computational studies could be devoted towards comparing the electronic structures of both pure and encapsulated metallocene molecules.

To complement the diffuse reflectance spectroscopy experiments, the solid-state photoluminescence properties of **1a**, **2a** and **3** were also investigated. The data were collected using an excitation wavelength of 300 nm, giving an excitation profile in the 350–550 nm region (Fig. 17b). Thus, we report for the first time the fluorescent behaviour of the parent crystalline sponge **1a**, which exhibits weak blue emission with a broad maximum at 442 nm. The inclusion of Fc and FcCHO effectively quenches the photoluminescence of the framework. As shown in a few other cases,[8b,11b] the excitation energy is transferred to the Fc, and is then quenched following an energy transfer mechanism.

2.7 **Solid-state NMR spectroscopy**

To further probe guest confinement effects, we turned our attention to solid-state nuclear magnetic resonance spectroscopy (SSNMR). More specifically, ^{13}C CPMAS SSNMR allows us to directly measure rotation of the Cp rings, and provides us with information on how compartmentalization of Fc in **1** may affect the dynamic motion of the guest species. Spectra were collected using the dipolar dephasing technique, which involves allowing a short delay without high power proton decoupling between the cross polarization contact time and the beginning of the FID data collection.[12] With this

method, and under these conditions, all rigid proton bearing carbon signals (–CH– and –CH_2–) will typically dephase to zero intensity during a 40 μsec dephasing delay because of the strong ^{13}C–^{1}H dipolar coupling. Non-proton bearing carbon signals, such as those from quaternary or carbonyl carbons, have reduced ^{13}C–^{1}H dipolar coupling due to the longer distance between the carbon and the proximate protons. As a result, their signals will dephase to a much lesser extent and survive the dephasing delay with attenuation based on the degree of dipolar coupling to the protons. The same is true for the signals of highly mobile proton bearing carbon signals such as those from rotating methyl groups. In this case, the ^{13}C–^{1}H dipolar coupling is reduced as a result of molecular motion, and, like the non-protonated carbons, their signals will survive the dephasing delay with attenuation based on the degree of dipolar coupling to the protons. The ^{13}C signal from the Cp rings of a pure crystalline Fc sample and the guest Fc in **2a** is shown in Figure 18 as a function of the dipolar dephasing delay. It is clear that in both cases the Cp signal survives dephasing delays much longer than 40 μsec, indicating that the Cp rings are mobile. It is also apparent that the attenuation of the Cp signals in **2a** is much less than that for pure Fc at all dephasing delays, which is indicative that the guest Fc in **2a** is much more mobile than pure Fc. Previous reports on pure Fc have established that the Cp rings are in fact already capable of rotating freely.[13] Thus, these data suggest that the barrier for rotation of the Cp ring is drastically altered once confined within **1a**. The enhancement of the mobility of the Cp rings may be explained by a sterically less hindered environment, compared to crystalline Fc, in which the molecules are packed in a tight and efficient manner. Indeed, the structure of Fc exhibits a packing arrangement in which the Cp rings adopt a perpendicular y-shaped geometry.[14] The representative $\pi\cdots\pi$ interactions are

compared to that of **2a** and **2b**, and yield much closer contacts (Table 2). These results clearly illustrate how the confinement of guest molecules in select environments, *i.e.* a network of weak non-covalent interactions, can impact molecular motion.

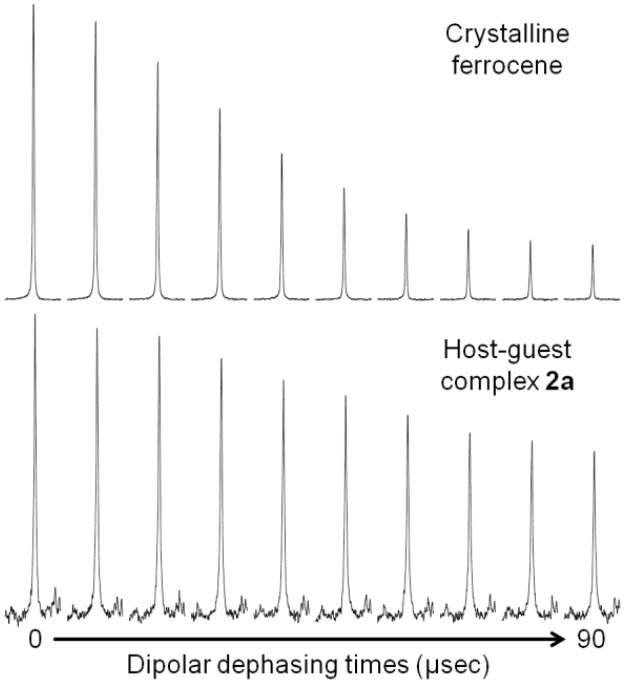

Figure 18. Comparison of the ^{13}C CP MAS SSNMR signals from the Cp rings of crystalline Fc and **2a** with dipolar dephasing times from 0-90 μsec.

2.8 **Conclusions**

In summary, we have successfully encapsulated metallocenes within a crystalline sponge and evaluated the host-guest interactions through single-crystal-to-single-crystal X-ray diffraction. Notably, we demonstrated that T-shaped $\pi\cdots\pi$ interactions are pivotal in the orientation of the Fc molecules, while face-to-face $\pi\cdots\pi$ interactions become predominant upon addition of an electron-withdrawing group on the Cp ring. We have also probed the confinement effects of the benchmark crystalline sponge, through diffuse reflectance spectroscopy, photoluminescence and SSNMR. Remarkably, the confinement effects of a

crystalline sponge have resulted in a significant disparity in the internal ring rotation of the Cp rings between samples of pure and encapsulated Fc molecules. Through this confinement effect study, we have highlighted how host frameworks can drastically impact the structure and electronic properties of guest molecules, by taking advantage of the structural visualization benefits of the crystalline sponge method. In terms of future work, we can think of utilizing the crystalline sponge method for more complex organometallic sandwich complexes. Of particular relevance to our group are Ln^{III} single-ion magnets (SIMs) that exhibit strong axial donors that often adopt similar sandwich-type configurations such as those found in $[Er(COT)_2]^-$ or [Er(COT)(Cp*)],[15] where COT = cyclooctatetraenide and Cp* = pentamethylcyclopentadienide. It would undoubtedly be fascinating to encapsulate such species and study the change in the SIM behaviour, since small structural changes, such as the tilt angle,[16] are critical in determining the performance of such molecules. Moreover, encapsulation within a porous framework may also bring about enhanced stability for these highly air-sensitive compounds.

2.9 Experimental section

2.9.1 General considerations

All manipulations were performed under aerobic conditions using materials as received from commercial suppliers (Sigma Aldrich, Strem Chemical). The ligand 2,4,6-tris(4-pyridyl)-1,3,5-triazine (TPT),[17] and parent MOFs **1a** and **1b**[18] were prepared according to previously published procedures.

2.9.2 **Synthesis**

Synthesis of 2a and 2b. As-synthesized single-crystals of **1a** and **1b** initially contain nitrobenzene in the void space of the lattice, and according to previous work, such molecules would prevent the diffusion of target guest compounds into the pores owing to the strong $\pi\cdots\pi$ interactions between the nitrobenzene solvent molecules and the triazine-based ligand.[19] The exchange of nitrobenzene by cyclohexane is therefore recommended, however, it was found that this additional step was unnecessary for the inclusion of ferrocene and ferrocene carboxaldehyde. The nitrobenzene solution can be carefully decanted, in a manner to keep the crystals in solution, and replaced by a solution of ferrocene (50 mg, 0.27 mmol) in cyclohexane (5 mL). The resulting mixture is heated to 50 ^{o}C over a period of one week in a capped vial. Successful inclusion can be identified by a change in color of the crystals from colorless to dark-brown, while maintaining their crystallinity, allowing for suitable diffraction data to be obtained on a conventional laboratory diffractometer. Compound **2a**: Selected IR: 3050 (w), 1617 (m), 1574 (m), 1514 (s), 1421 (m), 1372 (s), 1314 (m), 1212 (m), 1099 (w), 1058 (s), 1025 (s), 868 (m), 803 (s), 751 (m), 733 (m), 668 (s), 655 (s) cm^{-1}. NMR ^{1}H (DMSO-d_6, 400 MHz): δ 4.11 (s, ferrocene), 7.65 (d, $PhNO_2$), 7.82 (t, $PhNO_2$), 8.21 (d, $PhNO_2$), 8.62 (d, TPT), 8.92 (d, TPT) ppm. Compound **2b**: Selected IR: 3055 (w), 1622 (m), 1576 (m), 1514 (s), 1421 (m), 1372 (s), 1314 (m), 1212 (m), 1100 (w), 1058 (s), 1024 (s), 868 (m), 803 (s), 751 (m), 733 (m), 669 (s), 655 (s) cm^{-1}. NMR ^{1}H (DMSO-d_6, 400 MHz): δ 4.12 (s, ferrocene), 7.64 (d, $PhNO_2$), 7.82 (t, $PhNO_2$), 8.21 (d, $PhNO_2$), 8.63 (d, TPT), 8.92 (d, TPT) ppm.

Synthesis of 3. The same procedure was replicated for **3** as in **2a**/**2b**, except ferrocene carboxaldehyde (58 mg, 0.27 mmol) was dissolved in a mixture of benzene (2.5 mL) and cyclohexane (2.5 mL). Selected IR: 3066 (w), 1661 (w), 1618 (w), 1575 (w), 1575 (w), 1514 (s),

1422 (w), 1373 (m), 1343 (s), 1316 (m), 1214 (w), 1107 (w), 1059 (m), 1025 (m), 850 (m), 804 (s), 704 (s), 666 (w), 655 (s), 621 (w) cm^{-1}. NMR ^{1}H (DMSO-d_6, 400 MHz): δ 4.25 (m, FcCHO), 4.55 (t, FcCHO), 4.75 (d, FcCHO), 7.37 (s, benzene), 8.63 (d, TPT), 8.92 (d, TPT), 9.96 (s, FcCHO) ppm.

2.9.3 **Instrumentation and methods**

Single-crystal X-ray diffraction.

Compound **2a**

Single crystal X-ray diffraction data for **2a** were collected at 200(2) K on a Bruker-AXS KAPPA diffractometer equipped with a sealed Mo tube source (λ = 0.71073 Å) APEX II CCD detector. Data collection and processing were performed with the Bruker APEX II software package.[20] The structures were solved by direct methods and refined with full-matrix least-squares procedures using SHELXL.[21] All non-hydrogen atoms were refined anisotropically. The positions of the hydrogen atoms were calculated based on the geometry of related non-hydrogen atoms.

Compounds **2b** and **3**

Diffraction data for **2b** and **3** were collected on a Mar345 image plate using MoKα radiation (λ = 0.71073 Å, Rigaku UltraX 18S, Xenocs Fox3d mirrors). Prior to the X-ray experiments the crystals were flash-cooled to 150K in a N_2 gas flow. Data integration was performed by CrysalisPro[22] and the implemented absorption correction was applied. The structures were solved by direct methods SHELXS-97[21] and refined by full-matrix least-squares procedures using SHELXL2014[21]. All non-hydrogen atoms were refined anisotropically and H

atoms were placed at calculated positions and allowed to ride on the parent atoms with Ueq values 1.2 times higher than these parent atoms.

Solid-state NMR spectroscopy. Solid state ^{13}C CPMAS NMR spectra were collected on a Bruker AVANCE III 200 NMR spectrometer using a 7 mm CPMAS probe operating at a spinning speed of 4.5 kHz. The ^{1}H 90° pulse was 4.9 μsec. A contact time of 2 msec was used. In the case of pure crystalline ferrocene, spectra were collected with 32 scans. The ^{1}H T_1 relaxation time was quite long making a 60 sec recycle delay necessary. The spectra of complex **2a** were collected with 1400 scans. The ^{1}H T_1's were much shorter allowing a 2 sec recycle delay to be used.

Solution-state NMR spectroscopy. ^{1}H NMR of the digested samples were conducted on a Bruker Avance 400 MHz spectrometer equipped with an automatic sample holder and a 5 mm auto tuning broadband probe with Z gradient.

Infrared spectroscopy. IR spectra were collected on all samples in the solid state on a Varian 640 FT-IR spectrometer in the 525–4000 cm^{-1} range**.**

Diffuse reflectance spectroscopy. Diffuse-reflectance spectra were measured with a Varian Cary-100 spectrophotometer using polytetrafluoroethylene (PTFE) as a reference. Kubelka-Munk spectra were normalized to allow meaningful comparisons.

Solid-state luminescence. Fluorescence spectra were recorded using a Perkin Elmer LS-50 Luminescence spectrometer equipped with a Xenon lamp and a variable angle front-surface accessory. Solid samples were sandwiched between two quartz disks.

2.10 **References**

(1) J.-R. Li, J. Sculley and H.-C. Zhou, *Chem. Rev.*, 2012, **112**, 869–932.

(2) J. Lee, O. K. Farha, J. Roberts, K. A. Scheidt, S. T. Nguyen and J. T. Hupp, *Chem. Soc. Rev.*, 2009, **38**, 1450–1459.

(3) J. D. Rocca, D. Liu and W. Lin, *Acc. Chem. Res.*, 2011, **44**, 957–968.

(4) N. A. Khan, Z. Hasan and S. H. Jhung, *J. Hazard. Mater.*, 2013, **244**, 444–456.

(5) (*a*) T. K. Maji, G. Mostafa, R. Matsuda and S. Kitagawa, *J. Am. Chem. Soc.*, 2005, **127**, 17152–17153; (*b*) C.-L. Chen and A. M. Beatty, *J. Am. Chem. Soc.*, 2008, **130**, 17222–17223; (*c*) M. J. Manos, E. J. Kyprianidou, G. S. Papaefstathiou and A. J. Tasiopoulos, *Inorg. Chem.*, 2012, **51**, 6308–6314.

(6) Y. Inokuma, S. Yoshioka, J. Ariyoshi, T. Arai, Y. Hitora, K. Takada, S. Matsunaga, K. Rissanen and M. Fujita, *Nature*, 2013, **495**, 461–466.

(7) E. G. Derouane and C. D. Chang, *Microporous Mesoporous Mater.*, 2000, **35–6**, 425–433; (*b*) G. Sastre and A. Corma, *J. Mol. Catal. A: Chem.*, 2009, **305**, 3–7.

(8) (*a*) M. Meilikhov, K. Yusenko and R. A. Fischer, *Dalton Trans.*, 2010, **39**, 10990–10999; (*b*) P. P. Mazzeo, L. Maini, D. Braga, G. Valenti, F. Paolucci, M. Marcaccio, A. Barbieri and B. Ventura, *Eur. J. Inorg. Chem.*, 2013, 4459–4465; (*c*) R. Heck, O. Shekhah, O. Zybaylo, P. G. Weidler, F. Friedrich, R. Maul, W. Wenzel and C. Wöll, *Polymers*, 2011, **3**, 1565–1574.

(9) (*a*) X.-F. Gu, Y. Zhao, K. Li, M.-X. Su, F. Yan, B. Li, Y.-X. Du and B. Di, *J. Chromatogr. A*, 2016, **1474**, 130–137; (*b*) L. M. Hayes, C. E. Knapp, K. Y. Nathoo, N. J. Press, D. A. Tocher and C. J. Carmalt, *Cryst. Growth Des.*, 2016, **16**, 3465–3472; (*c*) T.

R. Ramadhar, S.-L. Zheng, Y.-S. Chen and J. Clardy, *Chem. Commun.*, 2015, **51**, 11252–11255; (*d*) L. M. Hayes, N. J. Press, D. A. Tocher and C. J. Carmalt, *Cryst. Growth Des.*, 2016, **17**, 858–863; (*e*) G. Brunet, D. A. Safin, M. Z. Aghaji, K. Robeyns, I. Korobkov, T. K. Woo and M. Murugesu, *Chem. Sci.*, 2017, **8**, 3171–3177.

(10) K. Biradha and M. Fujita, *Angew. Chem., Int. Ed.*, 2002, **41**, 3392–3395.

(11) (*a*) H. Kim, H. Chun, G.-H. Kim, H.-S. Lee and K. Kim, *Chem. Commun.*, 2006, 2759–2761; (*b*) S. A. Sapchenko, D. G. Samsonenko, D. N. Dybtsev, M. S. Melgunov and V. P. Fedin, *Dalton Trans.*, 2011, **40**, 2196–2203.

(12) S. J. Opella and M. H. Frey, *J. Am. Chem. Soc.*, 1979, **101**, 5854–5856.

(13) (*a*) A. Haaland and J. E. Nilsson, *Acta Chem. Scand.*, 1968, **22**, 2653–2670; (*b*) A. Gardner, J. Howard, T. Waddington, R. Richardson and J. Tomkinson, *Chem. Phys.*, 1981, **57**, 453–460.

(14) F. Takusgawa and T. F. Koetzle, *Acta Crystallogr. Sect. B*, 1979, **35**, 1074–1081.

(15) (*a*) S.-D. Jiang, B.-W. Wang, H.-L. Sun, Z.-M. Wang and S. Gao, *J. Am. Chem. Soc.*, 2011, **133**, 4730-4733; (*b*) L. Ungur, J. J. Le Roy, I. Korobkov, M. Murugesu and L. F. Chibotaru, *Angew. Chem. Int. Ed.*, 2014, **53**, 4413-4417.

(16) Z. Zhu, M. Guo, J. Tang, *Coord. Chem. Rev.*, 2019, **378**, 350-364.

(17) M.-X. Li, Z.-X. Miao, M. Shao, S.-W. Liang and S.-R. Zhu, *Inorg. Chem.*, 2008, **47**, 4481–4489.

(18) K. Biradha and M. Fujita, *Angew. Chem., Int. Ed.*, 2002, **41**, 3392–3395.

(19) Y. Inokuma, S. Yoshioka, J. Ariyoshi, T. Arai and M. Fujita, *Nat. Protoc.*, 2014, **9**, 246–252.

(20) *APEX Software Suite v. 2010*, Bruker AXS, Madison, WI, 2005.

(21) G. M. Sheldrick, *Acta Cryst.*, 2008, **A64**, 112–122.

(22) Rigaku Oxford Diffraction, (2014), CrysAlisPro Software system, version 1.171.37.31, Rigaku Corporation, Oxford, UK.

(23) M. Kawano, T. Haneda, D. Hashizume, F. Izumi and M. Fujita, *Angew. Chem., Int. Ed.*, 2008, **47**, 1269–1271.

Science does not mean idle resting upon a body of certain knowledge;
it means unresting endeavor and continually progressing development
toward an end which the poetic intuition may apprehend,
but which the intellect can never fully grasp
– Max Planck[4]

Chapter 3

Tuning the magnetic behaviour of Co(II) in high-dimensionality networks

3.1 **Published contributions**

Single-molecule magnetism arising from cobalt(II) nodes of a crystalline sponge

G. Brunet, D. A. Safin, J. Jover, E. Ruiz and M. Murugesu, *J. Mater. Chem. C*, 2017, **5**, 835-841.

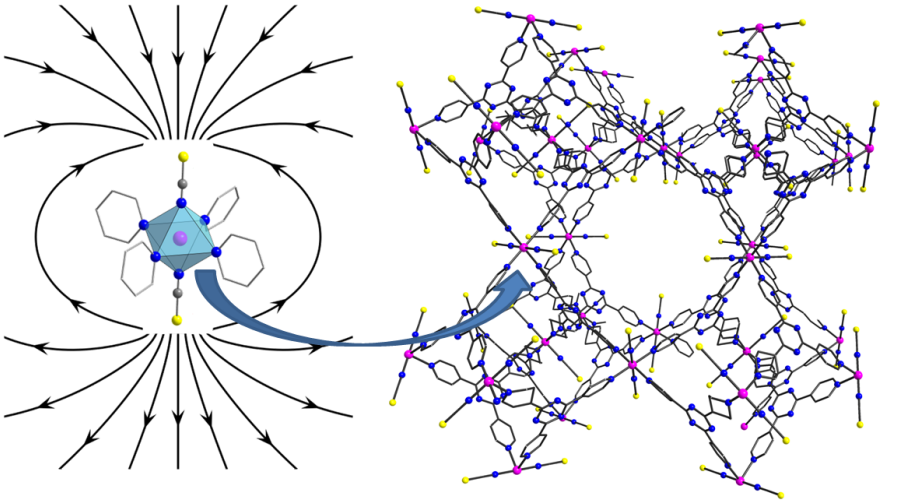

G. Brunet and M. Murugesu wrote the manuscript. G. Brunet performed the majority of the experiments. D. A. Safin assisted in the synthesis of the starting ligand.

J. Jover and E. Ruiz performed the *ab initio* calculations.

[4] *The Philosophy of Physics*, 1936.

3.2 **Abstract**

The highly versatile metal–organic framework (MOF), $\{[(Co(NCS)_2)_3(TPT)_4]\cdot a(H_2O)\cdot b(MeOH)\}_n$ (**1**), which is used in the revolutionary crystalline sponge method, displays characteristic single-molecule magnet (SMM) behaviour under applied static fields. We report the subtle effects of changes in the coordination environment of the Co^{II} ions in **1**, leading to drastically different magnetic behaviours of two additional related compounds, $\{[(Co(NCS)_2)_3(TPT)_4]\cdot c(H_2O)\}_n$ (**2**) and $\{[(Co(NCS)_2(H_2O)_{0.65}(MeOH)_{0.35})_3(TPT)_2]\cdot 2.4(H_2O)\}_n$ (**3**). Magnetic measurements reveal unquenched first order orbital angular momentum, and the presence of significant magnetic anisotropy in all compounds, which was corroborated through CASSCF-type calculations. Notably, the crystalline sponge is the first example of a 3D network built from Co^{II} single-ion magnets (SIMs) as nodes.

3.3 **Introduction**

In recent years, the drive towards molecular materials that behave as small nanomagnets has relied on the use of metal ions to generate non-zero spin ground states. The combination of large spin ground states with magnetic anisotropy can give rise to the magnet-like behaviour of slow relaxation of the magnetization. Molecular materials exhibiting such behaviour are commonly referred to as single-molecule magnets (SMMs) or single-ion magnets **(**SIMs**)** for polynuclear and mononuclear complexes, respectively.[1] When considering 3*d* transition metal ions, magnetic anisotropy is commonly achieved by unquenched orbital angular momentum due to the unequal filling of the *d* orbitals.[2] In this regard, Co^{II} ions in an octahedral ligand field are particularly interesting due to degenerate t_{2g} levels that are partially occupied, and thus, orbital angular momentum is not quenched. An additional key parameter in the rational design of SMMs is

control over the intermolecular interactions. Such interactions often hinder a precise understanding of the origin of the relaxation modes in SMMs, and moreover, can impede the observation of SMM-like behaviour.[3] Consequently, several different approaches have been established in order to minimize intermolecular interactions. Initially, the synthetic strategy consisted of incorporating a shell of peripheral protecting diamagnetic ligands and/or separating the spin carriers by large organic counterions.[4] Another approach involves the magnetic dilution method which incorporates a paramagnetic ion into a diamagnetic system, effectively isolating a single paramagnetic metal center.[5] A more recent strategy, however, involves fixing the metal centres in place through the use of rigid linkers that play the role of organic spacers.[6] Subsequently, we can modulate the linkers to increase or decrease the space between spin carriers, leading to high dimensionality networks. As such, metal-organic frameworks (MOFs) provide a fascinating approach at potentially controlling and enhancing SMM-like properties. While MOFs are generally associated with applications based on gas storage and separation,[7] the incorporation of magnetic moment carriers within the framework of a MOF, through either paramagnetic metal centres or radical linkers, can be an effective strategy towards fine-tuning the magnetic interactions between neighbouring moment carriers.[8]

Recently, a new subclass of MOFs, the so-called "crystalline sponges", were described in which guest encapsulation occurs in a solid-state-to-solid-state fashion, permitting the subsequent use of X-ray diffraction techniques to elucidate the crystal structure of the guest compound.[9] Our investigations on the cobalt-containing MOF $\{[Co(NCS)_2)_3(TPT)_4]\cdot a(H_2O)\cdot b(MeOH)\}_n$ (**1**), where TPT is the 2,4,6-tris(4-pyridyl)-1,3,5-triazine ligand, revealed two solid-state-to-solid-state transformations that significantly alter the structure and composition of the crystalline sponge.[10] Nevertheless, we were intrigued by the

potential of **1** to exhibit slow relaxation of the magnetization due to the octahedral ligand field of the Co^{II} ions which promotes significant magnetic anisotropy as a result of unquenched first-order orbital angular momentum. Herein, we report the SMM behaviour of a crystalline sponge, which reveals the first example of a three-dimensional network built from Co^{II} SIMs as nodes. The exciting advancement of incorporating metal nodes, which behave as individual nanomagnets, into porous solids, effectively yielding light-weight materials, is particularly appealing for use as spin qubits in quantum computation. Indeed, SMMs prove to be attractive candidates for high-density information storage, in part due to their molecular nature and long coherence times.[11] The discovery of a crystalline sponge exhibiting SMM behaviour paves the way for novel guest encapsulation studies, where both dia- and paramagnetic guests can influence the overall slow magnetic relaxation dynamics. In the present work, we have evaluated the magnetic properties of MOF **1** and the compounds obtained therefrom through solid-state transformations. All compounds exhibit frequency-dependent out-of-phase peaks or tails of signals, suggestive of SMM behaviour.

3.4 **Synthesis and structure**

In accordance with previously reported methods,[10] the parent MOF **1** is obtained by carefully layering a methanol solution of $Co(NCS)_2$ (40 mM, 1.0 mL) on top of a solution of TPT (6.3 mg) dissolved in 4.0 mL of *o*-dichlorobenzene and 1.0 mL of MeOH. After a period of 1 week, orange block-like single-crystals can be obtained alongside a microcrystalline pink powder, identified as compound **3**. In order to obtain compound **2**, the single-crystals of **1** can simply be left out of solution under ambient conditions for a period of 24 h, yielding the green semiamorphous material. The molecular structures of the three compounds studied herein will be presented succinctly, as they are described in detail elsewhere,[10] however the main features

which are of importance to the magnetic properties are presented. Compound **1** exhibits a 3D porous network, assembled by monomeric units of Co^{II} in a slightly distorted octahedral coordination environment (Fig. 19). The TPT ligands take up the equatorial positions, while the axial positions are occupied by nitrogen-bound thiocyanate anions. The Co^{II} ions are well-isolated, with the closest Co···Co separation being 13.39 Å, which occurs through the TPT ligand (Fig. 20). Subsequently, we expect zero or minimal magnetic interactions between the metal centres.

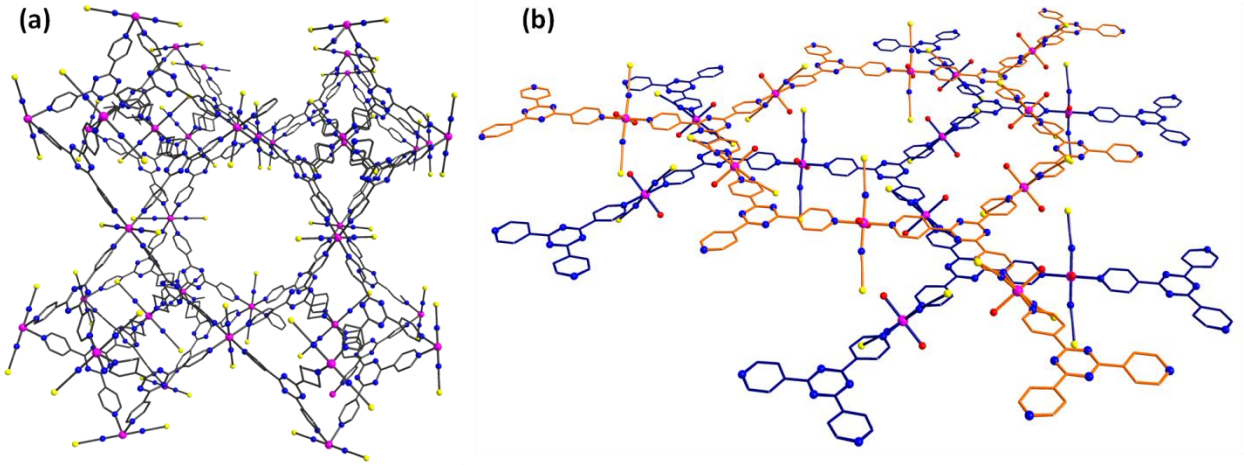

Figure 19. (a) Packing arrangement of **1**, illustrating the large pore dimensions of the 3D network. (b) View of the 2D planar sheet arrangement of **3**, with individual sheets displayed in orange and blue. Colour code: pink (Co), blue (N), red (O), yellow (S). Carbon atoms are represented as stick model for clarity. Hydrogen atoms and solvent molecules are omitted for clarity.

We have previously demonstrated that the removal of the single-crystals of **1** from solution, results in an irreversible transformation to a semiamorphous material in which the surface Co^{II} ions undergo a change in coordination environment from octahedral to tetrahedral.[10] This single-crystal-to-amorphous phase transition leads to the formation of $\{[Co(NCS)_2)_3(TPT)_4]\cdot c(H_2O)\}_n$ (**2**). The third compound studied in the present work, is obtained by evaporation of the MeOH layer during synthesis of **1**, and yields the densely packed layered

structure $\{[Co(NCS)_2(H_2O)_{0.65}(MeOH)_{0.35})_3(TPT)_2]\cdot 2.4(H_2O)\}_n$ (**3**) (Fig. 19). In this case, the Co^{II} ions remain in a distorted octahedral symmetry; however, two TPT ligands have been replaced by coordinated water and methanol molecules. While the nearest intralayer Co···Co separation in **3** is 13.35 Å, the closest metal-metal distance is 8.37 Å and occurs between adjacent sheets.

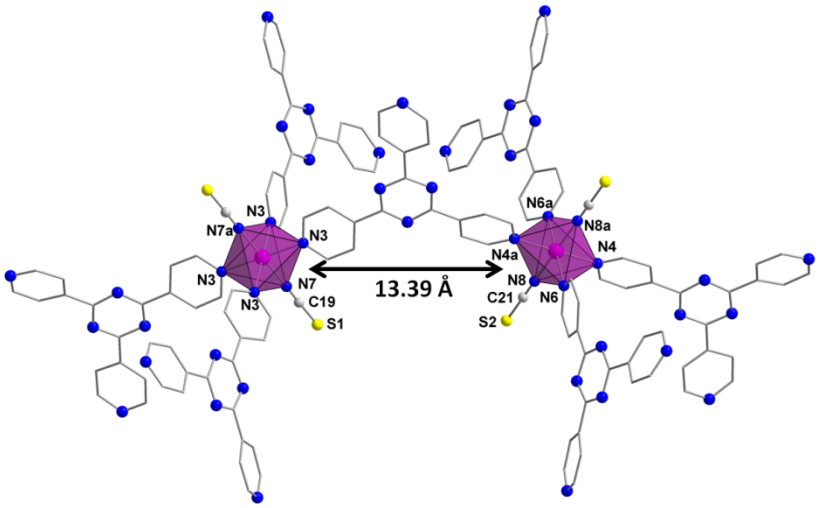

Figure 20. Molecular fragment of **1**, displaying the well-separated octahedral Co^{II} ions.

3.5 **Static magnetic properties**

An analysis of the magnetic properties of **1** allows us to elucidate the effects of structural collapse due to solvent evaporation, as observed in **2**, and of structural reorganization in **3**, on the overall magnetic behaviour. It is important to note that magnetic measurements of **1** were performed in paraffin oil in order to prevent solvent evaporation and to maintain its structural integrity. Variable temperature direct current (dc) susceptibility measurements were performed at 1000 Oe in the temperature range of 1.8–300 K using a SQUID magnetometer (Fig. 21). The room temperature χT products are 3.06, 2.64 and 2.94 cm^3 K mol^{-1} for compounds **1**, **2** and **3**, respectively. These values, while higher than

the anticipated spin-only value of 1.88 cm^3 K mol^{-1} for an S = 3/2 system, still fall in an acceptable range when compared to other experimentally observed high-spin Co^{II} ions with significant magnetic anisotropy.[12] The χT values remains fairly constant down to 200 K for all compounds investigated, before gradually decreasing upon further cooling. In all cases, the decrease of the χT product is most likely a consequence of magnetic anisotropy and/or thermal depopulation of the excited states rather than antiferromagnetic interactions due to the large distance separating the Co^{II} ions. This is especially valid for **1** and **3**, with the closest Co···Co distances being 13.39 Å and 8.37 Å, respectively.

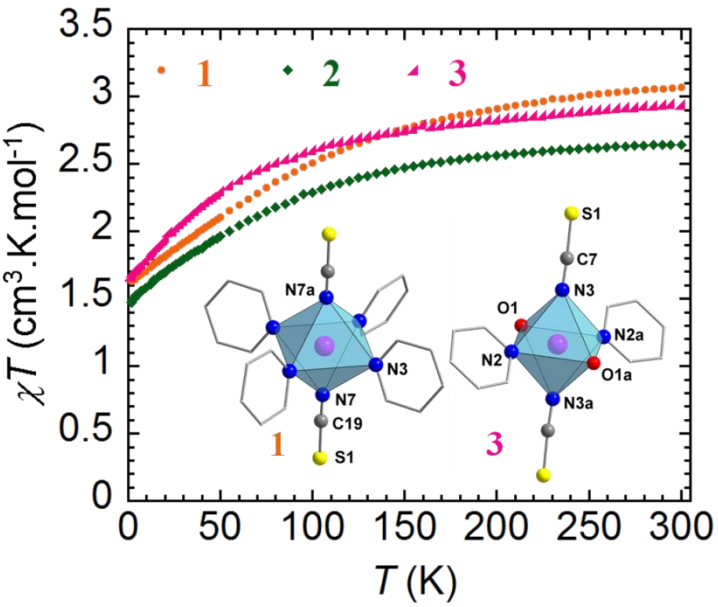

Figure 21. Temperature dependence of the magnetic susceptibility for compounds **1**–**3** in a χT *vs.* *T* plot at 1000 Oe.

For **2**, due to the structural rearrangement it is not possible to definitively rule out intermolecular interactions, however, based on the fact that **2** also contains tetrahedral Co^{II} ions, non-negligible anisotropy can also be expected. To confirm the presence of magnetic anisotropy, field dependent magnetization measurements (*M vs. H*) and reduced

magnetization studies were performed on all compounds presented herein (Fig. 22). In all cases, the magnetization curves reveal a rapid and steady increase of the magnetization at 1.8 K without clear saturation at 7 T. The non-saturation, as well as the non-superimposition of the iso-temperature lines in the *M vs. H*/*T* data, clearly confirms the presence of significant magnetic anisotropy.

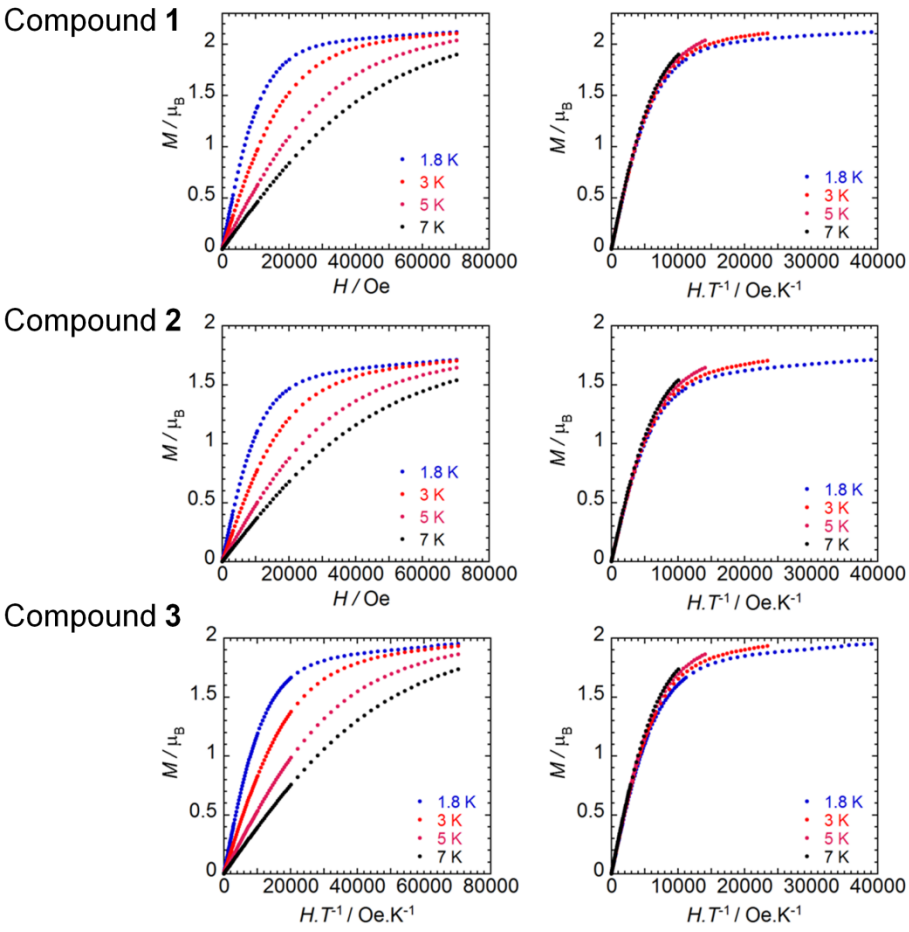

Figure 22. Magnetization *vs.* field measurements at 1.8, 3, 5 and 7 K for **1**, **2** and **3**, plotted as *M* vs *H* (left) and *M* vs *H*/*T* (right).

3.6 **Dynamic magnetic properties**

In recent years, mononuclear cobalt complexes with significant anisotropy were found to exhibit SMM-like behaviour.[13,14] This behaviour is primarily arising from the inherent magnetic anisotropy of the metal centre which is strongly influenced by the ligand field and coordination geometry/environment. To investigate potential slow relaxation of the magnetization dynamics, temperature dependent alternating current (ac) susceptibilities were measured under applied fields of 0 and 1000 Oe for compounds **1**–**3** (Fig. 23). For all compounds, an ac signal was only present under applied dc fields of 1000 Oe. This is generally indicative of the presence of significant quantum tunnelling of the magnetization due to non-negligible transverse anisotropy (*E*).

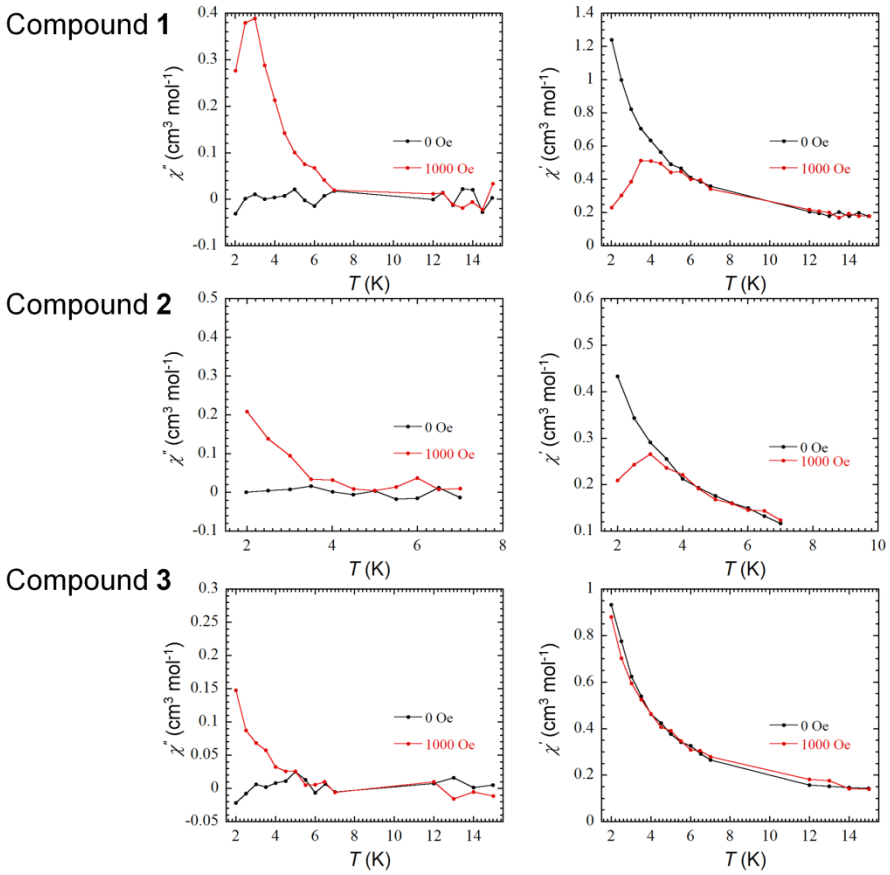

Figure 23. Temperature dependence of the in-phase χ' (left) and out-of-phase χ'' (right) ac susceptibility signals under applied dc fields of 0 and 1000 Oe for compounds **1-3**.

In the case of **1**, the emergence of a clear peak in the χ'' vs. T plot, rather than merely tails of peaks, as in the case of **2** and **3**, encouraged us to further examine the magnetic properties arising from this compound. The optimum applied dc field for **1**, where the minimum of the characteristic frequency was observed, was determined to be H_{dc} = 600 Oe (Fig. 24).

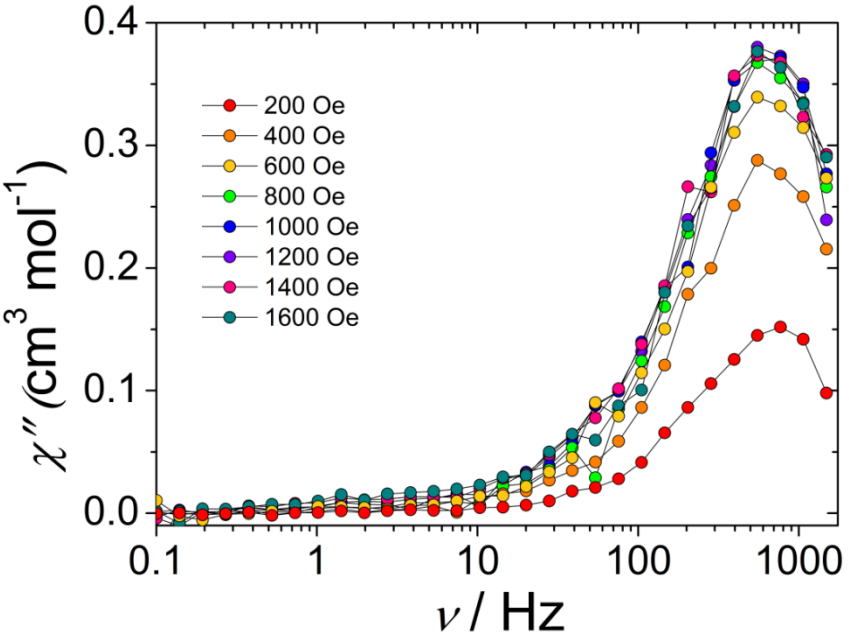

Figure 24. Out-of-phase ac susceptibility χ'' of **1** collected at 2 K under dc fields ranging from 200 Oe to 1.6 kOe in 200 Oe increments. Solid lines are guides for the eyes.

In the ac susceptibility data, the shifting of the peaks towards lower frequencies with decreasing temperatures is indicative of superparamagnet-like slow relaxation of a field-induced SMM (Fig. 25a). In order to reproduce the temperature dependence of the relaxation time, we initially considered the thermally-activated Orbach process. The fit of the linear portion of the Arrhenius plot afforded an effective energy barrier for the reversal of the magnetization of 7.0 K and $\tau_0 = 8.68 \times 10^{-6}$ s (Fig. 25b). This observable barrier is rather small, yet comparable to other mononuclear Co^{II} SMMs.[2b,13]

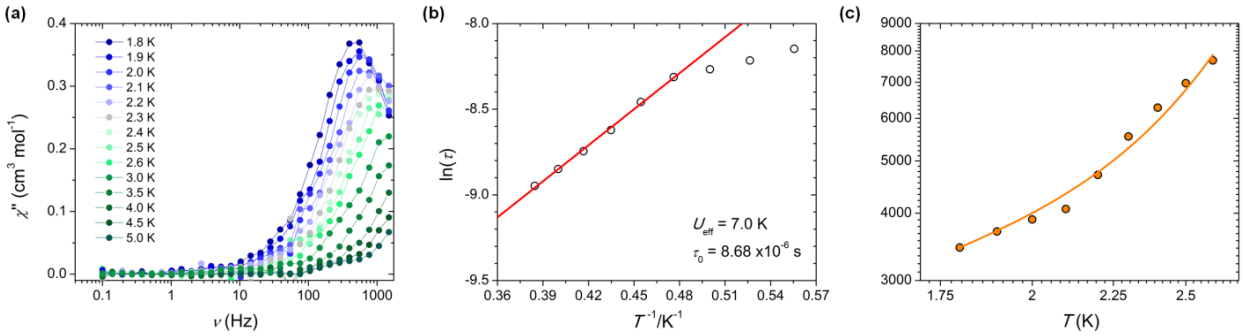

Figure 25. (a) Frequency dependence of the out-of-phase χ'' magnetic susceptibilities for **1**, under an applied optimum dc field of H_{dc} = 600 Oe. Lines serve as guides for the eyes. (b) Plot of ln(τ) *vs*. 1/T for **1**. The solid line represents the Arrhenius fit of the frequency-dependent data. (c) Temperature dependence of the relaxation rate for **1**, where the solid line corresponds to the fit based on the equation $1/\tau = A_{dir}H^4T + B_{Raman}T^n$, where H = 0.06 T. The parameters obtained from the best fit are A_{dir} = 1.43 * 10^8 s^{-1} K^{-1} T^{-4}, B_{Raman} = 0.94 s^{-1} $K^{-8.97}$ and n = 8.97.

Recent energy barriers reported for Co^{II}-based SIMs with structural dimensionalities greater than zero are summarized in Table 4. Such a behaviour is in agreement with the predicted positive D value for octahedral d^7 Co^{II} cations, as demonstrated in a number of prior studies.[2b,15] It is important to note however, that the activation energy derived from the Arrhenius plot is several orders of magnitude smaller than the energy gap between the ground and excited level doublets (*vide infra*). Thus, the absence of excited states with similar values to the activation energy allows us to preclude an Orbach mechanism, and consider uniquely the contributions from direct/Raman processes. The resulting fit of the τ^{-1} *vs*. T plot is in good agreement with the experimental data, and yields A_{dir} = 1.43 × 10^8 s^{-1} K^{-1} T^{-4}, B_{Raman} = 0.94 s^{-1} $K^{-8.97}$ and n = 8.97 (Fig. 25c). Subsequently, we confirm that the contribution of the one-phonon direct process dominates below 3 K, while the Raman exponent is in good agreement with the expected value of n = 9 for a Kramers system.[2b,15] To the best of our knowledge, **1** represents the first case of a 3D Co^{II}-based network exhibiting SIM behaviour.

Table 4. Compilation of the energy barriers of recent octahedral Co^{II} SIMs with extended structures (in one, two or three dimensions).

Compound	Dimensionality	SIM, H ≠ 0 (Oe)	U_{eff} (K)	τ_0 (s)	Ref.
$[Co(btm)_2(SCN)_2 \cdot H_2O]_n$	1D	1500	45.4	5.6×10^{-8}	14a
$[Co(azbbpy)(bpe)_{0.5}(DMF)(NCS)_2] \cdot 0.25H_20$	2D	1000	8.4	1.7×10^{-6}	14b
$[Co(azbbpy)(4,4'bipy)_{0.5}(DMF)(NCS)_2] \cdot MeOH$	2D	1000	14.0	1.2×10^{-6}	14b
$[Co(dca)_2(atz)_2]_n$	2D	1000	7.3	1.7×10^{-6}	14c
$[Co(dca)_2(bim)_2]_n$	2D	500–2500	6.5–13.3	0.37×10^{-6}	14d
$[Co(dca)_2(bmim)_2]_n$	2D	500–2500	16.5–22.2	6.3×10^{-7}	14d
$[Co(ppad)_2]_n$	2D	2000	16.4	5.0×10^{-6}	14e
$[Co(pbeb)_2(NCS)_2] \cdot 7DCB$	2D	250–1000	42.0–45.0 10.9–12.7	1.7×10^{-8} 4.1×10^{-6}	14f
$[Co(pbeb)_2(NCS)_2] \cdot 4TAN$	2D	1000	24.6 8.9	2.3×10^{-7} 7.8×10^{-6}	14f
$[Co(pbeb)_2(NCS)_2] \cdot 6TOL$	2D	1000	16.5 3.6	8.2×10^{-7} 3.0×10^{-5}	14f
$[Co(pbeb)_2(NCS)_2] \cdot 8PYR$	2D	1000	30.2 7.1	1.3×10^{-7} 1.0×10^{-5}	14f
$\{[Co(NCS)_2)_3(TPT)_4] \cdot a(H_2O) \cdot b(MeOH)\}_n$	3D	600	7.0	8.7×10^{-6}	this work

The observable difference in the generation of slow magnetic relaxation between **1** and **2** may be attributed to the change in coordination geometry from octahedral to tetrahedral. In theory, first-order orbital angular momentum, the principal contributor to magnetic anisotropy, is absent in a perfect tetrahedral geometry. However, it has been demonstrated that some distorted tetrahedral complexes exhibit non-negligible barriers even at zero applied dc fields due to the mixing of the electronic ground state and the anisotropic excited states.[17] The sign of the anisotropy is often dictated by the ligand field around the metal centre. In our case, due to the amorphous nature of **2**, it is not possible to identify any distortion in the coordination environment, and consequently, magneto-structural correlations cannot be performed. Nevertheless, through ac susceptibility measurements we can unequivocally conclude that **2** displays different structural features

than the parent MOF **1**. When comparing the magnetic behaviours of **1** and **3**, the weak ac signal observed for **3** can again be attributed to a change in the coordination environment of the Co^{II} ions. In comparison to **1**, two TPT nitrogen atoms are replaced by two oxygen atoms from coordinated H_2O and MeOH molecules. This change induces a weaker ligand field around the metal centre and a smaller separation of the t_{2g} and e_g sets. Such a variation in the electronic configuration is known to lead to a change in the local anisotropy of the metal centre (*i.e.* sign and strength), which subsequently leads to weaker spin-orbital coupling. This results in a change of the superparamagnetic properties through a decrease of the energy barrier for magnetization reversal.

3.7 *Ab initio* calculations

Ab initio calculations were performed on **1** and **3** in order to gain additional insight into the electronic and magnetic structures of the compounds presented in this thesis. The magnetic properties of the low-lying states of complexes **1** and **3** were analyzed by means of an *ab initio* multireference methodology; the computed second-order anisotropy parameters and excitation energies are summarized in Table 5. These values have been obtained from two different electronic structure calculations that have been carried out with the ORCA[18] and MOLCAS[19] software packages. ORCA produces two sets of results: CASSCF and NEVPT2 (which introduces the dynamic correlation effects), both including spin-orbit contributions. On the other hand MOLCAS has been only able to provide CASSCF results, including spin-orbit effects that have been introduced with the SO-RASSI method. As expected for octahedral Co^{II} complexes, large and positive *D* values are found.[2b] The calculated zero-splitting *D* parameters remain very similar regardless the method employed and are larger for compound **1**. These computed values

are not unusual since the spin relaxation mechanisms that depend on the lattice effects, and should contribute to reduce the *D* values, cannot be captured in a single-molecule calculation.

Table 5. CASSCF and NEVPT2 (Orca code) and CASSCF (Molcas code) computed *D*, |*E*| (in cm^{-1}), and *g*-values for the ground state of complexes **1** and **3**. δ and Δ (in cm^{-1}) are the computed first excitation energies before and after including the spin-orbit effects, respectively. The Δ value corresponds to the energy difference between the ground and the first excited Kramers' doublets.

Complex	D_{calc}	$\|E\|_{calc}$	δ	Δ	g_{xx}, g_{yy}, g_{zz}
1[a]	148.1	5.6	157.3	296.9	1.59 2.41 2.82
1[b]	136.7	14.7	200.3	278.1	1.64 2.35 2.90
1[c]	136.6	29.2	165.9	291.2	1.76 2.38 2.88
3[a]	99.8	18.2	379.2	209.3	1.80 2.59 2.98
3[b]	97.4	22.4	371.1	209.6	1.80 2.50 2.99
3[c]	99.1	24.4	354.4	215.4	1.80 2.58 3.02

[a]ORCA/CASSCF., [b]ORCA/NEVPT2, [c]MOLCAS/CASSCF.

The calculated *D* tensors for all compounds are very similar and show almost the same orientation (Figure 26). In all cases, a 3/2 ground state is found for both complexes before including the spin-orbit effects. In these conditions, the calculations show the existence of low-lying spin-orbit free excited states (δ in Table 5) with close energies to the ground state, showing a direct correlation of such energy difference with the calculated *D* value. This is also confirmed by the anisotropic *g*-values for the ground state of **1** and **3** (Table 5, the full *g* tensors can be found in the Supporting Information of the manuscript at http://www.rsc.org/suppdata/c6/tc/c6tc04703c/c6tc04703c1.pdf). Once the spin-orbit effects are included, a set of Kramers' doublets (KDs, Δ) is obtained for each complex. In the case of compound **1**, there are two low-lying KDs at around 280 and 450 cm^{-1}, which may participate in spin relaxation processes (*vide infra*). This situation changes slightly for complex **3**; while the first KD lies low at around 210 cm^{-1}, the second excited state is quite higher in energy (650 cm^{-1}). An exhaustive list of the excited state

energies, both with (Δ) and without (δ) spin-orbit contributions can be found in the aforementioned link for the Supporting Information. These data again show relatively high similarities between the employed theoretical methods.

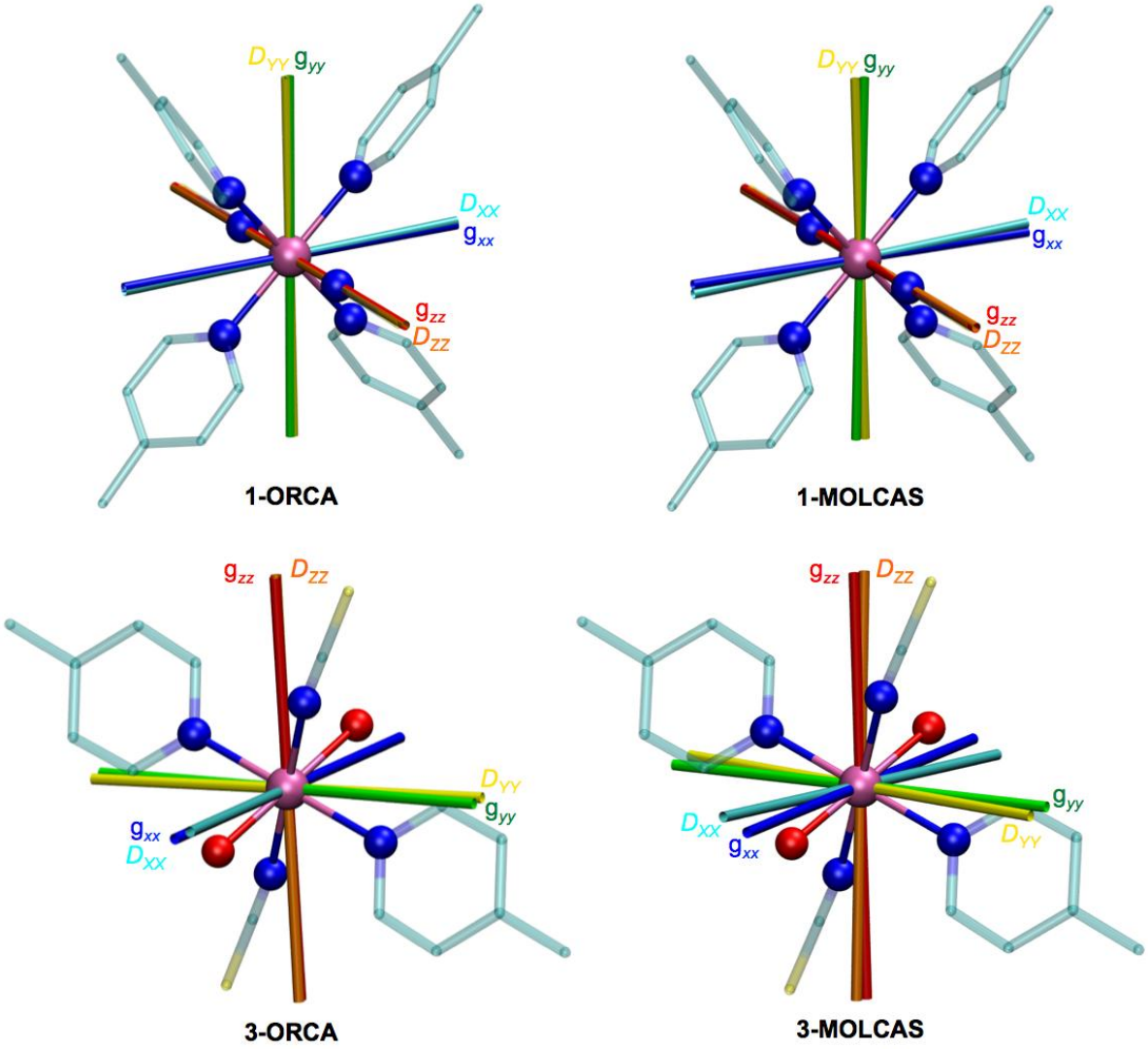

Figure 26. Orientation of the CASSCF computed *g*- and *D*-tensors for complexes **1** and **3** with ORCA and MOLCAS.

Extracting the excitation energies from CASSCF calculations is relatively easy and fast; nevertheless, identifying the metal d-orbitals involved in such transitions is not straightforward. For that reason, using a single-determinant wavefunction calculation (DFT) is often the method

of choice for obtaining a qualitative explanation of the excitation processes, in which the orbital composition is much easier to rationalize. By doing this, the excitation energies correspond to electronic transitions from the highest energy doubly occupied orbital to the higher energy semioccupied β-orbitals. The DFT calculations of complexes **1** and **3** have been carried out with the Gaussian09 package.[20] The final d-orbital splitting of the studied complexes, which allows the location of the lowest energy transitions, is shown in Figure 27.

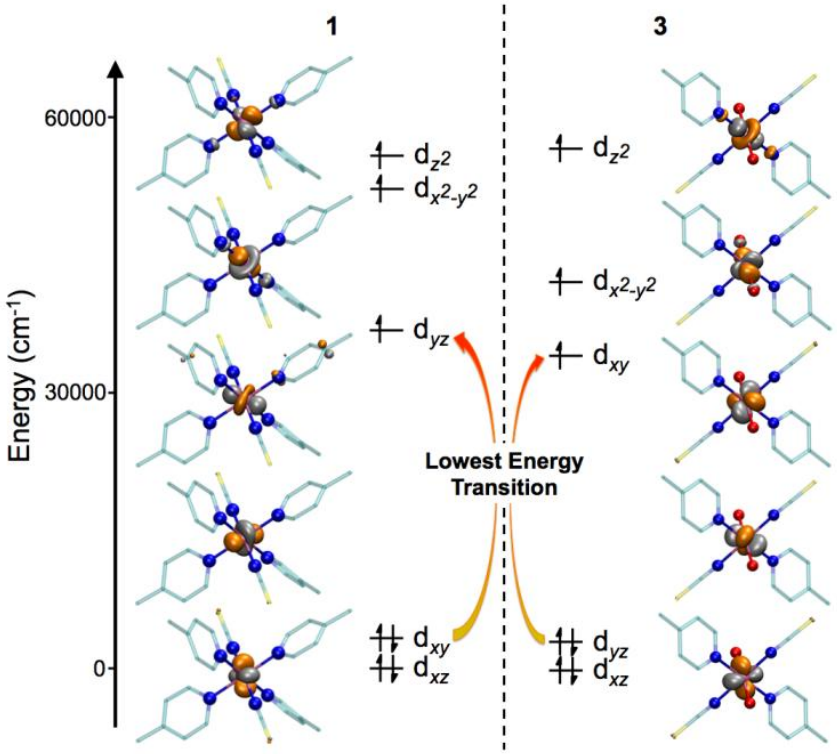

Figure 27. Co^{II} core and computed *d*-orbital splitting for complexes **1** (left) and **3** (right). Colour code: purple (Co), light blue (C), blue (N), red (O), yellow (S); H atoms have been omitted for clarity.

As may be observed, the degeneracy of the t_{2g} orbitals is broken and one of those moves up in energy, far from the last doubly occupied orbitals. In the case of complex **1**, the last doubly occupied orbital is d_{xy} and the first semioccupied orbital is d_{yz} (or d_{xz}, because those cannot be

distinguished). Since these orbitals have a different $|m_l|$ value *i.e.* ±2 and ±1, respectively, the *D* value should be positive.[2b,21] The reverse situation is found in complex **3**, in this case, the highest energy doubly occupied orbital is d_{yz} (or d_{xz}), while the lowest energy semioccupied orbital is d_{xy}. As before, a transition between these orbitals entails a change in $|m_l|$, thus producing a positive *D* value. The computed d-orbital splitting schemes confirm that the ligand field *i.e.* the separation between t_{2g} and e_g orbitals is smaller in compound **3**, in agreement with the experimental observations.

The computed relative energies of the lowest-lying KDs and the spin relaxation pathways of **1** and **3** are shown in Figure 28. In both cases, the spin relaxation mechanisms show a plausible pathway *via* a direct quantum tunneling (QTM) in the ground state under zero applied dc fields, as proposed from similar experiments. The matrix elements of the transition magnetic moments between states 1- and 1+ are 1.19 and 0.93 for **1** and **3**, respectively, much higher than the 0.1 value required to be associated with an efficient relaxation mechanism. In the case of **1**, the first two KDs may be accessible (aprox. 280 and 450 cm^{-1}) and able to participate in alternative relaxation pathways, either thermally assisted-QTM or Orbach processes. In complex **3** there is only one low-lying KD at around 210 cm^{-1} (the second lowest KD is located at almost 650 cm^{-1}); the alternative thermally assisted-QTM and Orbach spin relaxation processes seem plausible but are probably not able to compete with the ground state QTM. These relaxation processes provide an explanation to the relatively low experimentally observed U_{eff} values, despite the large *D* values of the Co^{II} compounds studied.

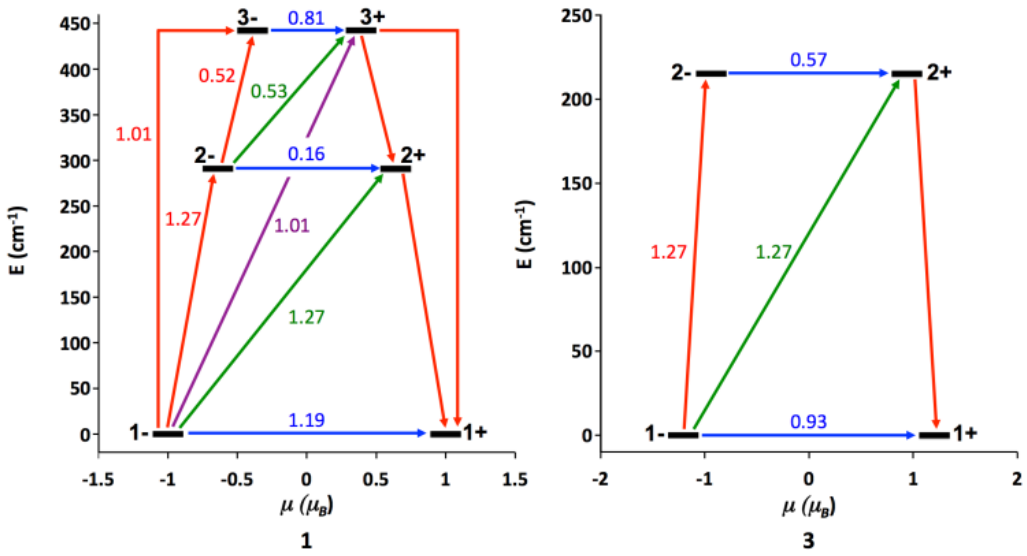

Figure 28. Lowest Kramers' doublets and *ab initio* computed relaxation mechanism in **1** (left) and **3** (right). The thick black lines imply KDs as a function of their magnetic moment along the main anisotropy axis. Red lines indicate the magnetization reversal mechanism. The blue lines correspond to ground state QTM and thermally assisted-QTM via the first and second excited KD, and green and purple lines show possible Orbach relaxation processes. The values close to the arrows indicate the matrix elements of the transition magnetic moments (above 0.1 an efficient spin relaxation mechanism is expected).[21]

3.8 **Conclusions**

We have reported the magnetic properties of three Co^{II} compounds, which were fully characterized through dc and ac susceptibility measurements, as well as electronic structure calculations. Interestingly, a 3D crystalline sponge displays single-molecule magnet-like behaviour under applied static fields, where each node individually acts as a nanomagnet. We have also demonstrated that the magnet-like behaviour of these nodes can be fine-tuned *via* manipulation of the coordination environment of the Co^{II} ions. Thus, changes in the coordination sphere of metal centres in extended networks could be easily monitored through their magnetic properties. Furthermore, we can envision how the magnetization dynamics of the porous host could be tuned by guest exchange and

similarly, how the intercalation of guest molecules could be detected *via* magnetism for novel sensor-based application

3.9 Experimental section

3.9.1 General considerations

All manipulations were performed under aerobic conditions using materials as received from commercial suppliers (Sigma Aldrich, Strem Chemical). The ligand 2,4,6-tris(4-pyridyl)-1,3,5-triazine (TPT) and compounds **1-3** were prepared according to previously published procedures.[10]

3.9.2 Instrumentation and methods

Magnetic measurements. The magnetic susceptibility measurements were obtained using a Quantum Design Superconducting Quantum Interference Device (SQUID) magnetometer MPMS-XL7 that functions between 1.8 and 300 K for direct current (dc) applied fields ranging from -7 to 7 T. Measurements were performed on polycrystalline samples of 14.7, 5.4 and 8.6 mg of complexes **1**, **2** and **3**, respectively. Compound **1** was measured in paraffin oil to prevent transformation of **1** to **2**, while compounds **2** and **3** were wrapped in a polyethylene membrane. Alternating current (ac) susceptibility measurements were performed under an oscillating ac field of 3.78 Oe and ac frequencies that ranged from 0.1 to 1500 Hz. Ferromagnetic impurities that were absent in all samples were investigated by collecting magnetization data at 100 K. All magnetic data were corrected for sample holders as well as other diamagnetic contributions.

Ab initio calculations. A detailed description of the methods and basis sets utilized for the *ab initio* calculations can be found in the Supporting Information of the original manuscript: http://www.rsc.org/suppdata/c6/tc/c6tc04703c/c6tc04703c1.pdf.

3.10 **References**

(1) D. Gatteschi, R. Sessoli and J. Villain, *Molecular Nanomagnets*, OUP, 2006.

(2) (*a*) G. A. Craig and M. Murrie, *Chem. Soc. Rev.*, 2015, **44**, 2135; (*b*) S. Gomez-Coca, E. Cremades, N. Aliaga-Alcade and E. Ruiz, *J. Am. Chem. Soc.*, 2013, **135**, 7010; (*c*) M. Atanasov, D. Aravena, E. Suturina, E. Bill, D. Maganas and F. Neese, *Coord. Chem. Rev.*, 2015, **289–290**, 177.

(3) (*a*) K. E. Vostrikova and D. Luneau, *J. Am. Chem. Soc.*, 2000, **122**, 718; (*b*) A. M. Ako, V. Mereacre, I. J. Hewitt, R. Clérac, L. Lecren, C. E. Anson and A. K. Powell, *J. Mater. Chem.*, 2006, **16**, 2579; (*c*) D. Luneau and P. Rey, *Coord. Chem. Rev.*, 2005, **249**, 2591.

(4) (*a*) T. Jurca, A. Farghal, P.-H. Lin, I. Korobkov, M. Murugesu and D. S. Richeson, *J. Am. Chem. Soc.*, 2011, **133**, 15814; (*b*) G. Christou, *Polyhedron*, 2005, **24**, 2065; (*c*) C. R. Ganivet, B. Ballesteros, G. de la Torre, J. M. Clemente-Juan, E. Coronado and T. Torres, *Chem. Eur. J.*, 2013, **19**, 1457.

(5) (*a*) F. Habib, P.-H. Lin, J. Long, I. Korobkov, W. Wernsdorfer and M. Murugesu, *J. Am. Chem. Soc.*, 2011, **133**, 8830; (*b*) S.-D. Jiang, B.-W. Wang, G. Su, Z.-M. Wang and S. Gao, *Angew. Chem.*, 2010, **122**, 7610; . (*c*) K. R. Meihaus, J. D. Rinehart and J. R. Long, *Inorg. Chem.*, 2011, **50**, 8484.

(6) (*a*) M. Kurmoo, *Chem. Soc. Rev.*, 2009, **39**, 1353; (*b*) M.-H. Zeng, B. Wang, X.-Y. Wang, W.-X. Zhang, X.-M. Chen and S. Gao, *Inorg. Chem.*, 2006, **45**, 7069; (*c*) M. Eddaoudi, D. B. Moler, H. Li, B. Chen, T. M. Reineke, M. O'Keeffe and O. M. Yaghi, *Acc. Chem. Res.*, 2001, **34**, 319.

(7) (*a*) J.-R. Li, R. J. Kuppler and H.-C. Zhou, *Chem. Soc. Rev.*, 2009, **38**, 1477; (*b*) U. Mueller, M. Schubert, F. Teich, H. Puetter, K. Schierle-Arndt and J. Pastré, *J. Mater.*

Chem., 2006, **16**, 626; (*c*) H. Furukawa, K. E. Cordova, M. O'Keeffe and O. M. Yaghi, *Science*, 2013, **341**, 1230444.

(8) (*a*) X. Zhang, V. Vieru, X. Feng, J.-L. Liu, Z. Zhang, B. Na, W. Shi, B.-W. Wang, A. K. Powell, L. F. Chibotaru, S. Gao, P. Cheng and J. R. Long, *Angew. Chem. Int. Ed.*, 2015, **54**, 9861; (*b*) R. Sibille, T. Mazet, B. Malaman, T. Gaudisson and M. François, *Inorg. Chem.*, 2012, **51**, 2885; (*c*) Z.-L. Huang, M. Drillon, N. Masciocchi, A. Sironi, J.-T. Zhao, P. Rabu and P. Panissod, *Chem. Mater.*, 2000, **12**, 2805.

(9) Y. Inokuma, S. Yoshioka, J. Ariyoshi, T. Arai, Y. Hitora, K. Takada, S. Matsuanaga, K. Rissanen and M. Fujita, *Nature*, 2013, **495**, 461.

(10) G. Brunet, D. A. Safin, I. Korobkov, A. Cognigni and M. Murugesu, *Cryst. Growth Des.*, 2016, **16**, 4043.

(11) (*a*) L. Bogani and W. Wernsdorfer, *Nat. Mater.*, 2008, **7**, 179; (*b*) M. J. Martínez-Pérez, S. Cardona-Serra, C. Schlegel, F. Moro, P. J. Alonso, H. Prima-García, J. M. Clemente-Juan, M. Evangelisti, A. Gaita-Ariño, J. Sesé, J. van Slageren, E. Coronado and F. Luis, *Phys. Rev. Lett.*, 2012, **108**, 247213; S. Hill, R. S. Edwards, N. Aliga-Alcade and G. Christou, *Science*, 2003, **302**, 1012.

(12) (*a*) T.-F. Liu, D. Fu, S. Gao, Y.-Z. Zhang, H. L. Sun, G. Su and Y.-J. Liu, *J. Am. Chem. Soc.*, 2003, **125**, 13976; (*b*) F. Habib, C. Cook, I. Korobkov and M. Murugesu, *Inorg. Chim. Acta.*, 2012, **380**, 378; (*c*) J. Vallejo, I. Castro, R. Ruiz-García, J. Cano, M. Julve, F. Lloret, G. De Munno, W. Wernsdorfer and E. Pardo, *J. Am. Chem. Soc.*, 2012, **134**, 15704; (*d*) R. Herchel, L. Váhovská, I. Potočňák and Z. Trávníček, *Inorg. Chem.*, 2014, **53**, 5896.

(13) J. M. Zadrozny, J. Liu, N. A. Piro, C. J. Chang, S. Hill, J. R. Long, *Chem. Commun.*, 2012, **48**, 3927.

(14) (*a*) Y.-Y. Zhu, M.-S. Zhu, T.-T. Yin, Y.-S. Meng, Z.-Q. Wu, Y.-Q. Zhang and S. Gao, *Inorg. Chem.*, 2015, **54**, 3716; (*b*) A. E. Ion, S. Nica, A. M. Madalan, S. Shova, J. Vallejo, M. Julve, F. Lloret and M. Andruh, *Inorg. Chem.*, 2015, **54**, 16; (*c*) J. Palion-Gazda, T. Klemens, B. Machura, J. Vallejo, F. Lloret and M. Julve, *Dalton Trans.*, 2015, **44**, 2989; (*d*) A. Świtlicka-Olszewska, J. Palion-Gazda, T. Klemens, B. Machura, J. Vallejo, J. Cano, F. Lloret and M. Julve, *Dalton Trans.*, 2016, **45**, 10181; (*e*) X. Liu, L. Sun, H. Zhou, P. Cen, X. Jin, G. Xie, S. Chen and Q. Hu, *Inorg. Chem.*, 2015, **54**, 8884; (*f*) J. Vallejo, F. R. Fortea-Pérez, E. Pardo, S. Benmansour, I. Castro, J. Krzystek, D. Armentano and J. Cano, *Chem. Sci.*, 2016, **7**, 2286.

(15) (*a*) E. Colacio, J. Ruiz, E. Ruiz, E. Cremades, J. Krzystek, S. Carretta, J. Cano, T. Guidi, W. Wernsdorfer and E. K. Brechkin, *Angew. Chemie. Int. Ed.*, 2013, **52**, 9130. (*b*) S. Gómez-Coca, A. Urtizberea, E. Cremades, P. J. Alonso, A. Camón, E. Ruiz and F. Luis, *Nat. Commun.*, 2014, **5**, 4300.

(16) X. Feng, J.-L. Liu, K. S. Pedersen, J. Nehrkorn, A. Schnegg, K. Holldack, J. Bendix, M. Sigrist, H. Mutka, D. Samohvalov, D. Aguilà, M.-L- Tong, J. R. Long and R. Clérac, *Chem. Commun.*, 2016, **52**, 12905.

(17) (*a*) M. R. Saber and K. R. Dunbar, *Chem. Commun.*, 2014, **50**, 12266; (*b*) S. Vaidya, A. Upadhyay, S. K. Singh, T. Gupta, S. Tewary, S. K. Langley, J. P. S. Walsh, K. S. Murray, G. Rajaraman and M. Shanmugam, *Chem. Commun.*, 2015, **51**, 3739.

(18) F. Neese, *WIREs Comput. Mol. Sci.*, 2012, **2**, 73.

(19) (*a*) G. Karlström, R. Lindh, P.-Å. Malmqvist, B. O. Roos, U. Ryde, V. Veryazov, P.-O. Widmark, M. Cossi, B. Schimmelpfennig, P. Neogrady and L. Seijo, *Comput. Matter Sci.*, 2003, **28**, 222; (*b*) V. Veryazov, P.-O. Widmark, L. Serrano-Andrés, R. Lindh and B. O. Roos, *Int. J. Quantum Chem.*, 2004, **100**, 626; (*c*) F. Aquilante, L. De Vico, N. Ferré, G. Ghigo, P.-å. Malmqvist, P. Neogrády, T. B. Pedersen, M. Pitoňák, M. Reiher, B. O. Roos, L. Serrano-Andrés, M. Urban, V. Veryazov and R. Lindh, *J. Comp. Chem.*, 2010, **31**, 224.

(20) M. J. Frisch, G. W. Trucks, H. B. Schlegel, G. E. Scuseria, M. A. Robb, J. R. Cheeseman, G. Scalmani, V. Barone, B. Mennucci, G. A. Petersson, H. Nakatsuji, M. Caricato, X. Li, H. P. Hratchian, A. F. Izmaylov, J. Bloino, G. Zheng, J. L. Sonnenberg, M. Hada, M. Ehara, K. Toyota, R. Fukuda, J. Hasegawa, M. Ishida, T. Nakajima, Y. Honda, O. Kitao, H. Nakai, T. Vreven, J. Montgomery, J. A., J. E. Peralta, F. Ogliaro, M. Bearpark, J. J. Heyd, E. Brothers, K. N. Kudin, V. N. Staroverov, R. Kobayashi, J. Normand, K. Raghavachari, A. Rendell, J. C. Burant, S. S. Iyengar, J. Tomasi, M. Cossi, N. Rega, N. J. Millam, M. Klene, J. E. Knox, J. B. Cross, V. Bakken, C. Adamo, J. Jaramillo, R. Gomperts, R. E. Stratmann, O. Yazyev, A. J. Austin, R. Cammi, C. Pomelli, J. W. Ochterski, R. L. Martin, K. Morokuma, V. G. Zakrzewski, G. A. Voth, P. Salvador, J. J. Dannenberg, S. Dapprich, A. D. Daniels, Ö. Farkas, J. B. Foresman, J. V. Ortiz and J. F. Cioslowski, D. J. Gaussian09, Revision D.01, Gaussian, Inc.: Wallingford CT, 2009.

(21) S. Gómez-Coca, D. Aravena, R. Morales and E. Ruiz, *Coord. Chem. Rev.*, 2015, **289–290**, 379.

Almost all aspects of life are engineered at the molecular level,
and without understanding molecules, we can only have
a very sketchy understanding of life itself
– Francis Crick[5]

Chapter 4

Directed supramolecular assembly of Ln^{III} ions using a nitrogen-rich ligand

4.1 Published contributions

A nitrogen-rich ligand as a scaffold for slow magnetic relaxation in dysprosium-based 0D and 1D architectures

G. Brunet, E. Sebastiao, T. G. Witkowski, I. Korobkov, B. Gabidullin, and M. Murugesu, *Dalton Trans.*, 2018, **47**, 11782-11787.

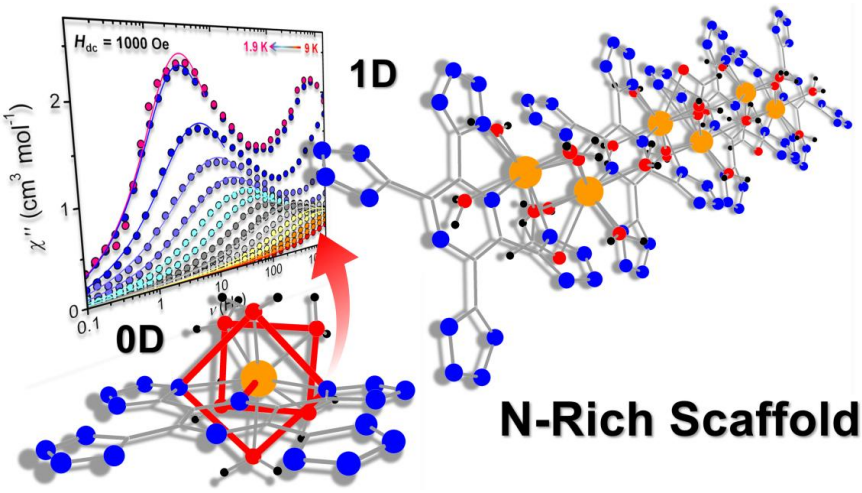

G. Brunet and M. Murugesu wrote the manuscript. G. Brunet performed the majority of the experiments. E. Sebatiao and T. G. Witkowski assisted in the synthesis of the compounds and ligand.

I. Korobkov and B. Gabidullin were responsible for the refinement of the single-crystal X-ray diffraction data.

[5] *What Mad Pursuit: A Personal View of Scientific Discovery.*

4.2 **Abstract**

A recently designed nitrogen-rich ligand is successfully applied as a scaffold for lanthanide ions to show that the intricate chemistry of energetic materials can be combined with other fields of research, including that of molecular magnetism. Herein, we report the synthesis of two different types of molecular architectures using a single ligand template, in which the discrete monomer exhibits single-molecule magnet-like behaviour along with two well-isolated modes of magnetic relaxation.

4.3 **Introduction**

Nitrogen-rich materials continue to garner significant attention within various fields of the scientific community, with a number of highly regarded reviews targeting not only their synthesis but also their current and potential applications.[1] While such nitrogen-rich compounds are often considered exclusively, albeit inadequately, as high-performance explosives, they are also at the centre of numerous niche applications in propellants and pyrotechnics, making them essential to modern life (*i.e.* airbag inflation, satellite propulsion systems, blast mining). Further adding to their attractiveness is the fact that they are often reliably synthesized through "click chemistry" methods,[2] eliciting predictable covalent assemblies. In comparison to other nitrogen-rich azoles, 5-substituted-1*H*-tetrazoles are particularly appealing in that they incorporate a maximal amount of nitrogen within a stable ring. Thus, they exhibit high positive heats of formation and generate large volumes of environmentally friendly nitrogen upon decomposition.

As part of our on-going research efforts in the development of competitive energetic materials, we have recently reported a new compound comprising four tetrazole moieties on a single pyrazine ring (Fig. 29), namely 2,3,5,6-tetra(1*H*-tetraol-5-yl)pyrazine (H_4TTP).[3] This novel high nitrogen content (N = 71.58%) energetic material is notably

characterized by high detonation parameters, an elevated temperature of decomposition, and a straightforward synthesis, making it a promising candidate for use in practical applications. As an extension of this work, we first sought to examine the coordination chemistry of the H_4TTP ligand to metal ions. The extended planarity of the ligand coupled with strong π-acceptor properties make H_4TTP a truly interesting scaffold with which to investigate metal ligation. In fact, polymetallic complexes based on a single rigid ligand framework have recently emerged as model systems to direct and control magnetic interactions.[4] The two coordination pockets linked by a central pyrazine ring are reminiscent of a terpy-like coordination,[5] and thus, we can easily envision the formation of discrete monomers and/or 1-D chains, depending on the occupancy of the coordination pockets. Beyond the potential architectures of the compound, the H_4TTP ligand possesses significant charge flexibility, where the neutral, anionic and cationic forms of the tetrazole moieties can co-exist,[6] depending on the bonding interactions with the metal centre.

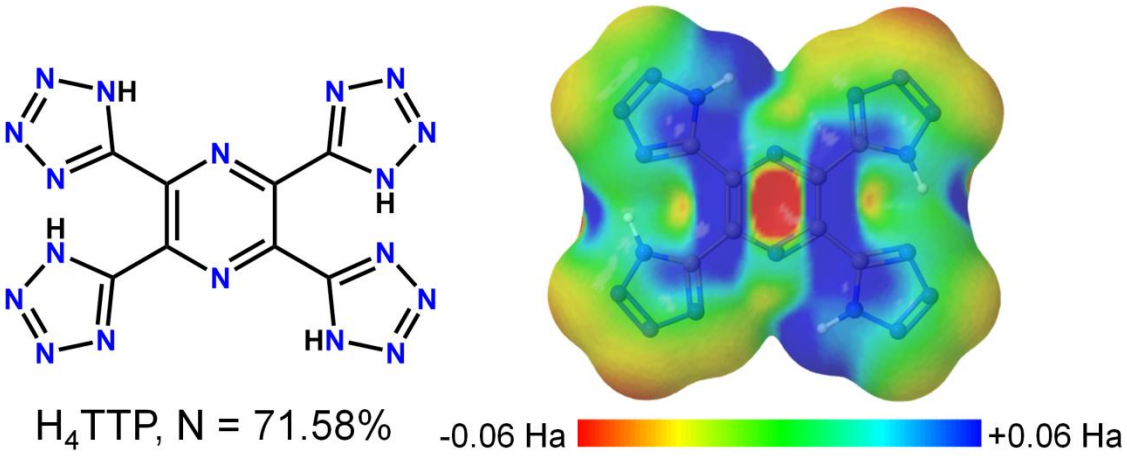

Figure 29. The calculated electrostatic potential of H_4TTP , viewed perpendicular to the plane encompassing the atoms. Colour ranges from red (V(r) ≤ –0.075 Hartree, electron-rich regions) to blue (V(r) ≥ +0.075 Hartree, electron-deficient regions).

In recent years, tetrazole-based ligands have been utilized as building blocks for the formation of high-dimensionality coordination compounds,[7] where functional groups on the ligand were seen to impact the overall coordination topology.[8] Other studies involving the coordination of nitrogen-rich ligands to metals have focused on the ability to sensitize Ln^{III} emission through an "antenna effect",[9] where ligand absorption and subsequent energy transfer could populate Laporte-forbidden *f–f* excited states. In the present case, we have focused on the use of Dy^{III} ions, providing large unquenched orbital angular momentum, a key component in the observation of slow relaxation of the magnetization, characteristic of Single-Molecule Magnets (SMMs). As such, we were encouraged to examine the magnetic properties of a nitrogen-rich ligand acting as a template for lanthanide ions, in our efforts to seek new SMMs.

4.4 Synthesis and structure

In this paper, we report the successful assembly of two isostructural mononuclear complexes obtained by hydrothermal synthesis, formulated as $[Ln(H_2TTP)(H_2O)_6]_2(H_2TTP)_{0.5} \cdot 6H_2O$ (Ln = Dy^{III}, **1a**; Gd^{III}, **1b**). The addition of formic acid to the reaction vessel yields 1-D chains of $[Dy_2(TTP)(\mu\text{-}OH)_{1.3}(\mu\text{-}HCOO)_{0.7}(H_2O)_6]_n$ (**2a**) and $[Gd_2(TTP)(\mu\text{-}OH)_{1.25}(\mu\text{-}HCOO)_{0.75}(H_2O)_6]_n$ (**2b**), which differ only slightly in terms of the occupancies of the bridging hydroxide and formate anions. Nevertheless, **2a** and **2b** can be considered as isostructural, as per the definition by the International Union of Crystallography (IUCr). All four compounds crystallize in the triclinic *P*–1 space group, and are obtained as either colourless (**1a**, **1b**) or orange (**2a**, **2b**) block-like crystals (Table 6).

Table 6. Crystallographic Data for **1a**, **1b**, **2a** and **2b**.

Compound	1a	1b	2a	2b
Empirical Formula	$DyC_{12}H_{27}N_{27}O_{12}$	$GdC_{12}H_{27}N_{27}O_{12}$	$Dy_2C_{8.70}H_{14}N_{18}O_{8.70}$	$Gd_2C_{8.75}H_{14}N_{18}O_{8.75}$
Crystal system	Triclinic	Triclinic	Triclinic	Triclinic
Space group	*P*–1	*P*–1	*P*–1	*P*–1
a (Å)	9.7883(6)	9.8069(5)	6.5214(2)	6.5239(2)
b (Å)	11.1740(6)	11.2059(6)	7.8070(2)	7.8414(2)
c (Å)	14.3567(8)	14.4149(7)	10.6509(3)	10.6792(3)
α (°)	101.599(3)	97.8160(10)	104.2559(12)	104.2714(12)
β (°)	97.500(3)	93.9320(10)	97.5429(14)	97.0307(14)
γ (°)	93.781(3)	93.9320(10)	98.3219(15)	97.8719(13)
V ($Å^3$)	1518.14(15)	1528.97(14)	512.09(3)	517.48(3)
Z	2	2	1	1
ρ_{calc} (g cm^{-3})	1.978	1.952	2.708	2.650
λ (Å)	0.71073	0.71073	0.71073	0.71073
T (K)	200(2)	200(2)	200(2)	200(2)
μ (mm^{-1})	2.566	2.273	7.332	6.444
F (000)	900	896	394	390
Reflections Collected	17057	14787	5663	5574
Independent Reflections	7372	7516	2479	2524
Reflections with $I > 2\sigma(I)$	6864	7166	2408	2482
Goodness of fit on F^2	1.080	1.070	1.108	1.032
R_1, wR_2 ($I > 2\sigma(I)$)[a]	0.0263, 0.0621	0.0173, 0.0424	0.0243, 0.0559	0.0219, 0.588
R_1, wR_2 (all data)	0.0295, 0.0640	0.0187, 0.0429	0.0251, 0.0565	0.0223, 0.0591

[a] $R = R_1 = \sum||F_o| - |F_c||/\sum|F_o|$; $wR_2 = \{\sum[w(F_o^2 - F_c^2)^2]/\sum[w(F_o^2)^2]\}^{1/2}$; $w = 1/[\sigma^2(F_o^2)+(ap)^2 + bp]$, where $p = [\max(F_o^2, 0) + 2F_c^2]/3$; and $Rw = [w(|F_o| - |F_c|)^2 / w|F_o|^2]^{1/2}$, where $w = 1 / \sigma^2(|F_o|)$.

Complexes **1a** and **1b** feature a mononuclear complex (Fig. 30), where the Ln^{III} ions are ennea-coordinate and are most closely described by a distorted spherical capped square antiprism geometry (C_{4v}), as indicated by SHAPE analysis (Table 7).[10] Each metal centre is chelated by one doubly deprotonated H_2TTP^{2-} ligand in a terpy-like fashion; with one nitrogen from two distinct tetrazole rings, and one nitrogen from the central pyrazine ring. The coordination environment is completed by six ligated water molecules. It is important to note that a second crystallographically independent H_2TTP^{2-} anion can be located in the lattice, in order to balance the charge on the $[Ln(H_2TTP)(H_2O)_6]^+$ cation.

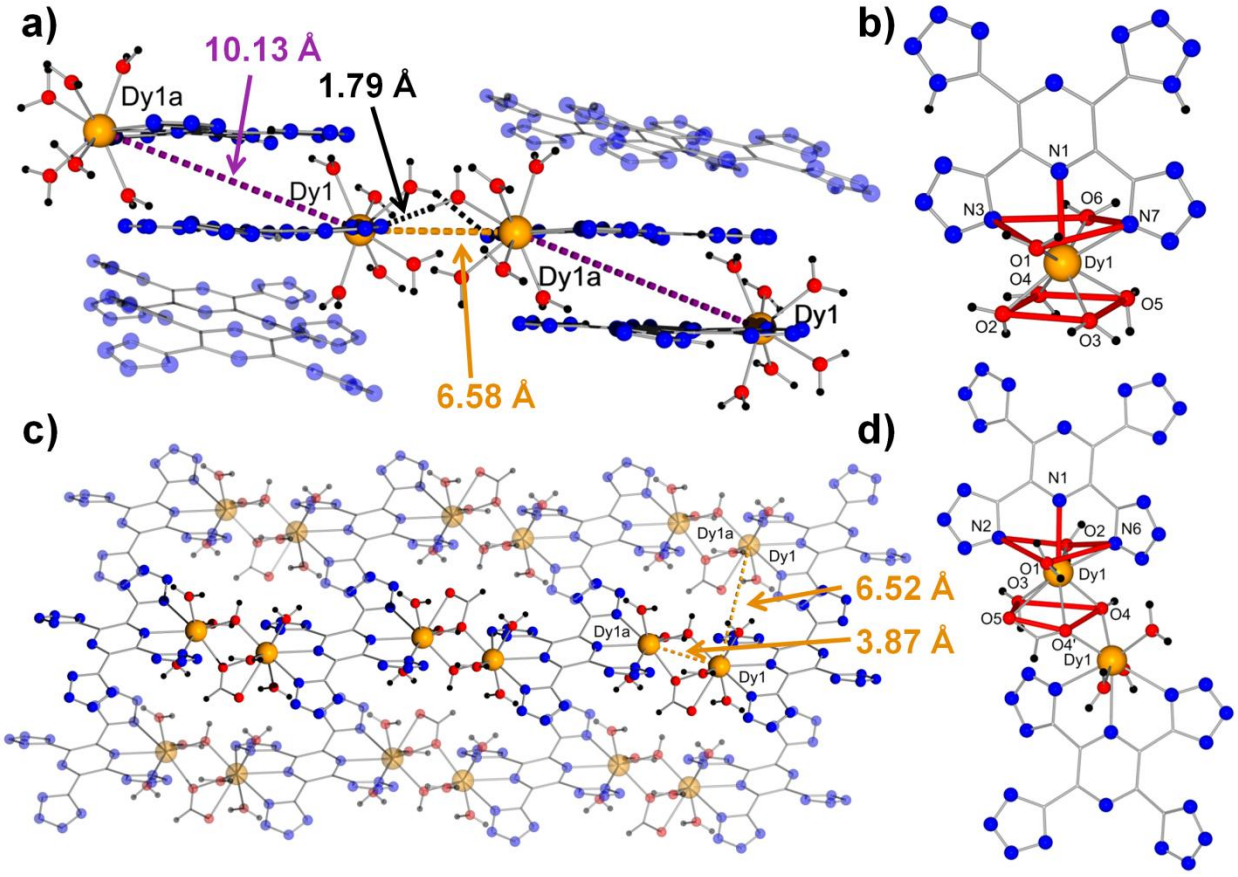

Figure 30. Molecular fragment of **1a** displaying the relevant intermolecular Dy···Dy distances (orange and purple dashed bonds) and selected H-bonds (black dashed bonds) (a). Distorted spherical capped square antiprism coordination environment of the mononuclear Dy^{III} ions in **1a** (b). Front-view of the linear 1-D chain structure of **2a** (c). Repeating dinuclear unit of the 1-D chain in **2a** showing the ennea-coordinate geometry of the Dy^{III} ions when bridged by formate anions (d). Colour code: orange (Dy), red (O), blue (N), black (H); while all unfilled vertices represent carbon atoms. Lattice water molecules and positional disorder are omitted for clarity.

This counter anion is located on an inversion centre and is disordered over two positions of equal occupancy. Also present in the lattice are six water molecules that form an extensive hydrogen bonded network, through either O–H···H or O–H···N interactions (Fig. 31). In fact, two short O–H···N hydrogen bonds (1.79 Å) link nearby Ln^{III} neighbors closely together through a distance of 6.58 Å; which may lead to some magnetic communication *via* hyperfine and/or dipolar spin-spin interactions (*vide infra*). Other important bond distances and angles are summarized in Table 8.

Table 7. SHAPE constants for the Dy^{III} centers in **1a**. The lowest shape constants are bolded.

SHAPE Code	Point Group	Description	Dy1
EP-9	D_{9h}	Enneagon	35.468
OPY-9	C_{8v}	Octagonal pyramid	23.529
HBPY-9	D_{7h}	Heptagonal bipyramid	18.998
JTC-9	C_{3v}	Johnson triangular cupola J3	15.916
JCCU-9	C_{4v}	Capped cube J8	8.643
CCU-9	C_{4v}	Spherical-relaxed capped cube	8.304
JCSAPR-9	C_{4v}	Capped square antiprism	**0.691**
CSAPR-9	C_{4v}	Spherical capped square antiprism	**0.495**
JTCTPR-9	D_{3h}	Tricapped trigonal prism J51	2.647
TCTPR-9	D_{3h}	Spherical tricapped trigonal prism	1.686
JTDIC-9	C_{3v}	Tridiminished icosahedrons J63	11.938
HH-9	C_{2v}	Hula-hoop	11.634
MFF-9	C_s	Muffin	1.268

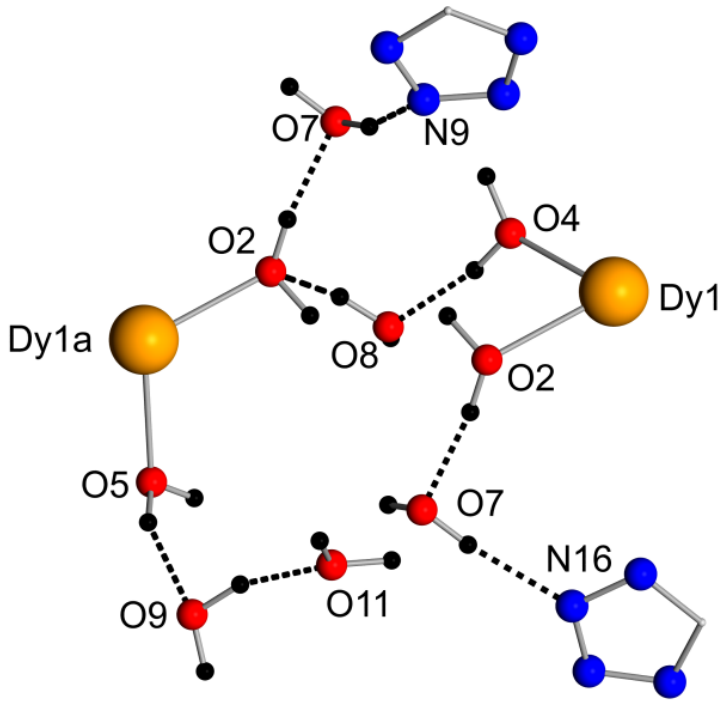

Figure 31. Representative examples of hydrogen bonds formed in **1a** and **1b**, which includes both coordinated and lattice water molecules, as well as nitrogen atoms from the tetrazole moieties of the H_2TTP^{2-} ligand.

Table 8. Select bond distances and angles of **1a** and **1b**.

Select bond distances (Å)			
Dy1-O1	2.387(2)	Gd1-O1	2.4211(13)
Dy1-O2	2.370(2)	Gd1-O2	2.3998(14)
Dy1-O3	2.387(2)	Gd1-O3	2.4188(13)
Dy1-O4	2.384(2)	Gd1-O4	2.4180(14)
Dy1-O5	2.384(2)	Gd1-O5	2.4129(13)
Dy1-N1	2.805(2)	Gd1-N1	2.8282(14)
Dy1-N3	2.494(2)	Gd1-N3	2.5217(14)
Dy1-N7	2.524(2)	Gd1-N7	2.5494(14)
Select angles (°)			
N3-Dy1-N1	60.47(7)	N3-Gd1-N1	60.07(4)
N7-Dy1-N1	59.70(7)	N7-Gd1-N1	59.46(4)

The addition of formic acid to the reaction conditions favours the formation of **2a** and **2b** as a 1-D chain, where both coordination pockets involving the nitrogen atoms of the pyrazine ring are filled (Fig. 30). In this instance, the H_4TTP ligand is fully deprotonated and we observe the linkage of two Ln^{III} ions by hydroxide and/or formate anions. These results clearly display the inherent versatility of the H_4TTP ligand in coordination chemistry, where various deprotonation states can be stabilized (H_2TTP^{2-} *vs.* TTP^{4-}). The coordination environment of the Ln^{III} ions in **2a** and **2b** is peculiar since they can be either 8- or 9-coordinate, depending on whether formates or hydroxides serve as the bridging ligand. The formate anions are bidendate, leading to a distorted ennea-coordinate geometry resembling that of a spherical capped square antiprism (Table 9). On the other hand, when hydroxides are present, the Ln^{III} ions are octa-coordinate and are most closely described by a distorted triangular dodecahedron (Table 10). Complexes **2a** and **2b** also exhibit centrosymmetry, yielding one crystallographically independent Ln^{III} ion. In regards to the packing arrangement, the linear chains are arranged in a parallel fashion and oriented in the same direction. The shortest intrachain Dy-Dy distance occurs

Table 9. SHAPE constants for the Dy^{III} centers in **2a** when coordinated to formate anions (9-coordinate). The lowest shape constant is bolded.

SHAPE Code	Point Group	Description	Dy1
EP-9	D_{9h}	Enneagon	32.537
OPY-9	C_{8v}	Octagonal pyramid	22.159
HBPY-9	D_{7h}	Heptagonal bipyramid	16.578
JTC-9	C_{3v}	Johnson triangular cupola J3	12.468
JCCU-9	C_{4v}	Capped cube J8	6.251
CCU-9	C_{4v}	Spherical-relaxed capped cube	6.026
JCSAPR-9	C_{4v}	Capped square antiprism	3.309
CSAPR-9	C_{4v}	Spherical capped square antiprism	**2.945**
JTCTPR-9	D_{3h}	Tricapped trigonal prism J51	3.110
TCTPR-9	D_{3h}	Spherical tricapped trigonal prism	3.126
JTDIC-9	C_{3v}	Tridiminished icosahedrons J63	11.950
HH-9	C_{2v}	Hula-hoop	8.883
MFF-9	C_s	Muffin	2.966

Table 10. SHAPE constants for the Dy^{III} centers in **2a** when coordinated to hydroxide anions (8-coordinate). The lowest shape constant is bolded.

SHAPE Code	Point Group	Description	Dy1
OP-8	D_{8h}	Octagon	29.645
HPY-8	C_{7v}	Heptagonal pyramid	24.568
HBPY-8	D_{6h}	Hexagonal pyramid	11.142
CU-8	O_h	Cube	6.955
SAPR-8	D_{4d}	Square antiprism	3.253
TDD-8	D_{2d}	Triangular dodecahedron	**2.088**
JGBF-8	D_{2d}	Johnson gyrobifastigium J26	11.878
JETBPY-8	D_{3h}	Johnson elongated triangular bipyramid J14	25.672
JBTPR-8	C_{2v}	Biaugmented trigonal prism J50	2.669
BTPR-8	C_{2v}	Biaugmented trigonal prism	2.142
JSD-8	D_{2d}	Snub diphenoid J84	5.148
TT-8	T_d	Triakis tetrahedron	7.798
ETBPY-8	D_{3h}	Elongated trigonal bipyramid	21.564

through the formate/hydroxide bridges, with a separation of 3.87 Å and is significantly shorter than the distance separating two Dy^{III} atoms through the pyrazine the pyrazine moiety of the TTP^{4-} ligand (8.12 Å). The shortest interchain metal-metal distance is found to be 6.52 Å, and

thus, intermolecular magnetic dipolar interactions, previously observed up to distances of 8-9 Å,[11] could influence the magnetic relaxation. While lanthanide-based SMMs are becoming increasingly predominant in the field of molecular magnetism, the coordination chemistry of nitrogen-rich ligands and their resulting magnetic properties remain lacklustre. Here, we provide a detailed magnetic investigation into two new coordination compounds where the Ln^{III} atoms were predictably assembled using a directing scaffold.

4.5 **Static magnetic properties**

Direct current (dc) magnetic susceptibility measurements were initially carried out to probe any potential magnetic interactions between the spin carrying units. The room temperature χT products for **1a** and **1b** are 14.42 and 7.78 cm^3 K mol^{-1}, respectively, under an applied field of 1000 Oe (Fig. 32). These values are in good agreement with the theoretical values for one isolated Dy^{III} (14.14 cm^3 K mol^{-1}) and Gd^{III} (7.88 cm^3 K mol^{-1}) ion. Analogously, the room temperature χT values for **2a** and **2b** are 25.63 and 15.36 cm^3 K mol^{-1} (Fig. 3), respectively, which are also in reasonable range of the expected values for two non-interacting Dy^{III} and Gd^{III} ions, respectively. In complex **1a**, the χT product remains constant down to approximately 100 K, until decreasing gradually to a minimum value of 10.70 cm^3 K mol^{-1} at 1.8 K. A similar behaviour is observed for **2b**, where the χT product decreases to 14.25 cm^3 K mol^{-1} at 1.8 K. Such decreases suggest the presence of weak antiferromagnetic interactions and/or the thermal depopulation of the ligand field excited levels. In the case of complexes **1b** and **2a**, an increase of the χT product at low temperatures is indicative of weak ferromagnetic interactions between the Ln^{III} ions. It is noteworthy that the nature of the magnetic interactions is dependent upon the identity of the metal center (Dy^{III} *vs.* Gd^{III}) and can lead to either ferromagnetic or antiferromagnetic

interactions. To probe the strength of the interactions between the Ln^{III} ions, the Gd^{III} analogues were synthesized. This effectively removes any contribution from orbital angular momentum, due to the half-filled 4*f*-shell of the Gd^{III} ion, and thus, we can provide an estimation of the magnetic exchange interaction between Ln^{III} metal centers.

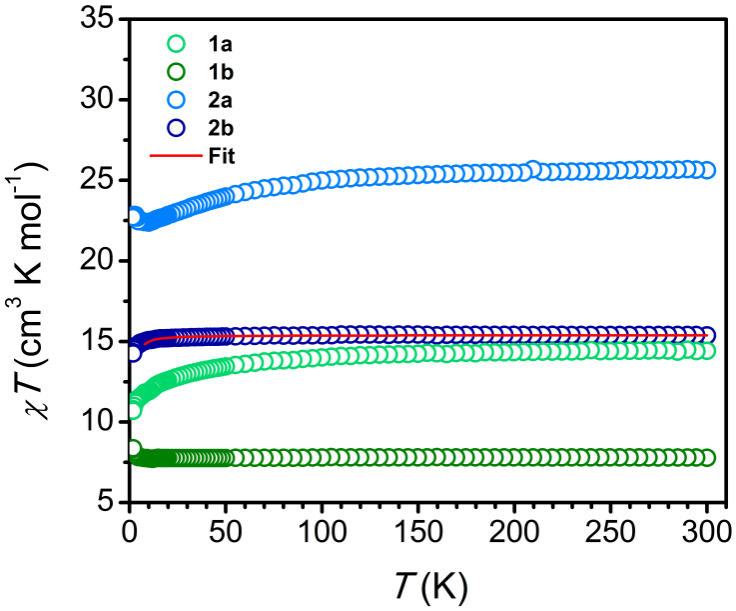

Figure 32. Temperature dependence of the molar magnetic susceptibility plotted as χT, for all compounds, collected under H_{dc} = 1000 Oe. For **2b**, a good fit is achieved by simplifying the system to a dinuclear model.

Given that there exists only one close $Gd^{III}\cdots Gd^{III}$ distance in **2b** (3.87 Å), through the double hydroxide/formate bridges, the magnetic susceptibility data can be suitably reproduced considering the simplest dimer model (Hamiltonian $H = -2JS_a \cdot S_b$ with $S_a = S_b = 7/2$). Application of the Van Vleck equation to Kambe's vector coupling scheme yields J = -0.01(1) cm^{-1} and g = 1.97(7), testifying to the weak nature of the exchange interactions, as expected for non-radical bridged 4*f* ions. Despite recent work demonstrating that hydroxide bridges can indeed lead to strong magnetic exchange,[12] the strength of the interactions in **2b** is in line with other similarly bridged systems.[13] Field dependence of the magnetization was also investigated up to fields of 7

T, clearly depicting the magnetic anisotropy of the dysprosium ions (Fig. 33). In fact, after a rapid increase at low fields, the magnetization increases linearly without clear saturation, even at 1.9 K and 7 T. Conversely, the *M vs.* HT^{-1} curves of the Gd^{III} analogues (**1b** and **2b**) superimpose on a single master curve highlighting the isotropic magnetic sites (Fig. 34). These dc magnetic susceptibility results are expected and concurrently confirm the weakness of the Ln···Ln interactions.

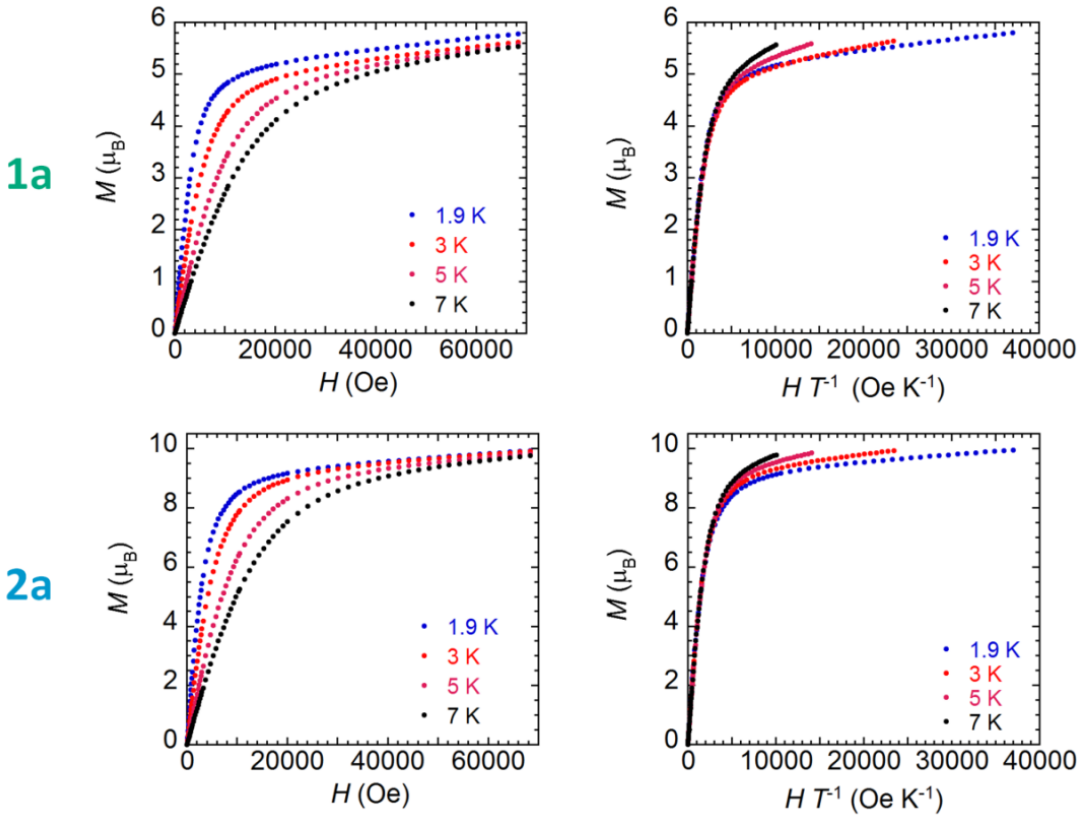

Figure 33. Field dependence of the magnetization (left) and field dependence of the reduced magnetization (right) at the indicated temperatures and up to 7 T for compounds **1a** and **2a**.

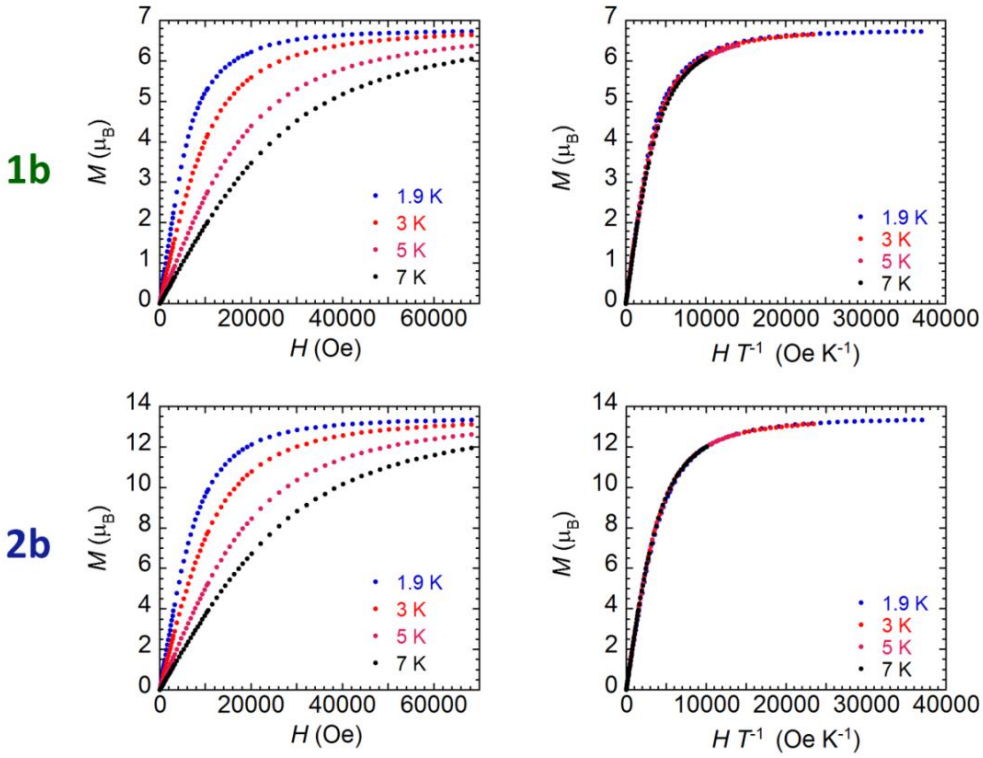

Figure 34. Field dependence of the magnetization (left) and field dependence of reduced magnetization (right) at the indicated temperatures and up to 7 T for compounds **1b** and **2b**.

4.6 **Dynamic magnetic properties**

In order to take advantage of the large unquenched orbital angular momentum of the Dy^{III} ions for generating SMM-like behaviour, we investigated the slow magnetic relaxation dynamics of **1a** and **2a** through ac susceptibility measurements. Interestingly, both compounds show two distinct magnetic relaxation processes. In the case of **1a**, two frequency-dependent peaks in the out-of-phase susceptibility (χ'') can be observed in the low temperature region and under an applied field of H_{dc} = 1000 Oe (Fig. 35a). The two thermal relaxation processes are also corroborated by plots of χ'' against the in-phase susceptibility χ' (Cole-Cole plots), where two semi-circles are present, corresponding to a fast (FR) and slow (SR) relaxation phase (Fig. 35c). The SR phase can be fit throughout

the temperature range of 1.9-9 K using a generalized Debye model, from which a distribution (α) of relaxation times (τ) can be extracted (Table 11). From this data, an Arrhenius plot can be assembled showing the temperature dependence of the magnetic relaxation time, yielding U_{eff}/k_B = 52.61(1) K and τ_0 = 1.20(6) × 10^{-7} s (Fig. 22d).

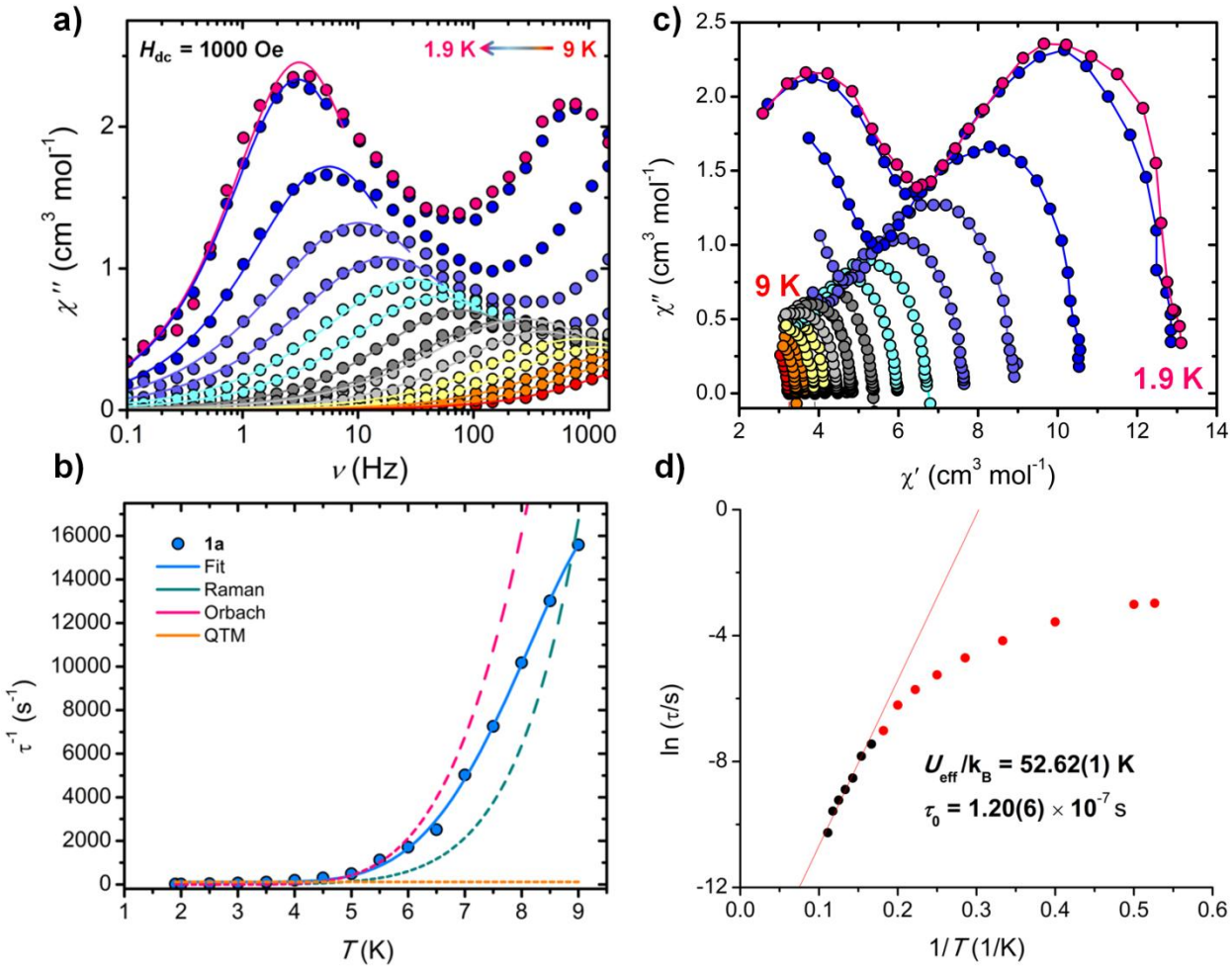

Figure 35. Frequency dependence of the χ'' magnetic susceptibility for **1a** under a 1000 Oe dc field, with the solid lines corresponding to the best-fits to a generalized Debye model (a). Temperature dependence of the magnetization relaxation times with the solid blue line representing the best-fit using eqn (1), and the dashed lines indicating the individual contributions of the magnetization relaxation for Raman, Orbach and QTM processes (b). Cole-Cole (Argand) plot for the ac susceptibility data collected at 1000 Oe and varying temperatures for **1a**. Solid-lines are guides for the eyes (c). Plot of ln (τ) *vs.* 1/T for **1a** under an applied field of 1000 Oe (d).

Unfortunately, characterization of the FR phase is more challenging since full out-of-phase signals are only present at very low temperatures (below 2 K). Moreover, under zero dc field, only tails of signals were observed, revealing that the application of a small dc field greatly influences the out-of-phase magnetic susceptibility. In turn, this directly reflects the fact that quantum tunnelling of the magnetization (QTM) does indeed play an important role in the magnetic relaxation of **1a**. Such a process is known to be highly dependent upon dipolar interactions and hyperfine coupling,[14] which can be ascribed to the close Dy···Dy distances and the extensive hydrogen-bonded network (*vide supra*).

Table 11. Values of the relaxation time (τ), α, χ_S and χ_T, for **1a** under a 1000 Oe dc field at varying temperatures. Red numbers indicate when values were restrained to remain physically reasonable (i.e. $\chi_S \geq 0$).

T (K)	τ (s)	α	χ_S	χ_T
1.9	0.0512(7)	0.152(8)	0.1696(2)	6.260(4)
2.0	0.0493(3)	0.153(1)	0.1590(5)	5.981(4)
2.5	0.0283(2)	0.230(3)	0.1038(9)	4.979(0)
3.0	0.0155(8)	0.290(6)	0.0859(7)	4.294(5)
3.5	0.0090(1)	0.303(1)	0.0798(3)	3.577(4)
4.0	0.0052(6)	0.303(8)	0.0521(1)	3.033(9)
4.5	0.0033(8)	0.286(1)	0.0238(2)	2.565(2)
5.0	0.0020(2)	0.256(4)	0.0127(8)	2.233(2)
5.5	0.0008(9)	0.296(1)	0.0127(8)	2.030(7)
6	0.0005(8)	0.320(9)	0.0052(1)	2.202(5)
6.5	0.0003(9)	0.269(2)	0.0033(7)	1.718(1)
7.0	0.0001(9)	0.291(9)	0.0013(1)	1.620(1)
7.5	0.0001(3)	0.243(8)	0	1.316(7)
8.0	0.0000982(2)	0.227(1)	0	1.166(8)
8.5	0.0000768(2)	0.175(8)	0	1.042(2)
9	0.0000349(7)	0.216(7)	0	1.041(2)

With this in mind, and to gain further insight into the magnetic relaxation dynamics, the τ^{-1} *vs.* T data was suitably fit to an equation (eqn (1)) encompassing Orbach, Raman and QTM processes (Fig. 35b):

$$\tau^{-1} = \tau_0^{-1}\exp(-U_{eff}/k_BT) + CT^n + \tau_{QTM}^{-1} \quad (1)$$

The best-fit parameters obtained were $\tau_0 = 1.38 \times 10^{-7}$ s, $U_{eff}/k_B = 48.68$ K, $C = 2.60 \times 10^{-4}$ s^{-1} $K^{-8.18}$, $n = 8.18$, and $\tau_{QTM} = 8.67 \times 10^{-3}$ s. Notably, the Orbach parameters are in good agreement with the ones obtained using an Arrhenius law. The n value is also close to the expected value of 9 for a Kramers ion. These data suggest that a thermally activated Orbach process is at the forefront of the SR phase. Other relevant spin-lattice relaxation processes include the Raman and direct processes. The latter is field dependent, and was therefore evaluated through variable field ac measurements. Once again, the SR phase was considered and fit to a generalized Debye model between fields of 200-2400 Oe (Fig. 36, left), with the best-fit parameters given in Table 12. This allows us to directly evaluate the impact of an external magnetic field on the relaxation time (Fig. 36, right). By fitting the τ^{-1} *vs.* H plot using the following equation:

$$\tau^{-1} = AH^4T + B_1/(1+B_2H^2) + \tau_0^{-1}\exp(-U_{eff}/k_BT) + CT^n, \quad (2)$$

we can simultaneously estimate the contribution of the direct process (AH^4T) and re-confirm the parameters obtained previously for QTM, Orbach and Raman processes.

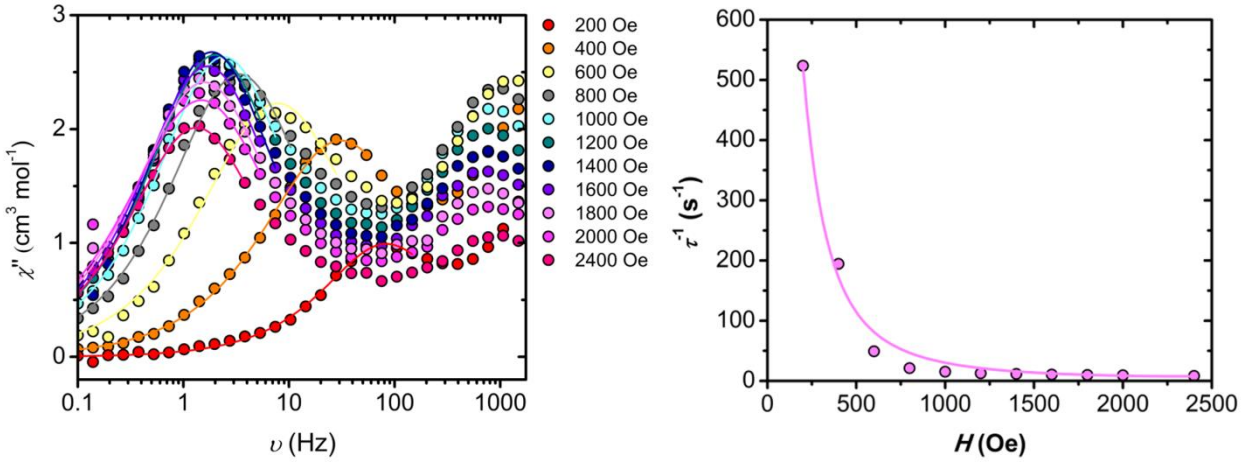

Figure 36. Frequency dependence of the χ'' magnetic susceptibility for **1a** collected at 2 K and varying fields. The best-fit to the generalized Debye model are shown by colored lines (left). Field dependence of the relaxation time for complex **1a**, plotted as τ^{-1} *vs* H and measured at 2 K. Solid line represents the best fit using the model described in the text (right).

Table 12. Values of the relaxation time (τ), α, χ_S and χ_T, for **1a** at 2 K under varying dc fields for the slow relaxation process.

***H* (Oe)**	**τ (s)**	**α**	**χ_S**	**χ_T**
200	0.0019(1)	0.127(9)	2.5994(6)	5.029(0)
400	0.0051(4)	0.234(4)	0.5235(7)	6.063(0)
600	0.0203(9)	0.231(0)	0.5074(0)	6.960(6)
800	0.0472(9)	0.184(2)	0.5916(1)	7.251(7)
1000	0.0657(4)	0.173(0)	0.5000(1)	7.440(9)
1200	0.0797(6)	0.174(4)	0.5037(6)	7.502(4)
1400	0.0857(1)	0.157(2)	0.5009(1)	7.371(0)
1600	0.0943(7)	0.172(9)	0.5026(1)	7.220(9)
1800	0.1010(8)	0.195(9)	0.5096(3)	7.104(0)
2000	0.107(4)	0.222(8)	0.5001(3)	6.945(6)
2400	0.119(6)	0.171(5)	0.6483(5)	5.935(4)

The best fit yielded values that are summarized in Table 13, and indicate that the direct process has a minimal contribution up to fields of 2400 Oe. Furthermore, there is no clear decrease of the relaxation time in the range of static fields investigated, which has previously been attributed to the direct process becoming predominant.[15] It is important to note, however that *n* in eqn (2) was fixed at 8.18 in order to provide comparative results to eqn (1), and to avoid overparameterization.

Table 13. Fitting parameters using eqn (2) for compound **1a**.

Parameter	**Value**
A (s^{-1} K^{-1} Oe^{-4})	2.91×10^{-14}
B_1 (s^{-1})	1563.16
B_2 (Oe^{-2})	4.99×10^{-5}
C (s^{-1} $K^{-8.18}$)	3.77×10^{-4}
τ_0 (s)	1.56×10^{-7}
U_{eff}/k_B (K)	42.06

Next, we carried out similar measurements on compound **2a**, which features a chain of Dy_2 units, and close interchain Dy···Dy distances (*vide supra*). As previously mentioned, **2a** also has the distinguishing characteristic of displaying two well-separated modes of magnetic relaxation. In contrast to **1a** however, where the SR and FR phases are

minimally influenced by applied fields, we can effectively control which relaxation mode is active by applying an external field in **2a**. This is clearly depicted in Fig. 37a, where at low fields, the FR mode is active, while an increase in the field strength results in suppressing this pathway and favouring the SR phase. The optimal fields to describe both processes were determined to be 0 and 1600 Oe for the FR and SR phases, respectively. Under zero applied fields, we can observe a full peak in the out-of-phase susceptibility of **2a** that is minimally influenced by the temperature (no significant shifting), and giving a signal that is very broad, extending from essentially 1 to 1500 Hz (Fig. 37b).

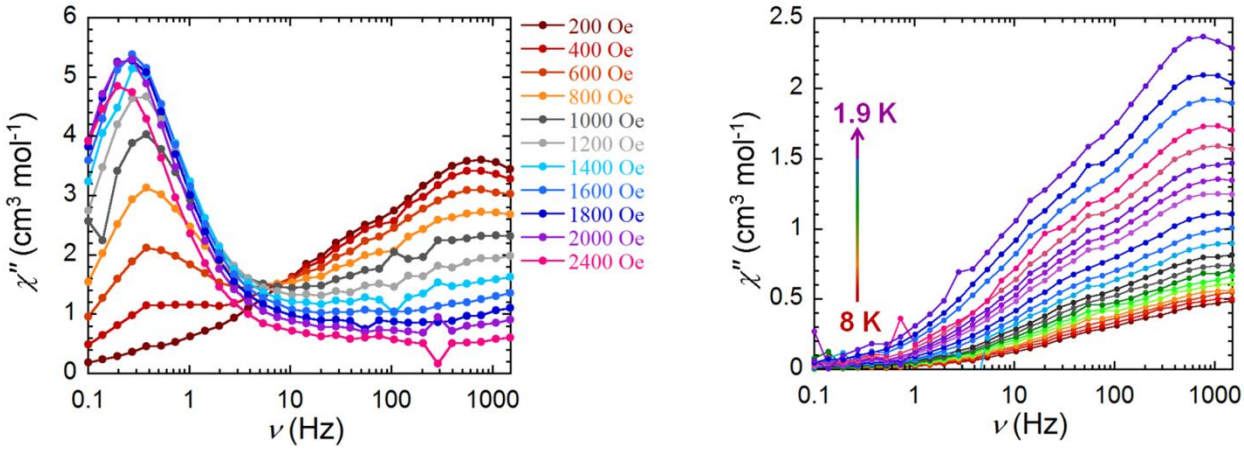

Figure 37. Frequency dependence of the χ'' magnetic susceptibility for **2a** collected at 2 K and varying applied dc fields. Solid lines are guides for the eyes (left). Frequency dependence of the χ'' magnetic susceptibility collected under zero applied field and temperatures ranging from 1.9 to 8 K for compound **2a** (right).

From this, we can conclude that multiple relaxation processes are in competition, and that the thermally-activated Orbach mechanism is not one of the main contributors. Investigation of the analogous data under an applied dc field of 1600 Oe, reveals full peaks at low frequencies, that shift below 4.5 K (Fig. 38). Fitting this data to a generalized Debye model yields large relaxation times that (Table 14), when applied to an

Arrhenius law, fall significantly outside the range for a thermally-activated process. This overall behaviour may be rationalized in part by the fact that two distinct Dy^{III} geometries co-exist in the same sample (8- *vs.* 9-coordinate), possibly giving an amalgamation of magnetic relaxation pathways. Additionally, the close proximity of intrachain and interchain Dy^{III} ions can also contribute to speeding up the relaxation processes, resulting in a rather convoluted magnetic relaxation behaviour.

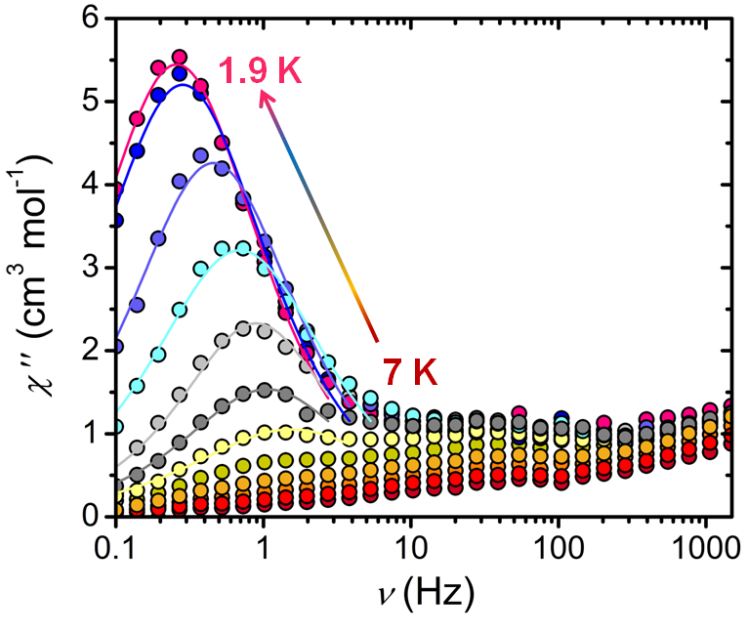

Figure 38. Frequency dependence of the out-of-phase component of the ac susceptibility under an optimal magnetic dc field of 1600 Oe for **2a**.

Table 14. Values of the relaxation time (τ), α, χ_S and χ_T, for **2a** under a 1600 Oe dc field at varying temperatures.

***T* (K)**	**τ (s)**	**α**	**χ_S**	**χ_T**
1.9	0.615(8)	0.099(7)	0.0158(4)	14.366(1)
2.0	0.561(0)	0.110(5)	0.0141(6)	12.401(1)
2.5	0.347(5)	0.0905(1)	0.0134(5)	9.828(0)
3.0	0.229(8)	0.118(6)	0.0114(2)	7.754(7)
3.5	0.178(4)	0.047(2)	0.0082(3)	6.410(7)
4.0	0.150(0)	0.103(9)	0.0075(0)	3.678(4)
4.5	0.102(9)	0.202(1)	0.0060(5)	2.982(9)

4.7 Conclusions

We have investigated the magnetic properties arising from four lanthanide complexes that are based on a single energetic ligand scaffold. Interestingly, both Dy^{III} analogs of the monomer and the chain exhibit two well-isolated magnetic relaxation processes which have been comprehensively investigated through ac susceptibility measurements. The combination of nitrogen-rich ligands with lanthanide ions has scarcely been reported, particularly when viewed from a magnetic standpoint. Our ongoing studies focus on expanding the coordination chemistry of the versatile H_4TTP ligand to improve not only the magnetic properties but also, potentially, its energetic properties.

4.8 Experimental section

4.8.1 General considerations

All manipulations were performed under aerobic conditions using chemicals and solvents from commercial sources (Acros Organics, Fisher Scientific, Alfa Aesar, and Strem Chemicals) and used as received without further purification.

4.8.2 Synthesis

Synthesis of 2,3,5,6-Tetra(1*H*-tetrazol-5-yl)pyrazine (H_4TTP). To a solution of pyrazine-2,3,5,6-tetracarbonitrile (20.0 mmol, 3.60 g) in 50 mL dimethyl sulfoxide, sodium azide (82.0 mmol, 5.34 g) is added in one portion. The mixture is stirred for 72 hours at 100 °C. Afterwards, the reaction mixture is poured onto ice and acidified with sulfuric acid. The obtained yellowish product is filtered, washed with water and then boiled in water for 0.5 h, the precipitate is filtered off and washed with water (yields 5.84 g, 83%). DSC (5 °C min^{-1}): 260 °C (dec.); ^{1}H NMR (300.00 MHz, dmso-d_6, ppm) δ: 7.16 (br., 4 H, N*H*); ^{13}C{^{1}H} NMR (75.0 MHz, dmso-d_6, ppm) δ: 154.0 (*C*N_4), 140.8 (*C*$_4$$N_2$); MS (TOF-MS-ES−): m/z: 351.0794 [M − H]$^-$

(Exact Mass: 351.0788). **Caution!** H_4TTP is an energetic compound with a potential sensitivity to various stimuli. While we encountered no issues in the handling of this nitrogen-rich molecule, proper protective measures (face shield, ear protection, body armor, Kevlar gloves, etc.) are recommended to be used at all times.

Synthesis of $[Dy(H_2TTP)(H_2O)_6]_2(H_2TTP)_{0.5} \cdot 6H_2O$ (1a). A mixture of $DyCl_3 \cdot 6H_2O$ (32.3 mg, 0.086 mmol) and H_4TTP (15.0 mg, 0.043 mmol) were sonicated for 10 min in 3 mL of H_2O. The resulting solution was then transferred in a 20 mL Teflon-lined stainless steel vessel, sealed, and heated to 160 °C for 3 days, and slowly cooled to room temperature over a period of 24 hours (5.41 °C h^{-1}). Clean yellow block-like crystals were obtained with a yield of 18 %. Anal. Calcd for $DyC_{12}H_{27}N_{27}O_{12}$: C 15.94%; H 3.01%; N 41.93%. Found: C 16.49%; H 2.53%; N 42.10%. Selected IR (cm^{-1}): 3174 (br), 1645 (m), 1477 (m), 1418 (s), 1338 (m), 1282 (m), 1213 (w), 1184 (m), 1074 (s), 667 (br).

Synthesis of $[Gd(H_2TTP)(H_2O)_6]_2(H_2TTP)_{0.5} \cdot 6H_2O$ (1b). The same procedure as **1a** was replicated for **1b**, but replacing the metal salt with $GdCl_3 \cdot 6H_2O$ (31.8 mg, 0.086 mmol). Colourless block-like crystals were obtained with a yield of 16 %. Anal. Calcd for $GdC_{12}H_{27}N_{27}O_{12}$: C 16.03%; H 3.03%; N 42.07%. Found: C 16.48%; H 2.62%; N 42.38%. Selected IR (cm^{-1}): 3175 (br), 1645 (m), 1477 (m), 1416 (s), 1338 (m), 1282 (m), 1213 (w), 1184 (m), 1073 (s), 666 (br).

Synthesis of $[Dy_2(TTP)(\mu\text{-}OH)_{1.3}(\mu\text{-}HCOO)_{0.7}(H_2O)_6]_n$ (2a). A mixture of $DyCl_3 \cdot 6H_2O$ (32.3 mg, 0.086 mmol), H_4TTP (15.0 mg, 0.043 mmol) and formic acid (16 μL, 0.424 mmol) were sonicated for 10 min in 3 mL of H_2O. The resulting solution was then transferred in a 20 mL Teflon-lined stainless steel vessel, sealed, and heated to 160 °C for 3 days, and slowly cooled to

room temperature over a period of 24 hours (5.41 °C h^{-1}). Yellow-orange block-like crystals were obtained with a yield of 15 %. Anal. Cald for $Dy_2C_{8.70}H_{14}N_{18}O_{8.70}$: C 12.51%; H 1.69%; N 30.19%. Found: C 12.67%; H 1.65%; N 29.05%. Selected IR (cm^{-1}): 3163 (br), 1666 (w), 1646 (m), 1641 (m), 1482 (m), 1305 (m), 1251 (m), 1234 (m), 1125 (m), 1049 (m), 680 (br).

Synthesis of $[Gd_2(TTP)(\mu\text{-}OH)_{1.25}(\mu\text{-}HCOO)_{0.75}(H_2O)_6]_n$ (2b). The same procedure as **2a** was replicated for **2b**, but replacing the metal salt with $GdCl_3{\cdot}6H_2O$ (31.8 mg, 0.086 mmol). Yellow block-like crystals were obtained with a yield of 11 %. Anal. Cald for $Gd_2C_{8.75}H_{14}N_{18}O_{8.75}$: C 12.73%; H 1.71%; N 30.53%. Found: C 12.99%; H 1.70%; N 29.71%. Selected IR (cm^{-1}): 3165 (br), 1666 (w), 1646 (m), 1641 (m), 1483 (m), 1305 (m), 1251 (m), 1234 (m), 1125 (m), 1049 (m), 686 (br).

4.8.3 Instrumentation and methods

Single-crystal X-ray diffraction.

Single crystal X-ray diffraction data were collected at 200(2) K on Bruker Smart and Kappa Apex II CCD diffractometers with graphite-monochromatised Mo-K_α radiation. Data collection and processing were performed with the Bruker APEX II software packages.[16] Semi-empirical adsorption corrections based on equivalent reflections were applied.[17] The structures were solved by direct methods and refined with full-matrix least-squares procedures using SHELXL[18] and WinGX.[19] All non-hydrogen atoms were refined anisotropically. The positions of the hydrogen atoms were calculated based on the geometry of related non-hydrogen atoms. In the crystal structures of **1a** and **1b** the H_2TTP^{2-} anion (C(9),…,N(36)) is located on an inversion centre and is disordered over two positions with equal occupancies fixed at 0.5. Due to the overlap of two positions, the molecule was refined with restraints on 1,2- and 1,3-distances (SAME command) and the H_2TTP molecule coordinated to Dy (C(1),…,N(18)) acted as an equivalent molecule.

Enhanced rigid-bond restraints (RIGU command) were applied to the atomic displacement parameters of these two molecules.

All hydrogen atoms of water molecules were refined with U_{iso} constrained at $1.5U_{eq}$ of the corresponding oxygen atoms and with O-H bond lengths restrained at 0.82Å (DFIX command), except H(10D), H(11A), H(11B), H(11C) atoms in **1a** that were refined as 'riding' (AFIX command) on the corresponding oxygen atoms. In **1a** and **1b** the 1,3-distances in the water molecules were restrained to be mutually equal (SADI command). The O(1),…,O(8) water molecules were not disordered. The O(9),…,O(12) molecules were each modelled as disordered over two positions; the atomic displacement parameters were constrained to be equal (EADP command) due to the proximity/overlap of the positions. In **1a**, the occupancy ratios were fixed at 0.5:0.5, while in **1b**, the occupancy ratios were not fixed and were refined to 0.536(5):0.464(5), 0.633(3):0.367(3), 0.498(3):0.502(3), 0.477(3):0.523(3), respectively. In **1a** and **1b** the hydrogen atoms H(14A), H(18A), H(25), H(32) of the N-H groups were refined using a riding model (AFIX command).

The structures of **2a** and **2b** show substitutional/occupancy disorder with a hydroxyl group and a formate anion sharing a common space. Their occupancy ratio was refined to about 0.65:0.35 (**2a**) and 0.625:0.375 (**2b**) and was fixed at the last stages of refinement. The hydrogen atoms of the hydroxyl group and the water molecules were refined using a riding model. The atomic displacement parameters of the formate were restrained in **2b** (SIMU and RIGU commands).

Infrared spectroscopy. Infrared spectra were performed with a Varian 640 FTIR spectrometer equipped with an ATR in the 4000 cm^{-1} to 600 cm^{-1} range.

Magnetic measurements. Magnetic susceptibility measurements were performed using a MPMS-XL7 Quantum Design SQUID magnetometer. Direct current (dc) susceptibility measurements were performed at temperatures ranging from 1.9 to 300 K, and up to applied fields of 7 T. Measurements were performed on crushed polycrystalline samples of 10.4, 10.1, 11.4 and 10.5 mg for compounds **1a**, **1b**, **2a** and **2b**, respectively, and wrapped in a polyethylene membrane. Alternating current (ac) susceptibility measurements were performed under an oscillating ac field of 3.78 Oe and ac frequencies ranging from 0.1 to 1488 Hz. Magnetization vs. field measurements were performed at 100 K in order to check for the presence of ferromagnetic impurities, which were found to be absent in all samples. Magnetic data was corrected for diamagnetic contributions using Pascal's constants.

4.9 References

(1) (*a*) R. P. Singh, R. D. Verma, D. T. Meshri and J. M. Shreeve, *Angew. Chem., Int. Ed.*, 2006, **45**, 3584–3601; (*b*) P. F.Pagoria, G. S. Lee, A. R. Mitchell and R. D. Schmidt, *Thermochim. Acta*, 2002, **384**, 187–204; (*c*) H. Guo and J. M. Shreeve, *Chem. Rev.*, 2011, **111**, 7377–7436; (*d*) D. M. Badgujar, M. B. Talawar, S. N. Asthana and P. P. Mahulikar, *J. Hazard. Mater.*, 2008, **151**, 289–305.

(2) (*a*) C. Ye, G. L. Gard, R. W. Winter, R. G. Syvret, B. Twamley and J. M. Shreeve, *Org. Lett.*, 2007, **9**, 3841–3844; (*b*) T. Abe, G.-H. Tao, Y.-H. Joo, R. W. Winter, G. L. Gard and J. M. Shreeve, *Chem.–Eur. J.*, 2009, **15**, 9897–9904.

(3) T. G. Witkowski, E. Sebastiao, B. Gabidullin, A. Hu, F. Zhang and M. Murugesu, *ACS Appl. Energy Mater.*, 2018, **1**, 589-593.

(4) (*a*) D. Pinkowicz, F. J. Birk, M. Magott, K. Schulte and K. R. Dunbar, *Chem.–Eur. J.*, 2017, **23**, 3548–3552; (*b*) M. A. Lemes, G. Brunet, A. Pialat, L. Ungur, I. Korobkov and

M. Murugesu, *Chem. Commun.*, 2017, **53**, 8660–8663; (*c*) K. S. Pedersen, J. Bendix and R. Clérac, *Chem. Commun.*, 2014, **50**, 4396–4415; (*d*) Y. Ma, G.-F. Xu, X. Yang, L.-C. Li, J. Tang, S.-P. Yan, P. Chen and D.-Z. Liao, *Chem. Commun.*, 2010, **46**, 8264–8266.

(5) (*a*) H. Feng, X.-P. Zhou, T. Wu, D. Li, Y.-G. Yin and S. W. Ng, *Inorg. Chim. Acta*, 2006, **359**, 4027–4035; (*b*) P. R. Andres and U. S. Schubert, *Adv. Mater.*, 2004, **16**, 1043–1068; (*c*) J. Granifo, M. T. Garland and R. Baggio, *Inorg. Chem. Commun.*, 2004, **7**, 77–81.

(6) (a) E. A. Popova, R. E. Trifonov and V. A. Ostrovskii, *ARKIVOC*, 2012, **1**, 45–65; (b) G. E. Kostakis, G. Abbas, C. E. Anson and A. K. Powell, *CrystEngComm*, 2009, **11**, 82–86; (c) G.Aromí, L. A. Barrios, O. Roubeau and P. Gamez, *Coord. Chem. Rev.*, 2011, **255**, 485–546.

(7) (*a*) X.-L. Tong, D.-Z. Wang, T.-L. Hu, W.-C. Song, Y. Tao and X.-H. Bu, *Cryst. Growth Des.*, 2009, **9**, 2280–2296; (*b*) P.-P. Liu, A.-L. Cheng, Q. Yue, N. Liu, W.-W. Sun and E.-Q. Gao, *Cryst. Growth Des.*, 2008, **8**, 1668–1674; (*c*) C. Huang, J. Wu, C. Song, R. Ding, Y. Qiao, H. Hou, J. Chang and Y. Fan, *Chem. Commun.*, 2015, **51**, 10353–10356; (*d*) C. Huang, X. Han, Z. Shao, K. Gao, M. Liu, Y. Wang, J. Wu, H. Hou and L. Mi, *Inorg. Chem.*, 2017, **56**, 4874–4884.

(8) (*a*) Y. Tao, J.-R. Li, Z. Chang and X.-H. Bu, *Cryst. Growth Des.*, 2010, **10**, 564–574; (*b*) T.-L. Hu, Y. Tao, Z. Chang and X.-H. Bu, *Inorg. Chem.*, 2011, **50**, 10994–11003.

(9) (*a*) M. Giraud, E. S. Andreiadis, A. S. Fisyuk, R. Demadrille, J. Pécaut, D. Imbert and M. Mazzanti, *Inorg. Chem.*, 2008, **47**, 3952–3954; (*b*) N. M. Shavaleev, S. V. Eliseeva, R. Scopelliti and J.-C. G. Bünzli, *Inorg. Chem.*, 2014, **53**, 5171–5178; (*c*) K. S. Kumar,

B. Schäfer, S. Lebedkin, L. Karmazin, M. M. Kappes and M. Ruben, *Dalton Trans.*, 2015, **44**, 15611–15619.

(10) D. Casanova, M. Llunell, P. Alemany and S. Alvarez, *Chem. – Eur. J.*, 2005, **11**, 1479–1494.

(11) K. R. Meihaus, J. D. Rinehart and J. R. Long, *Inorg. Chem.*, 2011, **50**, 8484–8489.

(12) J. Xiong, H.-Y. Ding, Y.-S. Meng, C. Gao, X.-J. Zhang, Z.-S. Meng, Y.-S. Zhang, W. Shi, B.-W. Wang and S. Gao, *Chem. Sci.*, 2017, **8**, 1288–1294.

(13) (*a*) Y. M. Litvinova, Y. M. Gayfulin, D. G. Samsonenko, A. S. Bogomyakov, W. H. Shon, S.-J. Kim, J.-S. Rhyee, Y. V. Mironov, *Polyhedron*, 2016, **115**, 174–179; (*b*) B. Liu, B. W. Wang, Z. M. Wang and S. Gao, *Sci. China Chem.*, 2012, **55**, 926–933.

(14) (*a*) E. M. Pineda, Y. Lan, O. Fuhr, W. Wernsdorfer and M. Ruben, *Chem. Sci.*, 2017, **8**, 1178–1185; (*b*) F. Pointillart, K. Bernot, S. Golhen, B. Le Guennic, T. Guizouarn, L. Ouahab and O. Cador, *Angew. Chem., Int. Ed.*, 2015, **54**, 1504–1507; (*c*) S. T. Liddle and J. van Slageren, *Chem. Soc. Rev.*, 2015, **44**, 6655–6669.

(15) E. Mamontova, J. Long, R. S. A. Ferreira, A. M. P. Botas, D. Luneau, Y. Guari, L. D. Carlos and J. Larionova, *Magnetochemistry*, 2016, **2**, 41.

(16) APEX 2, Bruker AXS Inc., Madison, Wisconsin, USA.

(17) G. M. Sheldrick, SADABS, Program for empirical X-ray adsorption correction, BrukerNonius, 2004.

(18) G. M. Sheldrick, *Acta. Cryst. C*, 2015, **71**, 3.

(19) L. J. Farrugia, *J. Appl. Crystallogr.*, 1999, **32**, 837.

An experiment is a question which science posts to Nature,
and a measurement is the recording of Nature's answer.
– Max Planck[6]

Chapter 5

Promoting magnetic communication and stimuli-responsive architectures through radical ligands

5.1 Published contributions

A tunable lanthanide cubane platform incorporating air-stable radical ligands for enhanced magnetic communication

G. Brunet, M. Hamwi, M. A. Lemes, B. Gabidullin and M. Murugesu, *Commun. Chem.*, 2018, **1**, 88.

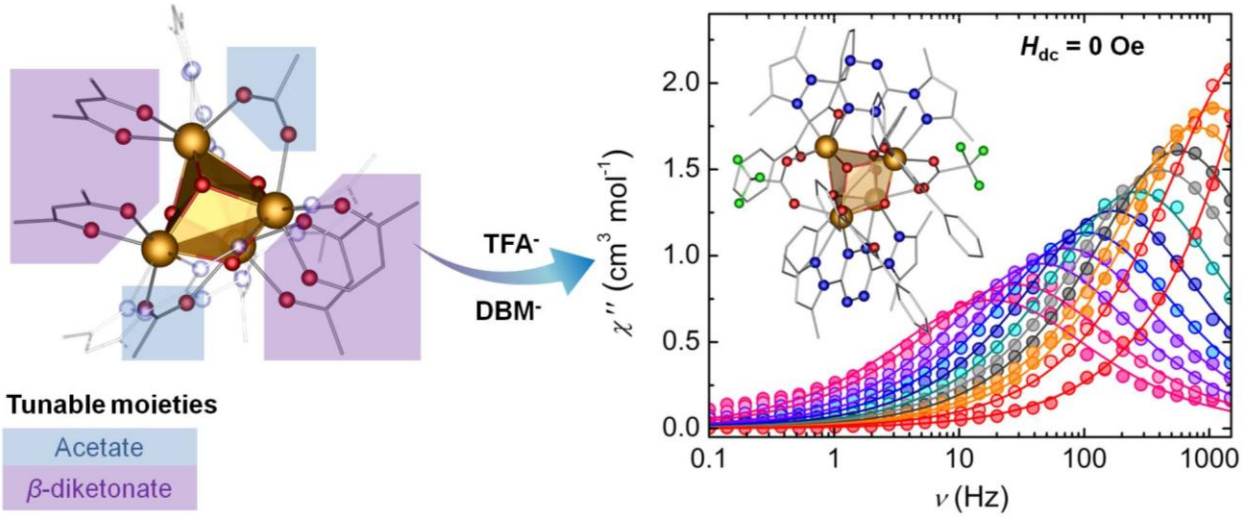

G. Brunet and M. Murugesu wrote the manuscript. G. Brunet performed the majority of the experiments. M. Hamwi and M. A. Lemes performed the synthesis of the compounds.

B. Gabidullin was responsible for the refinement of the single-crystal X-ray diffraction data.

[6] *Scientific Autobiography and other papers, 1949, p. 110.*

5.2 Abstract

The unique properties of polynuclear cluster-aggregates have long been staples in the molecular magnetism community. The initial success observed in high nuclearity transition metal complexes for generating exciting magnetic behaviours however, has not yet fully been extended to lanthanide-based clusters. This is in part due to the challenges related to promoting non-negligible magnetic interactions between two lanthanide ions. One promising route towards improving magnetic communication involves the incorporation of radical species. Here, we describe the preparation of tetranuclear $[Dy_4(\mu_3\text{-}OH)_4]^{8+}$ core structures that allow the incorporation of air-stable radical ligands. This combination paves the way for magnetically relevant lanthanide cubane cluster-aggregates capable of strong magnetic communication and improved spin-reversal barriers. Moreover, we show that the addition of electron donating groups lead to non-negligible antiferromagnetic coupling between the Dy^{III} centers and the $BPyTz^{\bullet-}$ ligands, while also simultaneously improving the slow magnetic relaxation dynamics in the absence of an applied field.

5.3 Introduction

The field of molecular magnetism saw a major breakthrough following the remarkable discovery that a nanosized $\{Mn_{12}\}$ cluster-aggregate could exhibit a bistable magnetic ground state and magnetic hysteresis.[1] This seminal work laid the foundation for decades worth of research into improving and perfecting control over the magnetic relaxation times of single-molecule magnets (SMMs).[2,3] In fact, up until recently, high-nuclearity cluster-aggregates based on first row transition metal ions were leading candidates in the design of data storage devices and quantum information processors.[4-6] This is in part due to the fact that such large cluster-aggregates have proven to be uniquely tunable, where chemical modifications on the capping ligands can be

readily introduced. Such modifications, while seemingly trivial, can lead to a drastic alteration in the magnetic behaviour through, for example, a reorientation of the magnetic anisotropy axes.[7-9] Thus, multiple synthetic strategies have been devised over the years in order to fine-tune and promote certain magnetic features in high-nuclearity cluster-aggregates of first row transition metal ions.[10,11] Despite this, progress toward improving the two defining SMM characteristics, energy barrier (U_{eff}) and blocking temperature (T_B), remained slow.

The recent shift towards *4f* ions in the field of molecular magnetism, however, has yielded impressive growth in mononuclear and dinuclear SMMs; largely due to the inherent magnetic anisotropy of the lanthanide elements.[12-15] Recently, our research efforts in the development of dinuclear SMMs stem from a desire to understand and overcome the challenges related to the magnetic coupling of core *4f* orbitals.[16,17] Due to the lack of strong magnetic coupling, the enhancement and control of the magnetic properties of lanthanide cluster-aggregates remain relatively lackluster. For example, progress thus far in the SMM behaviour of lanthanide cubane structures, which mimics a plethora of mixed-valent cubane Mn^{III}/Mn^{IV} complexes, has largely focused on the level of distortion within the $[Ln_4(\mu_3\text{-}OH)_4]^{8+}$ core.[18-20] It has previously been shown that larger Ln-OH-Ln angles can lead to a marginal improvement of their SMM-like properties; however in part due to the lack of significant magnetic coupling between the lanthanide ions, new strategies must be brought forward in order to further enhance their appeal and performance. In fact, they behave like a collection of single-ion magnets rather than a magnetically coupled system. If coupling could be introduced, however, akin to high-nuclearity transition metal complexes, lanthanide cluster-aggregates may also potentially lead to high performing exchange-coupled SMMs. Here, we propose an avenue to reinvigorate the field of magnetic lanthanide cubane cluster-aggregates, by incorporating air-stable radical ligands

within their frameworks, thereby promoting non-negligible magnetic interactions. This work focuses on the non-innocent redox properties of 3,6-bis(3,5-dimethylpyrazol-1-yl)−1,2,4,5-tetrazine (BPyTz), whose coordination to first row transition metal ions has previously yielded anionic air-stable radicals ($BPyTz^{\bullet-}$).[21,22] The ability of this ligand to generate air-stable radicals is rather unique compared to other radical-bridged systems, such as those based on 2,2′-bipyrimidine,[23] N_2,[24] or tetrapyridophenazine, [25] all of which are highly unstable in air and require strong reducing agents during synthesis. In the compounds presented herein, we observe the spontaneous generation of a radical upon metal coordination, and under ambient conditions. Moreover, we have yet to encounter any 1,2,4,5-tetrazine-ring opening reactivity in BPyTz, which has been observed in a closely related 3,6-bis(2′-pyrimidyl)−1,2,4,5-tetrazine (BPymTz) organic ligand.[26] These features render the open-shell $BPyTz^{\bullet-}$ ligand an ideal building block with which to facilitate and promote direct exchange coupling with lanthanide ions, despite deeply buried *4f* orbitals.

With this in mind, we demonstrate that the judicious combination of ligand frameworks can lead not only to highly complex structures, but can also allow for the targeted enhancement of specific magnetic properties. Thus, we present our investigations into precisely constructed radical-bearing [Dy^{III}_4] cubane cluster-aggregates, and their capacity to induce strong magnetic communication and zero-field SMM behaviour, features that have seldom been achieved in Ln^{III}-based cluster-aggregates. The incorporation of three distinct organic linkers within a single molecular system, affords a level of control that can be exploited to rationally fine-tune the properties of the cubane structure. As a proof of concept, we are able to tune the electronics of a single ligand while maintaining an identical structural core, and subsequently observe the impact on the magnetic behaviour. We first elect to combine the organic building block BPyTz with

acetate- and β-diketonate-based anions (Fig. 39), therefore allowing us to tune the electronics of the overall cluster-aggregate through the addition of electron withdrawing and/or donating groups. The implementation of such a strategy, which relies on modifying the functionalization of peripheral ligands, has become one of the most predominant methods for enhancing the slow magnetic relaxation properties of Ln^{III} SMMs.[17,27-30] This is in part due to the ease at which such modifications can be characterized in the solid-state, and the drastic improvements in the energy barriers that have been experimentally observed thus far. Our investigations into this radical-bridged $[Dy^{III}_4]$ cubane lead us to two promising variants that significantly outperform a closely related structure. [31] By adding strongly electron withdrawing fluorine groups on the OAc^- moiety and using either $acac^-$ (acetylacetonate) or DBM^- (dibenzoylmethanide), we are able to not only change the direction of the magnetic anisotropy axis, leading to improved SMM behaviour, but also examine the effect of imparting a slightly electron donating group on the $acac^-$ molecules by the addition of phenyl moieties. The resulting complexes are formulated as $[Dy_4(\mu_3\text{-}OH)_4(BPyTz^{\bullet-})_2(TFA)_2(acac)_4)]$ (**1**) and $[Dy_4(\mu_3\text{-}OH)_4(BPyTz^{\bullet-})_2(TFA)_2(DBM)_4)]\cdot 4(C_7H_8)$ (**2**), where TFA corresponds to trifluoroacetate. As such, we report the synthetic and structural details of radical-bridged lanthanide cubane cluster-aggregates, accompanied by an analysis of their magnetic behaviour.

5.4 **Synthesis and structure**

The synthesis of the desired cubane cluster-aggregate is promoted by the preparation of the Dy^{III} salt containing the selected terminal ligand (*i.e.* $Dy(DBM)_3$ and $Dy(TFA)_3$). The combination of two such precursors with BPyTz in a mixture of dichloromethane and tetrahydrofuran yields the cubane architecture (Fig. 39).

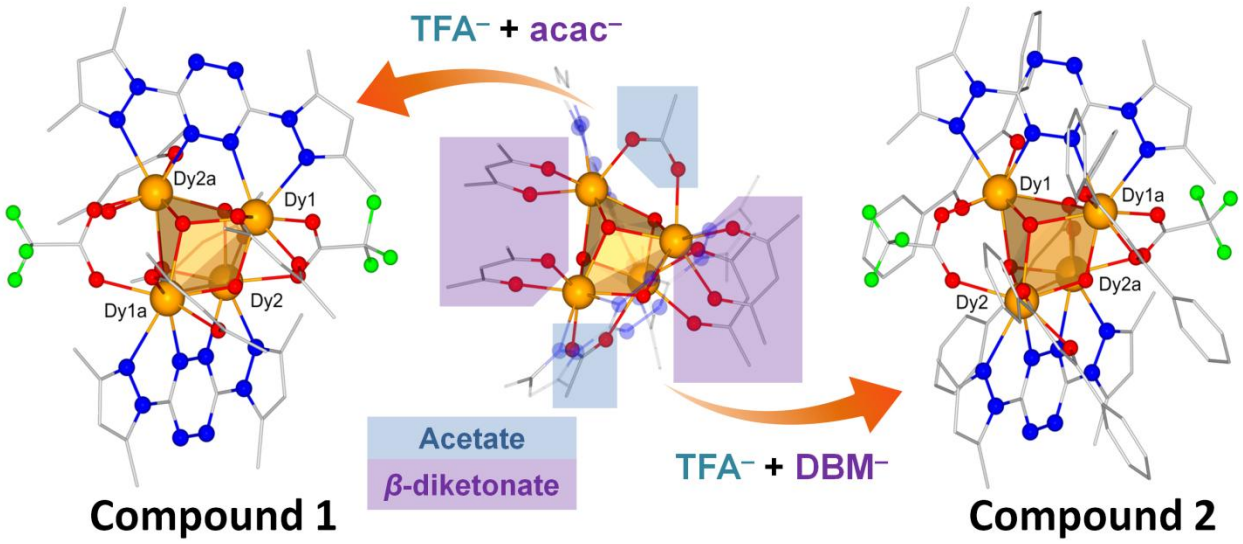

Figure 39. General synthetic route to isolate the described lanthanide-based cubane structures. The molecular structures of **1** and **2** are displayed, highlighting the tunability of the selected $[Dy_4(\mu_3\text{-}OH)_4]^{8+}$ core structure. The combination of BPyTz with acetate- and β-diketonate-based ligands allows the facile modulation of their magnetic properties. Orange, red, blue, and green spheres represent Dy, O, N, and F atoms, respectively, while gray vertices represent C atoms. Solvent molecules, disordered components, and H atoms are omitted for clarity.

It should be noted that the presence of hydroxide anions in the $[Dy_4(\mu_3\text{-}OH)_4]^{8+}$ core, despite the lack of a clear source of OH^-, is likely due to the use of hydrated metal salts and/or non-dried solvents. This has commonly been observed in the benchtop chemistry of large polynuclear transition metal- and lanthanide-based complexes.[32,33] The formation of a radical species under aerobic conditions can be readily distinguished in solution by the formation of either dark green or purple solutions. Crystallization of **1** and **2** is achieved by the slow vapor diffusion of an anti-solvent into the reaction medium. Full crystallographic data are provided in Table 15. The two cluster-aggregates crystallize in the monoclinic *C*2/*c* space group and share the same $[Dy_4(\mu_3\text{-}OH)_4]^{8+}$ core. The external coordination environment is completed by two $BPyTz^{\bullet-}$ radical ligands, two bidentate TFA^- anions, and four $acac^-$ (**1**) or four DBM^- (**2**) molecules (Fig. 39).

Table 15. Crystallographic data for compounds **1** and **2**.

Compound	**1**	**2**
Empirical Formula	$Dy_4C_{48}H_{60}N_{16}O_{16}F_6$	$Dy_4C_{116}H_{108}N_{16}O_{16}F_6$
Crystal system	Monoclinic	Monoclinic
Space group	*C*2/*c*	*C*2/*c*
a (Å)	25.031(3)	24.717(2)
b (Å)	14.3548(17)	21.8465(17)
c (Å)	22.476(3)	20.6345(16)
α (°)	90	90
β (°)	103.464(3)	94.387(4)
γ (°)	90	90
V (Å^3)	7854.1(17)	11109.7(15)
Z	4	4
ρ_{calc} (g cm^{-3})	1.591	1.642
λ (Å)	0.71073	0.71073
T (K)	200(2)	200(2)
μ (mm^{-1})	3.837	2.742
F (000)	3624	5448
Reflections Collected	59059	138204
Independent Reflections	11068	16816
Reflections with I > 2σ(*I*)	8122	11999
Goodness of fit on F^2	1.058	1.161
R_1, wR_2 ($I > 2\sigma(I)$)[a]	0.0669, 0.1597	0.0717, 0.1284
R_1, wR_2 (all data)	0.0939, 0.1802	0.1129, 0.1675

[a] $R = R_1 = \sum||F_o| - |F_c||/\sum|F_o|$; $wR_2 = \{\sum[w(F_o^2 - F_c^2)^2]/\sum[w(F_o^2)^2]\}^{1/2}$; $w = 1/[\sigma^2(F_o^2)+(ap)^2 + bp]$, where $p = [\max(F_o^2, 0) + 2F_c^2]/3$; and $Rw = [w(|F_o| - |F_c|)^2 / w|F_o|^2]^{1/2}$, where $w = 1 / \sigma^2(|F_o|)$.

Evidence for the *in-situ* one electron reduction of the BPyTz ligand is first provided by investigating the N-N bond lengths within the tetrazine moiety. Indeed, elongation of this bond beyond 1.36 Å would suggest the formation of a tetrazine-based radical anion, which is anticipated to lead to a stronger magnetic exchange.[34-37] Here, the average N-N bond lengths within the tetrazine moiety correspond to 1.38 and 1.39 Å, respectively for **1** and **2**, a clear indication of the reduced nature of the tetrazine-based ligand. The two crystallographically independent Dy^{III} ions are 8-coordinate and are best described by a square antiprismatic geometry - at the exception of Dy1 in **1**, which most closely resembles a biaugmented trigonalprism - as indicated by the SHAPE software (Table 16).[38] The heavily distorted nature of the cubane core is highlighted by average Dy-OH-Dy angles of 106.33 and 106.44^o for **1** and **2**,

respectively. It is also noteworthy that the unit cells of both complexes contain only four instances of the radical-bridged Dy^{III} cluster-aggregate, a vast improvement over the 18 molecules found in the unit cell of a related compound investigated by *ab initio* calculations.[28] This also serves to significantly simplify crystal-packing effects that could potentially be observed in the bulk magnetic properties. Moreover, in the structure of **2**, four partially disordered toluene molecules have been identified in the lattice. The closest intercluster Dy-Dy distances are 10.88 and 11.25 Å for **1** and **2**, respectively. Other relevant bond distances can be found in Table 17.

Table 16. SHAPE constants for the Dy^{III} centers in **1** and **2**. The lowest constants are bolded.

SHAPE Code	Point Group	Description	Compound 1		Compound 2	
			Dy 1	Dy 2	Dy 1	Dy 2
OP-8	D_{8h}	Octagon	27.487	30.040	32.788	25.016
HPY-8	C_{7v}	Heptagonal pyramid	18.608	18.417	19.376	19.93
HBPY-8	D_{6h}	Hexagonal pyramid	16.168	15.330	15.162	16.817
CU-8	O_h	Cube	12.824	12.183	9.454	11.369
SAPR-8	D_{4d}	Square antiprism	6.495	**5.392**	**1.916**	**1.185**
TDD-8	D_{2d}	Triangular dodecahedron	5.974	6.390	2.728	3.626
JGBF-8	D_{2d}	Johnson gyrobifastigium J26	17.087	15.443	14.762	15.253
JETBPY-8	D_{3h}	Johnson elongated triangular bipyramid J14	22.349	22.163	26.332	26.467
JBTPR-8	C_{2v}	Biaugmented trigonal prism J50	**4.557**	6.436	2.691	3.624
BTPR-8	C_{2v}	Biaugmented trigonal prism	6.123	6.637	2.644	2.843
JSD-8	D_{2d}	Snub diphenoid J84	6.914	8.839	5.034	6.136
TT-8	T_d	Triakis tetrahedron	12.944	12.867	10.031	12.012
ETBPY-8	D_{3h}	Elongated trigonal bipyramid	23.369	23.355	21.412	21.67

Table 17. Selected bond distances in **1** and **2**.

Compound 1				
Dy atom	**Bridging molecule**	**Metal-ligand distance (Å)**		
Dy1	OH^-	O1 – 2.348(6)	O2 – 2.364(6)	
	$BPyTz^{\bullet-}$	N1 – 2.563(9)	N3 – 2.470(8)	
	$acac^-$	O3 – 2.440(2)	O3' – 2.256(14)	O4 – 2.289(7)
	TFA^-	O7 – 2.376(7)		
Dy2	OH^-	O1 – 2.352(6)	O2 – 2.354(6)	
	$BPyTz^{\bullet-}$	N4 – 2.470(8)	N8 – 2.599(8)	
	$acac^-$	O5 – 2.309(8)	O6 – 2.328(8)	
	TFA^-	O8 – 2.359(7)		
Compound 2				
Dy atom	**Bridging molecule**	**Metal-ligand distance (Å)**		
Dy1	OH^-	O1 – 2.368(6)	O2 – 2.406(5)	
	$BPyTz^{\bullet-}$	N5 – 2.547(7)	N7 – 2.455(7)	
	DBM^-	O3 – 2.260(6)	O4 – 2.351(6)	
	TFA^-	O7 – 2.359(6)		
Dy2	OH^-	O1 – 2.365(5)	O2 – 2.389(5)	
	$BPyTz^{\bullet-}$	N1 – 2.548(7)	N3 – 2.455(6)	
	DBM^-	O5 – 2.327(6)	O6 – 2.264(5)	
	TFA^-	O8 – 2.375(6)		

5.5 Static magnetic properties

To probe potentially exciting magnetic properties arising from the introduction of a radical ligand within the cubane cluster-aggregate, we first performed static direct current (dc) magnetic susceptibility measurements between 1.8 and 300 K under an applied field of 1000 Oe (Fig. 40). The observed room temperature values of 53.71 and 56.49 cm^3 K mol^{-1} for **1** and **2**, respectively, are in close agreement with the 57.43 cm^3 K mol^{-1} expected for four Dy^{III} centres and two $BPyTz^{\bullet-}$ radical anions (g = 2.0). In both complexes, the χT product remains relatively constant until ~75 K, where we observe a slight decrease followed by an increase that is more pronounced in **2**. The maximum χT values are 47.16 and 58.69 cm^3 K mol^{-1} at 14 and 15 K, respectively for **1** and **2**. The initial decrease at higher temperatures (25-100 K) is likely attributed to the thermal depopulation of Stark sublevels, while the distinct increase at low temperatures (~8-30 K) is due to the spin alignment of the metal centres caused by non-negligible antiferromagnetic

interactions between the Dy^{III} ions and the $BPyTz^{\bullet-}$ radicals.[39-42] In addition to this, the fact that the increase is much more drastic in **2** compared to **1**, and occurs at a higher temperature, can be rationalized by a more significant coupling between the Dy^{III} metal centres and the ligand radical.

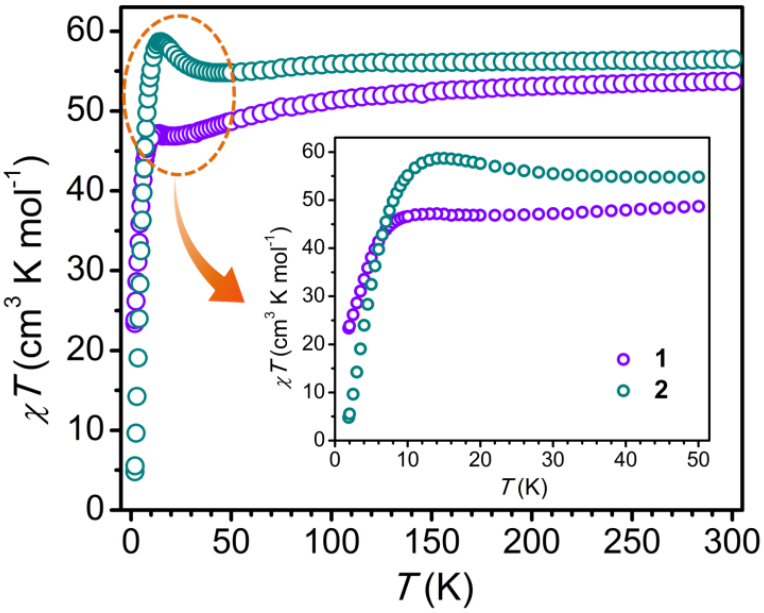

Figure 40. Temperature dependence of the χT product at 1000 Oe for **1** and **2**. The inset displays a zoomed-in region of the same plot at low temperatures.

This is further evidenced by the shorter Dy-N distances in **2** between the Dy^{III} ions and the nitrogen atoms originating from the tetrazine ring (2.47 Å in **1** *vs*. 2.45 Å in **2**). This enhancement in the magnetic coupling strength, brought upon by the simple replacement of $acac^-$ with DBM^- ligands, exemplifies the impact of electron-donating groups on the resulting magnetic interactions. Here, the addition of phenyl groups serve to simultaneously reduce the average Dy-O distance of the β-diketonates from 2.34 Å in **1**, to 2.30 Å in **2**, while also shortening the aforementioned Dy^{III}-radical distances (Fig. 41). The final decrease in the χT (below 10 K) can be attributed to intermolecular antiferromagnetic interactions, as reported in a molecular analog.[31]

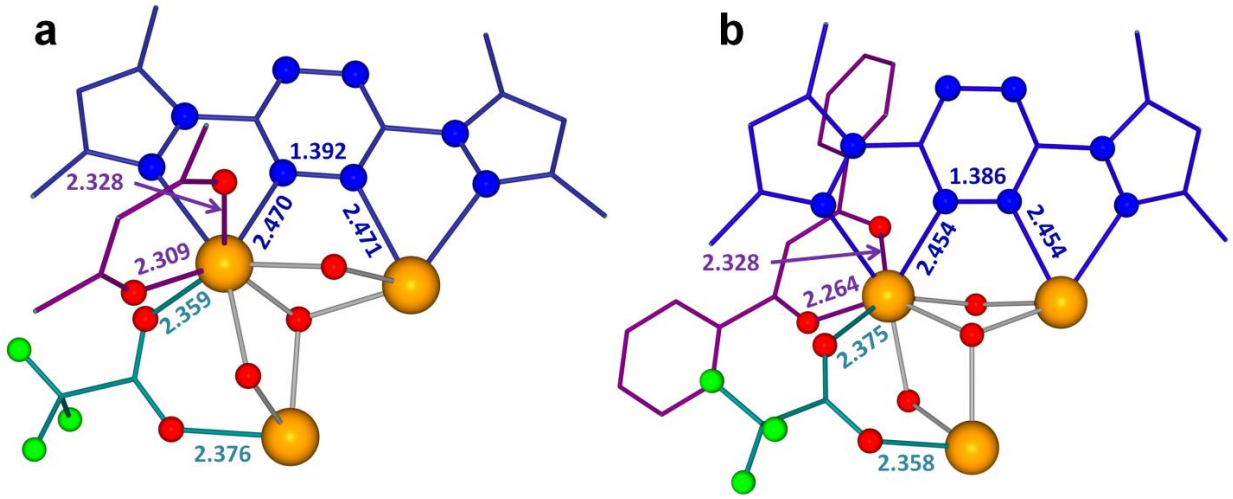

Figure 41. Molecular fragments of **1** (a) and **2** (b) with selected bond distances (Å), displaying the stronger Dy^{III}-radical interactions in **2** through the shorter average Dy-O (β-diketonates) and Dy-N distances (tetrazine).

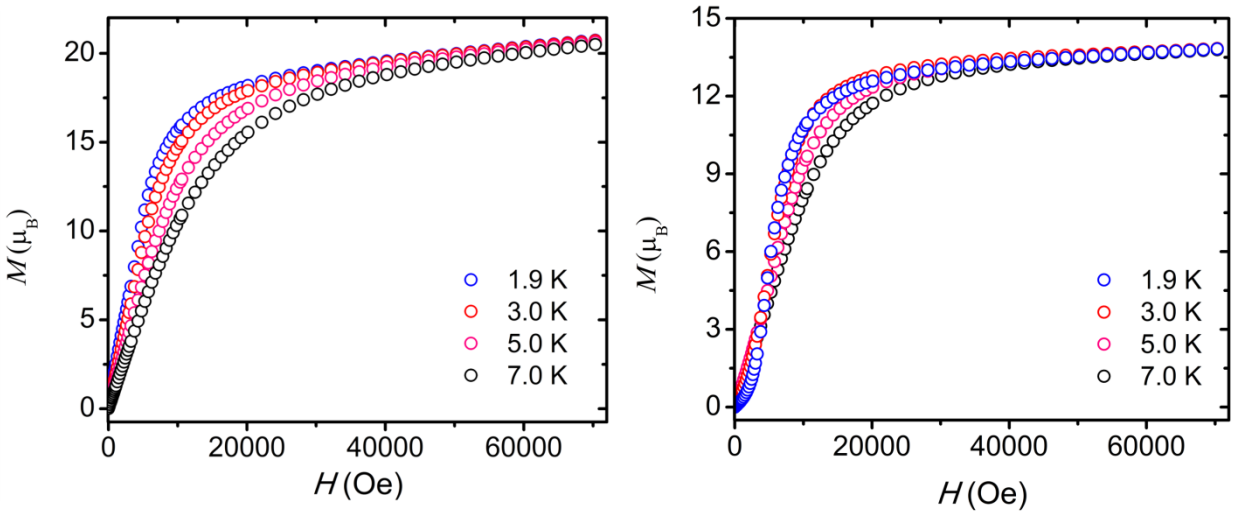

Figure 42. Field-dependent magnetization data collected at 1.9, 3, 5 and 7 K for compounds **1** (left) and **2** (right).

The strength of the intramolecular interactions in **2** can further be observed in the corresponding *M vs. H* plot which displays a distinctive "S-shape" curve, while no such feature exists in **1** (Fig. 42).

5.6 **Dynamic magnetic properties**

In order to verify the possibility of single-molecule magnet behaviour, we performed alternating current (ac) magnetic susceptibility measurements on **1** and **2**. In both cases, we observe an ac signal under 0 Oe dc field; however, in the case of **1**, only tails of peaks are observed within the limits of the magnetometer (Fig. 43). The shifting of the peaks in the out-of-phase (χ'') magnetic susceptibility as a function of frequency are indicative of slow magnetic relaxation. Interestingly, the intensity of the peaks diminishes with decreasing temperatures. This is in sharp contrast to the vast majority of SMMs, where the inverse behaviour is observed; a decrease in the temperature is generally accompanied by an increase in the χ'' intensity.[43,44] Such a feature further confirms the strength of the antiferromagnetic interactions between the Dy^{III} ions and the $BPyTz^{\bullet-}$ radical, and is reflective of the drastic decrease of χ at low temperatures. Fitting of this data using a generalized Debye equation yields the magnetic relaxation times (τ) for **2** in the temperature range of 1.8-3.5 K. In turn, the dominant magnetic relaxation mechanisms responsible for spin reversal can be evaluated by an analysis of the temperature dependence of the relaxation times (Fig. 44). In order to reproduce the temperature dependence of the relaxation time, we have fit τ^{-1} *vs.* T taking into account Orbach, Raman and quantum tunneling of the magnetization (QTM) processes, as given in eqn (1).

$$\tau^{-1} = \tau_0^{-1}\exp[-U_{\text{eff}}/(k_B T)] + CT^n + \tau_{\text{QTM}}^{-1} \quad (1)$$

The resulting fit is in good agreement with all data and afforded $\tau_0 = 5.51(9) \times 10^{-9}$ s, $U_{\text{eff}}/k_{\text{B}} = 31.44(3)$ K, $C = 0.55(5)$ s^{-1} $K^{-8.78}$, $n = 8.7(8)$ and $\tau_{\text{QTM}} = 8.44(8) \times 10^{-3}$ s. Notably, the Raman exponent (n) is close to the expected value of $n = 9$ for a Kramers systems. The attempt time (τ_0)

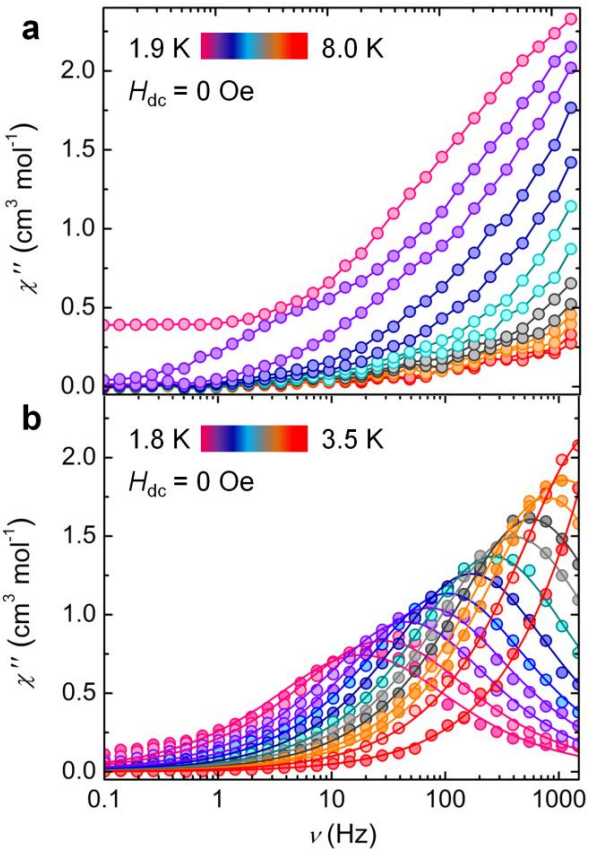

Figure 43. Slow magnetic relaxation observed by SQUID magnetometry. Frequency dependence of the out-of-phase (χ'') magnetic susceptibility under 0 Oe dc field for **1** (a) and **2** (b). For **1**, the solid lines serve as guides for the eyes while in **2**, they represent the best fit to a generalized Debye model.

is also well within the expected range for single-molecule magnets (10^{-6} to 10^{-10} s). Moreover, the spin-reversal barrier (U_{eff}) is in line with the one approximated using an Arrhenius plot (36.53(5) K; Fig. 44). (Table 18).[45-47] Thus, we demonstrate that the incorporation of open-shell ligands can improve the magnetic performance of Ln^{III}-based cluster-aggregates, however, at the same time, we maintain that such a feature cannot exclusively be relied on in order to optimize the anisotropy barrier. Additional factors such as dipolar exchange interactions and the symmetry of the Ln^{III} ions are also expected to play decisive roles.

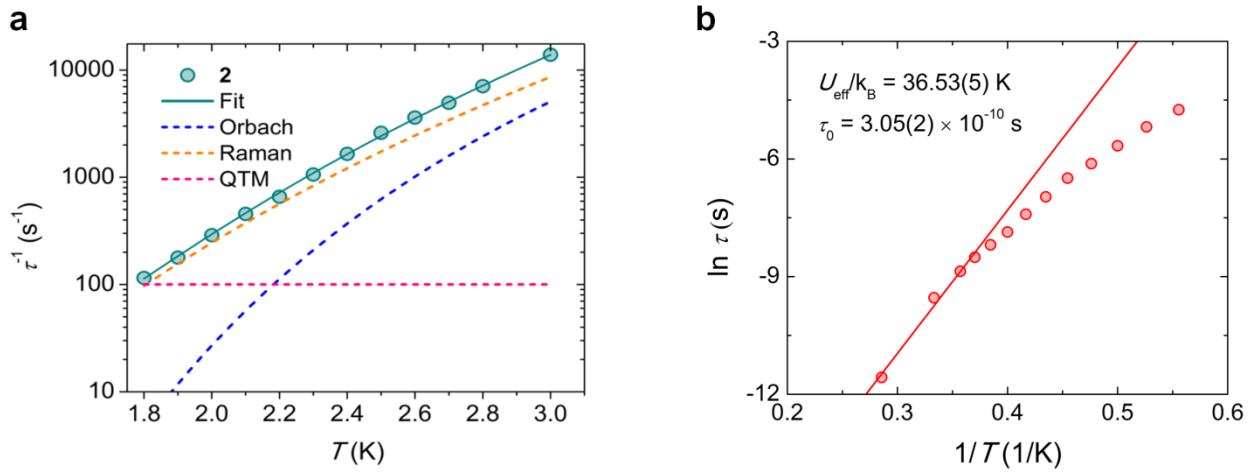

Figure 44. Temperature dependence of the magnetic relaxation times. The solid line represents the best-fit taking into account contributions from Orbach, Raman and QTM. The dashed lines indicate the individual contributions of each relaxation mechanism (a). Temperature dependence of the relaxation time, expressed as ln τ *vs.* 1/T (Arrhenius plot). The linear fit of the high temperature region yields an initial approximation of the energy barrier and attempt time (b). This value represents the third highest energy barrier at zero field within the class of Ln_4 cubanes.

Table 18. Compilation of the energy barriers of Ln^{III}-based cubane structures, highlighting the lack of high performing SMMs in this family. Those measured under an applied dc field have been left out.

Energy barriers of $[Ln_4(\mu_3\text{-}OH)_4]^{8+}$ containing clusters under zero dc field				
Compound	U_{eff}/k_B **(K)**	τ_0 **(s)**	H_{dc} **(Oe)**	**Ref**
$[Dy_4(\mu_3\text{-}OH)_4(\mu\text{-}TFA)_4(\mu_3\text{-}hfa)_4(phen)_4]$	67.0	1.2×10^{-8}	0	45
$[Dy_4(\mu_3\text{-}OH)_4(L^1)_8]_n$	40.2	5.4×10^{-8}	0	46
$[Dy_4(\mu_3\text{-}OH)_4(BPyTz^{\bullet-})_2(TFA)_2(DBM)_4)]\cdot 4(C_7H_8)$	31.4	5.5×10^{-9}	0	This work
$[Dy_4(OH)_4(TBSOC)_2(H_2O)_4(CH_3OH)_4]\cdot 4H_2O$	22.9	1.1×10^{-8}	0	47
$[Dy_8(OH)_8(phendox)_6(H_2O)_8]Cl_2(OH)_2\cdot 18H_2O\cdot 18MeOH$	4.3	1.3×10^{-6}	0	19
$[Dy_{11}(OH)_{11}(phendox)_6(phenda)_3(OAc)_3](OH)\cdot 40H_2O\cdot 7MeOH$	1.8	7.5×10^{-6}	0	19

5.7 Direction of the magnetic anisotropy

Since the ground state of **1** and **2** is defined by $M_J = \pm 15/2$, it is amenable to electrostatic analysis by Magellan,[48] providing an estimation of the orientation of the magnetic anisotropy axes (Fig. 45). Here, we find that the main magnetic axes are oriented towards either the TFA^-

anions or the centre of the tetrazine ring. The two distinct orientations are a by-product of having two crystallographically independent Dy^{III} ions within each cubane. It is interesting to note that the anisotropy axes in **2** are well aligned with the ideal axes generated from the Dy^{III} centres to the two aforementioned ligands. In fact, the deviation in **2** from TFA^- is only 5.19°, while the one from the tetrazine ring is calculated to be 12.2°. This is in contrast to **1**, where the deviation is more significant, with analogous angles calculated to be 21.8 and 17.8°, respectively. The implication of this result is that the chemical modification of secondary ligands ($acac^-$ *vs*. DBM^-) can influence the orientation of the magnetic anisotropy axis. The greater electron-donating ability of DBM^- compared to $acac^-$ yields stronger interactions with the $BPyTz^{\bullet-}$ radical, which in turn may shift the magnetic anisotropy axes towards the more negatively charged species so as to achieve greater minimization of the electrostatic potential energy.

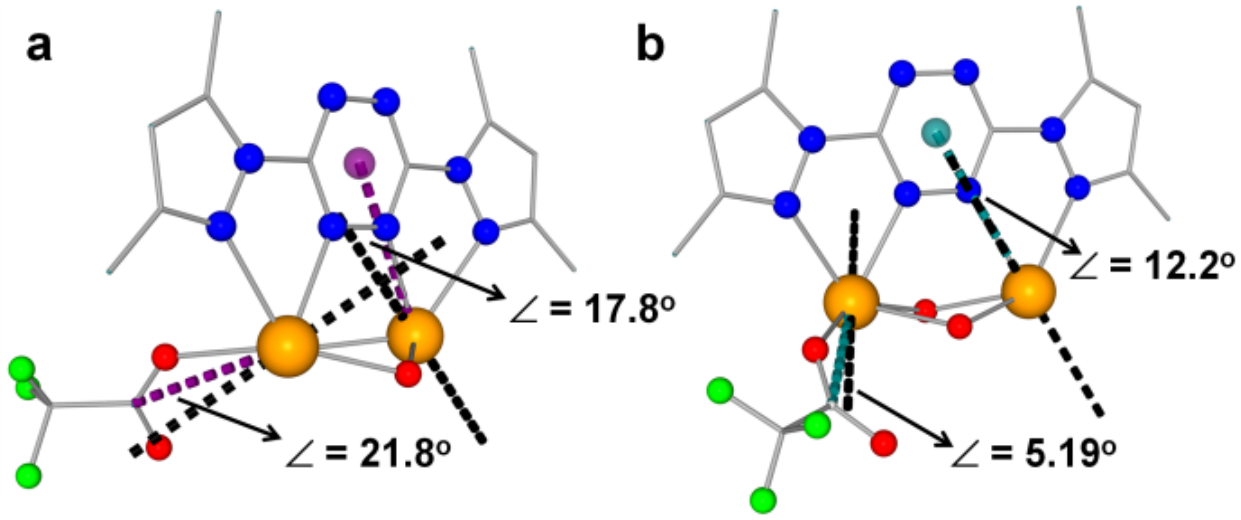

Figure 45. Electrostatic orientation of the main magnetic axes for the ground doublet of the two crystallographically independent Dy^{III} ions in **1** (a) and **2** (b), shown as dashed black lines. The dashed colored lines display the ideal orientation towards either the TFA^- anion or the centroid of the tetrazine ring, along with their respective angular deviations from the predicted anisotropy axis.

5.8 Conclusions

In summary, we report the exciting incorporation of air-stable radicals within lanthanide cubane cluster-aggregates. Modulation of the capping ligands has allowed for a significant improvement of the magnetic behaviour in terms of both magnetic coupling strength and relaxation barrier. This is in contrast to other lanthanide cubane structures that are generally obtained serendipitously and lack any real tunability of their physical properties. Using an identical $[Dy_4(\mu_3\text{-}OH)_4]^{8+}$ core structure, we have improved the out-of-phase magnetic susceptibility - from tails of peaks to frequency- and temperature-dependent ac signals - yielding an effective spin reversal barrier of 31 K in the absence of an applied field. Thus, we provide a blueprint towards improving the single-molecule magnet behaviour of lanthanide-based cluster-aggregates. Further adjustments to the ligand field from the capping ligands could promote even stronger magnetic interactions between the lanthanide ions and lead to desired remanent magnetization.

5.9 Experimental section

5.9.1 General considerations

The BPyTz ligand was prepared in accordance with previously reported methods,[49] as was the metal salt $Dy(TFA)_3$.[50] The $Dy(DBM)_3$ starting material was synthesized following a previously published procedure but with slight modifications.[51] A solution of $DyCl_3 \cdot 6H_2O$ in water was added dropwise to an equimolar solution of DBM and piperidine in ethanol, under constant stirring. The molar ratio of Dy/DBM was 1:3. The precipitate was then washed with ethanol and air-dried.

5.9.2 Synthesis

Synthesis of $[Dy_4(\mu_3\text{-}OH)_4(BPyTz^{\bullet-})_2(TFA)_2(acac)_4)]$ (1). $Dy(acac)_3 \cdot xH_2O$ (0.25 mmol, 208.8 mg) and $Dy(TFA)_3$ (0.125 mmol, 62.7 mg) were dissolved in a solvent mixture of CH_2Cl_2/THF

(1:1, 4 mL) and added to a 4 mL CH_2Cl_2 solution of BPyTz (0.125 mmol, 33.8 mg). The mixture was stirred for a few hours. The resulting dark purple solution was filtered under gravity. Dark green crystals were obtained by vapor diffusion using hexane as an antisolvent after approximately 2 days. Selected IR data for **1** (cm^{-1}): 3606(w), 1675(m), 1596(m), 1550(s), 1519(s), 1477(s), 1454(s), 1422(s), 1391(s), 1313(m), 1197(s), 1145(m), 1118(s), 1064(m), 1024(m), 983(m), 941(m), 841(m), 800(m), 784(m), 682(s). Elemental analysis: calcd for $Dy_4C_{51.5}H_{67}N_{16}O_{16}F_6$: C 28.39%; H 3.10%; N 10.29%. Found: C 28.86%; H 2.91%; N 10.31%. These results are consistent with approximately 3.5 CH_2Cl_2 solvent molecules contained within the lattice (see crystallographic refinement for further details).

Synthesis of $[Dy_4(\mu_3\text{-}OH)_4(BPyTz^{\bullet-})_2(TFA)_2(DBM)_4)]\cdot 4(C_7H_8)$ (2). $Dy(DBM)_3\cdot xH_2O$ (0.5 mmol, 229.9 mg) and $Dy(TFA)_3$ (0.25 mmol, 125.4 mg) were dissolved in a solvent mixture of CH_2Cl_2/THF (1:1, 5 mL) and added to a 5 mL CH_2Cl_2 solution of BpyTz (0.25 mmol, 67.6 mg). The mixture was stirred for a few hours. The resulting dark green solution was filtered under gravity. Black crystals were obtained by vapor diffusion using toluene as an antisolvent after approximately 2 days. Selected IR data for **2** (cm^{-1}): 3607(w), 2930(w), 2323(w), 1674(s), 1600(s), 1522(s), 1425(s), 1393(s), 1313(m), 1267(m), 1196(s), 1143(s), 1018(m), 984(m), 924(m), 842(m), 797(m), 699(s), 652(s), 616(m), 536(m). Elemental analysis: calcd for $Dy_4C_{116}H_{108}N_{16}O_{16}F_6$: C 50.73%; H 3.96%; N 8.16%. Found: C 50.07%; H 3.45%; N 7.79%.

5.9.3 **Instrumentation and methods**

Single-crystal X-ray diffraction.

The crystals of **1** and **2** were mounted on thin glass fibers using paraffin oil. Prior to data collection, the crystals were cooled to 200(2) K. The data were collected on a Bruker AXS

single-crystal diffractometer equipped with a sealed Mo tube (wavelength 0.71073 Å) and APEX II CCD detector. The raw data collection and reduction were done with the Bruker APEXII software package.[52] Semi-empirical absorption corrections based on equivalent reflections were applied.[53] Systematic absences in the diffraction dataset and unit-cell parameters were consistent with monoclinic *C*2/*c* (#15) for **1** and **2**. The structures were solved by direct methods and refined with full-matrix least-squares procedures based on F^2, using SHELXL[54] and WinGX[55]. Displacement ellipsoid plots were produced using ORTEP[56], and uncertainties were estimated using PLATON[57].

In **1**, all non-H atoms were refined anisotropically. The hydrogen atoms of hydroxyl groups (H1, H2) were located in a difference Fourier map and refined using bond distance and angle (H-to-Dy 1,3-distance) restraints (DFIX in Shelxl) and U_{iso} constrained at $1.2U_{eq}$ of the O atoms they were attached to. The remaining hydrogen atoms were placed in idealized positions. The acetylacetonate C13...C17,O3,O4 was disordered over two positions with 0.66(2):0.34(2) occupancy ratio. Bond distance and angle (1,3-distance) restraints (SAME in Shelxl) were applied to two positions of the molecule and the undisordered C18...C22,O5,O6 acetylacetonate (as a template). Enhanced rigid-bond restraints (RIGU in Shelxl) and restraints for approximately isotropic behaviour (ISOR in Shelxl) were applied to the ADPs. The trifluoroacetate C23,C24,O7,O8,F1…F3 was disordered over two positions with 0.58(3):0.42(3) occupancy ratio. It was refined with bond distance and angle (1,3-distance) restraints (SAME in Shelxl) for a proper geometry, as well as enhanced rigid-bond restraints (RIGU in Shelxl) and restraints for approximately isotropic behaviour (ISOR in Shelxl) applied to the ADPs.

The lattice contained highly disordered solvent/guest molecules that couldn't be modelled in a conventional way. Their contribution was accounted for using SQUEEZE routine of the

Platon package. The solvent-accessible area consists of four (equal) regions per unit cell with a total volume of 1924 $Å^3$ (24% of the total volume) containing 320 electrons, which can account for approximately 3.5 dichloromethane molecules. The highest residual density peak (3.46 e $Å^{-3}$ at 0.77 Å from Dy1) is of the same order of magnitude as the deepest hole (-2.71 e $Å^{-3}$ at 0.43 Å from H22A).

In **2**, all non-H atoms were refined anisotropically. The hydrogen atoms of hydroxyl groups (H1A, H2A) were located in a difference Fourier map and refined using bond distance restraints (DFIX in Shelxl), while the remaining hydrogen atoms were placed in idealized positions. The C10...C15 phenyl group was disordered over two positions with 0.51(2):0.49(2) occupancy ratio. It was refined using bond distance and angle (1,3-distance) restraints (SAME in Shelxl), as well as 'enhanced rigid-bond restraints' (RIGU in Shelxl) applied to the ADPs. The trifluoromethyl group C44,F1...F3 was disordered over two positions with 0.67(2):0.33(2) occupancy ratio. It was refined using bond distance and angle (1,3-distance) restraints (SAME in Shelxl), enhanced rigid-bond restraints (RIGU in Shelxl) and restraints for approximately isotropic behaviour (ISOR in Shelxl) applied to the ADPs, and equal ADP constraints (EADP in Shelxl) applied to some atom pairs (C44 – C44').

The toluene molecule C45...C51 was disordered over two positions with 0.58(3):0.42(3) occupancy ratio. Its phenyl ring was refined as a rigid body (AFIX 66/65 in Shelxl). The methyl group was refined using bond distance restraints (DFIX) and 1,3-distance restraints (SADI in Shelxl). Enhanced rigid-bond restraints (RIGU in Shelxl) and restraints for approximately isotropic behaviour (ISOR in Shelxl) were applied to the ADPs. The toluene molecule C52...C58 was disordered over two positions with 0.59(2):0.41(2) occupancy ratio. Its phenyl ring was refined as a rigid body (AFIX 66/65 in Shelxl). The methyl group was refined using bond

distance restraints (DFIX) and 1,3-distance restraints (SADI in Shelxl). Enhanced rigid-bond restraints (RIGU in Shelxl), restraints for approximately isotropic behaviour (ISOR in Shelxl), and restraints for similar ADPs for spatially close atoms (SIMU in Shelxl) were applied to the ADPs. The structure had some high residual density peaks: 6.02 $e \cdot Å^{-3}$ at 1.63 Å from H1, 5.86 $e \cdot Å^{-3}$ at 2.00 Å from H13, 5.82 $e \cdot Å^{-3}$ at 1.84 Å from H30. The deepest hole is -2.27 $e \cdot Å^{-3}$ at 1.53 Å from H2.

Infrared Spectroscopy. Infrared spectra were performed with a Varian 640 FTIR spectrometer equipped with an ATR in the 4000 cm^{-1} to 600 cm^{-1} range.

Magnetic measurements. Magnetic susceptibility measurements were performed using an MPMS-XL7 Quantum Design SQUID magnetometer. Direct current (dc) susceptibility measurements were performed at temperatures ranging from 1.9 to 300 K and performed on a crushed polycrystalline sample of 24.2 (**1**) and 17.3 mg (**2**), wrapped in a polyethylene membrane. Alternating current (ac) susceptibility measurements were performed under an oscillating ac field of 3.78 Oe and ac frequencies ranging from 0.1 to 1488 Hz. Magnetization vs. field measurements were performed at 100 K in order to check for the presence of ferromagnetic impurities, which were found to be absent. The magnetic data was corrected for diamagnetic contributions using Pascal's constants.

5.10 **References**

(1) R. Sessoli, D. Gatteschi, A. Caneshi, M. A. Novak, *Nature*, 1993, **365**, 141-143.

(2) A. J. Tasiopoulous, A. Vinslava, W. Wernsdorfer, K. A. Abboud, G. Christou, *Angew. Chem. Int. Ed.*, 2004, **43**, 2117-2121.

(3) M. Murrie, S. J. Teat, H. Stoeckli-Evans, H. U. Güdel, *Angew. Chem. Int. Ed.*, 2003, **42**, 4653-4656.

(4) C. J. Milios, A. Vinslava, W. Wernsdorfer, S. Moggach, S. Parsons, S. P. Perlepes, G. Christou, E. K. Brechin, *J. Am. Chem. Soc.*, 2007, **129**, 2754-2755.

(5) A. L. Barra, A. Caneschi, A. Cornia, F. Fabrizi de Biani, D. Gatteschi, C. Sangregorio, L. Sorace, *J. Am. Chem. Soc.*, 1999, **121**, 5302-5310.

(6) C.-I. Yang, W. Wernsdorfer, G.-H. Lee, H.-L. Tsai, *J. Am. Chem. Soc.*, 2007, **129**, 456-457.

(7) Y.-Y. Zhu, C. Cui, K. Qian, J. Yin, B.-W. Wang, Z.-M. Wang, S. Gao, *Dalton Trans.*, 2014, **43**, 11897-11907.

(8) A. Cornia, A. C. Fabretti, P. Garrisi, C. Mortalo, D. Bonacchi, D. Gatteschi, R. Sessoli, L. Sorace, W. Wernsdorfer, A.-L. Barra, *Angew. Chem. Int. Ed.*, 2004, **43**, 1136-1139.

(9) L. F. Jones, M. E. Cochrane, B. D. Koivisto, D. A. Leigh, S. P. Perlepes, W. Wernsdorfer, E. K. Brechin, *Inorg. Chim. Acta*, 2008, **361**, 3420-3426.

(10) O. Waldmann, *Inorg. Chem.*, 2007, **46**, 10035-10037.

(11) H. Oshio, N. Hoshino, M. Nakano, *J. Am. Chem. Soc.*, 2004, **126**, 8805-8812.

(12) C. A. P. Goodwin, F. Ortu, D. Reta, N. F. Chilton, D. P. Mills, *Nature*, 2017 **548**, 439-442.

(13) L. Norel, L. E. Darago, B. Le Guennic, K. Chakarawet, M. I. Gonzalez, J. H. Olshansky, S. Rigaut, J. R. Long, *Angew. Chem. Int. Ed.*, 2018, **130**, 1951-1956.

(14) F.-S. Guo, B. M. Day, Y.-C. Chen, M.-L. Tong, A. Mansikkamaki, R. A. Layfield, *Angew. Chem. Int. Ed.*, 2017, **56**, 11445-11449.

(15) S. Demir, M. I. Gonzalez, L. E. Darago, W. J. Evans, J. R. Long, *Nat. Commun.*, 2017, **8**, 2144.

(16) J. Long, F. Habib, P.-H. Lin, I. Korobkov, G. Enright, L. Ungur, W. Wernsdorfer, L. F. Chibotaru, M. Murugesu, *J. Am. Chem. Soc.*, 2011, **133**, 5319-5328.

(17) F. Habib, G. Brunet, V. Vieru, I. Korobkov, L. F. Chibotaru, M. Murugesu, *J. Am. Chem. Soc.*, 2013, **135**, 13242-13245.

(18) H. Ke, P. Gamez, L. Zhao, G.-F. Xu, S. Xue, J. Tang, *Inorg. Chem.*, 2010, **49**, 7549-7557.

(19) Y. L. Miao, J.-L. Liu, J.-Y. Li, J.-D. Leng, Y.-C. Ou, M.-L. Tong, *Dalton Trans.*, 2011, **40**, 10229-10236.

(20) X. Yi, K. Bernot, G. Calvez, C. Daiguebonne, O. Guillou, *Eur. J. Inorg. Chem.*, 2013, **34**, 5879-5885.

(21) M. A. Lemes, H. N. Stein, B. Gabidullin, K. Robeyns, R. Clérac, M. Murugesu, *Chem. Eur. J.*, 2018, **24**, 4259-4263.

(22) S. K. Tripathy, M. van der Meer, A. Sahoo, P. Laha, N. Dehury, S. Plebst, B. Sarkar, K. Samanta, S. Patra, *Dalton Trans.*, 2016, **46**, 12532-12538.

(23) S. Demir, J. M. Zadrozny, M. Nippe, J. R. Long, *J. Am. Chem. Soc.*, 2012, **134**, 18546-18549.

(24) J. D. Rinehart, M. Fang, W. J. Evans, J. R. Long, *Nat. Chem.*, 2011, **3**, 538-542.

(25) X. Ma, E. A. Suturina, S. De, P. Négrier, M. Rouzières, R. Clérac, P. Dechambenoit, *Angew. Chem. Int. Ed.*, 2018, **57**, 7841-7845.

(26) M. A. Lemes, A. Pialat, S. N. Steinmann, I. Korobkov, C. Michel, M. Murugesu, *Polyhedron*, 2016, **108**, 163-168.

(27) K. S. Pedersen, L. Ungur, M. Sigrist, A. Sundt, M. Schau-Magnussen, V. Vieru, J. Mutka, S. Rols, H. Weihe, O. Waldmann, L. F. Chibotaru, J. Bendix, J. Dreiser, *Chem. Sci.*, 2014, **5**, 1650-1660.

(28) S. K. Langley, L. Ungur, N. F. Chilton, B. Moubaraki, L. F. Chibotaru, K. S. Murray, *Inorg. Chem.*, 2014, **53**, 4303-4315.

(29) Y. Jiang, G. Brunet, R. J. Holmberg, F. Habib, I. Korobkov, M. Murugesu, *Dalton Trans.*, 2016, **45**, 16709-16715.

(30) G. Cucinotta, M. Perfetti, J. Luzon, M. Etienne, P.-E. Car, A. Caneschi, G. Calvez, K. Bernot, R. Sessoli, *Angew. Chem.*, 2012, **124**, 1638-1642.

(31) V. Vieru, N. Iwahara, D. Komijani, S. Hill, W. Wernsdorfer, L. F. Chibotaru, *J. Phys. Chem. C*, 2018, **122**, 11128-11135.

(32) P. Abbasi, K. Quinn, D. I. Alexandropoulos, M. Damjanovic, W. Wernsdorfer, A. Escuer, J. Mayans, M. Pilkington, T. C. Stamatatos, *J. Am. Chem. Soc.*, 2017, **139**, 15644-15647.

(33) T. Lacelle, G. Brunet, R. J. Holmberg, B. Gabidullin, M. Murugesu, *Cryst. Growth Des.*, 2017, **17**, 5044-5048.

(34) M. A. Lemes, G. Brunet, A. Pialat, L. Ungur, I. Korobkov, M. Murugesu, *Chem. Commun.*, 2017, **53**, 8660-8663.

(35) B. S. Dolinar, D. I. Alexandropoulos, K. R. Vignesh, T. James, K. R. Dunbar, *J. Am. Chem. Soc.*, 2018, **140**, 908-911.

(36) D. I. Alexandropoulos, B. S. Dolinar, K. R. Vignesh, K. R. Dunbar, *J. Am. Chem. Soc.*, 2017, **139**, 11040-11043.

(37) T. J. Woods, M. F. Ballesteros-Rivas, S. M. Ostrovsky, A. V. Palii, O. S. Reu, S. I. Klokishner, K. R. Dunbar, *Chem. – Eur. J.*, 2015, **21**, 10302-10305.

(38) D. Casanova, M. Llunell, P. Alemany, S. Alvarez, *Chem. – Eur. J.*, 2005, **11**, 1479-1494.

(39) P. Zhang, M. Perfetti, M. Kern, P. P. Hallman, L. Ungur, S. Lenz, M. R. Ringenberg, W. Frey, H. Stoll, G. Rauhut, J. van Slageren, *Chem. Sci.*, 2018, **9**, 1221-1230.

(40) J. D. Rinehart, M. Fang, W. J. Evans, J. R. Long, *J. Am. Chem. Soc.*, 2011, **133**, 14236-14239.

(41) B. S. Dolinar, S. Gómez-Coca, D. I. Alexandropoulos, K. R. Dunbar, *Chem. Commun.*, 2017, **53**, 2283-2286.

(42) F.-S. Guo, R. A. Layfield, *Chem. Commun.*, 2017, **53**, 3130-3133.

(43) Y.-N. Guo, G.-F. Xu, W. Wernsdorfer, L. Ungur, Y. Guo, J. Tang, H.-J. Zhang, L. F. Chibotaru, A. K. Powell, *J. Am. Chem. Soc.*, 2011, **133**, 11948-11951.

(44) I. Oyarzabal, J. Ruiz, J. M. Seco, M. Evangelisti, A. Camon, E. Ruiz, D. Aravena, E. Colacio, *Chem. – Eur. J.*, 2014, **20**, 14262-14269.

(45) H. Y. Wong, W. T. K. Chan, G.-L. Law, *Inorg. Chem.*, 2018, **57**, 6893-6902.

(46) C.-B. Han, Y.-L. Wang, Y.-L. Li, C.-M. Liu, Q.-Y. Liu, *Inorg. Chem. Commun.*, 2015, **58**, 91-94.

(47) C.-M. Liu, D.-Q. Zhang, X. Hao, D.-B. Zhu, *Cryst. Growth Des.*, 2012, **12**, 2948-2954.

(48) N. F. Chilton, D. Collison, E. J. L. McInnes, R. E. P. Winpenny, A. Soncini, *Nat. Commun.*, 2013, **4**, 2551.

(49) M. D. Coburn, G. A. Buntain, B. W. Harris, M. A. Hiskey, K-Y. Lee, D. G. Ott, *J. Heterocycl. Chem.*, 1991, **28**, 2049-2050.

(50) V. I. Belyi, A. A. Rastorguev, A. A. Remova, G. V. Romanenko, N. P. Sokolova, *J. Struct. Chem.*, 2004, **45**, 130-138.

(51) G. A. Crosby, M. Kasha, *Spectrochim. Acta*, 1958, **10**, 377-382.

(52) Bruker. APEX2, Bruker AXS Inc., Madison, Wisconsin, USA (2012).

(53) Bruker. SADABS, Bruker AXS Inc., Madison, Wisconsin, USA (2003).

(54) G. M. Sheldrick, *Acta Cryst.*, 2015, **A71**, 3-8.

(55) L. J. Farrugia, *J. Appl. Cryst.*, 1999, **32**, 837-838.

(56) L. J. Farrugia, *J. Appl. Cryst.*, 2012, **45**, 849-854.

(57) A. L. Spek, *Acta. Cryst.*, 2015, **C71**, 9-18.

5.11 **Submitted contributions**

A barrel-shaped metal-organic Blue-Box analog with photo-/redox-switchable behaviour

G. Brunet, E. A. Suturina, G. P. C. George, J. S. Ovens, C. Bucher and M. Murugesu

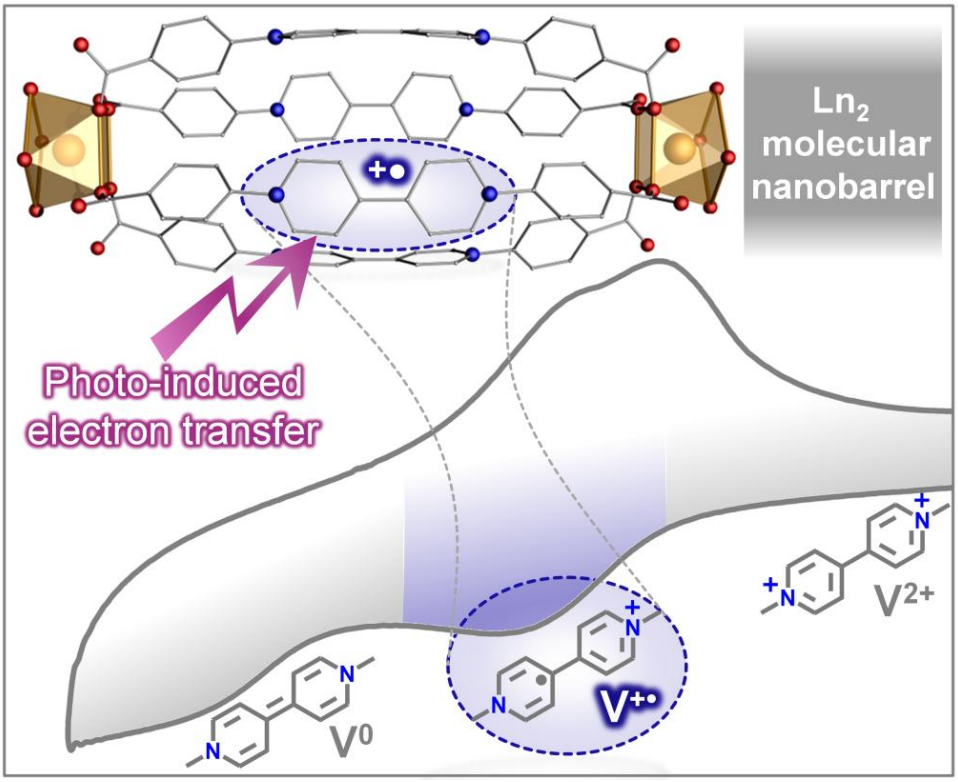

G. Brunet, C. Bucher and M. Murugesu wrote the manuscript. G. Brunet performed the majority of the experiments. G. P. C. George assisted with the synthesis of the organic ligand.

J. S. Ovens was responsible for the refinement of the single-crystal X-ray diffraction data.

E. A. Suturina performed the DFT calculations.

5.12 **Abstract**

Donor acceptor interactions are ubiquitous in the design and understanding of host-guest complexes. Despite their non-covalent nature, they can readily dictate the self-assembly of complex architectures. Here, we present a photo-/redox-switchable metal-organic nanocapsule, assembled using lanthanide ions and viologen building blocks, that relies on such donor-acceptor interactions. We highlight the potential of this unique barrel-shaped structure for the encapsulation of suitable electron donors, akin to the well-investigated "blue-box" macrocycles. The light-triggered reduction of the viologen units has been investigated by single-crystal-to-single-crystal X-ray diffraction experiments, complemented by magnetic, optical and solid-state electrochemical characterizations. Density functional theory (DFT) calculations were employed to suggest the most likely electron donor in the light-triggered reduction of the viologen-based ligand.

5.13 **Introduction**

The biology of living systems provides some of the most complex, yet efficient examples of how external stimuli can be used to trigger desired responses. Such cause and effect mechanisms rely on critical changes that occur at the molecular-scale, as a result of variations in external factors such as temperature, pressure or pH. In this regard, large polynuclear metal clusters have attracted significant attention over the last few years, due to their structural similarities to biologically active sites that control physiological responses.[1-3] The design of stimuli-responsive metal-organic supramolecular architectures has recently become a highly desirable,[4-15] yet challenging task, in part due to the ability to establish key structure-property relationships, useful to the development of biomimetic systems. More importantly, such molecules offer the potential to provide access to

"smart" molecular materials with increased functionality and utility in a variety of different fields, including that of catalysis,[16,17] magnetism,[18-21] sensing and electronics.[22-25]

The bottom-up strategy that we have been exploring over the past few years to gain access to stimuli-responsive functional metal-organic assemblies hinges on the design and implementation of advanced building blocks with enhanced size and complexity.[26-31] In line with these ambitious objectives, we are now reporting on our approach towards discrete photo-/redox-responsive metal-organic nanocapsules built from lanthanide ions and 4,4'-bipyridinium-based organic linkers. Our main goal here was to achieve a directed assembly of two lanthanide ions, selected for their large radius and high coordination numbers (≥8), with four stimuli-responsive electron-poor bridging organic ligands, so as to provide access to discrete cavitand-like structures with unique magnetic and/or molecular recognition properties. We anticipated that such metal-organic barrel-shaped structures could prove useful either as key precursors in the formation of larger polymeric assemblies or as discrete compounds, to achieve a redox-controlled encapsulation of electron-rich guests. In addition, this strategy could potentially enable the investigation of magnetic entanglement effects between two lanthanide ions mediated by redox-active ligands.[32-35] Along the same lines, the redox-controlled encapsulation of different guest molecules could also play a key role in defining the magnetic characteristics of the complex.

The 4,4'-bipyridinium-based organic linkers, better known as viologens ($\mathbf{V}^{2+}$), have been selected for their remarkable and well-defined redox-activity, wherein two consecutive Nernstian electron transfer processes can occur, leading to the successive

formation of a radical-cation ($\mathbf{V}^{+\bullet}$), and a neutral quinonic species ($\mathbf{V}^{0}$).[36-40] Further attractive features of viologen-based ligands include an outstanding stability of the cation radical state ($\mathbf{V}^{+\bullet}$) and an ability of most electron-acceptor $\mathbf{V}^{2+}$ derivatives to form stable charge transfer complexes with a wide range of electron donors.[41,42] One of the most well-known representative examples of this class of compound is the so-called "blue box" macrocycle, that features two viologen units held in a cofacial arrangement through paraxylene linkers. The prominence of such molecular arrangements is closely tied to Stoddart's achievements in the field of molecular machines and mechanically interlocked molecules.[43,44]

Building upon our previous achievements on air-stable radical-bridged complexes for probing magnetic exchange interactions,[34,45,45] we sought to devise a series of functional metal-organic architectures incorporating stimuli-responsive organic linkers displaying at least two accessible/stable redox states. Our efforts have focused on 1,1'-bis(4-carboxyphenyl)-(4,4'bipyridinium) dichloride (H_2bcbp·2Cl), which features two coordinating carboxylate moieties at each end of the molecule, to promote either the formation of high dimensionality coordination networks or extended nanocapsules upon metal coordination. As part of these ongoing efforts, we found that this rigid viologen-based ligand reacts with Dy^{III} cations to yield the discrete and highly symmetrical viologen-based metal-organic assembly $[Dy_2(bcbp)_4(H_2O)_8]Cl_6 \cdot H_2O$ (**1**) depicted in Figure 46.

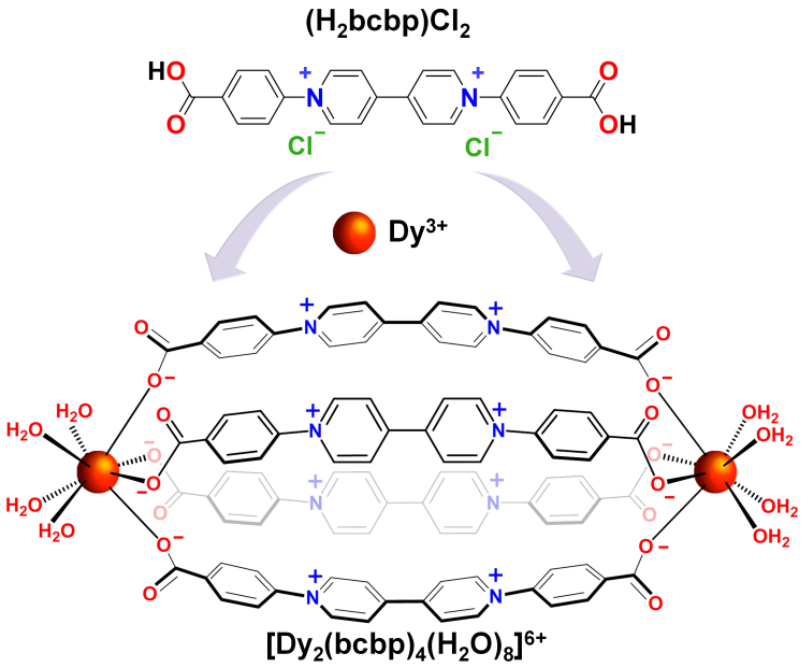

Figure 46. Schematic representation of the $(H_2bcbp)^{2+}$ ligand and of the title barrel-shaped dysprosium-viologen assembly.

5.14 **Structural details**

The complex **1** was synthesized by reacting $Dy(NO_3)_3 \cdot 6H_2O$ with $(H_2bcbp)Cl_2$ in a solvent mixture of DMF/MeCN/H_2O under slightly acidic solvothermal conditions. The resulting yellow plate monocrystals were isolated after slow cooling. The molecular structure, determined by single-crystal X-ray diffraction (Table 19), belongs to the tetragonal *I*4/*m* space group and reveals an unprecedented barrel-shaped nanocapsular arrangement. The staves of the barrel are represented by four bent $bcbp^{2-}$ ligands, the heads are comprised of two crystallographically equivalent Dy^{III} ions separated by 21.44 Å, and the hoops can be thought of the carboxylic acid moieties (Fig. 47). The charge of each discrete cationic $[M_2L_4]^{6+}$ barrel is balanced by six chloride anions; two of them (Cl2 and Cl3) are confined within the molecular cage (Fig. 47C), while another is found between the barrels (Cl1). The remaining Cl^- anions are generated by symmetry

operations within the molecule. Each Dy^{III} ion is coordinated by 8 oxygen atoms brought by 4 carboxylate moieties and by 4 water molecules acting as stoppers at both ends of the assembly.

Table 19: Crystal data and structure refinement.

Compound	**1**	**1'**	**2**	**2'**
Formula	$C_{96}H_{92}Cl_6Dy_2N_8O_{25}$	$C_{96}H_{92}Cl_6Dy_2N_8O_{25}$	$C_{96}H_{92}Cl_6N_8O_{25}Y_2$	$C_{96}H_{92}Cl_6N_8O_{25}Y_2$
FW (g mol^{-1})	2295.47	2295.47	2148.29	2148.29
Crystal color	yellow	green	yellow	green
Crystal system	Tetragonal	Tetragonal	Tetragonal	Tetragonal
Space group	*I*4/*m*	*I*4/*m*	*I*4/*m*	*I*4/*m*
Temperature (K)	296(2)	296(2)	204(2)	204(2)
a (Å)	12.719(3)	12.5784(8)	12.5122(5)	12.503(6)
b (Å)	12.719(3)	12.5784(8)	12.5122(5)	12.503(6)
c (Å)	29.303(7)	28.987(2)	29.0263(14)	28.791(17)
α (°)	90	90	90	90
β (°)	90	90	90	90
γ (°)	90	90	90	90
V (Å^3)	4741(3)	4586.2(7)	4544.2(4)	4501(5)
Z	2	2	2	2
μ (mm^{-1})	1.814	1.875	1.532	1.532
Refl. coll. / unique	18213/3116	25516/2915	1228/711	1228/792
Goodness-of-fit	1.091	1.124	1.343	1.096
[a]$R_1(I > 2\sigma(I))$	0.0554	0.0542	0.1060	0.0898
[b]wR_2 (all data)	0.1574	0.1651	0.3488	0.2352

[a]$R_1 = \Sigma||F_0| - |F_C||/\Sigma|F_0|$ and [b]$wR_2 = [\Sigma w(F_0^2 - F_C^2)^2/\Sigma w(F_0^2)^2]^{1/2}$

At first glance, due to the four-fold symmetry of the complex, a nearly perfect square antiprismatic (SAP) geometry is observed, with angles within each square equal to the ideal 45°. The coordination sphere of the lanthanide ion was then investigated by SHAPE analysis, revealing a slightly distorted SAP geometry (Table 20).[47] Upon further inspection, the distortion is induced by a slight contraction of the SAP environment, highlighted by the distance between the upper and lower planes containing the four oxygen atoms (d_{pp} = 2.47 Å) and the average distance between the oxygen atoms within each plane (d_{in} = 2.89 Å). Such deviations from an

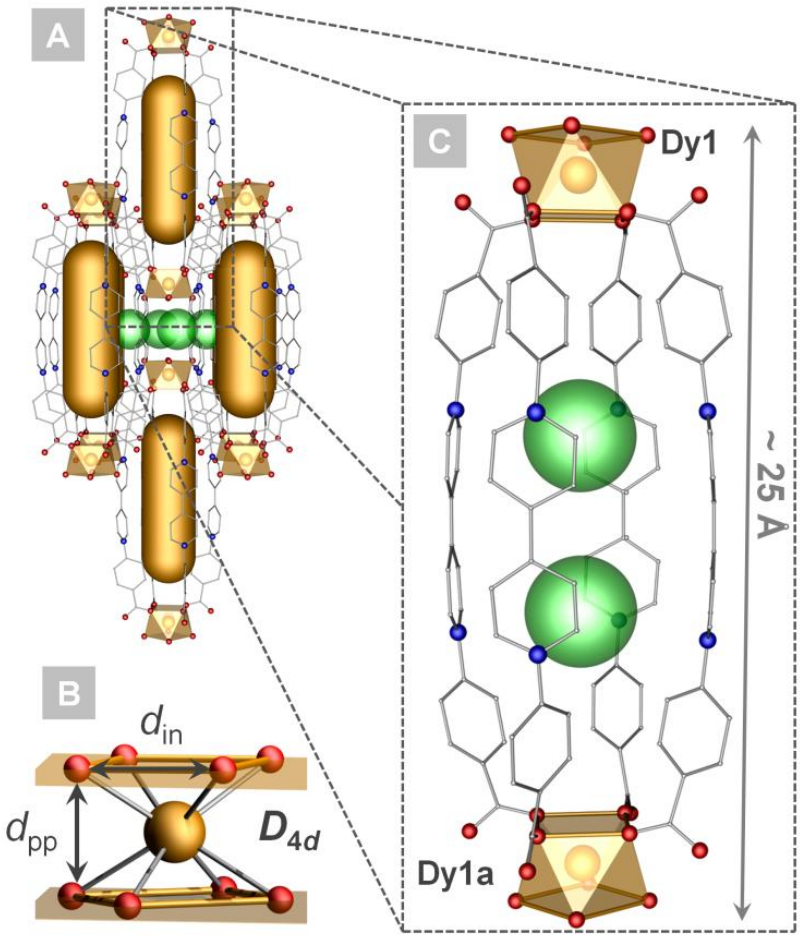

Figure 47. Packing arrangement of **1** along the *a*-axis, highlighting the cylindrical void space of the nanocapsule (A). The square antiprismatic geometry of the Dy^{III} ions (B), is shown alongside the molecular structure of the nanobarrel displaying encapsulated chloride anions (C). Selected chloride counter-anions, uncoordinated water molecules and hydrogen atoms have been omitted for clarity. Color code: Dy^{III}–orange, Cl-green, O-red, N-blue, and C-gray vertices.

ideal D_{4d} symmetry are expected to have a significant impact on the slow magnetic relaxation dynamics of the Dy^{III} ions (*vide infra*). In addition to the aforementioned four-fold symmetry, there is an inversion centre that lies in the middle of the void space of the capsule, making the overall structure highly symmetrical in nature. The internal area of **1** has been estimated using the SQUEEZE routine of PLATON,[48] revealing a void space of approximately 159 $Å^3$ and containing 64 electrons. These numbers are in good agreement with a structural model in which

Table 20: SHAPE constants for the Dy^{III} centre in 1. The lowest SHAPE constant is bolded.

SHAPE code	Point Group	Description	Dy1
OP-8	D_{8h}	Octagon	26.80502
HPY-8	C_{7v}	Heptagonal pyramid	24.46554
HBPY-8	D_{6h}	Hexagonal bipyramid	15.84706
CU-8	O_h	Cube	8.13960
SAPR-8	D_{4d}	Square antiprism	**0.32248**
TDD-8	D_{2d}	Triangular dodecahedron	2.33068
JGBF-8	D_{2d}	Johnson gyrofastigium J26	16.25168
JETBPY-8	D_{3h}	Johnson elongated triangular bipyramid J14	28.78826
JBTPR-8	C_{2v}	Biaugmented trigonal prism J50	3.05459
BTPR-8	C_{2v}	Biaugmented trigonal prism	2.15309
JSD-8	D_{2d}	Snub diphenoid J84	5.41050
TT-8	T_d	Triakis tetrahedron	9.01541
ETBPY-8	D_{3h}	Elongated trigonal bipyramid	23.68164

total of two Cl^- anions and two H_2O molecules can be encapsulated simultaneously within the nanocapsule. The Cl^- anions occupy two distinct positions within the capsule (Cl2 and Cl3) and the shortest distance measured between the center of a pyridinium ring and an offset chloride anion (Cl3) reaches 3.54 Å. This value is consistent with other viologen-halide distances found in literature.[49-53] On the other hand, the Cl2 atom is found lying at the centre of the capsule, at an equal distance (4.24 Å) to all viologen ligands. It appears that the cavity of **1** is ideally suited to Cl^-; all attempts to synthesize the Br^- and I^- analogs were unsuccessful. This may be due to size constraints within the capsule as we move towards larger halides (ionic radii of 1.67, 1.82 and 2.06 Å, for Cl^-, Br^- and I^-, respectively). On a larger scale, each of the nanocapsules are aligned parallel to one another, separated by a network of Cl^- anions (Fig. 47A). The nearest intercapsular Dy–Dy distance is 7.86 Å, where terminally coordinated H_2O molecules exhibit van der Waals and hydrogen-bonding interactions with the Cl^- anions to fill the gaps between the lanthanide ions (Fig. 48).

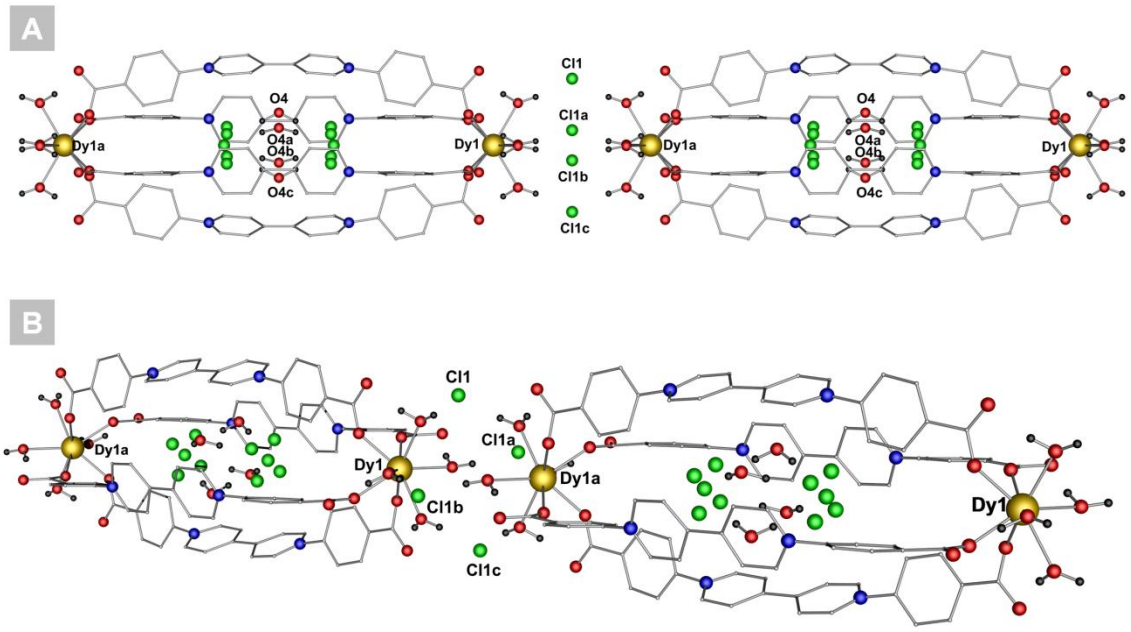

Figure 48. Packing arrangement of 1 displaying encapsulated Cl^- and H_2O molecules, as well as interbarrel Cl^- anions.

5.15 **Reduction of the nanobarrel**

The presence of four viologen-based ligands led us to explore the redox properties of **1**. We found that viologen radicals ($\mathbf{V^{+\bullet}}$) can be generated post-synthetically, within the crystal, in response to different environmental stimuli such as light, temperature or to selected chemical reducing agents. In all cases, the formation of $\mathbf{V^{+\bullet}}$ was easily revealed by a drastic color change of the single crystals, going from yellow to green, upon application of external stimuli (Fig. 49). The use of heat or chemical reducing agents, such as sodium dithionite, was found to trigger this change in color; however, this was unfortunately also accompanied by a loss in crystallinity of the single-crystals. On the other hand, when subjected to UV irradiation, the single-crystals retained crystallinity allowing for single-crystal-to-single-crystal X-ray diffraction measurements to be carried out, while also displaying a similar change in color (Fig. 49). The more mild nature of UV

irradiation, compared to chemical reduction or heat, allows the retention of crystallinity, even if less radicals are likely to be generated.[54,55] The structures of the photochemically reduced nanocapsules, wherein at least part of the $\mathbf{V^{2+}}$ units have been converted into the one electron reduced $\mathbf{V^{+\bullet}}$ have been retained, yet examination of some key bond lengths suggests the presence of viologen-based radicals (Fig. 49). To further confirm this, we have synthesized the diamagnetic yttrium analog (**2**), whose solid-state structure was identical to that of **1** (Table 19). The reduced structures of both Dy^{III} (**1'**) and Y^{III} (**2'**) analogs have been successfully elucidated using this strategy.

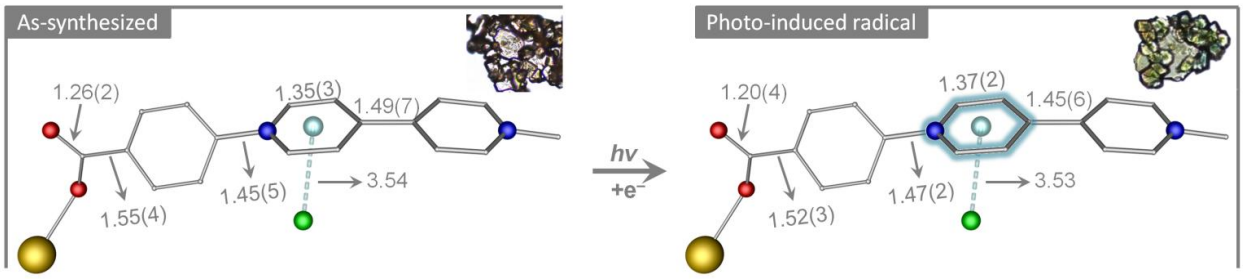

Figure 49. Comparison of the bond distances found in the as-synthesized and radical form of the viologen ligand in compounds **2** and **2'**, respectively. Optical microscopy pictures display the change in color of the crystals upon UV irradiation. Bond distances are denoted in Ångtröms. Color code: N-blue, Cl-green, Dy-yellow, O-red and C-gray vertices.

The maximum number of $\mathbf{V^{+\bullet}}$ species generated per capsule will in any case be limited by the number of electron donors available in the sample (possible mechanisms are discussed in the following section). These restrictions, taken together with the experimental data collected for **1'** and **2'**, led us to the conclusion that only a limited proportion of viologens end up being reduced in the crystals, as observed in other similar photoreduced systems.[54,55] The X-ray data collected after irradiation thus correspond to an average picture taking into account the ratio between reduced and non reduced viologens

in the four-order symmetry barrel-shaped structures. Still, we found that irradiation of **2** results in a significant shortening of the central C-C bond length from 1.49(7) to 1.45(6) Å. A shorter distance is a diagnostic feature of viologen radicals due to the delocalization of the single electron over both pyridinium rings.[56,57] The crystal structure of **1** before and after irradiation features almost the same central C-C bond length of 1.55(4) to 1.54(5) Å, respectively. There is also a pronounced shortening of the non-coordinated C-O bond length in the carboxylate fragment upon irradiation, from 1.26(2) Å to 1.204(17) Å in **2**, and 1.237(9) to 1.211(9) Å in **1**, as well as shortening of the C-COO^- bond from 1.55(4) to 1.52(3) Å in **2**, and 1.53(2) to 1.47(2) in **1**. These changes contribute to a slight contraction of the unit cell dimensions along the *a*- and *b*-axes (from 12.72 to 12.58 Å in **1** and from 12.51 to 12.50 Å in **2**), as well as along the *c*-axis (from 29.30 to 28.99 Å in **1**, and from 29.03 to 28.79 Å in **2**). The contraction along the *a*- and *b*-axes in **1** is in part associated with closer interactions between non-encapsulated Cl^- anions (Cl1) and the middle C atom of the ligand (changing from 3.60 to 3.57 Å), while it does not vary significantly in **2**. The distance between the encapsulated Cl^- anions (Cl3) and the pyridinium ring also shortens from 3.54 to 3.47 Å in **1**, and 3.54 to 3.53 Å in **2**.

To unequivocally confirm the presence of organic radicals within the crystals, we collected room-temperature electron paramagnetic resonance (EPR) spectra of the as-synthesized (**1** and **2**) and reduced capsules (**1'** and **2'**). The EPR spectra of the photochemically reduced compounds display a signal centered at g = 2.0025, consistent with the presence of viologen-based radicals (Fig. 50). Interestingly, the use of a chemical reducing agent yields a much stronger EPR signal, while maintaining an identical g value (Fig. 50C). This provides some insight into the number of radicals being generated when

reducing the nanocapsules through either UV irradiation or chemical reduction. While the EPR signal is drastically enhanced following chemical reduction, this process results in significant cracking and loss of crystallinity in the single-crystals, precluding single-crystal-to-single-crystal studies.

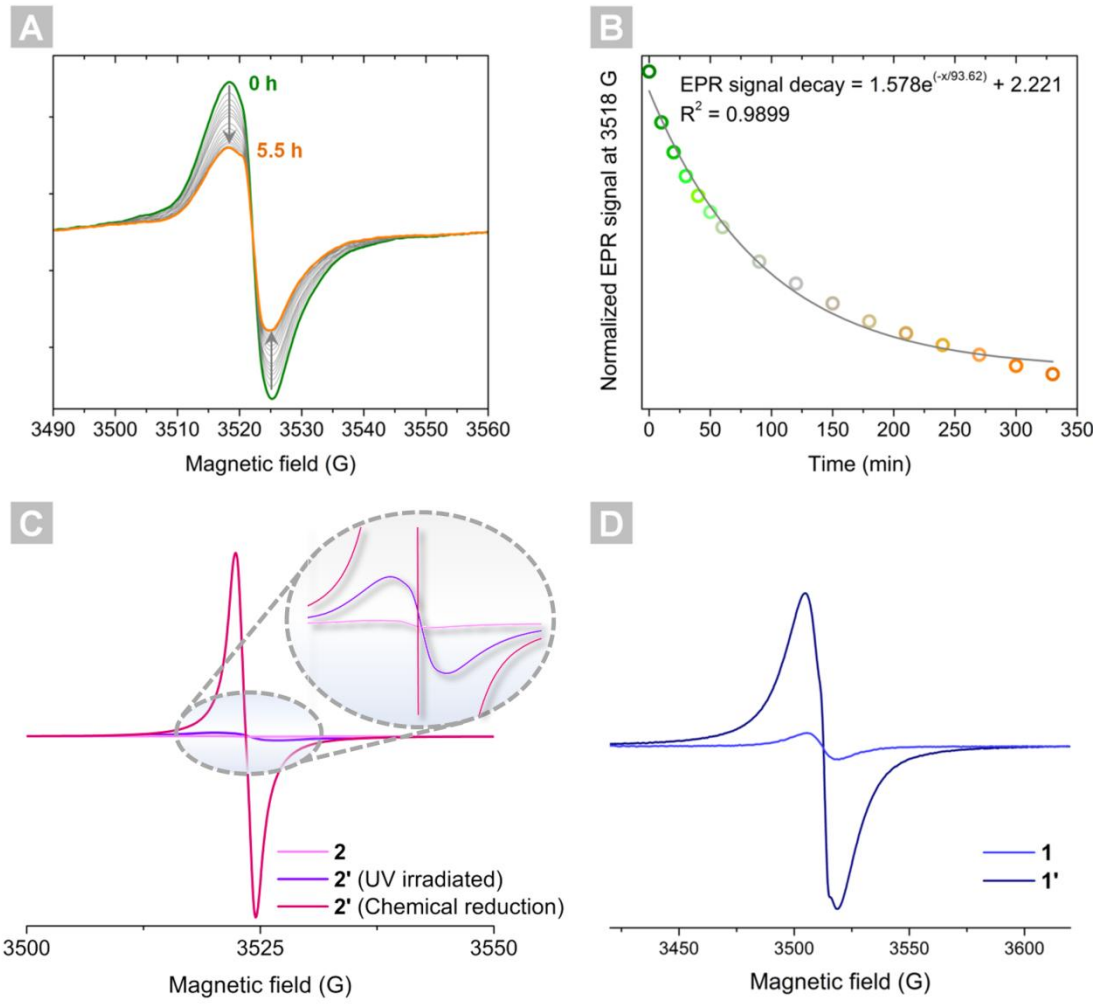

Figure 50. Time-dependent EPR data of a UV irradiated sample of **2**, measured over 5.5 hours at room temperature, revealing the gradual loss of photogenerated radicals over time (A). The kinetics of this process can be described by a first-order exponential decay function (B). Comparison of the EPR signal obtained from the as-synthesized, UV irradiated and chemically reduced nanocapsules (C). Solid-state EPR spectra of **1** and **1'** (UV irradiated) collected at room temperature (D).

The as-synthesized compounds also display an EPR signal, albeit much weaker than the irradiated samples, and is nearly impossible to distinguish when compared to the chemically

reduced compound, suggesting that ambient UV light likely reduces the structures of **1** and **2**. To investigate the stability of the photo-induced radicals, time-dependent EPR spectra were collected on **2'** over a period of 5.5 hours. We observe a clear decrease in the EPR signal over time, indicating the reversibility of the reduction process (Fig. 50A). The kinetics of this process was studied by examining the EPR signal at 3518 G, from which a first-order exponential equation was found to suitably reproduce the data (Fig. 50B).

5.16 **Mechanism of radical formation**

There are two possible explanations for the observed photochromic behaviour: (i) intermolecular electron transfer (from either Cl^- or H_2O) that changes the total charge of the ligand from 0 to -1, yielding $\mathbf{V^{+\bullet}}$ radical cations,[50,56] or (ii) intramolecular electron transfer from the carboxylic acid to the viologen moiety, resulting in a neutral bcbp ligand with two radical centres (one on the carboxylic acid, $COO^{\bullet}$, and one on the pyridinium moiety, $\mathbf{V^{+\bullet}}$)**.**[57] The former situation leads to spin density only on the pyridinium group, while the latter yields spin density on both the carboxylic acid and pyridinium groups, given the fact that two radical sites per ligand would be formed. Density functional theory (DFT) calculations carried out on the singlet and triplet states of the neutral bcbp ligand with a $\mathbf{V^{2+}}$ fragment, as well as the reduced $bcbp^{-\bullet}$ ligand show that both reduced and triplet states adopt shorter central C-C bonds than $\mathbf{V^{2+}}$ in the singlet state. However, the $C\text{-}COO^-$ bond gets shorter in the triplet state, while reduction leads to its elongation (Fig. 51).

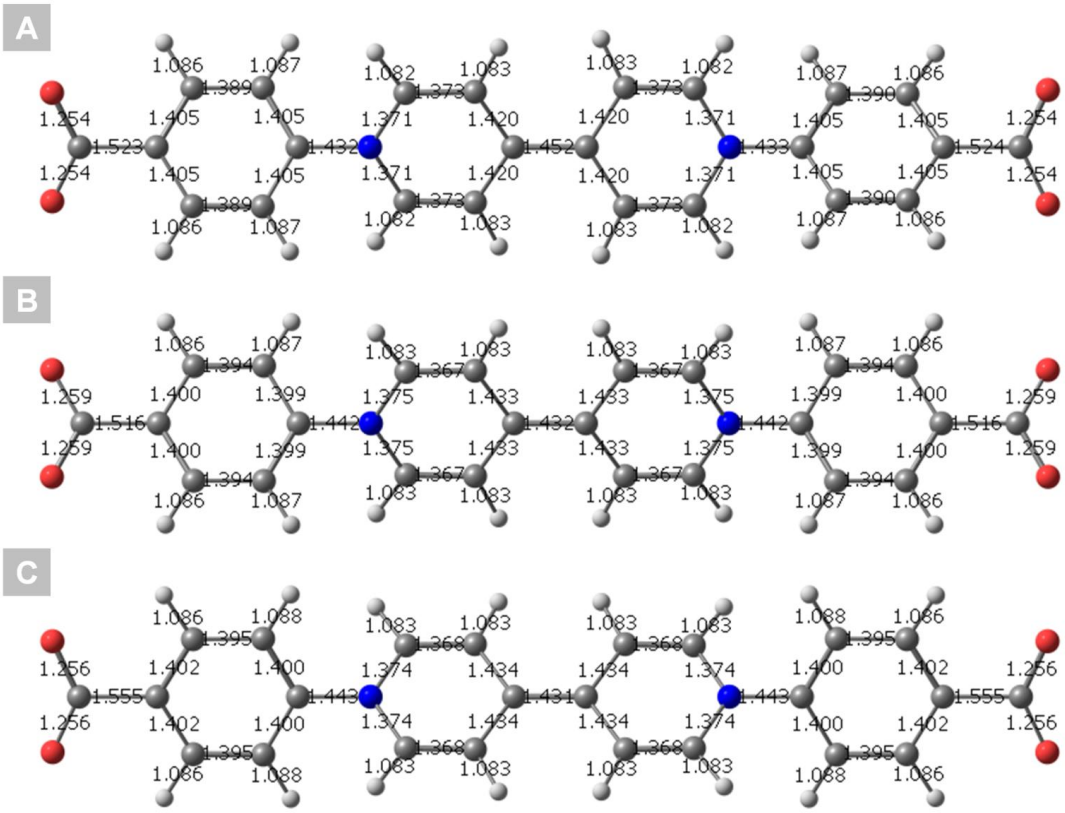

Figure 51. Optimised geometry of the neutral bcbp ligand in the singlet state (A), triplet state (B) and the reduced radical cation state (C).

Spin density distribution highlights the difference between two scenarios: in the case of an intermolecular electron transfer leading to the formation of a $\mathbf{V}^{+\bullet}$ radical-containing species, the spin density is localized almost solely on the viologen fragment, whereas the triplet state of the neutral ligand features spin density on both the carboxylate and the bypiridinium fragments (Fig. 52). It appears to be very difficult to unambiguously state whether the radical formation on the viologen fragments are associated to an intermolecular reduction mechanism or if it is a result of excitation to the triplet state of the ligand, as no information on the carboxylate group spin density is available from the experiment. In an attempt to test whether the encapsulated Cl^- anions or water molecules are likely to reduce the capsule, the lowest energy triplet and quintet states of the

$[H_2O,Cl_2@[Y_2(bcbp)_4(H_2O)_8]]^{4+}$ complex were optimized using the HF-3c method in ORCA.[59,60] Mulliken spin population of the encapsulated Cl^- and H_2O molecules is close to zero in both cases, suggesting that, at first instance, the carboxylate groups are likely to act as electron donors rather than the encapsulated Cl^- anions. Nevertheless, previous studies have established the ability of halides to act as electron donors for viologen-based ligands.[49,61,62] It is also interesting to note that despite the higher electronegativity of Cl compared to Br and I, they may provide more stable excited-state species. An extended model, where intermolecular Cl^- anions are also considered, indicates that the lowest triplet state of the capsule corresponds to the formation of intercapsular $Cl^{\bullet}$ radicals and $\mathbf{V}^{+\bullet}$. The reactivity of these radicals is the subject of further computational studies.

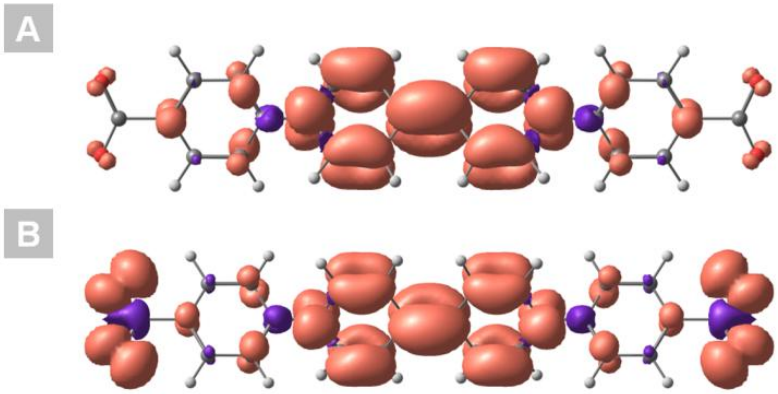

Figure 52. Spin density distribution plotted with contour value 0.001 for optimised (B3LYP/6-31+G*) $\mathbf{V}^{+\bullet}$ radical cation with an intermolecular electron donor (A) and $\mathbf{V}^{+\bullet}$ radical cation with intramolecular carboxylate donor in the triplet state (B).

5.17 **Diffuse reflectance spectroscopy**

The color change associated with the formation of a viologen radical species can be easily monitored by the naked eye. The solid-state diffuse reflectance spectra of **1** in the UV-vis-NIR range shows characteristic bands attributed to the presence of Dy^{III} ions and are a result of Laporte forbidden *f-f* transitions. The bands centered at 1294 and 960 nm can be

assigned to the transitions between the $^6H_{9/2}\leftarrow{}^6H_{15/2}$ and $^6H_{5/2}\leftarrow{}^6H_{15/2}$ states, while the 1102 nm band is a combination of the transitions between the $^6H_{7/2}\leftarrow{}^6H_{15/2}$, $^6F_{11/2}\leftarrow{}^6H_{15/2}$ and $^6H_{9/2}\leftarrow{}^6H_{15/2}$ manifolds. Importantly, the reduction of **1** by UV light results in the formation of an intense broad band in the visible range (600-800 nm) that features noticeable vibronic progression with a separation of ~1500 cm^{-1}, characteristic of double C-C bond stretching coupled to electronic transitions. Such a feature is reflective of an electron-transfer interaction from an electron donor to the pyridinium moiety of the viologen ligand (Fig. 53). A similar behaviour is observed for **2** and **2'**, at the exception of the noted *f-f* transitions (Fig. 53).

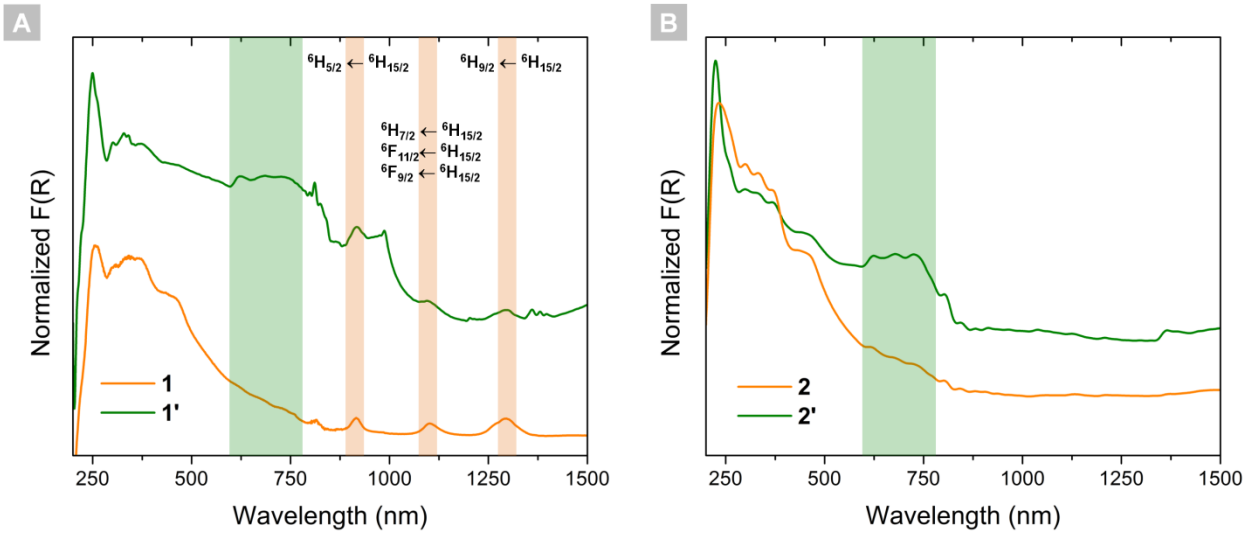

Figure 53. Normalized UV-vis-NIR diffuse reflectance spectra of **1** and **1'** (A), and **2** and **2'** (B) plotted as a Kubelka-Munk function. The bands associated with Laporte forbidden *f-f* transitions (from Dy^{III}) are highlighted in orange, while the principal charge-transfer interactions in the radical species are displayed in green.

5.18 **Magnetic behaviour**

Given the success of SAP chemical environments for the generation of high performance single-molecule magnets (SMMs),[63-65] we sought to explore the magnetic response of compounds **1** and **1'**. The D_{4d} symmetry is particularly attractive due to the fact that it can

minimize transverse crystal-field effects and suppress quantum tunneling of the magnetization – a major hurdle to overcome in the design of lanthanide-based SMMs. While this approach has been mainly applied to Tb^{III}-based double-decker compounds,[62,64] a few Dy^{III} compounds with D_{4d} symmetry have also been shown to display SMM behaviour.[66,67] As such, both samples were characterized in the solid-state by static (dc) and dynamic (ac) magnetization measurements. We found that the magnetic data for **1'** is identical to that of **1**, likely indicating that only a small ratio of the bipyridinium cations become radicals under UV irradiation, as stated above. This was further confirmed by our attempts to measure the organic radicals in **2'** which yielded a diamagnetic signal in the superconducting quantum interference device (SQUID) magnetometer, despite an EPR signal. Consequently, only the magnetic data for **1** will be presented hereafter.

The room temperature χT product, measured under an applied field of 1000 Oe, is 28.79 cm^3 K mol^{-1}, which is in strong agreement with the predicted value of 28.34 cm^3 K mol^{-1} for two isolated Dy^{III} ions (Fig. 54A). The decrease in the χT value at low temperatures is likely due to the thermal depopulation of the crystal-field split M_J levels and/or magnetic anisotropy. At the same time, *M vs*. *H* and *M vs*. HT^{-1} plots are consistent with what would be expected for weakly coupled anisotropic Dy^{III} ions (Fig. 54B,C). Ac magnetic susceptibility measurements were also performed to determine the slow magnetic relaxation dynamics and possible SMM behaviour.

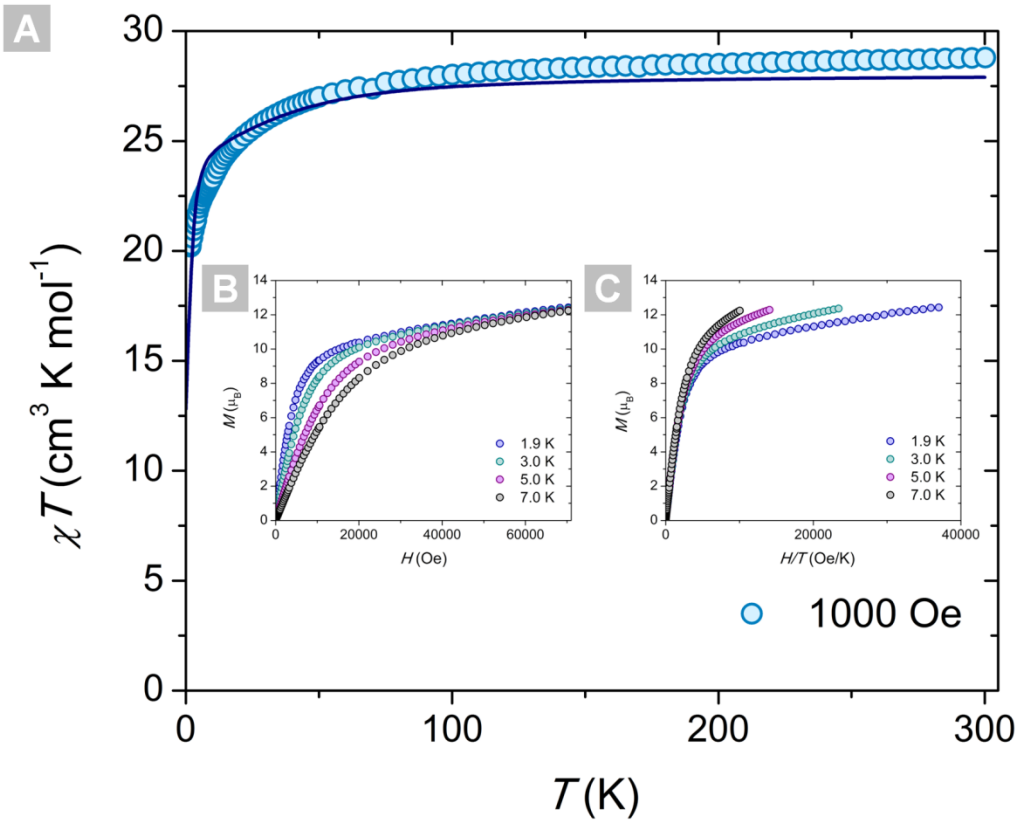

Figure 54. Temperature dependence of the χT product at 1000 Oe for compound **1**, and comparison with the calculated magnetic susceptibility shown as a solid blue line (A). Field dependence of the magnetization plotted as M vs. H (B) or M vs. HT^{-1} (C) at the indicated temperatures and fields of up to 7 T for compound **1**.

An ac signal was only observed by the application of an external dc field. Consequently, the influence of the field and temperature on the magnetic relaxation times was evaluated by fitting the ac susceptibility data to a generalized Debye model (Fig. 55A,B). In both cases, a suitable fit was obtained by considering only Raman and quantum tunneling of the magnetization (QTM) mechanisms (Fig. 55C,D). The slight structural distortions of the SAP geometry are likely the cause of the rather poor SMM behaviour, since ideal D_{4d} symmetries are expected to yield longer relaxation times and significant energy barriers.

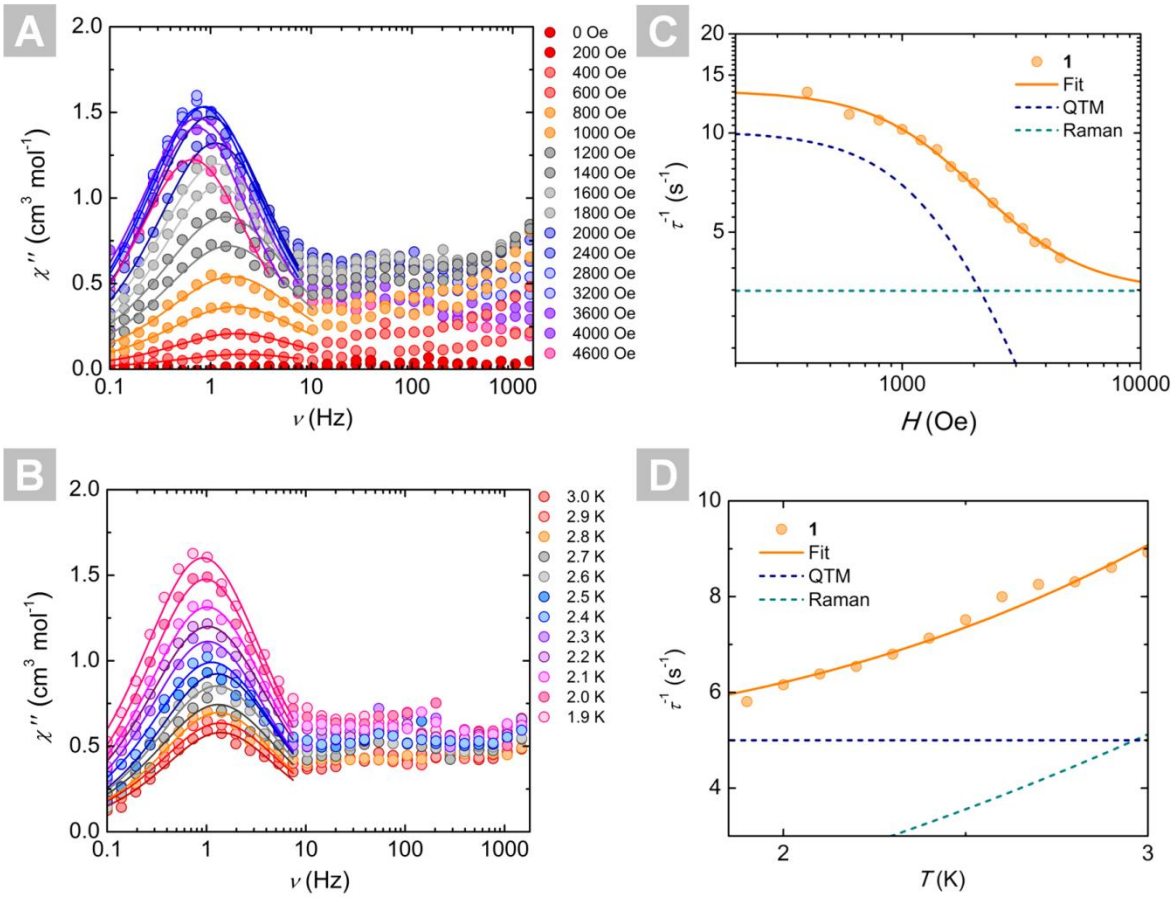

Figure 55. Field dependence of the out-of-phase (χ'') ac magnetic susceptibility at 2 K and varying dc fields for **1** (A). The solid lines correspond to the best fit to a generalized Debye model. The magnetic relaxation times obtained from the best fits are plotted as a function of the applied dc field, and further described by a model encompassing Raman and QTM terms: $\tau^{-1} = CT^n + \frac{B_1}{1+B_2H^2}$ (C). The best-fit parameters obtained are C = 0.40(7) s^{-1} $K^{-3.02}$, n = 3.02(5), B_1 = 10.11(8) s^{-2} and B_2 = 4.55(2) * 10^{-7} Oe^{-2}. Temperature dependence of the out-of-phase (χ'') ac magnetic susceptibility for **1**, under a 2400 Oe dc field and varying temperatures (B). The solid lines correspond to the best fit to a generalized Debye model. The magnetic relaxation times obtained from the best fits are plotted as a function of the temperature, and further described by the same parameters outlined in the field dependent data (Raman and QTM): $\tau^{-1} = CT^n + \tau^{-1}_{QTM}$ (D). The best-fit parameters obtained are C = 0.15(1) s^{-1} $K^{-3.10}$, n = 3.10(6) and τ^{-1}_{QTM} = 4.99(8) s^{-1}.

To complement the magnetic studies, *ab initio* ligand field analyses were performed on **1** (Fig. 56), indicating that the first excited state is located only 5 cm^{-1} above the ground state (Table 21). This is consistent with the dominant Raman and QTM

type of relaxation found in the ac experiments, and suggests the presence of easy-plane anisotropy rather than the required axial anisotropy for generating high performing Dy^{III}-based SMMs.[68,69]

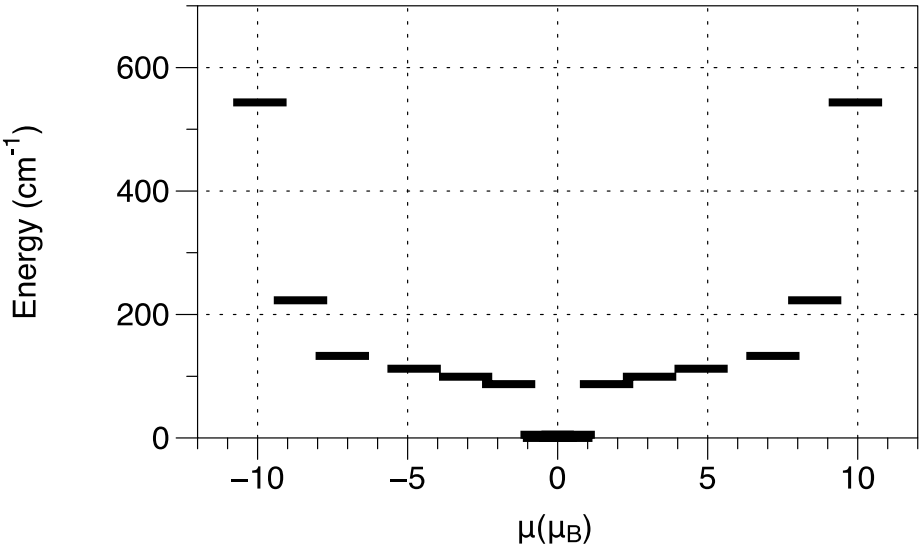

Figure 56. Ligand field splitting of the ground term with correcponding magnetic moment of each Kramers doublet computed using SINGLE_ANISO.

Table 21. Energies of the low-lying Kramers Doublets (KD) as obtained from *ab initio* calculations, and corresponding *g* tensors.

Term	Energy (cm^{-1})	g_X	g_Y	g_Z
$^6H_{15/2}$	0	0.53	9.89	10.31
	5.14	0.69	9.67	9.26
	87.20	3.26	9.25	9.43
	99.18	6.13	5.08	5.22
	112.24	9.56	5.51	5.55
	133.01	14.34	0.11	0.094
	223.10	17.13	0.11	0.11
	543.42	19.84	0.0002	0.0002

5.19 **Electrochemistry**

To further examine the redox behaviour of the nanocapsules, we have performed the electrochemical characterization of **1** in the solid state using Nafion as a negatively charged conducting matrix. The cyclic voltammogram depicted in Fig. 57A has been recorded at a vitreous carbon electrode modified with a finely grinded mixture of **1** and Nafion. The presence of dicationic viologen units in the capsule is confirmed by the observation of two reduction waves at $(E_{pc})_1$ = –0.35 V and $(E_{pc})_2$ = –0.6 V attributed to the successive formation of $\mathbf{V}^{+\bullet}$ and $\mathbf{V}^0$. The observation of Gaussian-shaped reoxidation peaks associated with the reduction of $\mathbf{V}^{+\bullet}$ at $(E_{pc})_2$ = –0.6 V suggests the existence of adsorption phenomena involving the neutral quinonic $\mathbf{V}^0$ species. The attribution of the first reduction wave to the one-electron reduction of $\mathbf{V}^{2+} \rightarrow \mathbf{V}^{+\bullet}$ could be further confirmed by spectroelectrochemistry experiments which involved regularly recording absorption spectra over time during the potentiostatic reduction of a fluoride-doped indium-tin oxide transparent electrodes (FTO) modified with a mixture of **1** in Nafion (Fig. 57B). The electrolysis carried out at E_{app} = –0.45 V led to the emergence of a series of bands in the visible range (400/800 nm) including a diagnostic signal centered at 600 nm, associated to a few shoulders between 600 and 800 nm, attributed to the one-electron reduction of all the $\mathbf{V}^{2+}$ units within the capsule. The absence of signals in the near-infrared region also supports the conclusion that the viologen cation radicals are too distant to interact through space, a result which is consistent with a distance of 4.93 Å measured in the solid state.

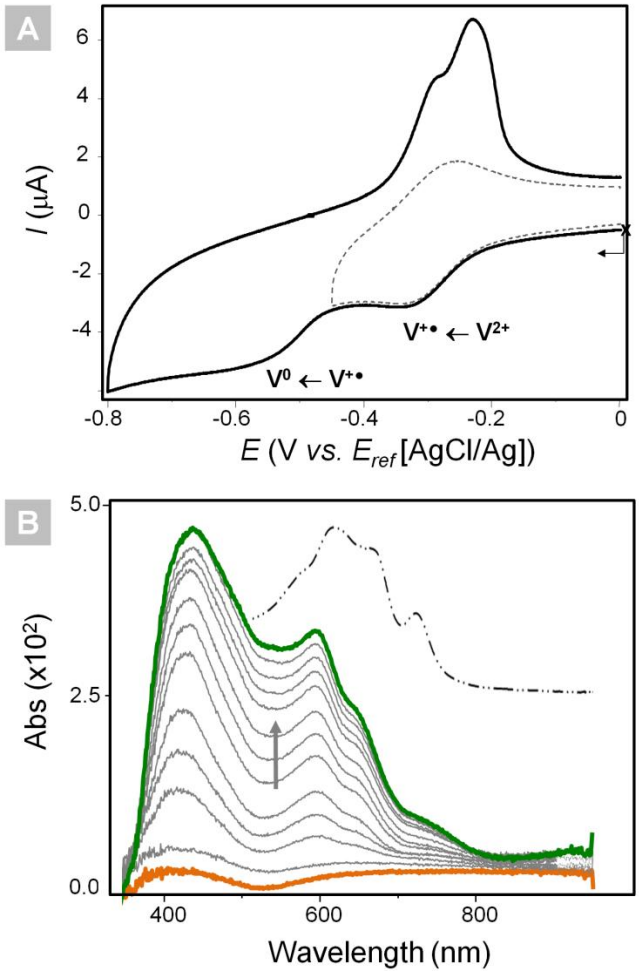

Figure 57. Solid-state CV curve recorded with a vitreous carbon electrode modified with a **1**/Nafion mixture (Ø 2mm, 50 mV/s) displaying the successive reduction waves attributed to the formation of $\mathbf{V}^{+\bullet}$ and $\mathbf{V}^{0}$ (A). *In situ* solid-state UV-vis-NIR spectroelectrochemical data recorded upon submitting a **1**/Nafion modified FTO electrode to a potentiostatic reduction at E_{app} = –0.45 V (B). The changes reveal the color progression from yellow to green associated to the formation of viologen radical species within the nanocapsule. For comparison, the absorption spectrum of a reference compound generated in solution, the cation radical of 1,1'-dimethyl-4,4'-bipyridinium, is shown in the dashed line.

5.20 **Conclusions**

Viologen-based complexes have a remarkable ability to undergo reversible electron transfer reactions under a variety of stimuli. In such cases, the chemical environment surrounding the viologen group is crucial to generating radical species. Indeed, the

presence of a suitable electron donor residing near the pyridinium ring is the determining factor in whether two redox states can be achieved. While no requirement has been clearly established in terms of minimum distance between donor and acceptor atoms, it is generally accepted that a distance in the 3.50 Å range is required to enable an intermolecular electron transfer in the solid-state.[70,71] As such, it is easy to envision how external stimuli, such as pressure, temperature, or even hydration levels, could play a key role in providing the required threshold for radical formation. Although nearly 150 lanthanide compounds coordinated to viologen linkers have been synthesized, only a select few (~5) have been shown to enable the formation of a radical species.[70,72-75] This illustrates the difficulty in promoting supramolecular arrangements that favor electron transfer processes. Among the few compounds that display a viologen-based photo-activated electron transfer, the majority forego a proper identification of the electron donating species. In fact, to this day, the mechanism of formation for such radical-based intermediates remains speculative. At the current stage, we cannot entirely rule out any possible electron donation mechanisms arising from potential nearby intra- or intermolecular donors. Another scenario already mentioned in the literature involves photoionization of a viologen unit to form $\mathbf{V^{3+}}$ and subsequent generation of $\mathbf{V^{+\bullet}}$ and $\mathbf{V^{2+}}$ species.[76] This process would then rely entirely upon an electron transfer between the viologen ligands themselves. We can, however, rule out the possibility of radicals interacting through space between two capsules (*vide supra*). With this in mind, the generation of $Cl^{\bullet}$ species is to be expected should the Cl^{-} anions act as donor atoms. Such species are highly reactive and short-lived, which makes reversibility of this process

highly unlikely. Attempts to observe $Cl^{\bullet}$ species within their expected range in the EPR spectra has so far been unsuccessful.

To summarize, a new nanocapsular arrangement has been achieved using viologen building blocks and lanthanide ions. The complex exhibits an impressive multi-stimuli responsive behaviour where reduction of the viologen ligand can be accessed by three different means: light, chemical reduction, and temperature. The photo-induced radical-bearing nanobarrel has been comprehensively characterized and probed by DFT calculations in order to elucidate the most likely electron donor responsible for the redox behaviour. The presence of radical species within the nanocapsule has been confirmed by EPR, diffuse reflectance spectroscopy, and by electrochemical means. Such synthetic approaches should assist in the design of new and efficient molecules that can be utilized in light harvesting and thermal sensing devices, as we extend the richness of organic donor-acceptor materials towards discrete metal-organic cages.

5.21 **Experimental section**

5.21.1 **General considerations**

Unless otherwise stated, all materials were commercially available and used without further purification. All solvents were of analytical grade and use without further purification. $Dy(NO_3)_3 \cdot 6H_2O$ and $Y(NO_3)_3 \cdot 6H_2O$ were purchased from Strem Chemicals. 1-chloro-2,4-dinitrobenzene and 4,4'-bipyridine were purchased from Alfa Aesar. Hydrochloric acid (~38%) and other solvents were purchased from Fisher Scientific. All compounds were obtained through solvothermal synthesis and characterized by single-crystal X-ray diffraction studies.

5.21.2 **Synthesis**

Synthesis of 1,1'-bis(4-carboxyphenyl)-(4,4'bipyridinium) dichloride (H_2bpcp·2Cl). The ligand was synthesized in accordance with previously described procedures.[77]

Synthesis of $[Dy_2(bpcp)_4(H_2O)_8]Cl_6·H_2O$ (1). Compound **1** was synthesized by combining $Dy(NO_3)_3·6H_2O$ (11.5 mg; 0.025 mmol) and H_2bpcp·2Cl (20 mg; 0.05 mmol) in a solvent mixture consisting of 2 mL of DMF, 0.5 mL of MeCN and 0.5 mL of H_2O. The resulting solution was placed in a 20 mL scintillation vial and 23 μL of concentrated HCl (37%) were added. Following 10 min of sonication, the vial was heated to 80 °C for 36 hours and cooled to room temperature over an additional 15 hours, yielding phase pure yellow plate crystals. Yield = 34.9 %. Elemental analysis found (calcd) for $C_{96}H_{92}Cl_6Dy_2N_8O_{25}$: C 49.89 (50.23) %, H 3.92 (4.04)%, N 5.19 (4.88)%. Selected IR (solid, cm^{-1}): 3270 (br), 3110 (w), 3031 (m), 1602 (s), 1549 (s), 1497 (w), 1441 (w), 1386 (s), 1252 (m), 1230 (m), 1175 (w), 1101 (w), 1021 (w), 840 (s), 784 (s), 701 (s), 644 (s).

Synthesis of $[Y_2(bpcp)_4(H_2O)_8]Cl_6·H_2O$ (2). Compound **2** was synthesized by combining $Y(NO_3)_3·6H_2O$ (9.6 mg; 0.025 mmol) and H_2bpcp·2Cl (20 mg; 0.05 mmol) in a solvent mixture consisting of 2 mL of DMF, 0.5 mL of MeCN and 0.5 mL of H_2O. The resulting solution was placed in a 20 mL scintillation vial and 23 μL of concentrated HCl (37%) were added. Following 10 min of sonication, the vial was heated to 80 °C for 36 hours and cooled to room temperature over an additional 15 hours, yielding phase pure yellow plate crystals. Yield = 36.4 %. Elemental analysis found (calcd) for $C_{96}H_{92}Cl_6Y_2N_8O_{25}$: C 53.38 (53.67) %, H 4.01 (4.32)%, N 5.57 (5.22)%. Selected IR (solid, cm^{-1}): 3246 (br), 3110 (w), 3028 (m), 1603 (s), 1551 (s), 1497 (w), 1442 (w), 1386 (s), 1252 (m), 1230 (m), 1175 (w), 1101 (w), 1021 (w), 840 (s), 784 (s), 701 (s), 645 (s).

Synthesis of the reduced compounds (1' and 2'). The isolation of the reduced compounds can be obtained in three different ways: UV-irradiation, heating and chemical reduction. The reduction using light was performed by exposing single-crystals of **1** to four UV lamps of 5 W at a wavelength of 390 nm for one hour. Reduction of **1** by heat was carried out by heating the compound in the solid-state to 80 ^{o}C for 3 hours. The chemical reduction of **1** (50 mg) can also be achieved by suspending the complex in a 10 mL solution of 0.0287 mM sodium dithionite in H_2O. It should be noted that the photoreduced compound will slowly revert back to yellow within 48 hours. Given the retention of crystallinity in the UV irradiated samples, we have focused on this specific stimulus to describe the viologen reduction behaviour.

5.21.3 **Instrumentation and methods**

Infrared spectroscopy. FT-IR spectra were recorded on a Nicolet Nexus 550 FT-IR spectrometer equipped with an ATR using transmission mode in the 4000-600 cm^{-1} range.

Elemental analysis. Combustion analysis was performed by Galbraith Laboratories (Tennessee, USA).

Diffuse reflectance spectroscopy. UV-vis-NIR spectra were recorded using a Varian Cary-100 spectrophotometer using polytetrafluoroethylene (PTFE) as reference. Kubelka-Munk spectra were normalized to allow for meaningful comparisons.

Electron paramagnetic resonance spectroscopy. EPR spectra of were collected on polycrystalline samples (roughly 75-100 mg) with an X-band Bruker EMX spectrometer at 298 K.

Single-crystal X-ray diffraction. Crystallographic data were collected from single crystals mounted on thin glass fibers using parabar oil and secured with clear nail polish. Data for **1** and **1'** were collected on a Bruker Smart ApexII single-crystal diffractometer equipped with a graphite monochromator, whereas data for **2** and **2'** were collected on Bruker Kappa ApexII single-crystal diffractometer equipped with a Triumph monochromator. Both instruments are equipped with a sealed tube Mo K$\boldsymbol{\alpha}$ source ($\boldsymbol{\lambda} = 0.71073$ Å), an ApexII CCD detector and a dry compressed air cooling system. Samples **1** and **1'** were collected at room temperature while **2** and **2'** were cooled to 200(2) K during data collection. Raw data collection and processing were performed with the Apex3 software package from Bruker.[78] Initial unit cell parameters were determined from 36 data frames from select $\boldsymbol{\omega}$ scans. Semi-empirical absorption corrections based on equivalent reflections were applied.[79] Systematic absences in the diffraction data-set and unit-cell parameters were consistent with the assigned space group. Compounds **1'** and **2'** were merohedral twins with an apparent point group of $\boldsymbol{4/mmm}$ and a true point group of $\boldsymbol{4/m}$. Data were detwinned with a twin fraction of approx. 0.225 (**1'**) and 0.133 (**2'**) using XPrep, a component of the Apex3 software suite. The initial structural solutions were determined using ShelxT direct methods,[80] and refined with full-matrix least-squares procedures based on $\boldsymbol{F^2}$ using ShelXle.[81] Hydrogen atoms were placed geometrically and refined using a riding model. Compounds **2** and **2'** contained pseudo-merohedral twin domains (in addition to the merohedral twinning already observed in **2'**). Data were separated into twin domains using Platon and twin fractions were refined in ShelXle.[82]

Electrochemistry. Cyclic voltammetry (CV) data have been recorded using a SP300 Bilogic potentiostat. The analytical studies were conducted under an argon atmosphere (argon stream) in a standard one–compartment, three–electrodes electrochemical cell. Measurements have been

carried out in water (15mΩ . cm obtained from an ElgaPurelab purification system) using $LiClO_4$ as supporting electrolytes (0.1 M). Vitreous carbon (Ø = 3 mm) working electrodes (CH Instruments) were polished with 1 mm diamond paste before each recording. A home-made AgCl/Ag (saturated KCl) electrode was used as a reference.

Spectroelectrochemical measurements. SEC experiments were carried out at room temperature under an argon atmosphere (argon stream) in a standard one–compartment, three–electrodes electrochemical cell with a biologic SP300 potentiostat coupled to an MCS 500 or MCS 601 UV-NIR Zeiss spectrophotometer connected to a measuring stand through optical fibers. Measurement have been carried out using transparent Fluorine-doped Tin-Oxide electrodes obtained from Flexitec (R ~14Ω). A mixture of **1** (a few crystals, typically 1-2 mg) suspended in a Nafion® solution (Aldrich, 500 μL of a perfluorinated resin 5% wt in water/alcohol) was carefully grinded in a mortar bowl for 10 minutes The modified electrodes were then prepared upon depositing a few drops of this mixture onto the carbon or FTO surface. The electrodes were then left to dry on the side for 15-20 minutes before use.

Magnetic susceptibility measurements. Magnetic experiments were performed on a Quantum Design SQUID magnetometer MPMS-XL7 operating between 1.9 and 300 K, and applied fields of up to 7 T. Direct current (dc) susceptibility measurements were performed on a finely ground polycrystalline sample of 11.0 mg for **1**, restrained in a matrix of vacuum grease and wrapped in a polyethylene membrane. Alternating current (ac) susceptibility measurements were performed under an oscillating ac field of 3.78 Oe and ac frequencies ranging from 0.1 to 1488 Hz. Prior to the experiments, the field dependence of the magnetization was measured at 100 K in order to detect the presence of any bulk ferromagnetic impurities. The samples appeared to be free of any

significant ferromagnetic impurities. The magnetic impurities were corrected for the sample holder and the intrinsic diamagnetic contributions.

Computational details. Calculations of magnetic properties and ligand field parameters have been conducted using MOLCAS 8.0 program package[83] using the crystal structure of a model fragment. CASSCF calculations with $4f^9$ active space were performed using ANO-RCC-VTZP basis sets for Dy,[84] ANO-RCC-VDZP for O and N atoms,[85] and ANO-RCC-VDZ for C and H.[86] Spin-orbit coupling was computed using AMFI approximation[87] for the 21 sextets and 128 quartets and 130 doublet states. Temperature dependence of magnetic susceptibility and crystal field parameters of the ground multiplet were computed as implemented in SINGLE_ANISO.[88]

Analysis of the structure and spin states energies of a free bcbp ligand was done with Gaussian[89] software using B3LYP functional[90] and 6-31+G* basis set. Geometry optimisation was followed by a harmonic frequencies calculation to ensure that the optimized structure corresponded to a minimum. Spin density countour plots were generated with Chemcraft software.

The entire barrel with two encapsulated chlorine anions and water molecule (215 atoms total) was optimised with the recently developed semi-empirical approach HF-3c[91] as implemented in ORCA 4.0[92], which accounts for dispersion interactions expected to affect the structure of the barrel.

5.22 **References**

(1) J. Esselborn, C. Lambertz, A. Adamska-Venkatesh, T. Simmons, G. Berggren, J. Noth, J. Siebel, A. Hemschemeier, V. Artero, E. Reijerse, M. Fontecave, W. Lubitz and T. Happe, *Nat. Chem. Biol.*, 2013, **9**, 607-609.

(2) J. D. Lawrence, H. Li, T. B. Rauchfuss, M. Bénard and M.-M. Rohmer, *Angew. Chem. Int. Ed.*, 2011, **40**, 1768-1771.

(3) E. Salvadeo, L. Dubois and J.-M. Latour, *Coord. Chem. Rev.*, 2018, **374**, 345-375.

(4) A. J. McConnell, C. S. Wood, P. P. Neelakandan and J. Nitschke, *Chem. Rev.*, 2015, **115**, 7729-7793.

(5) M. Han, R. Michel, B. He, Y.-S. Chen, D. Stalke, M. John and G. H. Clever, *Angew. Chem. Int. Ed.*, 2013, **52**, 1319-1323.

(6) P. J. Lusby, P. Müller, S. J. Pike and A. M. Z. Slawin, *J. Am. Chem. Soc.*, 2009, **131**, 16398-16400.

(7) D. S. Kim, J. Chang, S. Leem, J. S. Park, P. Thordarson and J. L. Sessler, *J. Am. Chem. Soc.*, 2015, **137**, 16038-16042.

(8) J. Park, L.-B. Sun, Y.-P. Chen, Z. Perry and H.-C. Zhou, *Angew. Chem. Int. Ed.*, 2014, **53**, 5842-5846.

(9) S. K. Samanta, J. Quigley, B. Vinciguerra, V. Briken and L. Isaacs, *J. Am. Chem. Soc.*, 2017, **139**, 9066-9074.

(10) K. Nakabayashi, M. Kawano and M. Fujita, *Angew. Chem. Int. Ed.*, 2005, **44**, 5322-5325.

(11) K. Yazaki, S. Noda, Y. Tanaka, Y. Sei, M. Akita and M. Yoshizawa, *Angew. Chem. Int. Ed.*, 2016, **55**, 15031-15034.

(12) S. Bivaud, J.-Y. Balandier, M. Chas, M. Allain, S. Goeb and M. Sallé, *J. Am. Chem. Soc.*, 2012, **134**, 11968-11970.

(13) V. Croué, S. Goeb and M. Sallé, *Chem. Commun.*, 2015, **51**, 7275-7289.

(14) M. Yamashina, Y. Sei, M. Akita and M. Yoshizawa, *Nat. Commun.*, 2014, **5**, 4662.

(15) D. Samanta, D. Galaktionova, J. Gemen, L. J. W. Shimon, Y. Diskin-Posner, L. Avram, P. Král and R. Klajn, *Nat. Commun.,* 2018, **9**, 641.

(16) L.-X. Cai, S.-C. Li, D.-N. Yan, L.-P. Zhou, F. Guo and Q.-F. Sun, *J. Am. Chem. Soc.*, 2018, **140**, 4869-4876.

(17) J. L. Bolliger, A. M. Belenguer and J. R. Nitschke, *Angew. Chem. Int. Ed.,* 2013, **52**, 7958-7962.

(18) O. Satu, J. Tao and Y.-Z. Zhang, *Angew. Chem. Int. Ed.*, 2007, **46**, 2152-2187.

(19) T. Liu, H. Zheng, S. Kang, Y. Shiota, S. Hayami, M. Mito, O. Sato, K. Yoshizawa, S. Kanegawa and C. Duan, *Nat. Commun.,* 2013, **4**, 2826.

(20) O. Sato, *Nat. Chem.*, 2016, **8**, 644-656.

(21) J. A. DeGayner, I.-R. Jeon, L. Sun, M. Dincă and T. D. Harris, J. Am. Chem. Soc., 2017, 139, 4175-4184.

(22) H.-Y. Li, Y.-L. Wei, X.-Y. Dong, S.-Q. Zang and T. C. W. Mak, *Chem. Mater.,* 2015, **27**, 1327-1331.

(23) Q. Sui, P. Li, N.-N. Yang, T. Gong, R. Bu and E.-Q. Gao, *ACS Appl. Mater. Int.,* 2018, **10**, 11056-11062.

(24) S. Goeb, S. Bivaud, P. I. Dron, J.-Y. Balandier, M. Chas and M. Sallé, *Chem. Commun.*, 2012, **48**, 3106-3108.

(25) Y. Liu, W. Zhao, C.-H. Chen and A. H. Flood, *Science*, 2019, **365**, 159-161.

(26) C. Kahlfuss, T. Gibaud, S. Denis-Quanquin, S. Chowdhury, G. Royal, F. Chevallier, E. Saint-Aman and C. Bucher, *Chem. – Eur. J.* 2018, **24**, 13009-13019.

(27) A. Iordache, M. Oltean, A. Milet, F. Thomas, B. Baptiste, E. Saint-Aman and C. Bucher, *J. Am. Chem. Soc.*, 2012, **134**, 2653-2671.

(28) D. P. August, G. S. Nichol and P. J. Lusby, *Angew. Chem. Int. Ed.*, 2016, **55**, 15022-1502.

(29) D. Yang, J. Zhao, L. Yu, X. Lin, W. Zhang, H. Ma, A. Gogoll, Z. Zhang, Y. Wang, X.-J. Yang and B. Wu, *J. Am. Chem. Soc.*, 2017, **139**, 5946-5951.

(30) D. Preston, S. M. McNeil, J. E. M. Lewis, G. I. Giles and J. D. Crowley, *Dalton Trans.*, 2016, **45**, 8050-8060.

(31) G. Pognon, C. Boudon, K. J. Schenk, M. Bonin, B. Bach and J. Weiss, *J. Am. Chem. Soc.*, 2006, **128**, 3488-3489.

(32) S. Demir, J. M. Zadrozny, M. Nippe and J. R. Long, *J. Am. Chem. Soc.*, 2012, **134**, 18546-18549.

(33) E. M. Fatila, M. Rouzières, M. C. Jennings, A. J. Lough, R. Clérac and K. E. Preuss, *J. Am. Chem. Soc.*, 2013, **135**, 9596-9599.

(34) G. Brunet, M. Hamwi, M. A. Lemes, B. Gabidullin and M. Murugesu, *Commun. Chem.*, 2018, **1**, 88.

(35) B. S. Dolinar, S. Gómez-Coca, D. I. Alexandropoulos and K. R. Dunbar, *Chem. Commun.*, 2017, **53**, 2283-2286.

(36) C. Kahlfuss, S. Denis-Quanquin, N. Calin, E. Dumont, M. Garavelli, G. Royal, S. Cobo, E. Saint-Aman and C. Bucher, *J. Am. Chem. Soc.*, 2016, **138**, 15234−15242.

(37) C. Kahlfuss, A. Milet, J. Wytko, J. Weiss, E. Saint-Aman and C. Bucher, *Org. Lett.*, 2015, **17**, 4058-4061.

(38) K. Moon, J. Grindstaff, D. Sobransingh and A. E. Kaifer, *Angew. Chem. Int. Ed.*, 2004, **43**, 5496-5499.

(39) L. Zhang, T.-Y. Zhou, J. Tian, H. Wang, D.-W. Zhang, X. Zhao, Y. Liu and Z.-T. Li, *Polym. Chem.*, 2014, **5**, 4715-4721.

(40) G. Das, T. Prakasam, S. Nuryyeva, D. S. Han, A. Abdel-Wahab, J.-C. Olsen, K. Polychronopoulou, C. Platas-Iglesias, F. Ravaux, M. Jouiad and A. Trabolsi, *J. Mater. Chem. A*, 2016, **4**, 15361-15369.

(41) H. D. Correia, S. Chowdhury, A. P. Ramos, L. Guy, G. J.-F. Demets and C. Bucher, *Polym. Int.*, 2019, **68**, 572-588.

(42) L. Striepe and T. Baumgartner, *Chem. – Eur. J.*, 2017, **23**, 16924-16940.

(43) Y. Wang, M. Frasconi and J. F. Stoddart, *ACS Cent. Sci.*, 2017, **3**, 927-935.

(44) A. R. Pease, J. O. Jeppesen, J. F. Stoddart, Y. Lio, C. P. Collier and J. R. Heath, *Acc. Chem. Res.*, 2001, **34**, 433-444.

(45) M. A. Lemes, G. Brunet, A. Pialat, L. Ungur, I. Korobkov and M. Murugesu, *Chem. Commun.*, 2017, **53**, 8660-8663.

(46) M. A. Lemes, H. N. Stein, B. Gabidullin, K. Robeyns, R. Clérac and M. Murugesu, *Chem. – Eur. J.*, 2018, **24**, 4259-4263.

(47) D. Casanova, M. Llunell, P. Alemany and S. Alvarez, *Chem. – Eur. J.*, 2005, **11**, 1479-1494.

(48) A. L. Spek, *Acta Crystallogr. Sect. C*, 2015, **71**, 9-18.

(49) X.-Y. Lv, M.-S. Wang, C. Yang, G.-E. Wang, S.-H. Wang, R.-G. Lin and G.-C. Guo, *Inorg. Chem.*, 2012, **51**, 4015-4019.

(50) C. Sun, G. Xu., X.-M. Jiang, G.-E. Wang, P.-Y. Guo, M.-S. Wang and G.-C. Guo, *J. Am. Chem. Soc.*, 2018, **140**, 2805-2811.

(51) N. Leblanc, M. Allain, N. Mercier and L. Sanguinet, *Cryst. Growth Des.*, 2011, **11**, 2064-2069.

(52) J.-K. Sun, P. Wang, C. Chen, X.-J. Zhou, L.-M. Wu, Y.-F. Zhang and J. Zhang, *Dalton Trans.*, 2012, **41**, 13441-13446.

(53) J.-J. Liu, Y.-F. Guan, M.-J. Lin, C.-C. Huang, W.-X. Dai, *Cryst. Growth Des.*, 2016, **16**, 2836-2842.

(54) F. Wan, L.-X. Qiu, L.-L. Zhou, Y.-Q. Sun and Y. You, *Dalton Trans.* 2015, **44**, 18320-18323.

(55) T. P. Le, J. E. Rogers and L. A. Kelly, *J. Phys. Chem. A*, 2000, **104**, 6778-6785.

(56) O. Toma, M. Leroux, N. Mercier, M. Allain, A. H. Kassiba, S. K. K. Swamy, J. Dittmer, *Eur. J. Inorg, Chem.*, 2016, **7**, 1036-1043.

(57) W. W. Porter and T. P. Vaid, *J. Org. Chem.*, 2005, **70**, 5028-5035.

(58) Q. Sui, X.-T. Ren, Y.-X. Dai, K. Wang, W.-T. Li, T. Gong, J.-J. Fang, B. Zou, E.-Q. Gao and L. Wang, *Chem. Sci.* 2017, **8**, 2758-2768.

(59) R. Sure and S. Grimme, *J. Comput. Chem.*, 2013, **34**, 1672-1685.

(60) F. Neese, *Wiley Interdiscip. Rev.: Comput. Mol. Sci.*, 2012, **2**, 73-78.

(61) J.-K. Sun, P. Wang, Q.-X. Yao, Y.-J. Chen, Z.-H. Li, Y.-F. Zhang, L.-M. Wu and J. Zhang, *J. Mater. Chem.*, 2012, **22**, 12212-12219.

(62) L. A. Vermeulen and M. E. Thompson, *Nature*, 1992, **358**, 656-658.

(63) N. Ishikawa, M. Sugita, T. Ishikawa, S. Koshihara and Y. Kaizu, *J. Am. Chem. Soc.*, 2003, **125**, 8694-8695.

(64) M. A. AlDamen, J. M. Clemente-Juan, E. Coronado, C. Martí-Gastaldo and A. Gaita-Ariño, *J. Am. Chem. Soc.*, 2008, **130**, 8874-8875.

(65) N. Ishikawa, M. Sugita and W. Wernsdorfer, *Angew. Chem. Int. Ed.*, 2005, **44**, 2931-2935.

(66) G.-J. Chen, C.-Y. Gao, J.-L. Tian, J. Tang, W. Gu, X. Liu, S.-P. Yan, D.-Z. Liao and P. Cheng, *Dalton Trans.*, 2011, **40**, 5579-5583.

(67) S.-D. Jiang, B.-W. Wang, G. Su, Z.-M. Wang and S. Gao, *Angew. Chem. Int. Ed.*, 2010, **49**, 7448-7451.

(68) J. J. Baldoví, J. J. Borrás-Almenar, J. M. Clemente-Juan, E. Coronado and A. Gaita-Ariño, *Dalton Trans.*, 2012, **41**, 13705-13710.

(69) J.-L. Liu, Y.-C. Chen and M.-L. Tong, *Chem. Soc. Rev.*, 2018, **47**, 2431-2453.

(70) H. Chen, G. Zheng, M. Li, Y. Wang, Y. Song, C. Han, J. Dai and Z. Fu, *Chem. Commun.*, 2014, **50**, 13544-13546.

(71) G. Xu, G.-C. Guo, M.-S. Wang, Z.-J. Zhang, W.-T. Chen and J.-S. Huang, *Angew. Chem. Int. Ed.*, 2007, **46**, 3249-3251.

(72) J.-K. Sun, L.-X. Cai, Y.-J. Chen, Z.-H. Li and J. Zhang, *Chem. Commun.*, 2011, **47**, 6870-6872.

(73) D.-F. Shen, S. Li, H. Liu, W. Jiang, Q. Zhang and G.-G. Gao, *J. Mater. Chem. C*, 2015, **3**, 12090-12097.

(74) Y.-Q. Sun, F. Wan, X.-X. Li, J. Lin, T. Wu, S.-T. Zheng and X. Bu, *Chem. Commun.*, 2016, **52**, 10125-10128.

(75) W. Yang, H.-R. Tian, J.-P. Li, Y.-F. Hui, X. He, J. Li, S. Dang, Z. Xie and Z.-M. Sun, *Chem. – Eur. J.*, 2016, **22**, 15451-15457.

(76) E. E. Méndez, C. Crespo-Hernández, R. Figueroa, R. Arce and E. Quiñones, *J. Photochem. Photobiol. A*, 2001, **142**, 19-24.

(77) J. -J. Liu, Y.-F. Guan, M.-J. Lin, C.-C. Huang and W.-X. Dai, *Cryst. Growth Des.*, 2015, **15**, 5040-5046.

(78) APEX Softward Suite v 2010 Bruker AXS Inc. Madison Wisconsin USA, 2010.

(79) R. H. Blessing, *Acta Crystallogr., Sect. A: Found. Crystallogr.*, 1995, **51**, 33–38.

(80) G. M. Sheldrick, *Acta Crystallogr., Sect. A: Found. Crystallogr.*. 2008, **A64**, 112–22.

(81) C. B. Hübschle, G. M. Sheldrick and B. Dittrich, *J. Appl. Crystallogr.*, 2011, **44**, 1281–1284.

(82) A. L. Spek, *J. Appl. Crystallogr.*, 2003, **36**, 7-13.

(83) F. Aquilante, J. Autschbach, R. K. Carlson, L. F. Chibotaru, M. G. Delcey, L. De Vico, N. Ferré, L. M. Frutos, L. Gagliardi and M. Garavelli, *J. Comput. Chem.*, 2016, **37**, 506-541.

(84) B. O. Roos, R. Lindh, P.-Å. Malmqvist, V. Veryazov, P.-O. Widmark and A. C. Borin, *J. Phys. Chem. A*, 2008, **112**, 11431-11435.

(85) B. O. Roos, R. Lindh, P.-Å. Malmqvist, V. Veryazov and P.-O. Widmark, *J. Phys. Chem. A*, 2004, **108**, 2851-2858.

(86) P.-O. Widmark, P.-Å. Malmqvist, B. O. Roos, *Theor. Chim. Acta*, 1990, **77**, 291-306.

(87) B. A. Heß, C. M. Marian, U. Wahlgren and O. Gropen, *Chem. Phys. Lett.*, 1996, **251**, 365-371.

(88) L. F. Chibotaru and L. Ungur, *J. Chem. Phys.*, 2012, **137**, 064112.

(89) M. J. Frisch, G. W. Trucks, H. B. Schlegel, G. E. Scuseria, M. A. Robb, J. R. Cheeseman, G. Scalmani, V. Barone, G. A. Petersson, H. Nakatsuji, M. C. X. Li, A. Marenich, J. Bloino, B. G. Janesko, R. Gomperts, B. Mennucci, H. P. Hratchian, J. V. Ortiz, A. F. Izmaylov, J. L. Sonnenberg, D. Williams-Young, F. Ding, F. Lipparini, F. Egidi, J. Goings, B. Peng, A. Petrone, T. Henderson, D. Ranasinghe, V. G. Zakrzewski, N. R. J.

Gao, G. Zheng, W. Liang, M. Hada, M. Ehara, K. Toyota, R. Fukuda, J. Hasegawa, M. Ishida, T. Nakajima, Y. Honda, O. Kitao, H. Nakai, T. Vreven, K. Throssell, J. A. M. Jr., J. E. Peralta, F. Ogliaro, M. Bearpark, J. J. Heyd, E. Brothers, K. N. Kudin, V. N. Staroverov, T. Keith, R. Kobayashi, J. Normand, K. Raghavachari, A. Rendell, J. C. Burant, S. S. Iyengar, J. Tomasi, M. Cossi, J. M. Millam, M. Klene, C. Adamo, R. Cammi, J. W. Ochterski, R. L. Martin, K. Morokuma, O. Farkas, J. B. Foresman and D. J. Fox, Revision D.01 ed., Gaussian, Inc., Wallingford CT, 2016.

(90) A. D. Becke, *J. Chem. Phys.*, 1993, **98**, 5648-5652.

(91) R. Sure and S. Grimme, *J. Comp. Chem.*, 2013, **34**, 1672-1685.

(92) F. Neese, *Wiley Interdiscip. Rev.: Comput. Mol. Sci.*, 2012, **2**, 73-78.

At that time any sensible reasonable chemist would have said our chances of creating a crystal were zero, that you'd get tangled bird's nests – amorphous, nasty stuff that you couldn't handle.
– Richard Robson[7]

Chapter 6

Design strategy for the controlled generation of cationic framewoks

6.1 Published contributions

Design strategy for the controlled generation of cationic frameworks and ensuing anion-exchange capabilities

G. Brunet, K. Robeyns, R. P. S. Huynh, J.-B. Lin, S. P. Collins, G. A. Facey, G. K. H. Shimizu, T. K. Woo and M. Murugesu, *ACS Appl. Mater. Int.*, 2019, **11**, 3181-3188.

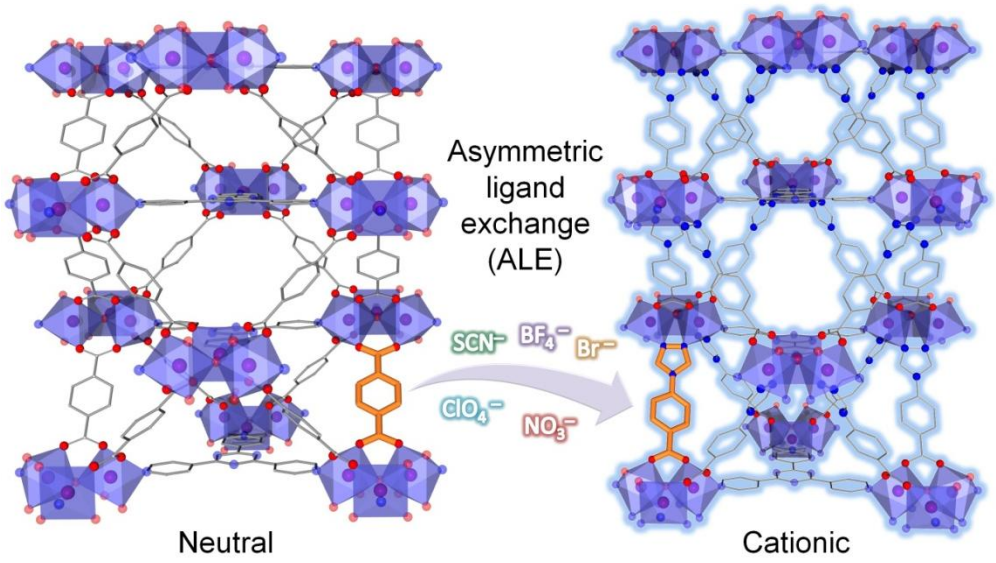

G. Brunet and M. Murugesu wrote the manuscript. G. Brunet performed the majority of the experiments. R. P. S. Huyhn, J.-B. Lin and G. K. H. Shimizu performed the gas adsorption experiments. S. P. Collins and T. K. Woo performed the DFT calculations. G. A. Facey assisted with the solid-state NMR experiments. K. Robeyns was responsible for the refinement of the single-crystal X-ray diffraction data.

[7] *In regards to the development of a new class of porous solids, thereafter named metal-organic frameworks.*

6.2 **Abstract**

Cationic frameworks are an emerging class of exceptional solid adsorbents capable of encapsulating highly toxic and persistent anionic pollutants. The controlled generation of cationic frameworks, however, lags behind the abundant design strategies devised to control the structures and topologies of neutral frameworks. In this regard, we report a rational approach that allows the conversion of the synthetic approach toward constructing a neutral framework into one allowing for the synthesis of a cationic one without incurring any changes to the overall topology or the selected metal ion. We demonstrate that the replacement of a functional group on an organic linker that promotes a similar coordination mode, but bearing one less negative charge, can yield the systematic generation of cationic frameworks. Moreover, we confirm the cationic nature of the metal–organic frameworks through preliminary anion-exchange experiments and propose a method to retain permanent porosity in cationic frameworks through the use of strongly binding anions. Altogether, these results show great promise for the construction of tunable nanoporous frameworks capable of carrying out anion-exchange processes.

6.3 **Introduction**

Research focused on metal–organic frameworks (MOFs) has been ongoing for a few decades; however, the intricacies related to this class of crystalline porous materials continue to be revealed to this day.[1–8] The development of MOFs is largely driven by the fact that they can encapsulate an impressive variety of guest molecules, ranging from greenhouse gases[9–11] to antitumoral and antiviral drugs.[12–14] Thus, multiple synthetic and design strategies have been devised over the years to promote specific structural topologies that can ultimately offer highly selective inclusion behaviours and predictable chemical transformations.[15–22] Among the many

desired properties of MOFs, the capture of charged species has grown into an intense area of research because of the harmful impact of a number of ionic pollutants on human health and the environment.[23–40] The use of MOFs for ion-exchange applications is encouraged because of the fact that they can be obtained in both cationic and anionic forms, in contrast to other materials that are generally only obtainable in one form or the other (i.e., zeolites and layered double hydroxides).[41–50]

Recently, cationic frameworks have joined the forefront of ion-exchange technologies because of their potential ability to remove toxic anions such as ClO_4^-, AsO_4^{3-}, and $Cr_2O_7^{2-}$,[51–57] all of which are strictly regulated by the US Environmental Protection Agency during the purification of drinking water.[58] The initial strategy for obtaining a positively charged framework consisted of employing neutral polytopic organic ligands such as polypyridine- or imidazole-based linkers;[59–61] however, these structures generally elicited poor stability and limited tunability. Subsequent attempts to control ionicity were elegantly demonstrated by Bu and co-workers[62] in secondary building units consisting of planar trimers, where control over the oxidation state of the metal ions (M^{II} *vs*. M^{III}) as well as the preemptive coordination of neutral ligands to the open metal sites of the trimer can indeed yield cationic frameworks. Similarly, the direct stripping of terminally coordinated F^- anions from the metal clusters of MOFs has also been shown to generate a cationic scaffolding.[63] With our goal of providing alternative routes to framework cationization, we report here an accessible and practical strategy for the systematic generation of cationic frameworks. This process involves replacing linear dicarboxylates, one of the most commonly used organic building blocks in MOF synthesis, with an asymmetric linker featuring a nearly identical coordination mode but with one less negative charge. More specifically, we have designed an asymmetric ligand-exchange (ALE) method, in which a

carboxylic acid functionality is replaced by a 1,2,4-triazole moiety, effectively maintaining a similar binding mode that would permit an original and existing framework topology to be retained while also reducing the amount of negative charge on the organic building block (Fig. 58). The strength of the present approach lies in its ability to control the charge of the framework while also retaining all of the benefits associated with the desired structural topology and reactivity of an existing neutral or anionic MOF. This can ultimately lead to the directed synthesis of high-performance ion-capturing materials.

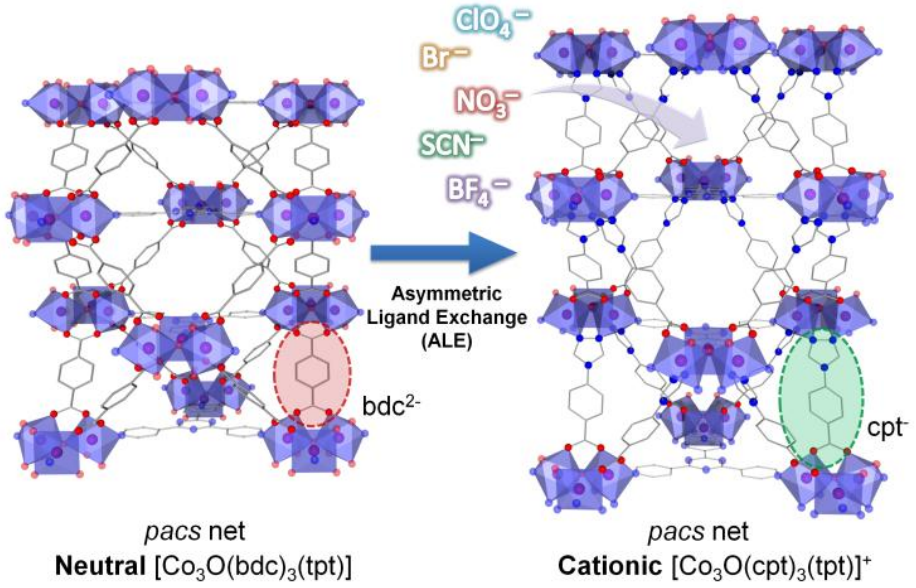

Figure 58. Depiction of the general ALE method for framework cationization, achieved by replacing a linear dicarboxylic acid linker with an asymmetric ligand containing a similar coordination mode but with one less negative charge (*i.e*. a triazole moiety).

Building on our previous work, where we employed the asymmetrically binding 4-(4′-carboxyphenyl)-1,2,4-triazole (Hcpt) ligand for constructing a variant of the iconic MIL-88 framework (*acs* type),[64] we have partitioned the pore spaces using the symmetry-matching tritopic 2,4,6-tri(4-pyridiyl)-1,3,5-triazine (tpt) ligand for implementing the ALE strategy. The

linear dicarboxylates of the 9-connected trimers have been successfully replaced with three different asymmetric linkers of varying lengths (Fig. 59), leading to an isoreticular series of MOFs with different pore sizes and densities (**UOTT-1**, **UOTT-2**, and **UOTT-3**, where UOTT stands for the University of Ottawa). We further demonstrate that control over the anions initially present in the pores can be achieved by employing different starting metal salts. Interestingly, direct visualization of the anions within the pore space, using single-crystal X-ray diffraction, reveals that these occupy symmetry-matching positions, thereby maintaining the necessary C_3 symmetry.[65] To the best of our knowledge, this is the first time guest molecules (solvents or counterions) have been located crystallographically in the *pacs*-MOF platform (*pacs* stands for partitioned *acs* net).[19,21,66] This offers invaluable insights into the host–guest interactions, a key criterion in the rational optimization of porous materials. In addition to this, we have characterized the MOFs in terms of the affinity of small monoanions to the framework, the ease at which they can be replaced, and the effect of the binding strength of the anions on their permanent porosity. These materials, although unfortunately not stable in aqueous media, still display a near-complete exchange of BF_4^- for NCS^- anions, when run on a simple gravity filtration column of a packed bed of the MOF. As such, we successfully confirm the cationization process through proof-of-principle anion-exchange experiments. Although other highly stable and selective MOFs do exist for anion-exchange processes,[67–71] in this work, we focus on addressing the lack of synthetic strategies for obtaining topologically desired cationic frameworks.

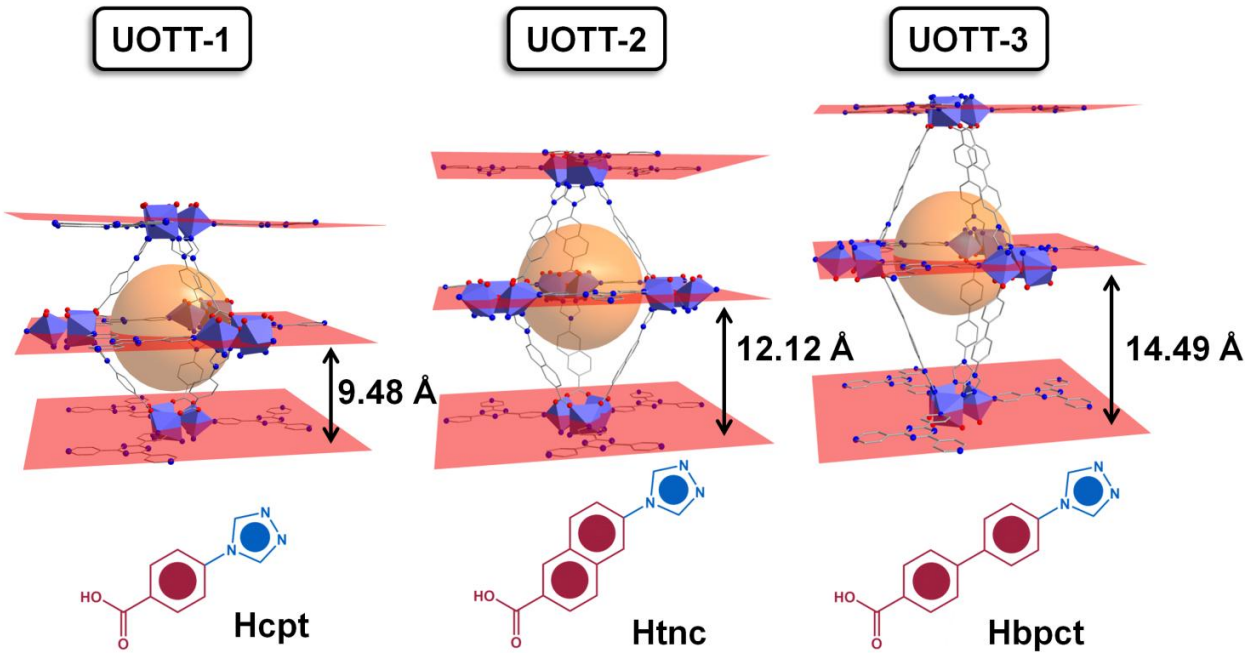

Figure 59. Structures of **UOTT-1**, **2** and **3**, displaying the elongation of the charged framework with varying lengths of the asymmetric linker. Host-guest interactions can thus be tuned, along with their porosities and densities.

6.4 Synthesis and structure

Single-crystal X-ray diffraction studies reveal that all compounds investigated belong to either the trigonal or the hexagonal crystal system (Table 22). The first series of cationic MOFs (**UOTT-1**) presented in this work are assembled by combining the asymmetric 4-(4′-carboxyphenyl)-1,2,4-triazole (Hcpt) ligand and tritopic 2,4,6-tris(4-pyridyl)-1,3,5-triazine (tpt) ligands and differ in terms of their counteranions. To provide additional control on the cationic frameworks, we have synthesized and designed two new asymmetric ligands by expanding the Hcpt ligand central ring to naphthalene (Htnc; **UOTT-2**) and biphenyl moieties (Hbpct; **UOTT-3**). It is worth mentioning that, to the best of our knowledge, no structure has been reported with the two latter linkers (Htnc and Hbpct). This effectively yields an isoreticular family of charged frameworks, where anions of varying sizes and compositions can be contained within the porous network. Expansion of the MOF is clearly evidenced by the elongation of the *c*-axis length from

~19 to 30 Å and the relatively constant *a*- and *b*-axis. In all cases, the Co_3 trimer is charge-balanced by a single monoanion residing in the pore space. Whereas this type of metal cluster topology is commonly attributed to a mixed di- and trivalent configuration for Fe, Co, and Ni,[72,73] the present compounds reveal that all three Co ions are in a +2 oxidation state. This is corroborated by bond valence sum calculations (i.e., Co1 = 1.90 for **NO_3@UOTT-1**) and charge considerations. Additionally, magnetic susceptibility measurements performed on **NCS@UOTT-1** are well within the expected range for three isolated high-spin Co^{II} ions (5.62 cm^3 K mol^{-1}) exhibiting significant magnetic anisotropy, with a room temperature χT value of 7.13 cm^3 K mol^{-1} (Fig. 60). Two similar MOFs containing oxo-centered trinuclear $\{Co_3\}$ cores and coordinated to the Hcpt ligand also report all three cobalt ions being in a +2 oxidation state.[22,64]

Table 22. Single-crystal X-ray data for **UOTT-1**, **2** and **3**.

Compound	Formula[a]	*a,b* (Å)	*c* (Å)	Space group	Anion localized
NO_3@UOTT-1	$\{[Co_3(\mu_3\text{-}O)(cpt)_3(tpt)]\cdot NO_3\}_n$	16.7567(5)	19.0343(7)	$P6_3/mc$	Yes
Br@UOTT-1	$\{[Co_3(\mu_3\text{-}O)(cpt)_3(tpt)]\cdot Br\}_n$	16.6968(9)	18.9684(10)	$P6_3/mc$	Yes
NCS@UOTT-1	$\{[Co_3(\mu_3\text{-}O)(cpt)_3(tpt)]\cdot NCS\}_n$	16.8384(10)	19.0516(13)	$P6_3/mc$	Yes
NO_3@UOTT-2	$\{[Co_3(\mu_3\text{-}O)(tnc)_3(tpt)]\cdot NO_3\}_n$	16.6264(7)	24.2500(13)	$P31c$	No
ClO_4@UOTT-2	$\{[Co_3(\mu_3\text{-}O)(tnc)_3(tpt)]\cdot ClO_4\}_n$	16.6138(8)	24.2258(12)	$P31c$	Yes
NO_3@UOTT-3	$\{[Co_3(\mu_3\text{-}O)(bpct)_3(tpt)]\cdot NO_3\}_n$	16.6267(3)	28.9795(7)	$P6_3/mc$	Yes
BF_4@UOTT-3	$\{[Co_3(\mu_3\text{-}O)(bpct)_3(tpt)]\cdot BF_4\}_n$	16.7599(5)	29.0651(9)	$P6_3/mc$	Yes

[a]cpt = 4-(4′-carboxyphenyl)-1,2,4-triazole; tnc = 6-(4*H*-1,2,4-triazol-4-yl)-2-naphthoic acid; bpct = 4′-(4*H*-1,2,4-triazol-4-yl)biphenyl-4-carboxylic acid; and tpt = 2,4,6-tri(4-pyridyl)-1,3,5-triazine.

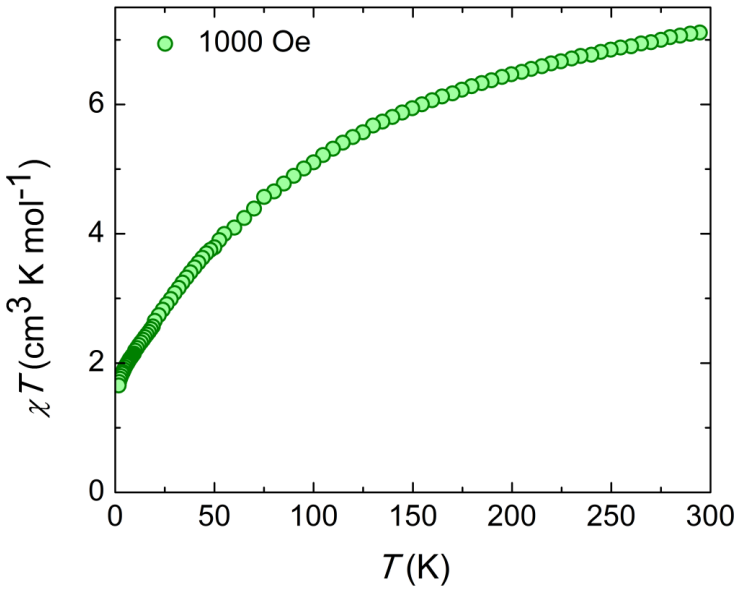

Figure 60. Variable-temperature dc magnetic susceptibility ($\chi = M/H$ per mole of compound) data for **NCS@UOTT-1**, collected under an applied field of 1000 Oe.

With a carefully engineered series of cationic MOFs in hand, we turned our attention to their anion-exchange capabilities. Not only can the **UOTT-1–3** series be prepared with different anions based simply on the choice of starting cobalt salts, but also, the anions can be replaced post-synthetically through exchange experiments. The first indication of being able to encapsulate anions of varying sizes and nature was through direct crystallographic visualization. In fact, the Br^-, NSC^-, ClO_4^-, and BF_4^- anions were successfully refined owing in part to their large electron densities and highly ordered states. The NO_3^- anions were also localized in **NO_3@UOTT-1** and **NO_3@UOTT-3** because of their very high crystal quality, despite being disordered. The lower electron density of NO_3^-, in combination with somewhat poorer-diffracting crystals, made it more difficult to observe the anionic guest in **NO_3@UOTT-2**. The crystallographic studies reveal that the anions take up significantly different positions within the framework to both maintain the necessary symmetry and optimize the host–guest interactions. For example, the bromide anions in **Br@UOTT-1** are stabilized by multiple dipole–dipole

interactions with H15 and H18, through distances of 2.95 and 2.74 Å, respectively, originating from the hydrogen atoms of either the benzene or the triazole ring of the Hcpt ligand (Fig. 61). Comparatively, the NCS^- anions in **NCS@UOTT-1** sit above the trinuclear cluster and are linked to the triazole moieties through S···π interactions (Fig. 62). Such host–guest interactions are strong and occur between the sulfur atom of NCS^- molecules and the centroid of adjacent triazole rings through a distance of 3.54 Å. In the case of **ClO_4@UOTT-2**, the ClO_4^- anions participate in anion···π interactions with the naphthalene rings of the tnc^- ligand (Fig. 63). The perchlorates adopt three distinct crystallographic orientations in the lattice, with occupancy factors of 0.33. All three overlapping orientations experience anion–host interactions between an oxygen atom (O52, O53, or O55) and a centroid of a naphthalene ring. These weak interactions are characterized by an average oxygen···centroid distance of 3.59 Å. Additional host–anion interactions involving NO_3^- and BF_4^- anions are shown in Figures 64–66.

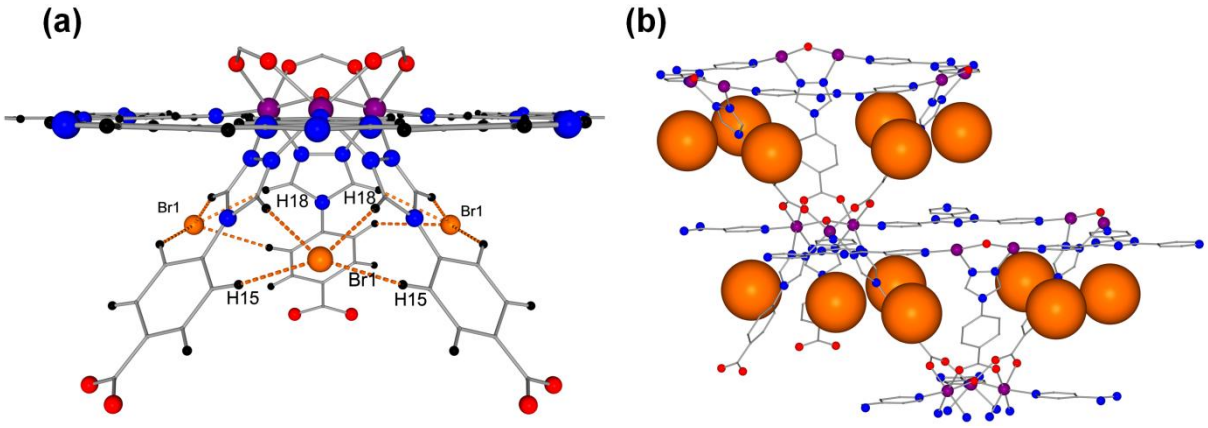

Figure 61. Molecular fragment of **Br@UOTT-1** displaying the dipole-dipole interactions between the Br^- anions and the hydrogen atoms of the benzene and 1,2,4-triazole rings of the cpt^- ligands (a). The positions of the Br^- anions within the MOF are shown in a space-filling model (b).

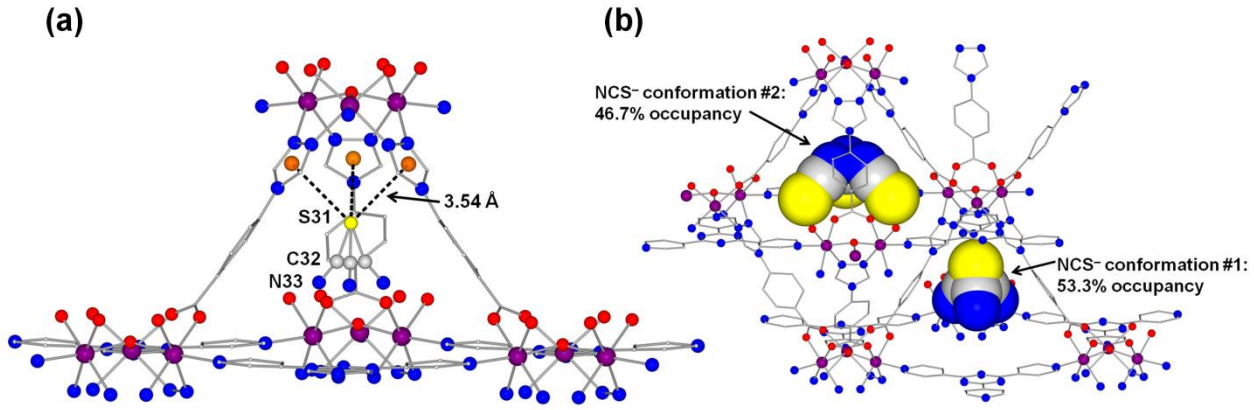

Figure 62. Molecular fragment of **NCS@UOTT-1** displaying the S···π interactions between the NCS^- anions and the centroid of the 1,2,4-triazole ring (a). The positions of the NCS^- anions within the MOF are shown in a space-filling model (b). All 3 symmetry equivalent positions of the NCS^- anions are shown to display all possible orientations.

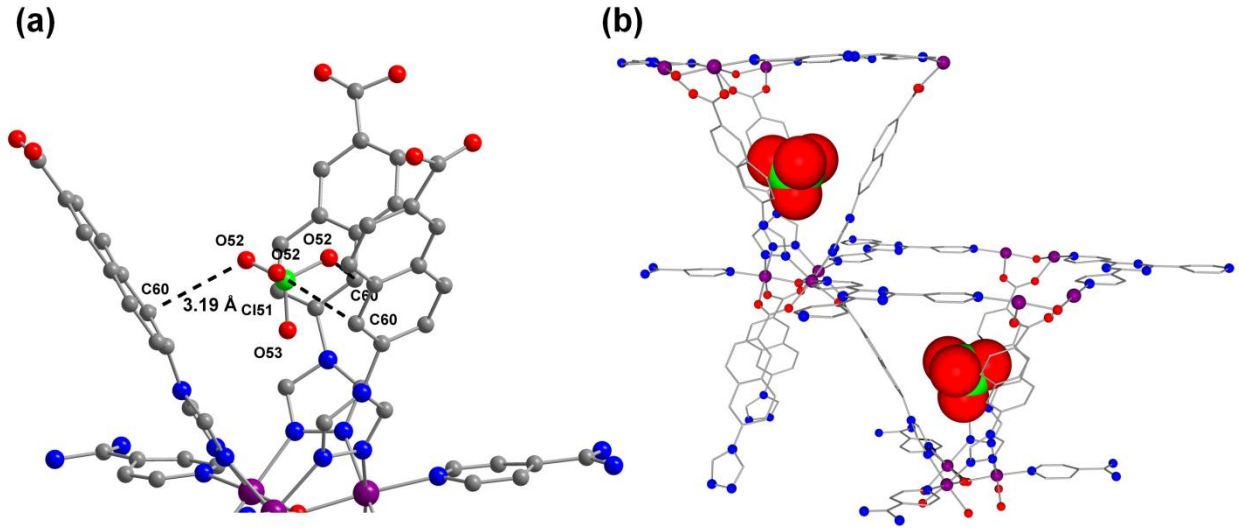

Figure 63. Molecular fragment of **ClO_4@UOTT-2** displaying the anion···π interactions between the ClO_4^- anions and the naphthalene rings of the tnc^- ligand (a). The positions of the ClO_4^- anions within the MOF are shown in a space-filling model (b).

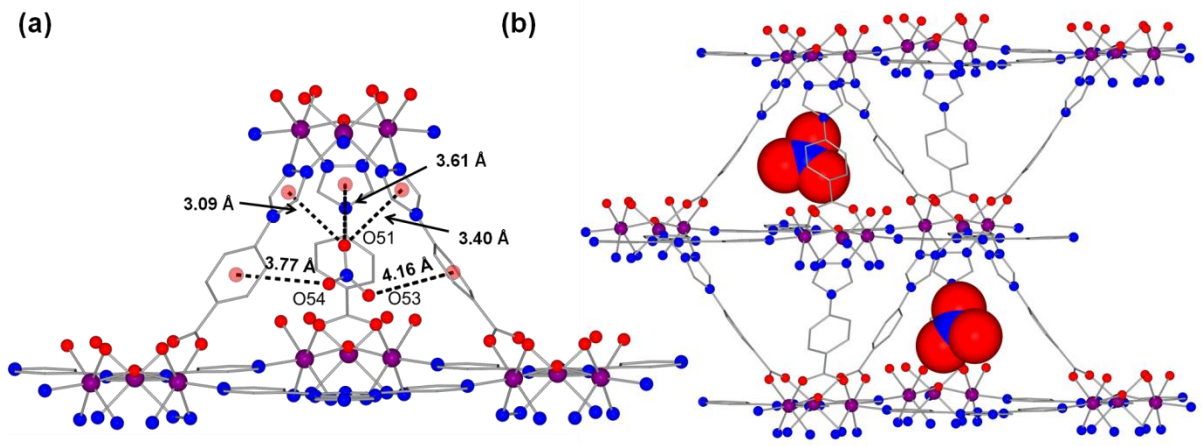

Figure 64. Molecular fragment of **NO_3@UOTT-1** displaying the anion-π interactions between the NO_3^- anions and the centroids of the benzene and 1,2,4-triazole rings of the cpt^- ligands (a). The positions of the NO_3^- anions within the MOF are shown in a space-filling model (b). Positional disorder has been omitted for clarity.

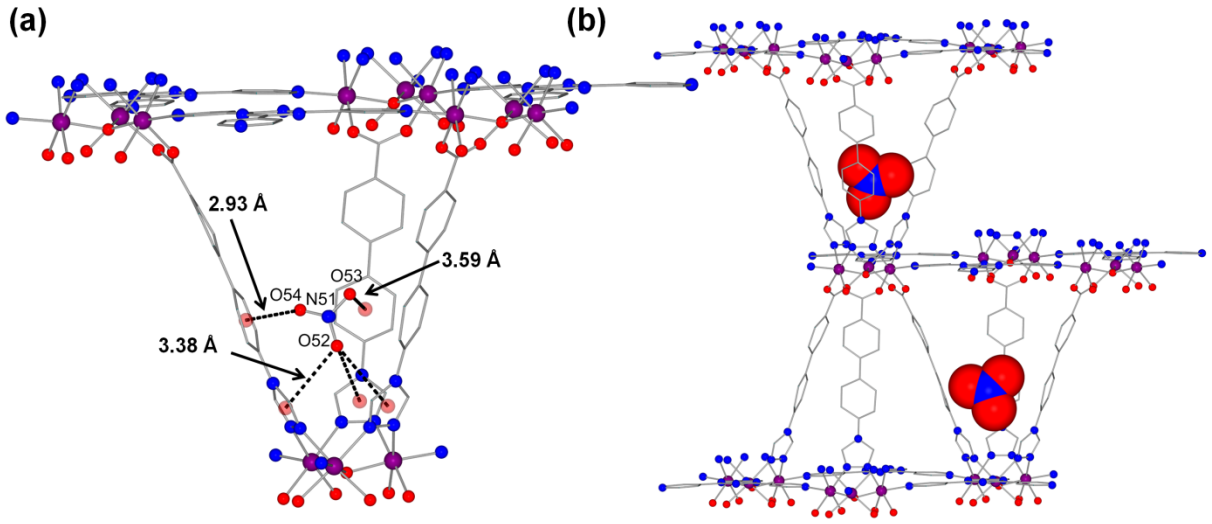

Figure 65. Molecular fragment of **NO_3@UOTT-3** displaying the anion···π interactions between the NO_3^- anions and the benzene and 1,2,4-triazole rings of the $bpct^-$ ligand (a). The positions of the NO_3^- anions within the MOF are shown in a space-filling model (b). Positional disorder is omitted for clarity.

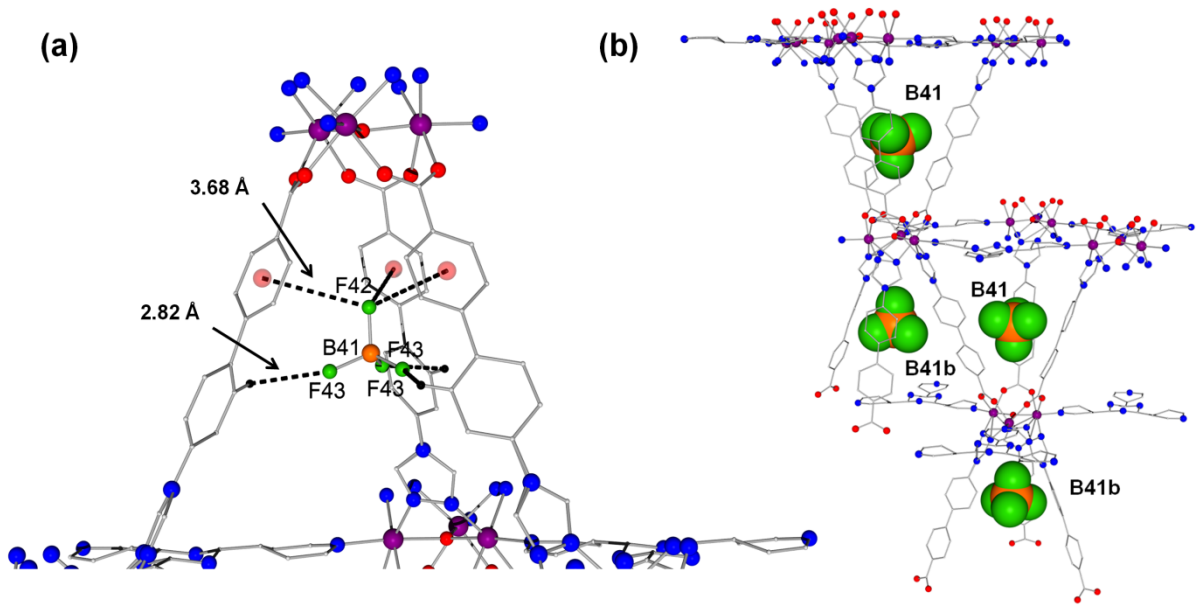

Figure 66. Molecular fragment of **BF_4@UOTT-3** displaying the anion···π and hydrogen bond interactions between the BF_4^- anions and the biphenyl rings of the $bpct^-$ ligand (a). The positions of the BF_4^- anions within the MOF are shown in a space-filling model (b).

6.5 **Kinetic infrared spectroscopy study**

Beyond the crystallographic evidence, the individual anions can also be confirmed by FT-IR spectroscopy, as shown in Fig. 67. Characteristic bands belonging to NO_3^-, NSC^-, ClO_4^-, and BF_4^- anions are readily distinguished at ≈1390, 2068, 1090, and 754 cm^{-1}, respectively. To investigate anion affinity, we have selected the Hcpt-based frameworks and performed kinetic FT-IR studies, allowing us to directly probe the binding strength of the anions. In a typical experiment, samples of **UOTT-1** were immersed in a chloroform solution containing a different anion. By following the aforementioned bands through FT-IR spectroscopy, it is possible to observe the anion-exchange process, thus providing a means of determining the order of affinity of the guests (Fig. 68 and 69). To summarize these results, we have determined the following order of affinity of the guest anions: $NCS^- > BF_4^- > Br^- > ClO_4^- > NO_3^-$, as outlined in Table 23. Furthermore, these results are corroborated by the density functional theory (DFT)-calculated

binding energies of the anions to the framework (*vide infra*). Interestingly, the incorporation of strongly binding NCS^- anions is accompanied by a drastic change in the color of the materials from orange to green. Thus, the presented compounds have the ability to act as visual colorimetric anion sensors for NCS^-. Due to the fact that a single monoanion is required to balance the charges, the optimal capacity of the **UOTT-1** materials ranges from 51.5 to 93.1 mg g^{-1} for the five anions studied.

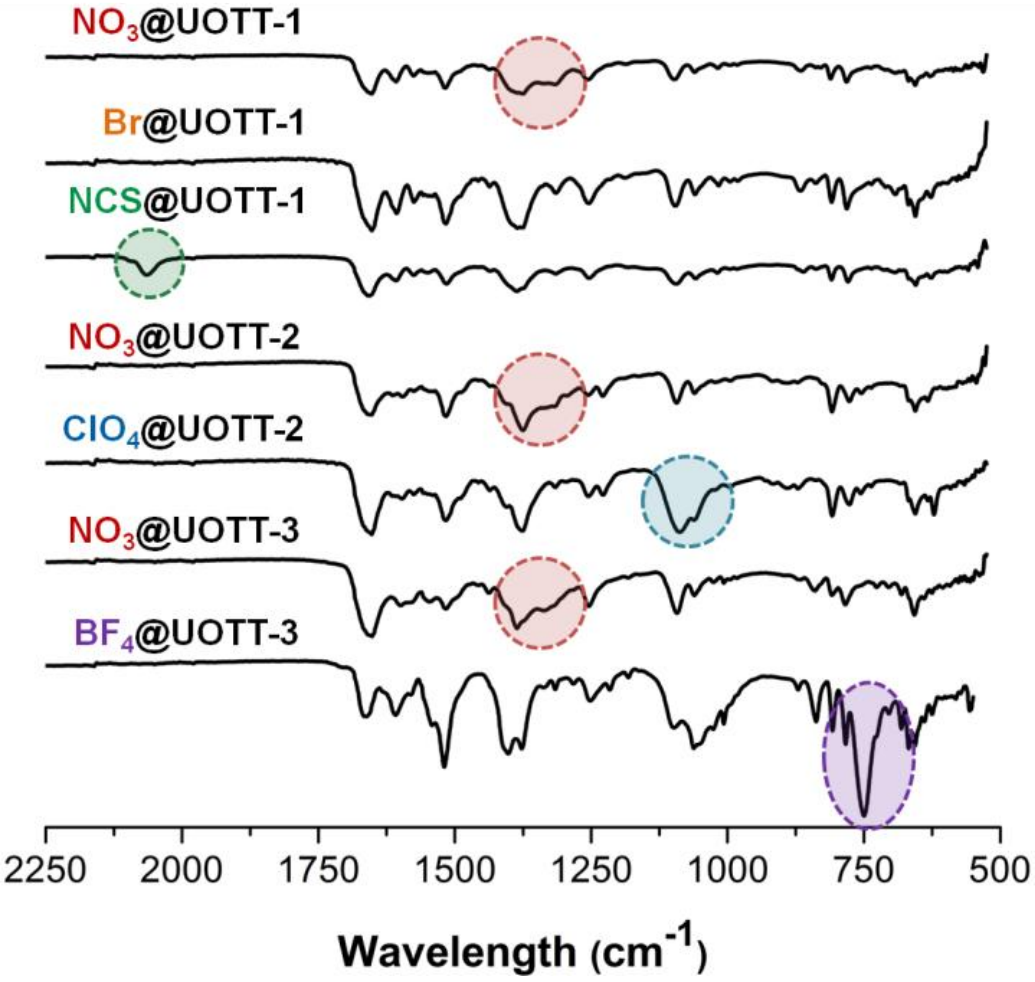

Figure 67. IR spectra of the as-synthesized MOFs, highlighting select bands of the corresponding anions.

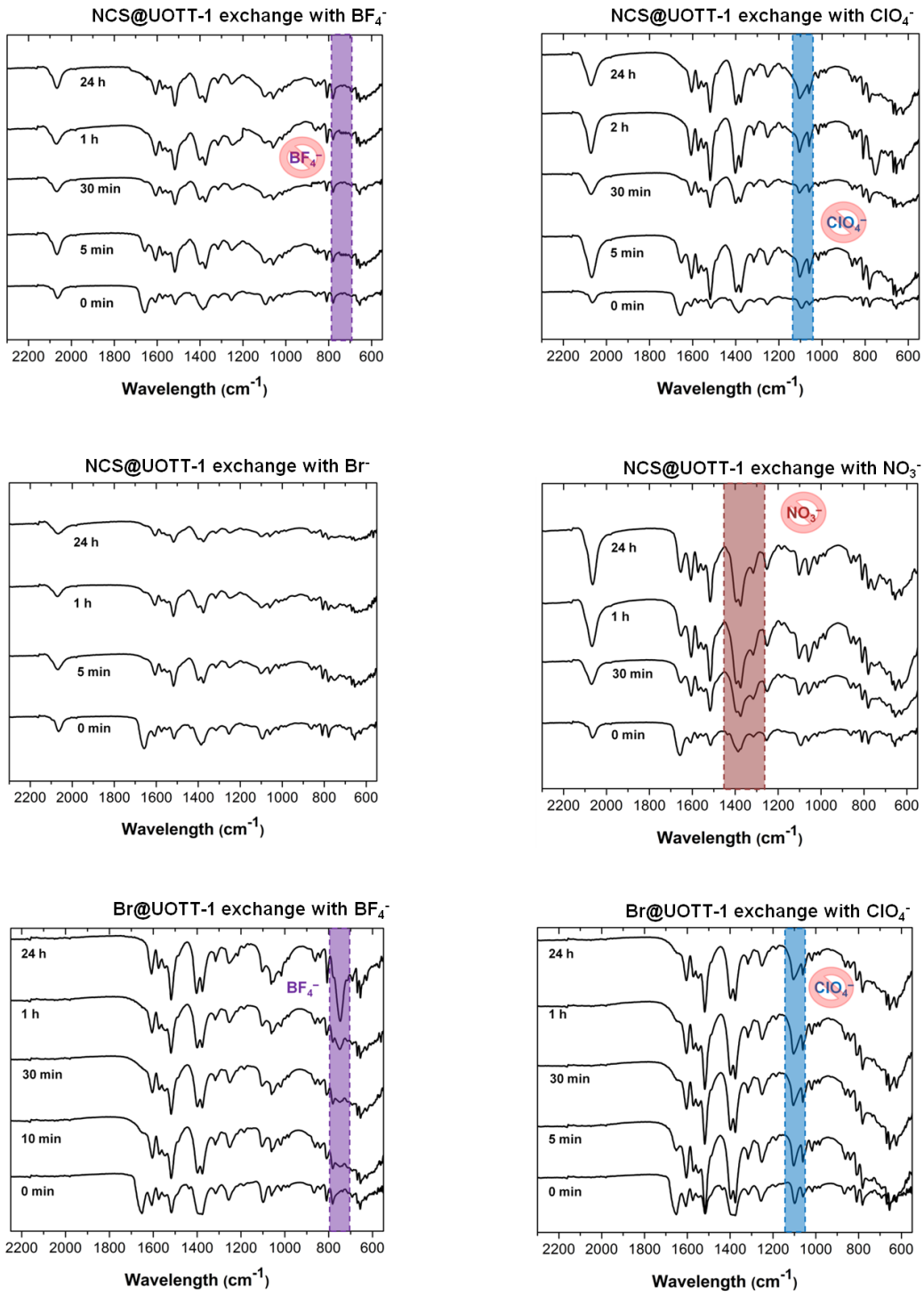

Figure 68. Infrared spectra of **NCS@UOTT-1** and **Br@UOTT-1** recorded over 24 hours, soaked in chloroform solutions of different tetrabutylammonium salts.

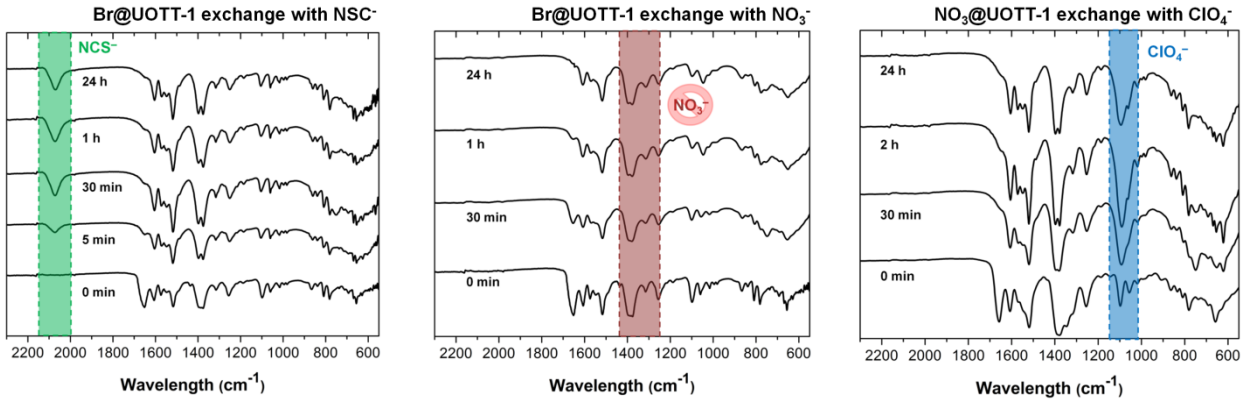

Figure 69. Infrared spectra of **Br@UOTT-1** and **NO_3@UOTT-1** recorded over 24 hours, soaked in chloroform solutions of different tetrabutylammonium salts.

In the previous FT-IR spectra, it should be noted that the disappearing band at ~1650 cm^{-1} corresponds to C=O stretches originating from DMF solvent molecules that are exchanged with $CHCl_3$ and are not affiliated with any anions. This also testifies to the fact that DMF solvent molecules are readily exchanged with $CHCl_3$, allowing for milder activation conditions to be used for the N_2 gas sorption experiments (*vide infra*).

Table 23. Summary of the anion-exchange process followed by FT-IR.

NCS@UOTT-1		**Br@UOTT-1**		**NO_3@UOTT-1**	
Anion to uptake	**Ion exchange**	**Anion to uptake**	**Ion exchange**	**Anion to uptake**	**Ion exchange**
BF_4^-	No	BF_4^-	Yes	ClO_4^-	Yes
ClO_4^-	No	ClO_4^-	No		
Br^-	No	NCS^-	Yes		
NO_3^-	No	NO_3^-	No		

6.6 Nuclear magnetic resonance spectroscopy

To complement the FT-IR studies and to determine the exchange capacity of the MOF, we have performed a series of solid-state NMR (ssNMR) and solution NMR spectroscopy experiments. Accurate determination of the extent of ion exchange is critical in assessing the efficacy of a material for any industrial application. Here, we show that nearly 100% of the BF_4^- anions in

BF_4@UOTT-3 can be exchanged by NSC^-, and this can be achieved by simple gravity filtration of a tightly packed bed of the MOF (Fig. 70). We have elected to perform these studies using BF_4^- anions because of the ease with which they can be monitored using NMR spectroscopy compared with other small monoanions (i.e., 100% natural abundance of ^{19}F). The ^{19}F magic-angle spinning (MAS) ssNMR spectrum of **BF_4@UOTT-3** was collected at room temperature before and after running the column. The initial material clearly reveals the presence of BF_4^- anions, with a peak centered at −161.6 ppm. Following anion exchange, by running a solution of tetrabutylammonium thiocyanate in chloroform through a packed bed of **BF_4@UOTT-3**, the resulting ^{19}F MAS ssNMR spectrum lacks all evidence of a peak for BF_4^- anions, suggesting that they have been fully exchanged. The anion-exchange process not only is essentially quantitative, but also occurs on a short time scale. By exchanging only one of the two carboxylic acids within the organic linker for a triazole group, we ensure that a single monoanion is required to balance the charges. Therefore, we avoid filling the entirety of the pore space with anions, thus maintaining significant porosity, which in turn likely contributes to the fast exchange kinetics that is observed in both NMR and FT-IR. The broad band centered at approximately −136.0 ppm, present in both spectra, was confirmed as being probe background by running a blank under identical conditions, whereas NaF was used as an internal standard, should there have been a need for a quantitative estimate of the amount of remaining BF_4^- anions. To unequivocally confirm the anion-exchange process, ^{19}F NMR was also performed on the resulting solution that passed through the MOF column, clearly revealing the exchanged BF_4^- anions as two resonance peaks separated by 0.05 ppm. The low-frequency 1:1:1:1 quartet corresponds to $^{11}BF_4^-$, whereas the high-frequency resonance is an unresolved 1:1:1:1:1:1:1 septet, identified as $^{10}BF_4^-$.

Moreover, the intensity ratio of 20:80 matches very well with the natural abundances of ^{10}B and ^{11}B, respectively.

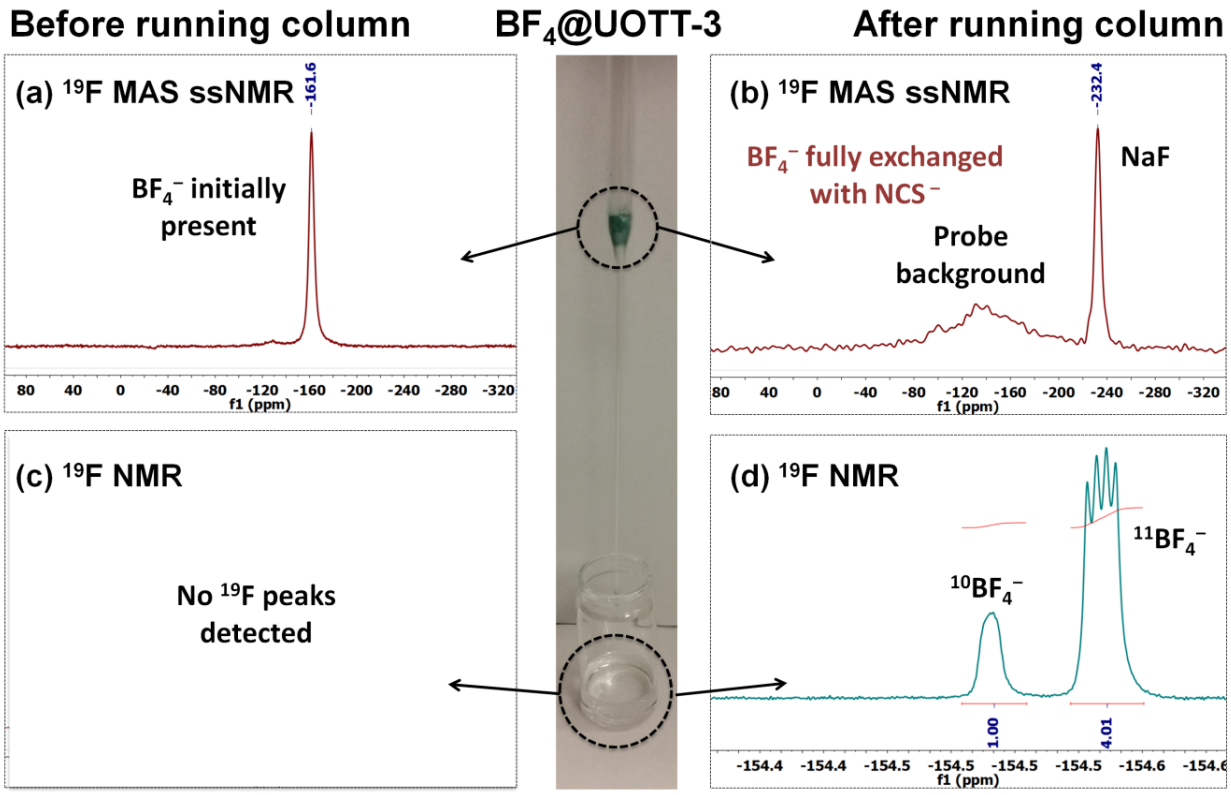

Figure 70. Solid-state and solution ^{19}F NMR spectra recorded before and after running a chloroform solution of tetrabutylammonium thiocyanate through a packed bed of **BF_4@UOTT-3**. Solid-state ^{19}F MAS NMR spectra of the as-synthesized **BF_4@UOTT-3** sample (a) and after running the gravity filtration column (b). Solution-state ^{19}F NMR before (c) and after running the column (d), displaying the emergence of BF_4^- anions.

6.7 Effect of the anion-binding strength on N_2 gas adsorption behaviours

As mentioned, cationic MOFs are generally less stable than their neutral counterparts. It is also tempting to gauge the robustness of a MOF based solely on the metal cation and organic linkers. Given the highly porous and tunable features of the present isoreticular MOFs, we sought to examine their ability to generate permanently porous structures and how different anions, with varying binding strengths, may impact this behaviour. To gain further insight, we tested all

MOFs under various activation conditions for N_2 gas sorption experiments. The optimal conditions consisted of exchanging the dimethylformamide solvent molecules with $CHCl_3$ and subsequent activation at 100 °C overnight. It should be noted that the activation of the as-synthesized samples at 150 °C, as reported for a closely related material,[74] resulted in the sublimation of a white product that was identified as the starting ligand. This is presumably due to the partial collapse of the cationic frameworks upon activation (*vide infra*). The Brunauer–Emmett–Teller (BET) surface areas obtained through the milder activation conditions and $CHCl_3$ solvent-exchange procedure are reported in Table 24. The lower-than-expected values further suggest partially collapsed structures upon activation. Nevertheless, the N_2 sorption isotherms indicate that all samples, with the exception of **NO_3@UOTT-2** and **NO_3@UOTT-3**, display permanent porosity (Fig. 71) and a dependence of the porosity on the anion present.

Table 24. Summary of the N_2 gas sorption data for the **UOTT-1**, **UOTT-2**, and **UOTT-3** families using optimal activation conditions. The experimental BET surface area values display a clear dependence with the strength of the anion binding energies, as determined through DFT calculations.

Compound code	Calculated BET surface area (m^2/g)	Experimental BET surface area (m^2/g)	Anion binding energy (kJ/mol)	Total pore volume (cm^3/g)
NO_3@UOTT-1	2202.5	474.1	61.8	0.305
Br@UOTT-1	2163.5	691.8	78.6	0.419
NCS@UOTT-1	2196.8	824.7	94.4	0.324
NO_3@UOTT-2	2638.6	24.9	34.8	0.029
ClO_4@UOTT-2	2541.7	836.0	66.9	0.339
NO_3@UOTT-3	3107.0	18.8	24.7	0.026
BF_4@UOTT-3	3034.7	508.2	41.5	0.259

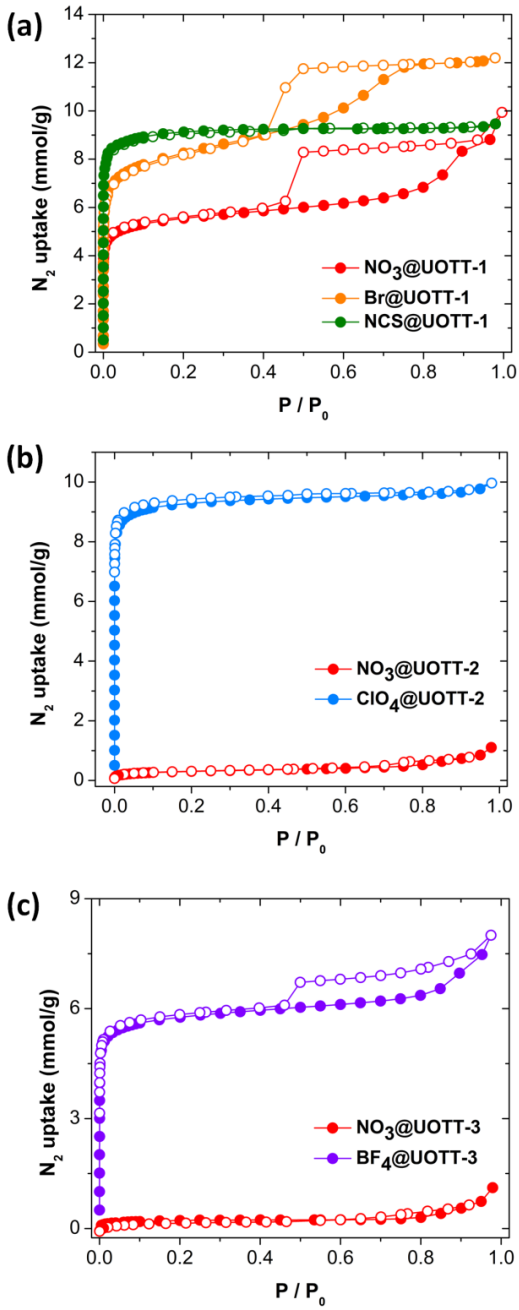

Figure 71. N_2 adsorption isotherms for the **UOTT-1** (a), **UOTT-2** (b) and **UOTT-3** (c) series, collected at 77 K. The isotherms suggest a strong dependence of the porosity upon the binding strength of the anion. The presence of hysteresis in the more weakly bound anions may be attributed to the mobility and reorientation of the anions upon gas loading.

The partial structural collapse in the cationic frameworks is further substantiated by powder X-ray diffraction data (Fig. 72), where we observe a significant loss in the crystallinity and long-range order of the two aforementioned samples upon activation. Interestingly, the use

of different anions in the frameworks of **UOTT-2** and **UOTT-3** (instead of NO_3^-) allows the retention of porosity as in the case of **ClO_4@UOTT-2** and **BF_4@UOTT-3**. In fact, these findings, in conjunction with other recently reported cationic frameworks,[75] suggest that more strongly binding anions limit the contraction of the framework upon activation and allow the frameworks to better retain porosity. Indeed, the binding energies of the anions and their respective frameworks were calculated by DFT (Table 24), which revealed that the NO_3^- anions continually give the lowest binding energies. Within the **UOTT-1** family, the significant difference in the experimental BET surface area among the three different anions (NO_3^-, Br^-, and NCS^-) cannot be explained simply by their varying sizes and geometries. It is noteworthy that there is a clear trend between the DFT-calculated binding energies and the experimental BET surface areas, where the more strongly binding anions result in markedly higher surface areas. Further evidence of the importance of the binding strength of the anions for maintaining porosity can be observed in the shape of the N_2 isotherms. The more weakly bound anions display hysteresis, whereas this behaviour is absent in the more strongly bound anions. Such a feature presumably originates from the reorientation of the anions to better accommodate the gaseous molecules and is reinforced by the fact that the opening of the hysteresis is greatest in the weakest bound anion (NO_3^-). We cannot, however, entirely rule out the possibility of a phase change upon gas loading.

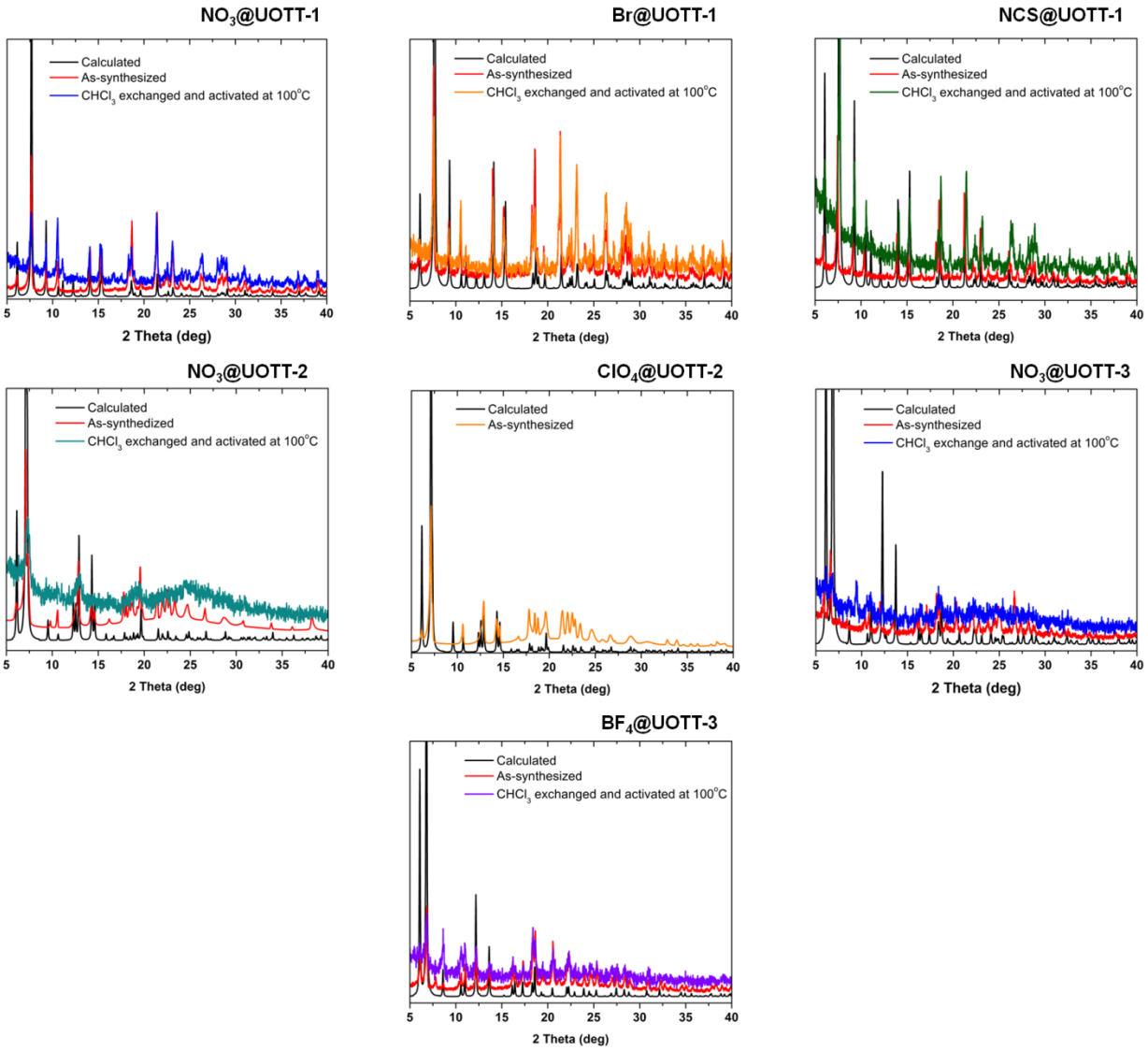

Figure 72. PXRD patterns of the calculated, as-synthesized and solvent exchanged and activated cationic MOF samples. In some cases, the loss in crystallinity following solvent exchange and activation is shown, likely due to partial structural collapse, resulting in minimal N_2 uptake.

It was also found that the larger MOF variants led to lower binding energies, as expected. The binding energies for NO_3^- decrease from 61.8 to 34.8 and 24.7 kJ mol^{-1} when going from **UOTT-1** to **UOTT-2** and **UOTT-3**, respectively. This may explain why **NO_3@UOTT-1** retains porosity, whereas **NO_3@UOTT-2** and **NO_3@UOTT-3** exhibit significant structural collapse upon activation. In fact, within this family of MOFs, it appears that an anion would require a

binding energy of >40 kJ mol^{-1} to keep the pores open upon activation. Furthermore, the calculated binding energies confirm the previously established trend of anion affinity (*vide supra*), with NCS^- being the most strongly bound anion (94.4 kJ mol^{-1}). Overall, this represents a rare example where permanent porosity can be tuned *via* the anion-exchange process and provides an avenue toward tuning the structural stability of cationic frameworks. As such, we demonstrate that the exchange of weakly bound anions, such as NO_3^- ions in this case, with more strongly binding anions provides a facile avenue to retain porosity. Therefore, we can foresee overcoming some of the porosity limitations that have frequently been plaguing cationic MOFs.

6.8 **Conclusion**

In this work, we have demonstrated a strategy that allows for the generation of a charged framework without any alterations to the desired topology or metal ions. Furthermore, we have shown the importance of the anion-binding strength in tuning the porosity of such materials, which is vital in retaining the desirable features of MOFs. An increase in the binding strength of the anion allows the cationic frameworks to display improved surface areas. In this family of MOFs, a binding strength of >40 kJ mol^{-1} appears to be required to maintain porosity. In addition to this, we can envision further tuning of the *pacs* platform using a combination of techniques, such as the pore-space partition and the ALE strategy, allowing for an optimization of the hydrophobicity and basicity of the organic linkers, which may lead to desired hydrolytic stability. Here, the ALE method joins a limited group of strategies for framework ionization that targets exciting applications encompassing anionic drug delivery and chemical sensing. This proof-of-principle study, where a series of cationic frameworks have been rationally constructed, can serve as a blueprint toward the design of high-performance anion-exchange materials.

6.9 Experimental section

6.9.1 General considerations

All manipulations were performed under aerobic conditions using materials as received from commercial suppliers (Strem Chemical, Sigma Aldrich). The organic ligands 4-(4'-carboxyphenyl)-1,2,4-triazole (Hcpt)[76] and 2,4,6-tri(4-pyridyl)-1,3,5-triazine (tpt)[77] were prepared according to previously published procedures.

6.9.2 Synthesis

Synthesis of 6-(4*H*-1,2,4-triazol-4-yl)-2-naphthoic acid (Htnc): Formic acid hydrazide (90%, 0.11 g, 1.83 mmol) was placed in a microwave tube containing 5 mL of 99% EtOH. After dissolution, triethylorthoformate (0.47 mL, 2.83 mmol) was added and the sealed tube was mounted in a Biotage initiator microwave. After 5 min at 150 ^{o}C, a clear slightly pink solution was obtained, corresponding to the formation of diformylhydrazide. The vial cap was opened and 6-amino-2-naphthoic acid (0.34 g, 1.82 mmol) was added immediately after the first reaction and placed back in the microwave. The reactions conditions for the formation of Htnc remained the same as in the previous step. The product precipitated in the form of a pale grey powder and was washed with ethanol and diethyl ether. NMR ^{1}H (DMSO-d_6, 400 MHz): δ (ppm) 13.16 (br, 1H), 9.31 (s, 2H), 8.70 (s, 1H), 8.37 (m, 2H), 8.06 (m, 2H), 7.98 (dd, 1H). Yield: 57.5 %.

Synthesis of 4'-(4*H*-1,2,4-triazol-4-yl)biphenyl-4-carboxylic acid (Hbpct): Formic acid hydrazide (90%, 0.11 g, 1.83 mmol) was placed in a microwave tube containing 5 mL of 99% EtOH. After dissolution, triethylorthoformate (0.47 mL, 2.83 mmol) was added and the sealed tube was mounted in a Biotage initiator microwave. After 5 min at 150 ^{o}C, a clear slightly pink solution was obtained, corresponding to the formation of diformylhydrazide. The vial cap was opened and 4'-aminobiphenyl-4-carboxylic acid (0.39 g, 1.83 mmol) was added immediately

after the first reaction and placed back in the microwave. The reactions conditions for the formation of Hbpct remained the same as in the previous step. The product precipitated in the form of a pale orange powder and was washed with ethanol and diethyl ether. NMR ^{1}H (DMSO-d_6, 400 MHz): δ (ppm) 12.90 (br, 1H), 9.18 (s, 2H), 8.01 (d, 2H), 7.91 (d, 2H), 7.84 (d, 2H), 7.82 (d, 2H). Yield: 41.8%.

Synthesis of NO_3@UOTT-1: In a 20 mL glass vial, $Co(NO_3)_2 \cdot 6H_2O$ (60 mg, 0.20 mmol), Hcpt (38 mg, 0.20 mmol), and tpt (21 mg, 0.067 mmol) were placed in 3 mL of DMF. The resulting mixture was sonicated for 10 min, after which the contents of the glass vial were transferred to a 23 mL Teflon cup and sealed into a stainless steel autoclave. Next, the vessel was heated to 120 ^{o}C for 48 hours and cooled to room temperature over an additional 24 hours, yielding a mixture of orange block-like crystals and microcrystalline powder corresponding to the same compound. Phase purity was confirmed by powder X-ray diffraction. Yield = 43.4 %.

Synthesis of Br@UOTT-1: In a 20 mL glass vial, anhydrous $CoBr_2$ (44 mg, 0.20 mmol), Hcpt (38 mg, 0.20 mmol), and tpt (21 mg, 0.067 mmol) were placed in 4.5 mL of DMF. The resulting mixture was sonicated for 10 min, after which the contents of the glass vial were transferred to a 23 mL Teflon cup and sealed into a stainless steel autoclave. Next, the vessel was heated to 120 ^{o}C for 72 hours and cooled to room temperature over an additional 48 hours, yielding pale orange block-like crystals. Phase purity was confirmed by powder X-ray diffraction. Yield = 35.3%.

Synthesis of NCS@UOTT-1: In a 20 mL glass vial, $Co(NCS)_2$ (36 mg, 0.20 mmol), Hcpt (38 mg, 0.20 mmol), and tpt (21 mg, 0.067 mmol) were placed in 4.5 mL of DMF. The resulting mixture was sonicated for 10 min, after which the contents of the glass vial were transferred to a

23 mL Teflon cup and sealed into a stainless steel autoclave. Next, the vessel was heated to 120 ^{o}C for 72 hours and cooled to room temperature over an additional 48 hours, yielding green block-like crystals. Phase purity was confirmed by powder X-ray diffraction. Yield = 30.6%.

Synthesis of NO_3@UOTT-2: In a 20 mL glass vial, $Co(NO_3)_2 \cdot 6H_2O$ (60 mg, 0.20 mmol), Htnc (48 mg, 0.20 mmol), and tpt (21 mg, 0.067 mmol) were placed in 4.5 mL of DMF. The resulting mixture was sonicated for 10 min, after which the contents of the glass vial were transferred to a 23 mL Teflon cup and sealed into a stainless steel autoclave. Next, the vessel was heated to 120 ^{o}C for 72 hours and cooled to room temperature over an additional 48 hours, yielding orange block-like crystals. Phase purity was confirmed by powder X-ray diffraction. Yield = 31.6%.

Synthesis of ClO_4@UOTT-2: In a 20 mL scintillation vial, $Co(ClO_4)_2 \cdot 6H_2O$ (75 mg, 0.20 mmol), Htnc (48 mg, 0.20 mmol), and tpt (21 mg, 0.067 mmol) were placed in 4.0 mL of DMF. The resulting mixture was sonicated for 10 min and heated to 120 ^{o}C for 48 hours and cooled to room temperature over an additional 48 hours, yielding orange block-like crystals. Phase purity was confirmed by powder X-ray diffraction. Yield = 37.6%.

Synthesis of NO_3@UOTT-3: In a 20 mL glass vial, $Co(NO_3)_2 \cdot 6H_2O$ (60 mg, 0.20 mmol), Hbpct (53 mg, 0.20 mmol), and tpt (21 mg, 0.067 mmol) were placed in 5.0 mL of DMF. The resulting mixture was sonicated for 10 min, after which the contents of the glass vial were transferred to a 23 mL Teflon cup and sealed into a stainless steel autoclave. Next, the vessel was heated to 120 ^{o}C for 48 hours and cooled to room temperature over an additional 48 hours, yielding orange block-like crystals. Phase purity was confirmed by powder X-ray diffraction. Yield = 38.2%.

Synthesis of BF_4@UOTT-3: In a 20 mL glass vial, $Co(BF_4)_2 \cdot 6H_2O$ (68 mg, 0.20 mmol), Hbpct (53 mg, 0.20 mmol), and tpt (21 mg, 0.067 mmol) were placed in 4.5 mL of DMF. The resulting

mixture was sonicated for 10 min, after which the contents of the glass vial were transferred to a 23 mL Teflon cup and sealed into a stainless steel autoclave. Next, the vessel was heated to 120 ^{o}C for 48 hours and cooled to room temperature over an additional 48 hours, yielding orange block-like crystals. Phase purity was confirmed by powder X-ray diffraction. Yield = 35.9%.

Activation of samples for gas sorption: To achieve optimal activation conditions, all MOFs were filtered, washed with DMF, and subsequently immersed in $CHCl_3$ over 3 days. At least once a day, the $CHCl_3$ solution was decanted and replaced by a fresh solution of $CHCl_3$. The exchange of DMF by $CHCl_3$ is clearly evidenced in the time-resolved FT-IR studies, where we observe the disappeared of the C=O peak at ~1650 cm^{-1}.

6.9.3 **Instrumentation and methods**

Single-crystal X-ray diffraction. Single crystal X-ray diffraction data were collected on a Bruker Kappa Apex II CCD diffractometer with graphite-monochromatised Mo-Kα radiation. Prior to the diffraction experiment, the crystals were flash frozen to 200 K using cooled air. Data collection was performed with the Bruker APEX II software package[78] and processing was performed with the Bruker APEX II software package or CrysAlis^{PRO} (Version 1.171.37.35). Data were corrected for absorption (SADABS[79] when processed by APEX II, or by the implemented absorption correction when CryAlis^{PRO} was used[80]). The structures were solved by SHELXT[81] and refined by full matrix least-squares against F^2 using SHELXL2014/7.[82] All non-hydrogen atoms were refined anisotropically with H atoms placed in riding mode with isotropic temperature factors fixed at 1.2 times the U_{eq} factors of the parent atoms. The obtained MOF structures comprise of a tpt ligand that is common to all reported structures and a second organic linker that is used to control the pore size of the MOFs.

The asymmetric linkers consist of a triazole head separated by an aromatic ring system (phenyl, naphtyl or biphenyl) from a carboxylic acid tail, which are positioned onto a mirror plane, running through the length of the linkers. In the here reported structures, the aromatic ring system is found to be disordered and appropriate restraints were needed to properly refine this disorder, apart for the refinement of structure **NO3@UOTT-1**, where the data quality allowed unrestrained refinement of the whole framework. In structure of **BF4@UOTT-3**, the triazole and carboxylate anchor points are interchanged in a 50/50 ratio, which is refined as an additional disorder on top of the disorder of the biphenyl system as found in the other structures.

The structures are found to crystallize in non-centrosymmetric space groups ($P6_3/mc$ or $P31c$), see Tables 25-27, and were all refined as twinned by inversion. The symmetry reduction from $P6_3/mc$ to its subgroup $P31c$ for the **UOTT-2** structures is a direct result of the point symmetry of the **UOTT-2** linker, which due to its naphthalene moiety, does not hold an internal mirror plane/rotation axis. Nevertheless, the nature of the observed disorder for the **UOTT-2** linker, mimics the higher $P6_3/mc$ symmetry.

The located anions were found in the electron density using the ligand fitting tool in Coot[83] and refined as rigid moieties in the case of ClO_4 and NO_3, the occupancies were set to accommodate the site multiplicity, in accordance to the charge balance of the cationic MOFs. The NCS^- anion in **NCS@UOTT-1** was refined with bond distance and angle distance restraints and the BF_4^- anion in **BF4@UOTT-3** was found to be disordered over 2 sites both on 3 fold axes, with 73/27 ratio. Similarity restraints were added to the bond distances and the angle distances. The nitrate anion in **NO_3@UOTT-1** was found to be disordered around the 3-fold axis.

For structure of **NO_3@UOTT-2**, the anion was not located, this is on one hand explained by the low electron density of the NO_3^- anion, which could be even lower in case of disorder (as in **NO_3@UOTT-1**) and on the other hand because of the lower crystal quality (refinement cut-off 0.88 Å). Moreover, the tpt ligand is also found to be fully disordered over two positions. For most of the datasets, data cut-offs were imposed either during data integration or during refinement. The resolution cut-off (if any) are reported in Tables 25-27. The completeness is either to the resolution corresponding to the sin θ/λ ratio of 0.6, or to the imposed resolution cut-off.

Table 25: Crystallographic data for the **UOTT-1** series.

Compound	**NO_3@UOTT-1**	**Br@UOTT-1**	**NCS@UOTT-1**
Empirical Formula	$Co_3C_{45}H_{30}N_{16}O_{10}$	$Co_3C_{45}H_{30}N_{15}O_7Br$	$Co_3C_{46}H_{30}N_{16}O_7S$
Formula weight (g/mol)	1131.64	1149.54	1127.71
Crystal system	Hexagonal	Hexagonal	Hexagonal
Space group	$P6_3/mc$	$P6_3/mc$	$P6_3/mc$
a (Å)	16.7567(5)	16.6968(9)	16.8384(10)
b (Å)	16.7567(5)	16.6968(9)	16.8384(10)
c (Å)	19.0343(7)	18.9684(10)	19.0516(13)
α (°)	90	90	90
β (°)	90	90	90
γ (°)	120	120	120
V (Å^3)	4628.5(3)	4579.6(5)	4678.0(6)
Z	2	2	2
ρ_{calc} (g cm^{-3})	0.812	0.834	0.801
T (K)	200(2)	200(2)	200(2)
Wavelength (Å)	0.71073	0.71073	0.71073
μ (mm^{-1})	0.571	1.008	0.584
F (000)	1146	1154	1142
Crystal size	0.19 × 0.16 × 0.16	0.27 × 0.13 × 0.09	0.28 × 0.20 × 0.04
θ range (°) / resolution (Å)	1.765 to 30.608 / 0.70	1.771 to 24.753 / 0.85	1.759 to 25.231 / 0.83
Reflections Collected	70484	37714	17060
Independent reflections	4875	2916	2721
Completeness (%)	99.9	99.9	99.9
Data / restr. / param.	4875 / 31 / 170	2916 / 40 / 147	2721 / 113 / 163
Goodness of fit on F^2	1.045	1.004	1.072
R_1, wR_2 ($I > 2\sigma(I)$)[a]	0.0404, 0.0880	0.0368, 0.0941	0.0644, 0.1459
R_1, wR_2 (all data)	0.0480, 0.0923	0.0469, 0.988	0.0754, 0.1539
Flack (twin by inversion)	0.28(2)	0.54(3)	0.28(6)
Δρ max and min (e.Å^3)	0.577 and -0.248	0.375 and -0.322	0.577 and -0.631

[a] $R = R_1 = \sum||F_o| - |F_c||/\sum|F_o|$; $wR_2 = \{\sum[w(F_o^2 - F_c^2)^2]/\sum[w(F_o^2)^2]\}^{1/2}$; $w = 1/[\sigma^2(F_o^2)+(ap)^2 + bp]$, where $p = [\max(F_o^2, 0) + 2F_c^2]/3$; and $Rw = [w(|F_o| - |F_c|)^2 / w|F_o|^2]^{1/2}$, where $w = 1/\sigma^2(|F_o|)$.

Table 26: Crystallographic data for the **UOTT-2** series.

Compound	**NO_3@UOTT-2**	**ClO_4@UOTT-2**
Empirical Formula	$Co_3C_{57}H_{36}N_{15}O_7$	$Co_3C_{57}H_{36}N_{15}O_{11}Cl$
Formula weight (g/mol)	1219.80	1319.25
Crystal system	Trigonal	Trigonal
Space group	$P3_1c$	$P3_1c$
a (Å)	16.6264(7)	16.6138(8)
b (Å)	16.6264(7)	16.6138(8)
c (Å)	24.2500(13)	24.2258(12)
α (°)	90	90
β (°)	90	90
γ (°)	120	120
V (Å^3)	5805.5(6)	5790.9(6)
Z	2	2
ρ_{calc} (g cm^{-3})	0.698	0.757
T (K)	200(2)	200(2)
Wavelength (Å)	0.71073	0.71073
μ (mm^{-1})	0.456	0.485
F (000)	1240	1338
Crystal size	0.28 × 0.20 × 0.04	0.28 × 0.20 × 0.04
θ range (°) / resolution (Å)	2.196 to 23.814 / 0.88	1.415 to 25.669 / 0.82
Reflections Collected	20098	25592
Independent reflections	5110	7121
Completeness (%)	99.9	100.0
Data / restr. / param.	5110 / 324 /364	7121 / 358 / 394
Goodness of fit on F^2	1.004	1.045
R_1, wR_2 ($I > 2\sigma(I)$)[a]	0.0517, 0.1344	0.0587, 0.1499
R_1, wR_2 (all data)	0.0795, 0.1491	0.0945, 0.1790
Flack (twin by inversion)	0.19(5)	0.48(4)
Δρ max and min (e.Å^3)	0.236 and -0.352	0.376 and -0.521

[a] $R = R_1 = \sum||F_o| - |F_c||/\sum|F_o|$; $wR_2 = \{\sum[w(F_o^2 - F_c^2)^2]/\sum[w(F_o^2)^2]\}^{1/2}$; $w = 1/[\sigma^2(F_o^2)+(ap)^2 + bp]$, where $p = [\max(F_o^2, 0) + 2F_c^2]/3$; and $Rw = [w(|F_o| - |F_c|)^2 / w|F_o|^2]^{1/2}$, where $w = 1 / \sigma^2(|F_o|)$.

Table 27: Crystallographic data for the **UOTT-3** series.

Compound	**NO_3@UOTT-3**	**BF_4@UOTT-3**
Empirical Formula	$Co_3C_{63}H_{42}N_{16}O_{10}$	$Co_3C_{63}H_{42}N_{15}O_7BF_4$
Formula weight (g/mol)	1359.91	1384.71
Crystal system	Hexagonal	Hexagonal
Space group	$P6_3/mc$	$P6_3/mc$
a (Å)	16.6267(3)	16.7599(5)
b (Å)	16.6267(3)	16.7599(5)
c (Å)	28.9795(7)	29.0651(9)
α (°)	90	90
β (°)	90	90
γ (°)	120	120
V (Å^3)	6938.0(3)	7070.4(5)
Z	2	2
ρ_{calc} (g cm^{-3})	0.651	0.650
T (K)	200(2)	200(2)
Wavelength (Å)	0.71073	0.71073
μ (mm^{-1})	0.387	0.382
F (000)	1386	1406
Crystal size	0.39 × 0.25 × 0.15	0.29 × 0.27 × 0.11
θ range (°) / resolution (Å)	1.994 to 26.022 / 0.81	1.568 to 25.242 / 0.83
Reflections Collected	99904	41545
Independent reflections	5068	4743
Completeness (%)	99.8	99.8
Data / restr. / param.	5068 / 109 / 220	4743 / 344 / 252
Goodness of fit on F^2	1.033	1.103
R_1, wR_2 ($I > 2\sigma(I)$)[a]	0.0329, 0.0715	0.0501, 0.1168
R_1, wR_2 (all data)	0.0333, 0.0717	0.05, 0.1188
Flack (twin by inversion)	0.58(2)	0.51(4)
Δρ max and min (e.Å^3)	0.373 and -0.355	0.354 and -0.265

[a] $R = R_1 = \sum||F_o| - |F_c||/\sum|F_o|$; $wR_2 = \{\sum[w(F_o^2 - F_c^2)^2]/\sum[w(F_o^2)^2]\}^{1/2}$; $w = 1/[\sigma^2(F_o^2)+(ap)^2 + bp]$, where $p = [\max(F_o^2, 0) + 2F_c^2]/3$; and $Rw = [w(|F_o| - |F_c|)^2 / w|F_o|^2]^{1/2}$, where $w = 1/\sigma^2(|F_o|)$.

No solvent or other guest molecules could be located in the porous MOF structures, leaving large unoccupied solvent accessible voids (Table 28). These voids were treated by the Platon Squeeze procedure to account for the diffuse solvent contribution to the calculated structure factors.

Table 28. Summary of the accessible void space within the described cationic MOFs.

Compound code	Solvent accessible void (platon) ($Å^3$)	Unit cell Volume ($Å^3$)	Ratio
NO_3@UOTT-1	2561	4628.5	0.55
Br@UOTT-1	2506	4579.6	0.55
NCS@UOTT-1	2284	4678.0	0.49
NO_3@UOTT-2	3507 (†)	5805.5	0.60 († 0.57)
ClO_4@UOTT-2	3249	5790.9	0.56
NO_3@UOTT-3	4330	6938.0	0.62
BF_4@UOTT-3	4052 (‡)	7070.4	0.57 (‡ 0.60)

(†) As the NO_3^- anion was not located this void volume and ratio, taking into account the molecular volume of the nitrate anion, the corrected ratio would be 0.57
(‡) The BF_4^- anion was found over 2 sites, correcting for this lower calculated solvent accessible void, would result in a 0.60 ratio.

Powder X-ray diffraction. PXRD data for bulk samples were carried out using a Rigaku Ultima IV X-ray powder diffractometer. The Parallel Beam mode was employed to collect the data (λ = 1.541836 Å).

Infrared spectroscopy. IR analyses were performed with a Nicolet 6700 FT-IR spectrometer equipped with an ATR in the 4000-600 cm^{-1} range.

Magnetic measurements. Magnetic susceptibility measurements were performed using an MPMS-XL7 Quantum Design SQUID magnetometer. Direct current (dc) susceptibility measurements were performed at temperatures ranging from 1.9 to 300 K and performed on a crushed polycrystalline sample of 10.8 mg, and wrapped in a polyethylene membrane. Magnetization vs. field measurements were performed at 100 K in order to check for the presence of ferromagnetic impurities, which were found to be absent. The magnetic data was corrected for diamagnetic contributions using Pascal's constants.

Solid-state NMR spectroscopy. Solid-state ^{19}F MAS NMR spectra were collected on a Bruker AVANCE III 200 NMR spectrometer operating at 188.2 MHz equipped with a 2.5 mm MAS probe. The samples were spun at 25 kHz at the magic angle. The data were collected using a Hahn echo pulse sequence with delays synchronized to the MAS rotor cycle. The 90° pulse was 2.1 μsec. Spectra were collected with 128 scans using a recycle time of 5 seconds. Chemical shifts are reported with respect to $CFCl_3$ at 0 ppm.

Solution-state NMR spectroscopy. Solution-state ^{19}F NMR spectra were collected on a Bruker AVANCE II 300 NMR spectrometer operating at 282.5 MHz equipped with a 5 mm BBOF probe. The data were collected using a simple one-pulse sequence with using 30° pulses (3.0 μsec). Spectra were collected with 16 scans using a recycle time of 30 seconds. Chemical shifts are reported with respect to $CFCl_3$ at 0 ppm.

Computational details. Binding energies were calculated using periodic density functional theory (DFT) calculations using the *Vienna Ab initio Simulation Package* (VASP)[84,85] using the PBE functional[86,87] with a plane wave cut-off of 520 eV. Binding energies were calculated by using the atomic framework positions found in the SCXRD data. Initially, the empty frameworks had the positions of the hydrogen atoms optimized, where charge was neutralized with a constant background charge. Using those framework atomic positions, the anions were placed in their SCXRD positions and optimized with the framework atoms frozen. Anion binding energies were calculated using equation (**1**):

$$E_{\text{binding}} = -\frac{1}{2}\left(E_{MOF-anion} - E_{MOF\ empty} - 2E_{anion}\right) \quad (\mathbf{1})$$

where the energy of the anion was determined by placing it in an cell of the same dimensions as the MOF. The factor of ½ and 2 in the equation comes from the fact that there are two anions per unit cell required to neutralize the framework.

Gas adsorption measurements. The adsorption isotherms for N_2 (99.999%) were conducted using an Accelerated Surface Area & Porosimetry System (ASAP) 2020 supplied by Micromeritics Instruments Inc. The dry sample (~40 mg) was loaded into a glass analysis tube. For activation of the as-synthesized samples, the tube was heated at 150 °C under vacuum on a Schlenk line (~10^{-2} mbar) for 16 hours. However, this resulted in sublimation of starting material and thus the gas sorption analyses were not performed on these samples. The $CHCl_3$ exchanged samples were activated directly on the ASAP 2020, which were under vacuum (~10^{-6} mbar) and heated in two stages, initially to 60 °C at 1 °C min^{-1} for 2 hours then to 100 °C at 1 °C min^{-1} for 16 hours. After this, the outgas rate was less than 1 μbar hr^{-1}. The samples were then backfilled with N_2 before being transferred to the analysis port. Here, they were evacuated for a further 120 min before the analyses started.

6.10 **References**

(1) T. D. Bennett, A. K. Cheetham, A. H. Fuchs, F.-X. Coudert, *Nat. Chem.*, 2017, **9**, 11-16.

(2) H. Kim, S. Yang, S. R. Rao, S. Narayanan, E. A. Kapustin, H. Furukawa, A. S. Umans, O. M. Yaghi and E. N. Wang, *Science*, 2017, **356**, 430-434.

(3) M. Zhao, K. Yuan, Y. Wang, G. Li, J. Guo, L. Gu, W. Hu, H. Zhao and Z. Tang, *Nature*, 2016, **539**, 76-80.

(4) C. H. Hendon, A. J. Rieth, M. D. Korzzyński and M. Dincă, *ACS Cent. Sci.*, 2017, **3**, 554-563.

(5) R. J. Marshall, Y. Kalinovskyy, S. L. Griffin, C. Wilson, B. A. Blight and R. S. Forgan, *J. Am. Chem. Soc.*, 2017, **139**, 6253-6260.

(6) A. T. Gallagher, J. Y. Lee, V. Kathiresan, J. S. Anderson, B. M. Hoffman and D. T. Harris, *Chem. Sci.*, 2018, **9**, 1596-1603.

(7) P. A. Julien, C. Mottillo and T. Friščić, *Green Chem.*, 2017, **19**, 2729-2747.

(8) W. Zhang, G. Lu, C. Cui, Y. Liu, S. Li, W. Yan, C. Xing, Y. R. Chi, Y. Yang and F. A. Huo, *Adv. Mater.*, 2014, **26**, 4056-4060.

(9) J. Liu, P. K. Thallapally, B. Peter McGrail, D. R. Brown and J. Liu, *Chem. Soc. Rev.*, 2012, **41**, 2308-2322.

(10) O. Shekah, Y. Belmabkhout, Z. Chen, V. Guillerm, A. Cairns, K. Adil and M. Eddaoudi, *Nat. Commun.*, 2014, 4228.

(11) R. Vaidhyanathan, S. S. Iremonger, G. K. H. Shimizu, P. G. Boyd, S. Alavi and T. K. Woo, *Science*, 2010, **330**, 650-653.

(12) P. Horcajada, R. Gref, T. Baati, P. K. Allan, G. Maurin, P. Couvreur, G. Férey, R. E. Morris and C. Serre, *Chem. Rev.*, 2012, **112**, 1232-1268.

(13) C. He, K. Lu, D. Liu and W. Lin, *J. Am. Chem. Soc.*, 2014, **136**, 5181-5184.

(14) Q. Hu, J. Yu, M. Liu, Z. Dou and Y. Yang, *J. Med. Chem.*, 2014, **57**, 5679-5685.

(15) D. Aulakh, J. R. Varghese and M. Wriedt, *Inorg. Chem.*, 2015, **54**, 1756-1764.

(16) T. Islamoglu, S. Goswani, Z. Li, A. J. Howarth, O. K. Farha and J. T. Hupp, *Acc. Chem. Res.*, 2017, **50**, 805-813.

(17) H.-C. Zhou and S. Kitagawa, *Chem. Soc. Rev.*, 2014, **43**, 5415-5418.

(18) K. Sumida, D. Stück, L. Mino, J.-D. Chai, E. D. Bloch, O. Zavorotynska, L. J. Murray, M. Dincă, S. Chavan, S. Bordiga, M. Head-Gordon and J. R. Long, *J. Am. Chem. Soc.*, 2013, **135**, 1083-1091.

(19) X. Zhao, X. Bu, Q.-G. Zhai, H. Tran and P. Feng, *J. Am. Chem. Soc.*, 2015, **137**, 1396-1399.

(20) R. Kannanppan, C. Bucher, E. Saint-Aman, J.-C. Moutet, A. Milet, M. Oltean, E. Métay, S. Pellet-Rostaing, M. Lemaire and C. Chaix, *New. J. Chem.*, 2010, **34**, 1373-1386.

(21) Q.-G. Zhai, X. Bu, X. Zhao, D.-S. Li and P. Feng, *Acc. Chem. Res.*, 2017, **50**, 407-417.

(22) D.-M. Chen, J.-Y. Tian, C.-S. Liu and M. Du, *Chem. Commun.*, 2016, **52**, 8413-8416.

(23) T. N. Mandal, A. Karmakar, S. Sharma and S. K. Ghosh, *Chem. Rec.*, 2018, **18**, 154-164.

(24) X. Ji, R.-T. Wu, L. Long, C. Guo, N. M. Khashab, F. Huang and J. L. Sessler, *J. Am. Chem. Soc.*, 2018, **140**, 2777-2780.

(25) B. Manna, A. K. Chaudhari, B. Joarder, A. Karmakar and S. K. Ghosh, *Angew. Chem., Int. Ed.*, 2013, **52**, 998-1002.

(26) X. Li, H. Xu, F. Kong and R. Wang, *Angew. Chem., Int. Ed.*, 2013, **52**, 13769-13773.

(27) A. J. Howarth, M. J. Katz, T. C. Wang, A. E. Platero-Prats, K. W. Chapman, J. T. Hupp and O. K. Farha, *J. Am. Chem. Soc.*, 2015, **137**, 7488-7494.

(28) Y. Li, Z. Yang, Y. Wang, Z. Bai, T. Zheng, X. Dai, S. Liu, D. Gui, W. Liu, M. Chen, L. Chen, L. Diwu, L. Zhu, R. Zhou, Z. Chai, T. E. Albretch-Schmitt and S. Wang, *Nat. Commun.*, 2017, **8**, 1354.

(29) Q. Zhang, J. Yu, J. Cai, L. Zhang, Y. Cui, Y. Yang, B. Chen and G. Qian, *Chem. Commun.*, 2015, **51**, 14732-14734.

(30) B.-Q. Song, X.-L. Wang, Y.-T. Zhang, X.-S. Wu, H.-S. Liu, K.-Z. Shao and Z.-M. Su, *Chem. Commun.*, 2015, **51**, 9515-9518.

(31) H. Fei, C. S. Han, J. C. Robins and S. R. J. Oliver, *Chem. Mater.*, 2013, **25**, 647-652.

(32) Z. Li, H. Li., X. Guan, J. Tang, Y. Yusran, Z. Li, M. Xue, Q. Fang, Y. Yan, V. Valtchev S. Qiu, *J. Am. Chem. Soc.*, 2017, **139**, 17771-17774.

(33) J. Li, X. Wang, G. Zhao, C. Chen, Z. Chai, A. Alsaedi, T. Hayat and X. Wang, *Chem. Soc. Rev.*, 2018, **47**, 2322-2356.

(34) R. J. Drout, K. Otake, A. J. Howarth, T. Islamoglu, L. Zhu, C. Xiao, S. Wang and O. K. Farha, *Chem. Mater.*, 2018, **30**, 1277-1284.

(35) M. A. Patino, T. Smith, W. Zhang, P. S. Halasyamani and M. A. Hayward, *Inorg. Chem.*, 2014, **53**, 8020-8024.

(36) Z. Bai, Y. Wang, Y. Li, W. Liu, L. Chen, D. Sheng, J. Diwu, Z. Chai, T. E. Albrecht-Schmitt and S. Wang, *Inorg. Chem.*, 2016, **55**, 6358-6360.

(37) S. Beck, S. Lieber, F. Schaper, A. Geyer and H.-H. Brintzinger, *J. Am. Chem. Soc.*, 2001, **123**, 1483-1489.

(38) K. M. Ok, J. Baek, P. S. Halasyamani and D. O'Hare, *Inorg. Chem.*, 2006, **45**, 10207-10214.

(39) J. Li, X. Dai, L. Zhu, C. Xu, D. Zhang, M. A. Silver, P. Li, L. Chen, Y. Li, D. Zuo, H. Zhang, C. Xiao, J. Chen, J. Diwu, O. K. Farha, T. E. Albrecht-Schmitt, Z. Chai and S. Wang, *Nat. Commun.*, 2018, **9**, 3007.

(40) L. Zhu, D. Sheng, C. Xu, X. Dai, M. A. Silver, J. Li, P. Li, Y. Wang, Y. Wang, L. Chen, C. Xiao, J. Chen, R. Zhou, C. Zhang, O. K. Farha, Z. Chai, T. E. Albrecht-Schmitt and S. Wang, *J. Am. Chem. Soc.*, 2017, **139**, 14873-14876.

(41) L. Zhaoping, R. Ma, M. Osada, N. Iyi, Y. Ebina, K. Takada and T. Sasaki, *J. Am. Chem. Soc.*, 2006, **128**, 4872-4880.

(42) K.-H. Goh, T.-T. Lim and Z. Dong, *Water Res.*, 2008, **42**, 1343-1368.

(43) M. Meyn, K. Beneke and G. Lagaly, *Inorg. Chem.*, 1990, **29**, 5201-5207.

(44) B. Sels, D. De Vos, M. Buntinx, F. Pierard, A. K.-D. Mesmaeker and P. Jacobs, *Nature*, 1999, **400**, 855-857.

(45) A. M. Fogg, J. S. Dunn, S.-G. Shyu, D. R. Cary and D. O'Hare, *Chem. Mater.*, 1998, **10**, 351-355.

(46) G. M. Haggerty and R. S. Bowman, *Environ. Sci. Technol.*, 1994, **28**, 452-458.

(47) A. M. Yusof and N. A. N. N. Malek, *J. Hazard. Mater.*, 2009, **162**, 1019-1024.

(48) X. Liu, U. Ravon and A. Tuel, *Angew. Chem. Int. Ed.*, 2011, **50**, 5900-5903.

(49) D. T. Tran, P. Y. Zavalij and S. R. J. Oliver, *J. Am. Chem. Soc.*, 2002, **124**, 3966-3969.

(50) F. Geng, R. Ma and T. Sasaki, *Acc. Chem. Res.*, 2010, **43**, 1177-1185.

(51) I. R. Colinas, K. K. Inglis, F. Blanc and S. R. J. Oliver, *Dalton Trans.*, 2017, **46**, 5320-5325.

(52) P.-F. Shi, B. Zhao, G. Xiong, Y.-L. Hou, P. Cheng, *Chem. Commun.*, 2012, **48**, 8231-8233.

(53) S. Rapti, A. Pournara, D. Sarma, I. T. Papadas, G. S. Armatas, A. C. Tsipis, T. Lazarides, M. G. Kanatzidis and M. J. Manos, *Chem. Sci.*, 2016, **7**, 2427-2436.

(54) S. R. J. Oliver, *Chem. Soc. Rev.*, 2009, **38**, 1868-1881.

(55) S. Wang, E. V. Alekseev, J. Diwu, W. H. Casey, B. L. Phillips, W. Depmeier and T. E. Albretch-Schmitt, *Angew. Chem. Int. Ed.*, 2010, **49**, 1057-1060.

(56) H.-R. Fu, Z.-W. Xu and J. Zhang, *Chem. Mater.*, 2015, **27**, 205-210.

(57) W. Liu, Y. Wang, Z. Bai, Y. Li, Y. Wang, L. Chen, L. Xu, J. Diwu, Z. Chai and S. Wang, *ACS Appl. Mater. Inter.*, 2017, **9**, 16448-16457.

(58) United States Environmental Protection Agency: https://www.epa.gov/dwreginfo.

(59) F. Robinson, M. J. Zaworotko, *J. Chem. Soc., Chem. Commun.*, 1995, 2413-2414.

(60) H. Fei, D. L. Rogow and S. R. J. Oliver, *J. Am. Chem. Soc.*, 2010, **132**, 7202-7209.

(61) M. Eddaoudi, D. B. Moler, H. Li, B. Chen, T. M. Reineke, M. O'Keeffe and O. M. Yaghi, *Acc. Chem. Res.*, 2001, **34**, 319-330.

(62) X. Zhao, C. Mao, K. T. Luong, Q. Lin, Q.-G. Zhai, P. Feng and X. Bu, *Angew. Chem., Int. Ed.*, 2016, **55**, 2768-2772.

(63) C. Mao, R. A. Kudla, F. Zuo, X. Zhao, L. J. Mueller, X. Bu and P. Feng, *J. Am. Chem. Soc.*, 2014, **136**, 7579-7582.

(64) T. Aharen, F. Habib, I. Korobkov, T. J. Burchell, R. Guillet-Nicolas, F. Kleiz and M. Murugesu, *Dalton Trans.*, 2013, **42**, 7795-7802.

(65) Q.-G. Zhai, X. Bu, C. Mao, X. Zhao, L. Daemen, Y. Cheng, A. J. Ramirez-Cuesta and P. Feng, P. *Nat. Commun.*, 2016, **7**, 13645.

(66) S.-T. Zheng, X. Zhao, S. Lau, A. Fuhr, P. Feng and X. Bu, *J. Am. Chem Soc.*, 2013, **135**, 10270-10273.

(67) R. Custelcean and B. A. Moyer, *Eur. J. Inorg. Chem.*, 2007, **2007**, 1321-1340.

(68) L. Carlucci, G. Ciani, S. Maggini, D. M. Proserpio and M. Visconti, *Chem. – Eur. J.*, 2010, **16**, 12328-12341.

(69) X. Zhao, X. Bu, T. Wu, S.-T. Zheng, L. Wang and P. Feng, *Nat. Commun.*, 2013, **4**, 2344.

(70) Z. Hasan and S. H. Jhung, *J. Hazard. Mater.*, 2015, **283**, 329-339.

(71) N. A. Khan, Z. Hasan and S. H. Jhung, *J. Hazard. Mater.*, 2013, **244-245**, 444-456.

(72) A. C. Sudik, A. P. Côté and O M. Yaghi, *Inorg. Chem.*, 2005, **44**, 2998-3000.

(73) S. Wongsakulphasatch, F. Nouar, J. Rodriguez, L. Scott, C. Le Guillouzer, T. Devic, P. Horcajada, J.-M. Grenèche, P. L. Llewellyn, A. Vimont, G. Clet, M. Daturi and C. Serre, *Chem. Commun.*, 2015, **51**, 10194-10197.

(74) Q. Gao, X.-L. Zhao, Z. Chang, J. Xu and X.-H. Bu, *Dalton Trans.*, 2016, **45**, 6830-6833.

(75) J.-B. Lin and G. K. H. Shimizu, *Inorg. Chem. Front.*, 2014, **1**, 302-305.

(76) T. Aharen, F. Habib, I. Korobkov, T. J. Burchell, R.; Guillet-Nicolas, F. Kleiz and M. Murugesu, *Dalton Trans.*, 2013, **42**, 7795–7802.

(77) M.-X. Li, Z.-X. Miao, M. Shao, S.-W. Liang and S.-R. Zhu, *Inorg. Chem.*, 2008, **47**, 4481–4489.

(78) *APEX Software Suite v. 2010*, Bruker AXS, Madison, WI, 2005.

(79) Bruker *SADABS*, Bruker AXS Inc., Madison, WI, 2001.

(80) Rigaku Oxford Diffraction, *CrysAlisPro Software system*, version 1.173.37.35, Rigaku Corporation, Oxford, UK, 2018.

(81) G. M. Sheldrick, *Acta Cryst.*, 2015, **A71**, 3-8.

(82) G. M. Sheldrick, *Acta Cryst.*, 2015, **C71**, 3-8.

(83) P. Emsley, B. Lohkamp, W. G. Scott and K. Cowtan, *Acta. Cryst.*, 2010, **D66**, 486-501.

(84) G. Kresse and M. Marsman, *VASP Manual*, 2014.

(85) G. Kresse and J. Furthmüller; *Phys. Rev. B*, 1996, **54**, 11169-11186.

(86) J. P. Perdew, J. A. Chevary, S. H. Vosko, K. A. Jackson, M. R. Pederson, D. J. Singh and C. Fiolhais, *Phys. Rev. B*, 1993, **48**, 4978.

(87) J. P. Perdew, K. Burke and M. Ernzerhof, *Phys. Rev. Lett.*, 1996, **77**, 3865-3868.

Every generation has the right to build its own world out of the materials of the past, cemented by the hopes of the future.
– Herbert Hoover[8]

Chapter 7

Conclusions and outlook

As we continue to enhance our control over hybrid metal-organic assemblies, the key parameters that dictate certain properties and behaviours are becoming ever clearer. This sets the stage for novel applications and future technologies that will undoubtedly surpass the current state-of-the-art. As demonstrated throughout this *Thesis*, materials that are built upon coordination bonds can be utilized in a number of different ways, ranging from ion capture, to crystallographic visualization and single-molecule magnetism. Each of these, in their own right, has exciting potential applications within the nanosciences.

In chapter 2, we looked at how a crystalline sponge host can impact the physical properties of a guest molecule, particularly in terms of its molecular dynamics. Ultimately, this hinges on the chemical environment in which the guest compound finds itself, and clearly demonstrates how encapsulation within a porous material can drastically alter some specific properties. The initial design of the project relied largely on these principles. In fact, the selection of the ferrocene-based molecules was not random; we were interested in extending this strategy to other metallocene sandwich compounds, some of which are among the highest-performing single-molecule magnets. On one hand, we could tune the chemical environment of the SMM, through confinement within a select space. As described in this *Thesis*, the performance of an

[8] *Speech at the Republican National Convention, Chicago, 1944.*

SMM relies heavily upon various molecular vibrations (*i.e.* Raman processes), and therefore, guest encapsulation could provide a means towards improving the blocking temperature of these molecules. On the other hand, we can also potentially improve the stability of these molecules, which are notorious for being highly air-sensitive, thereby rendering any potential applications slightly more troublesome to achieve.

In Chapter 3, we focused on the magnetic behaviours that can arise from such porous assemblies. More specifically, the magnetic isolation of paramagnetic metal centres may provide a way of nanostructuring SIMs within a MOF. This would allow for additional control on magnetic relaxation pathways, where through-barrier processes could be limited by restricting or minimizing molecular vibrations. While diamagnetic MOFs might be the best approach towards studying the encapsulation of SMMs within a host structure, we can easily envision a scenario where the paramagnetic nature of both host and guest compounds could be synergistic. Further work could also be directed at the inclusion of different guest species and evaluating the change in SMM-like behaviour arising from the host network. In fact, even a change in the solvent molecule has been known to tune the magnetic behaviour of porous MOFs.

The design of a new nitrogen-rich ligand within the group that features coordination pockets reminiscent of terpy-like ligands, prompted us to evaluate the coordination chemistry of this specific chelate (Chapter 4). Due to the highly oxophilic nature of the lanthanide ions, and the lack of nitrogen-coordinated Ln^{III} SMMs, we thought it might be interesting to test whether the H_4TTP ligand could coordinate to Dy^{III} ions. We successfully obtained two different kinds of architectures and evaluated the differences in their magnetic behaviour. While their SMM characteristics are not particularly groundbreaking, the formation of coordination polymers with nitrogen-rich ligands is quite appealing from an energetic materials perspective. In fact,

preliminary efforts the same ligand and Cu(II), an environmentally friendly metal ion, has yielded a ladder-like 2D sheet arrangement with promising detonation parameters. It would be fascinating to continue investigations in this area to provide non-toxic explosives, with the main by-product being N_2.

In Chapter 5, we looked at how radical ligands be can promote strong magnetic communication and stimuli-responsive materials. The work on Dy_4 cubanes is notable since there still remain some challenges in making magnetically relevant lanthanide cluster-aggregates. This is mainly due to the difficulty in the magnetic coupling of Ln^{III} ions, however the use of radical ligands may provide a way of achieving this goal, and in doing so, reinvigorate the field of high nuclearity Ln^{III} clusters. Alternatively, redox active ligands, such as those based on viologen moieties, are extremely promising for a number of applications, including molecular sensors and catalysis. This essentially imbues the material with a "smart" functionality, where specific triggers can lead to a change in the property of the molecule. This was illustrated through the design of a beautiful nanobarrel structure that is multi-stimuli responsive. Currently, through collaboration with ENS Lyon, we are developping additional systems using similar viologen building blocks for catalytic C-C bond cleavage, and for the electrochemical reduction of CO_2.

Lastly, Chapter 6 addresses a distinct need for new strategies to systematically cationize nanoporous frameworks. This was done by applying a new method, termed the ALE method, which replaces linear dicarboxylates with asymmetric linkers that feature one less negative charge, but maintain similar binding modes. Thus, we have gained access to a new series of cationic frameworks, and even proposed a method of retaining porosity in such systems, through the use of strongly binding anions. These advances will undoubedtly assist in the design of

cationic MOFs and encourage applications based on purification or ion exchange. Our newly developed method of retaining porosity in charged frameworks is routinely being applied to other systems in the group, as we continue to refine and improve upon the technique.

Overall, this *Thesis* provides but a flavor of the rich chemistry that is attainable from the use of metal-organic assemblies. There remains a wide range of directions that can be undertaken to further improve and make use of the projects described herein. It is my hope that these studies will lay the foundation for future research programs involving new and current members of the group, as well as others in field, in seeking to continue to advance our control over such nanomaterials.